NASA-CR 72605
LMSC-A903316

INTERIM REPORT

THERMAL PERFORMANCE OF MULTILAYER INSULATIONS

by

G. R. Cunnington, C. W. Keller and G. A. Bell

LOCKHEED MISSILES & SPACE COMPANY
Sunnyvale, California 94088

prepared for

NATIONAL AERONAUTICS AND SPACE ADMINISTRATION

20 April 1971

CONTRACT NAS3-12025

Nasa Lewis Research Center
Cleveland, Ohio 44135
James R. Barber, Project Manager
LIQUID ROCKET TECHNOLOGY BRANCH

FOREWORD

The Lockheed Missiles & Space Company is submitting this Interim Report in partial completion of the requirements of Contract NAS 3-12025, Thermal Performance of Multilayer Insulations, dated June 27, 1968. The total scope of work, data, results and conclusions pertinent to this program are being presented in two report volumes. This first volume covers analytical and experimental activities performed under Tasks I and II of the contract. The second volume is being submitted as the Final Report and describes the analytical and experimental activities performed under Task III.

CONTENTS

CONTENTS (Cont'd)

ILLUSTRATIONS

ILLUSTRATIONS (Cont'd)

ILLUSTRATIONS (Cont'd)

ILLUSTRATIONS (Cont'd)

ILLUSTRATIONS (Cont'd)

TABLES

ABSTRACT

Analytical and experimental studies were conducted to assess the thermal performance of four multilayer insulations: double-aluminized Mylar/silk net, double-goldized Mylar/silk net, crinkled single-aluminized Mylar, and double-aluminized Mylar/Tissuglas. Heat flux and optical property measurements were obtained for a wide range of variables including number of layers, applied compressive pressures, thickness, and boundary temperatures. A series of equations were developed which characterize the thermal performance of each of the four insulations. All four insulations exhibited reproducibility of heat flux as function of compressive pressure within $\pm$ 20 percent. The silk net and Tissuglas spacer composites exhibited reproducibility of heat flux as a function of layer density within $\pm$ 30 percent, whereas that for the crinkled Mylar system varied up to $\pm$ 80 percent. Comparison of insulation and liquid hydrogen boiloff weights per unit area for a typical design heat flux of 0.300 Btu/hr ft^2 (0.946 w/m^2) and a 30-day mission revealed that the Tissuglas spacer system was optimum if the design layer density values were achieved, but that the double-goldized Mylar/silk net composite was optimum if the actual layer density values exceeded the design values by 30 percent or more.

Section 1
SUMMARY

The primary goal of this program was to develop a series of related analytical expressions that can be evaluated and used to predict accurately the thermal performance of each of four multilayer insulations as installed on a cryogen tank and exposed to a vacuum environment. The four insulations are: double-aluminized 1/4-mil Mylar with double silk net spacers, double-goldized 1/4-mil Mylar with double silk net spacers, crinkled single-aluminized 1/4-mil Mylar, and double-aluminized 1/4-mil Mylar with Tissuglas spacers. Both analytical and experimental studies were conducted to assess the heat transfer characteristics and the thermal performance of these insulations. Heat flux measurements were obtained for multiple specimens of each composite system for hot boundary temperatures of 500°R (278°K) and 610°R (339°K), and for cold boundary temperatures of 37°R (20°K) and 140°R (77°K). The heat flux values were obtained as a function of the number of layers, applied compressive pressure, and specimen thickness over a wide range of these parameters.

All four insulations exhibited reproducibility of heat flux as a function of applied compressive pressure within $\pm$ 20 percent. The reproducibility of heat flux as a function of layer density was found to be within $\pm$ 30 percent for the silk net and the Tissuglas spacer systems; however, it varied up to $\pm$ 80 percent for the crinkled, single-aluminized Mylar system.

Insulation and propellant boiloff weight increments per unit area were compared for the four insulations applied to storage of liquid hydrogen for 30 days in a space environment. For a typical design heat flux of 0.300 Btu/hr ft^2 (0.946 w/m^2), it was found that the Tissuglas spacer system exhibited the minimum incremental system weight of 1.34 lbm/ft^2 (6.54 kg/m^2) if the design layer density values were achieved, and if maximum heat flux penalties based on reproducibility were included. For these conditions, the unit system weights were only slightly higher for the silk net spacer systems, and significantly higher for the crinkled Mylar system. It was also shown, however,

that the double-goldized Mylar/silk net system exhibited the lowest unit system weight if the actual layer density values achieved in practice were higher than the design values by 30 percent or more.

Section 2
INTRODUCTION

This report describes work performed under Tasks I and II of an analytical and experimental study program conducted to investigate the thermal performance of multilayer insulations which may be used for the long-term storage of cryogens in space. This work was sponsored by the Liquid Rocket Technology Branch, Lewis Research Center, National Aeronautics and Space Administration, Cleveland, Ohio.

The program goal was the development and verification of an analytical technique for accurately predicting the thermal performance of multilayer insulations when applied to an actual cryogen storage tank. The technical approach to the problem was to determine by small scale laboratory tests the heat transfer characteristics, in a direction normal to the insulation layers, of several candidate insulations as a function of boundary temperatures, compressive loading, thickness, and number of layers. These data then were used to derive and subsequently to evaluate the accuracy of an analytical expression which describes the one-dimensional thermal performance of each candidate insulation in terms of the above variables. Verification of the usefulness of the expression as a means for predicting tank-installed performance then was accomplished through testing of one selected insulation system on a 4-ft-(1.22-m-) diameter tank calorimeter under Task III.

To accomplish the program objective, the study effort was divided into three consecutive tasks. During the initial phase, Task I, the accuracy and repeatability of the experimental apparatus used for heat transfer studies was demonstrated. Also, the degree of sample-to-sample reproducibility was established for two types of multilayer insulation. Task II was directed toward the measurements of heat transfer characteristics of multiple specimens of four insulations and the derivation and subsequent evaluation of an analytical model describing the thermal conduction and radiation processes for these insulations. Using this model, equations were established for predicting the

thermal performance of the tank test insulation in terms of boundary temperatures, layer density and total number of layers. Under Task III one insulation system, double-goldized Mylar with silk net spacers, was applied to the 4-ft-(1.22-m-) diameter tank, and tests were conducted to demonstrate the accuracy of the thermal performance prediction procedure.

Section 3 of this report discusses the Task I effort. It includes the approaches taken to measure thermal performance and to demonstrate measurement accuracy and repeatability. Specifications for the test materials and procedures established for preparation of test specimens are described. Results of heat transfer tests of multiple specimens of two insulations are presented to illustrate the reproducibility of these materials. Tests were conducted with LN_2 and LH_2 cryogens. The two insulations used for these studies are double-aluminized 1/4-mil Mylar, with two layers of silk net for each spacer, and crinkled, single-aluminized 1/4-mil Mylar. These were selected as they represent the separate-spacer and integral-spacer concepts in multilayer insulation. Also, the effects of compressive loading and number of layers on thermal performance are qualitatively evaluated.

A flat plate type of apparatus was chosen for the thermal performance tests as with this device heat transfer rates can be determined as a function of applied compressive pressure and thickness on a single specimen without disrupting the specimen or vacuum or temperature conditions. The "boil-off calorimeter" technique was used for heat-flux measurements. It has good accuracy over the range of the test requirements of this program and is readily adaptable to the flat plate configuration (Ref. 1). The Lockheed 16-in.-(40.6-cm-) diameter double-guarded flat plate calorimeter (FPC) apparatus (Ref. 2) was used for all laboratory heat transfer studies in Tasks I and II.

As thermal radiation plays an important role in certain regimes of multilayer insulation heat transfer (Ref. 3), it is necessary to understand the behavior of the thermal radiation characteristics of the reflective shields as a

function of temperature in the analysis of the overall heat transport process. Measurements of the total hemispherical emittance, as a function of temperature, of several samples of each type of reflective shield were initiated in Task I in order that the data would be available for the analytical studies of Task II.

The derivation of the analytical heat transfer model is discussed in Section 4, and the resultant equations for computation of the heat flux through the four insulations are given in terms of temperature, compressive pressure or layer density, number of layers and radiative properties of shields and spacers.

Experimental results of heat transfer tests conducted on multiple specimens of the following insulations are discussed in Section 4.

- Double-aluminized 1/4-mil Mylar with two layers of silk net* for each spacer
- Double-goldized 1/4-mil Mylar with two layers of silk net for each spacer
- Crinkled, single-aluminized 1/4-mil Mylar
- Double-aluminized Mylar with Tissuglas** paper spacers

Tests were performed at boundary temperatures of 610°R and 500°R (339°K and 278°K) to 140°R and 37°R (77°K and 20°K). Compressive pressures were varied from 1×10^{-4} to 1×10^{-1} psi (0.69 to 690 N/m^2). Specimens were composed of 5, 10, 20 and 40 radiation shields. The results of the studies of temperature dependence of the total hemispherical emittance of the radiative shields are also presented in this section. Finally, the predictions of thermal performance for the selected tank test insulation, double-goldized 1/4-mil Mylar with silk net spacers, are discussed.

---

* John Heathcoat Co.
** Pallflex Products Co.

Section 3

TASK I - INSULATION REPEATABILITY AND CALORIMETER CHECKOUT

The overall objectives of this portion of the program were to demonstrate the repeatability of the Flat Plate Calorimeter (FPC) apparatus for multilayer insulation heat transfer data and subsequently to determine the reproducibility of two types of insulation material. These results form the basis for evaluation of the data from tests of multiple specimens of four multilayer insulations investigated in Task II. The specific objectives of Task I were to:

- Demonstrate the absolute accuracies of the measurements of heat rate, boundary temperatures, compressive load, and specimen thickness in the FPC apparatus.
- Determine the repeatability of insulation heat flux measurements in the FPC. Ideally, this information would result from the calibration data. However, because of the high degree of anisotropy in multilayer insulations, the presence of the test specimen may alter the heat flow paths in a manner such that the repeatability is a function of not only the repeatabilities of each measurement, but also of the effect of a specimen on the measurement. As no standard material of known reproducibility exists for the multilayer class of insulation, the repeatability to be expected for the Task II heat transfer tests is determined from a series of tests on a single specimen under identical conditions.
- Determine the degree of sample-to-sample reproducibility based upon tests of several specimens of the same material.

Total hemispherical emittance measurements on representative specimens of each reflective shield material also were initiated in Task I. These data are necessary for the heat transfer analysis in Task II, as well as the evaluations of the factors contributing to observed reproducibility in the performance of several specimens of the same insulation system.

3.1 EXPERIMENTAL APPARATUSES AND PROCEDURES

3.1.1 Flat Plate Calorimeter Measurements

In this device the thermal energy transferred through an insulation specimen is measured by a calorimetric method. All of the energy crossing the cold boundary in the central portion of a disk-shaped specimen is intercepted by a fluid maintained at or near its normal boiling point. This energy goes totally into the boiling of the calorimeter fluid (LH_2 or LN_2 for this program). Heat flux is calculated from the fluid thermodynamic properties and the measured boiloff rate. The apparatus also includes provisions for measuring compressive force applied to the specimen and the separation between hot and cold boundary surfaces in contact with the insulation.

Experimental Apparatus The flat plate apparatus consists essentially of calorimeter and guard cryogen reservoirs, a hot-boundary surface plate, a vacuum chamber and pumping system, and a means for remotely changing and measuring specimen thickness (see Figs. 3-1 and 3-2). The calorimeter portion is a 6.25-in.(15.9-cm)-diameter by 8-in.-(20.3-cm)-high vessel constructed of stainless steel with an 0.25-in.-(0.64-cm)-thick copper plate that contacts the specimen. The calorimeter is filled with copper wool to improve internal heat transfer and has concentric fill and vent tubes entering at the top. The inner guard reservoir is constructed from stainless steel and measures 16-in.(40.6-cm)O.D. by 6.5-in.(16.5-cm)I.D. and it surrounds the sides and top of the calorimeter vessel. A copper cylinder is placed vertically in the guard chamber to minimize thermal gradients and also to ensure that the measuring section fill and vent-line thermal grounding remains at constant temperature and is not a function of cryogen level. All surfaces contacting the insulation are painted with a flat black paint* having a total hemispherical emittance (Ref. 4) ranging from 0.78 at 90°R (50°K) to 0.95 at 540°R (300°K). The outer guard reservoir, of all stainless steel construction, is 28-in.(71.1-cm)O.D. by 23-in.(58.4-cm)I.D. and surrounds the inner guard as shown in Fig. 3-2. Three 2-in.-(5.1-cm)-diameter passages are located 120 degrees apart in the side wall of this vessel for viewing the specimen

*Finch Paint and Chemical Co. "Cat-a-lac", Code 463-3-8.

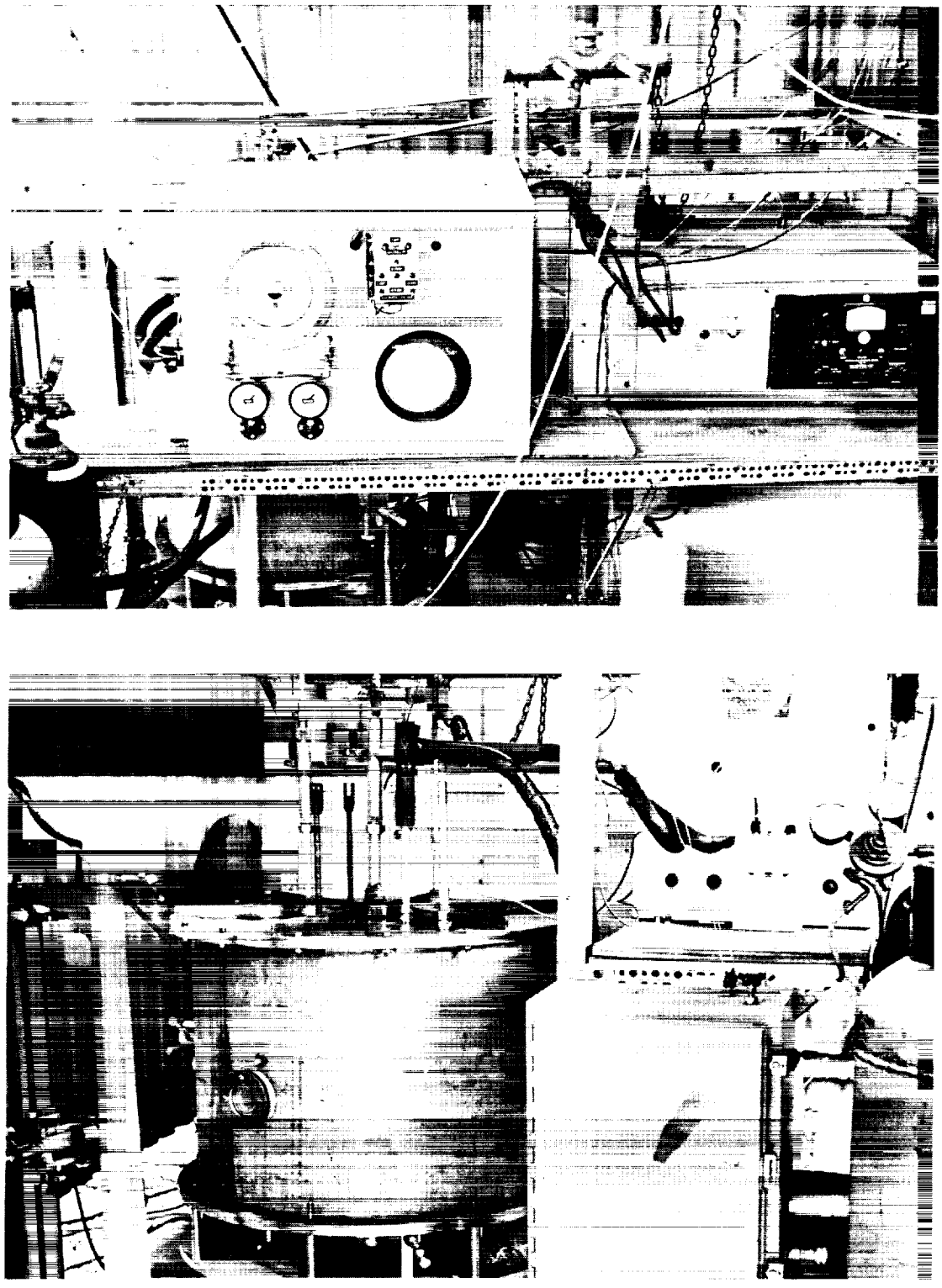

Fig. 3-1 Flat Plate Calorimeter (FPC)

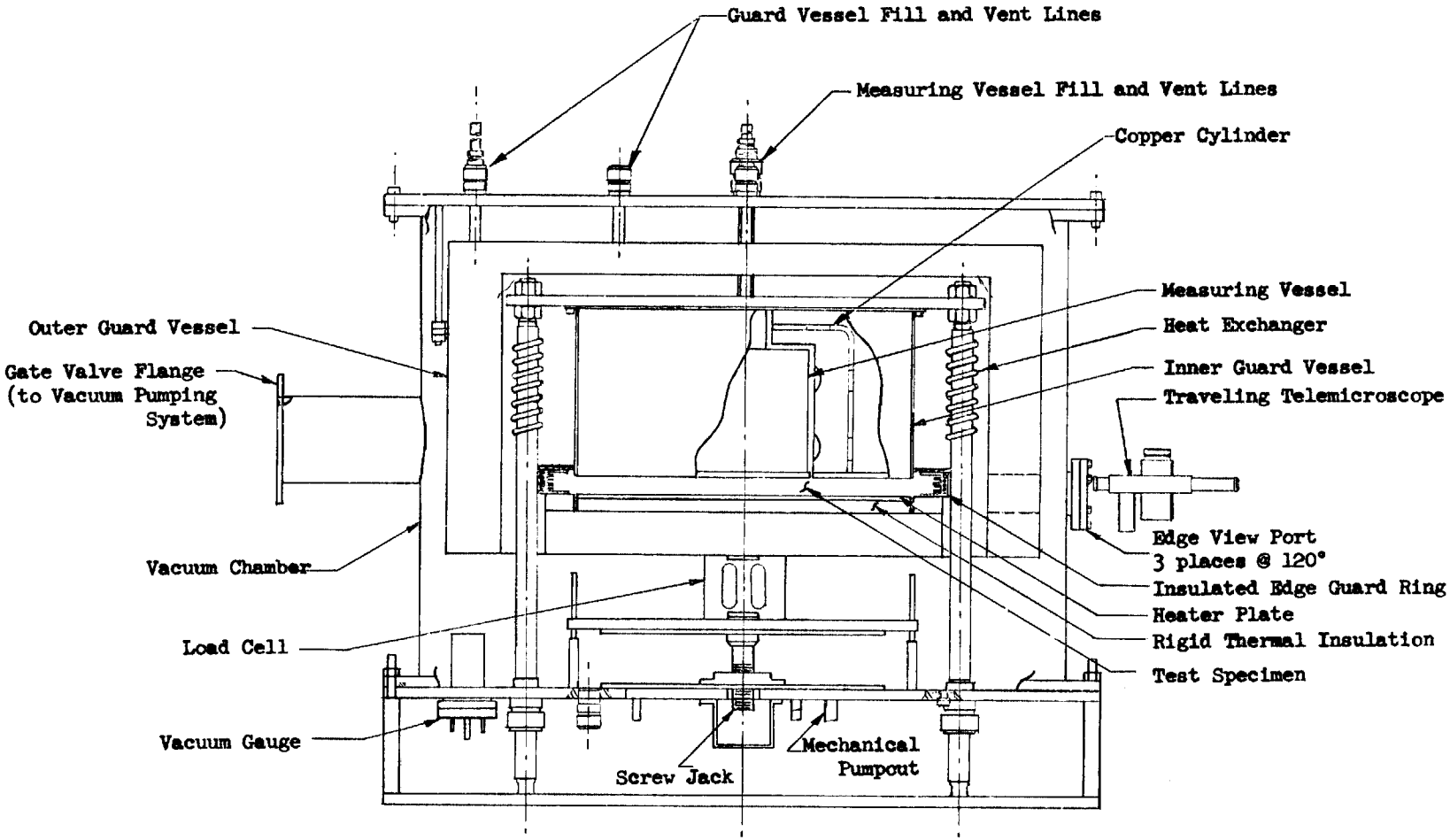

Fig. 3-2 Flat Plate Calorimeter Schematic

and boundary plate edges. Outer guard level is maintained within 0.5-in. (1.3-cm) of the top by an automatic level sensor-fill device. Compressive forces on the calorimeter section are transmitted to the guard section through three spherical glass contacts. Adjustment means are provided to maintain the surfaces contacting the insulation in the same plane within 4×10^{-3} in. (1×10^{-2}cm). Calorimeter section vent and fill lines are thermally grounded to the guard reservoir, and a radiation baffle is provided in the fill line. A platinum resistance thermometer is attached to the thermal connection between the measuring section fill and vent line and the inner guard reservoir for monitoring of any temperature changes with guard liquid level. Three carbon-resistance thermometers are placed vertically in the guard at the vent position to sense cryogen level. The outer edge of the inner guard is also instrumented with a resistance thermometer and a copper-constantan thermocouple.

Hot boundary temperature is maintained by a 16-in.-(40.6-cm)-diameter by 0.25-in.-(0.64-cm)-thick copper heater plate painted black* on the surface in contact with the insulation. A stainless-steel-sheathed "Kanthal" heater winding is brazed to the underside of this plate, and the assembly is thermally insulated from the water-cooled support plate. Five chromel-alumel thermocouples are peened into the plate, one for control and four for hot-boundary-temperature measurement. Control of heat temperature to $\pm$ 0.5°R ($\pm$0.3°K) is achieved using a Leeds and Northrop CAT controller with null detector and set-point unit in conjunction with a silicon-controlled-rectifier power supply. An edge-guard unit is provided for control of the radiative environment viewed by the circumferential edge of the specimen. This unit may be operated at temperatures between 700°R (389°K) and 140°R (77°K). Five chromel-alumel thermocouples are attached to the ring for temperature control and measurement.

* Finch Paint and Chemical Co. "Cat-a-lac", Code 463-3-8.

The compressive force exerted on the specimen is measured by a strain-gage-type load cell centrally located between the hot boundary surface unit and a moveable plate having linear bearing guides. The plate is raised and lowered by a remotely operated screw-type jack located in the bottom of the main vacuum chamber. The load cell accuracy is $\pm$ 0.1 lbf ($\pm$0.4N) for forces up to 100 lbf (445 N).

Specimen thickness is determined by measurement of the separation between the fixed calorimeter and guard surface and the moveable heater plate surface. Plate separation is measured optically using Gaertner Model M101AT microscopes with Model M301A micrometer slides mounted at three viewports located 120 degrees apart. Accuracy of the distance measurement is 1×10^{-3} in. (2.5×10^{-3} cm).

The vacuum chamber is fabricated from stainless steel and is 30-in. (76.2-cm) in diameter by 24-in. (61-cm) high. The pumping system includes a 4-in. (10.2-cm) LN_2 trapped oil diffusion pump and a 15-cfm (0.42 m^3 per min) fore pump. During testing, chamber pressure is maintained at 5×10^{-6} torr or less before filling of the cryogen reservoirs. During heat flux measurements chamber pressure is 1×10^{-6} torr or less.

The instrumentation provided for continuous data acquisition is primarily that required for temperature, pressure, compressive load and calorimeter-section boiloff measurements. A 12-point stripchart recorder is used for monitoring thermocouples. A Leeds and Northrop K-3 precision potentiometer used in conjunction with an amplifier and precision current supply is used for resistance thermometry and measurement of hot boundary thermocouples. Boiloff gas temperature is measured with a mercury-in-glass thermometer in the wet-test meter, and gas pressure at the meter is measured with a Wallce and Tiernan absolute pressure gage. Ionization gages are used for vacuum-chamber pressure measurement. The calorimeter boiloff gas flow is measured simultaneously by a thermal-type mass flowmeter (Schucco) and a precision wet-test meter connected in series (Fig. 3-3). The mass flowmeter and guard-to-calorimeter differential pressure transducer outputs are continuously recorded

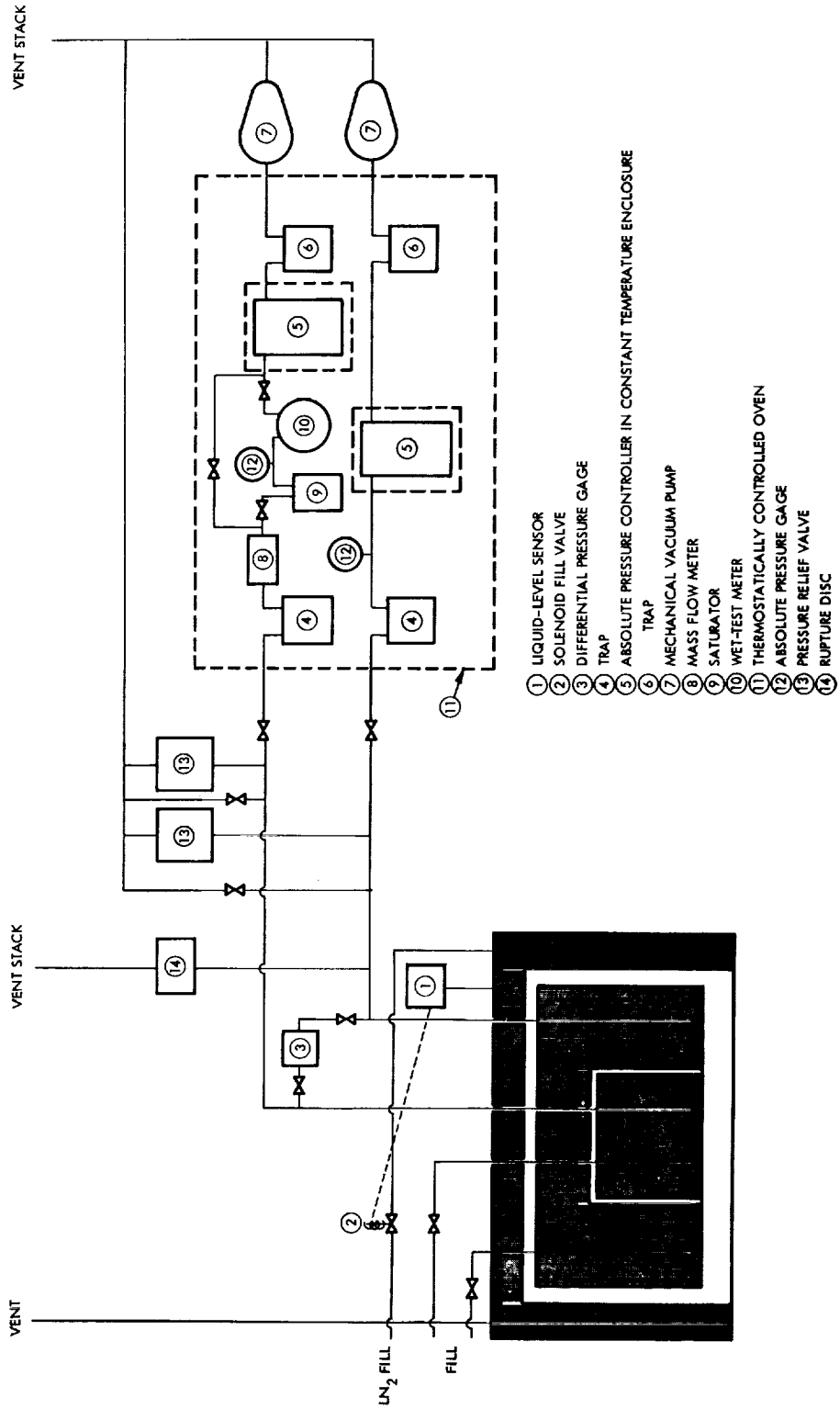

Fig. 3-3 Flow Control and Instrumentation Schematic

on variable-range, adjustable-zero recorders. Gas pressures in both the calorimeter and guard reservoir are maintained to within 0.03 in. Hg (0.76 mm Hg) by cartesian type manostats connected to both flow circuits and located upstream from mechanical vacuum pumps. The manostats are adjusted to maintain the guard reservoir at a pressure of 0.08 in. Hg (2 mm Hg) greater than that in the calorimeter vessel. Because the flow-measuring devices and the manostats are sensitive to ambient temperature changes, they are located in a constant-temperature box. The manostats are also placed in separate ovens in this enclosure for precise control of their temperatures. A record of the wet-test meter flow, based on one complete revolution of 0.11 ft^3 (3 liters) is recorded as a function of time. Load cell output is continuously recorded on a variable-range, adjustable - zero, 10-in. (25.4 -cm) strip chart recorder (Leeds and Northrop AZAR-W). Auxiliary equipment is provided for control of heater temperatures and automatic filling of the outer guard reservoir.

Experimental Procedures Prior to the start of each test the load cell calibration is checked by placing a 1.00 lbm (0.454 kg) weight, equivalent to a 4.98×10^{-3} psi (34.3 N/m^2) compressive load, in the center of the hot boundary surface plate. The tare load of this hot boundary unit is compensated for by an adjustable zero feature of the load cell electronic unit. The plate is then moved up and down to verify that the cell output is not affected by variations in bearing friction in the plate guides. The weight is removed, and the insulation specimen is placed on the hot boundary plate. The uncompressed thickness of the specimen is determined by raising the lower plate until the upper insulation surface is visually observed to contact the cold surface plate, and the spacing between plates is measured at the three viewing ports. The separation between the hot and cold surfaces is then set to at least two times the initial specimen thickness so that the insulation is not subjected to any compressive loading during evacuation of the apparatus. After a chamber pressure of 5×10^{-6} torr is achieved, the cryogen reservoirs are filled, and the hot boundary plate is raised until the desired initial thickness or compressive load is achieved. The hot boundary temperature is

set, and the test is continued until equilibrium conditions are attained as determined by constant boil-off data for periods of 3 to 72 hours, this time being a function of the specimen heat rate and cryogen. When a minimum of four complete revolutions of the wet test meter, a total of 0.42 ft^3 (12 liters) of boiloff flow, show agreement to within 5 percent, equilibrium conditions are considered to be met. The continuous record of the mass flow meter is also examined for this time period to confirm that steady state was reached. Temperatures are recorded at hourly intervals, and test reservoir to inner guard reservoir pressure differential and load cell output are continuously recorded. Plate separation and the wet test meter temperature and pressure are recorded periodically throughout the test duration. The time to complete one test condition varies from 8 to 96 hours depending upon the insulation configuration and the cryogen used to achieve the desired cold boundary temperature.

The next test point is obtained by raising (or lowering) the hot boundary temperature to the next level without changing thickness or load. At the conclusion of this test the thickness (load) is changed, and the test repeated for both of the hot boundary temperatures. This sequence is repeated for additional increments of load until the maximum desired value is reached. The load is then decreased in several increments with data taken for both hot boundary temperatures. For a single specimen, heat flux is measured at each compressive load for two hot boundary temperatures with a single cold boundary temperature, either $37^{\circ}R(20^{\circ}K)$ or $140^{\circ}R$ $(77^{\circ}K)$.

The rate of heat input to the calorimeter, Q_c, is computed from

$$Q_c = \dot{v} \Delta H_v \rho$$

where $\dot{v}$ is the volumetric boiloff rate, ΔH_v is the latent heat of vaporization and ρ is the gas density at the wet test meter temperature and pressure. The pressure of the cryogen is the total pressure at the meter minus the

partial pressure of water (saturation conditions) for the meter temperature. Specimen heat flux is computed by dividing Q_c by the calorimeter surface area, 0.213 ft^2 (1.98 x $10^{-2} m^2$).

Apparatus Calibration The accuracies of the individual measurements associated with the Flat Plate Calorimeter testing were determined from a series of experiments designed to separately evaluate each of the following parameters:

- o Hot boundary temperature
- o Separation between boundaries (i.e., thickness)
- o Load cell force measurement
- o Wet test and mass flow meter calibration
- o Calorimeter heat rate

Accuracy of the hot boundary temperature measurement was confirmed by comparison of the thermocouples installed in the surface plate with a calibrated platinum resistance thermometer attached to the plate surface. Tests were performed in vacuum with a glass fiber paper composite placed between the hot and cold surfaces. Checks were made at 500°R (278°K), 550°R (306°K) and 610°R (339°K). Prior to installation in the plate, the thermocouples were individually calibrated at the triple point and at the boiling point of water. Maximum uncertainty in hot boundary temperature measurement is 1°R (0.6°K).

The accuracy of the measurement of plate separation using the telescopes was verified by placing gage blocks between the surface plates. The lower plate was then raised until solid contact between the block and upper plate was established. Distance between plate edge reference marks was measured at each telescope location. Maximum uncertainty in this measurement was found to be 1 x 10^{-3} in. (2.54 x 10^{-3} cm).

Load cell calibration was accomplished by comparison against standard load cells in a testing machine and through the use of dead weight loads. Over the force range of 0 to 100 lbf (0 to 445 N) the maximum uncertainty is 0.1 lbf

(0.4 N) which corresponds to a pressure of 5×10^{-4} psi (3.45 N/m^2) in the flat plate apparatus. From 100 to 400 lbf (445 to 1779 N) the accuracy is 0.2 lbf (0.9 N) corresponding to a compressive pressure of 1×10^{-3} psi (6.9 N/m^2).

The wet test meter was calibrated using a water displacement method to force a calibrated volume of saturated air through the meter at constant pressure. Calibration runs were made at flow rates of 0.0048, 0.0103, 0.0163, 0.0353, 0.0689, 0.122, 0.177, 0.252, and 0.357 ft^3/hr (0.136, 0.292, 0.461, 1.00, 1.95, 3.45, 5.00, 7.14, and 10.1 ℓ/hr, respectively). From these data a curve of indicated versus true flow rates was established. At flow rates of 0.177 ft^3/hr (5.0 ℓ/hr) or greater the time flow rate was within 1 percent of the indicated flow rate. The maximum deviation of a smooth curve passed through all points and any single data point is 0.3 percent. The uncertainty in total volume displaced is 0.5 percent, and the resultant maximum uncertainty in volume flow rate is 0.8 percent. The mass flow meter was calibrated against the wet test meter, using GH_2 and GN_2, in the Flat Plate Calorimeter flow loop. Mass flow meter maximum uncertainty is 5×10^{-6} lbm/hr (2.27×10^{-6} kg/hr) over the 5×10^{-4} to 1×10^{-2} lbm/hr (2.27×10^{-4} to 4.54×10^{-3} kg/hr) range.

Calibration of the calorimeter section was accomplished by introducing a known amount of thermal energy into the cold surface plate, and comparing this energy with that calculated from boiloff data. Any extraneous thermal exchanges between the calorimeter section and the remainder of the apparatus, such as through the fill and vent lines, are determined by this procedure. Also, it provides a direct comparison between energy entering the cold surface and that computed from boiloff volume measurements, computed gas density, and latent heat of vaporization of the cryogen.

The experiment is conducted with the configuration shown schematically in Fig. 3-4. The 1/2-w resistor is attached to the midpoint of the calorimeter surface plate with a silver-filled epoxy cement, and its exposed surfaces are

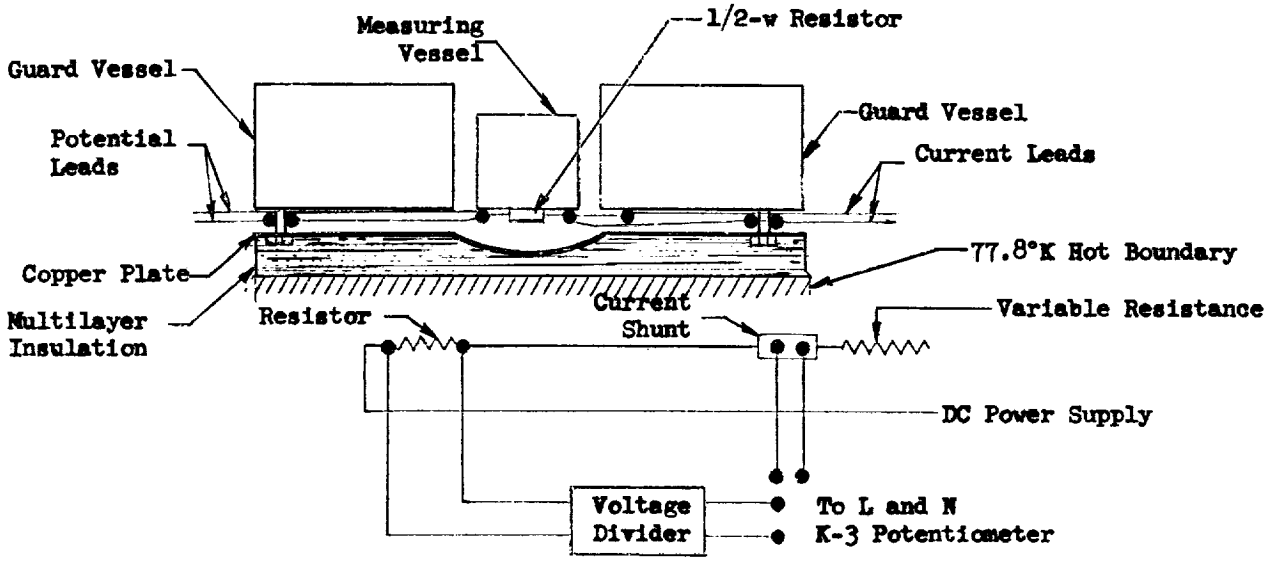

Fig. 3-4 Calorimeter Heat Input Calibration Configuration

covered with an aluminum tape to minimize radiative losses to the surroundings. The calorimeter surface is polished copper for this test. A dished, 1/8-in.-(0.318-cm)-thick polished copper plate is attached to the inner guard surface, using indium wire to increase heat transfer, in order to provide an enclosure at guard temperature. The lower surface of the plate is insulated with 1 in. (2.54 cm) of multilayer insulation, and the hot boundary is maintained at $140^{\circ}R$ ($77^{\circ}K$). Under these conditions, heat transfer from the copper plate to the test section is by radiation only. By thermally connecting the plate to the guard and by insulating it from any higher temperature surroundings, it remains uniformly at the temperature of the inner guard which is approximately $0.05^{\circ}R$ ($0.028^{\circ}K$) above calorimeter temperature. Under these conditions, the only heat input into the calorimeter is that from the resistor plus any from the inner guard to the calorimeter or down the fill and vent tube which is not intercepted by the radiation baffle and guard. The maximum uncertainty in electrical power measurement is 1.03×10^{-5} Btu/hr (3.02×10^{-6} w).

An initial test point was obtained for LH_2 with zero electrical input to the resistor. Under these conditions the calorimeter section boiloff was 8.1 x 10^{-4} ft^3/hr (2.3 x 10^{-2} ℓ/hr) which corresponds to a heat rate of 7 x 10^{-4} Btu/hr (2.05 x 10^{-4}w). Because of the extremely small boiloff rate, a better evaluation of the calorimeter section heat rate accuracy is obtained by comparison of heat rates at electrical inputs corresponding to the estimated range of heat fluxes for the insulations to be investigated. With both cryogens the heat rate determined from boiloff data agreed with the electrical power to within 1 x 10^{-3} Btu/hr (2.9 x 10^{-4}w) over the range of inputs of 1.02 x 10^{-2} to 2.56 Btu/hr (2.99 x 10^{-3} to 0.75 w). Five data points were obtained for each cryogen.

Experimental Uncertainties The maximum uncertainty in specimen heat flux is the sum of the individual maximum uncertainties in boiloff volume flow rate ($\dot{v}$), gas density (ρ), calorimeter extraneous heat leak ($\bar{Q}_c$), cryogen latent heat of vaporization (ΔH_v), and heat transfer cross-sectional area, (A_c). No independent measurements were made of the latent heats of vaporization of the two cryogens, and it is assumed the uncertainty in these values is zero. For the heat transfer area it is assumed that no two-dimensional effects are present so that this area is equal to the cold plate surface area of the calorimeter. The error in this term is less than 0.1 percent and is neglected. The resultant maximum percentage uncertainty in heat flux becomes

$$\delta(Q_c/A_c) = \frac{\Delta(Q_c/A_c)}{Q_c/A_c} \times 100 = \left[\frac{\Delta(\dot{v})}{\dot{v}} + \frac{\Delta(\rho)}{\rho} + \frac{\Delta(Q_c)}{Q_c}\right] \times 100 \qquad (3.1)$$

where Q_c is the total calorimeter heat rate. The last term on the right side of equation 3.1 ranges from 1.5 to <0.1 percent. For the lowest value of heat flux measured, on the order of 0.1 Btu/hr ft^2 (0.315 w/m^2), the maximum uncertainty is calculated to be 4.5 percent; and this decreases to 3.0 percent at heat fluxes of 1.0 Btu/hr ft^2 (3.15 w/m^2) or greater. This is in good

agreement with the calorimeter heat rate calibration data. For an electrical heat input of 1.02×10^{-2} Btu/hr (2.99×10^{-3}w), the heat rate based upon boiloff data was 1.12×10^{-2} Btu/hr (3.28×10^{-3}w). Subtracting the zero input value of 7×10^{-4} Btu/hr (2.05×10^{-4}w) from the latter figure yields a difference of 3 percent.

The maximum uncertainty for the compressive load data is the sum of the uncertainties in force measurement and insulation specimen area; the percentage error is

$$\delta(P) = \frac{\Delta(P)}{P} \times 100 = \left[\frac{\Delta(F)}{F} + \frac{\Delta(A_s)}{A_s}\right] \times 100 \qquad (3.2)$$

where P is pressure, F is Force and A_s is specimen area in compression. The specimen area uncertainty is estimated to be nearly 2 percent assuming an accuracy of $\pm$ 1/8-in. ($\pm$0.318-cm) in the specimen diameter. The resulting maximum error in pressure varies from 50 percent at the lowest loads, 1×10^{-3} psi (6.90 N/m^2) to less than 3 percent at 0.1 psi (690 N/m^2).

Layer density maximum uncertainty is directly proportional to the maximum error in thickness which is the sum of the errors in measurement of separation between plates and the flatness deviations of the two surfaces. These errors are 1×10^{-3} in. (2.54×10^{-3}cm) and 4×10^{-3} in. (1.02×10^{-2} cm) respectively. For the minimum thicknesses investigated, this corresponds to a maximum uncertainty of 9 percent.

The error introduced by two dimensional heat transfer is a function of specimen thickness and the ratio of normal to parallel thermal conductivities of the particular insulation. For the majority of tests this error was less than 1 percent. However, for the thickest specimen the two dimensional effect was significant and corrections were made in the data as discussed in Section 3.5.

3.1.2 Total Hemispherical Emittance Measurements

A calorimetric method was selected for measurement of the total hemispherical emittance of each shield material over the temperature range of 100 to 560°R (56 to 311°K). This method was chosen because it measures total hemispherical emittance directly, is not affected by surface conditions (i.e., crinkled or smooth), and accuracy is very good over the entire temperature range.

Experimental Apparatus The Calorimetric Emittance Apparatus consists of a 2-1/2-in.-(6.35-cm-) diameter by 3/16-in-(0.476-cm-) thick aluminum, brass or copper sample substrate mounted to a liquid nitrogen or liquid hydrogen cooled vacuum chamber (see Fig. 3-5). Sample temperature is controlled from cryogen temperature to 560°R (311°K) using a spiral wound heater imbedded in a 2-1/4-in.-(5.72-cm-) diamater copper heating block. Temperature readout is provided using a Rosemount Engineering Company 104 AH1 platinum resistance thermometer.

Radiated sample energy is collected using a blackbody absorber mounted to the cryogenically cooled supporting structure within 30 mils (0.76 mm) of the sample front face. This absorber consists of a series of thin wall metal tubes, 3/16-in. (0.476-cm) O.D. by 10 mil (0.25-mm) wall by 1-in. (2.54-cm) long, fitted to the interior of an aluminum shell. The inside of the shell and tubes are coated with "Cat-a-lac" flat black epoxy paint. The geometry of the blackbody coupled with the high absorptance of the paint leads to a calculated theoretical absorptance of 0.97. The blackbody thermal link is selected so that absorbed sample energy raises blackbody temperature between 10 and 20°R (6 and 11°K) above that of the bath once thermal equilibrium is reached. For the present experiments, two thermal links were needed: three 20-mil-(0.51-cm-) diameter stainless steel wires were used for sample temperatures between 100 and 290°R (56 and 160°K), while a 1/4-in (0.635-cm) O.D. by 20-mil (0.51-cm) wall stainless tube was used for sample temperatures between 290 and 560°R (160 and 311°K). Blackbody temperature is monitored using a platinum or germanium resistance thermometer.

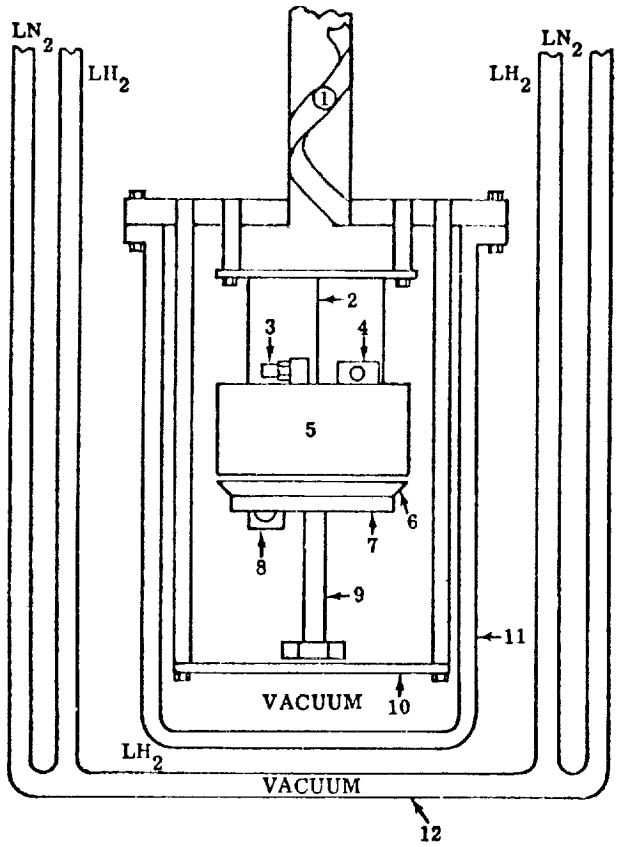

1 COPPER RADIATION STRAP
2 BLACKBODY THERMAL LINK (THREE 20-mil STAINLESS WIRES)
3 GERMANIUM RESISTANCE THERMOMETER
4 BLACKBODY HEATER
5 BLACKBODY ABSORBER
6 SAMPLE SUBSTRATE
7 SAMPLE HEATER
8 PLATINUM RESISTANCE THERMOMETER
9 SAMPLE THERMAL LINK
10 COPPER SUPPORTING STRUCTURE
11 VACUUM-TIGHT EXPERIMENTAL CHAMBER
12 DOUBLE WALL DEWAR

Fig. 3-5 Calorimetric Emittance Apparatus

Experimental Procedure The procedure used to obtain emittance and calibration measurements is described below. For the emittance measurement the black body and samples are clamped in place with the front faces spaced approximately 30 mils (0.76 mm) apart. The shell assembly is then bolted together and lowered into the 1.06-ft^3 (30-liter) dewar. While at room temperature the apparatus is evacuated to a pressure of 10^{-5} torr. Liquid nitrogen is then added to the dewar's guard section while the space surrounding the shell assembly is filled with liquid hydrogen. The pressure is then reduced to 10^{-8} torr.

After allowing both the sample and blackbody receiver to cool to sink temperature, the sample heater is set for the desired sample temperature. The thermal energy from the sample's front surface increases the temperature of the body. For the measurements obtained during this program, the blackbody thermal link was chosen so that blackbody temperature would not exceed $70^{\circ}R$ ($39^{\circ}K$) when using liquid hydrogen as the thermal ground. This minimizes the radiation energy lost by the blackbody receiver, both to the blackened shell walls and to the front face.

Once sample and blackbody temperature equilibrium are attained (after approximately 18 hr), their respective temperatures are recorded. A four-lead technique is used for these measurements. A Leeds and Northrop K-3 potentiometer is used for voltage measurements. Current measurements are made using a precision standard resistor in conjunction with the K-3 potentiometer.

To define the thermal energy reaching the blackbody from the sample, it is necessary to calibrate the blackbody receiver. This is accomplished by allowing the sample to cool to the cryogenic bath temperature and supplying heat energy to the receiver through a 200-ohm carbon resistor heater mounted to its back face. Once blackbody thermal equilibrium is attained, the power dissipated in the carbon resistor is measured and the temperature (thermometer resistance) is recorded. The process is then repeated for different power levels. A curve of blackbody temperature versus power input to the blackbody is then generated. This technique produces a very reproducible curve, since

not only the blackbody thermal link, but all the leads to the resistors mounted on its back face are thermally grounded to the cryogenic bath.

Emittance Calculations With a radiating sample present, the heat rate reaching the blackbody thermal link is equal to the radiated sample energy, which is absorbed by the blackbody, minus the radiated blackbody energy, which is either absorbed by the sample or the chamber walls. Therefore, the heat rate to the blackbody thermal link is given by:

$$Q_\ell = A_s\sigma T_s^4 F \frac{\epsilon_s a_b}{1-F^2(1-\epsilon_s)(1-a_b)} - A_b\sigma T_b^4 F \frac{\epsilon_b a_s}{1-F^2(1-\epsilon_b)(1-a_s)} - Y_s \quad (3.3)$$

where Y_s is the blackbody radiation exchange with the walls during the sample run. During calibration the heat rate reaching the link is:

$$Q_\ell = Q_c - Q_r - Y_c \quad (3.4)$$

where:

$$Q_r = A_b\sigma T_b^4 F \frac{\epsilon_b a_s'}{1-F^2(1-\epsilon_b)(1-a_s')} - A_s\sigma T_c^4 F \frac{\epsilon_s a_b'}{1-F^2(1-\epsilon_s)(1-a_b')} \quad (3.5)$$

, Q_c is the calibration power input, and Y_c is the blackbody radiation exchange with the walls during calibration.

Thus, Q_ℓ has been defined with a radiating sample present, and with a calibration heat input Q_c; so, for corresponding blackbody temperatures combining Eqs. (3.3), (3.4) and (3.5) yields

$$A_s\sigma T_s^4 F \frac{\epsilon_s a_b}{1-F^2(1-\epsilon_s)(1-a_b)} - A_b\sigma T_b^4 F \frac{\epsilon_b a_s}{1-F^2(1-\epsilon_b)(1-a_s)} - Y_s$$

$$= Q_c - A_b\sigma T_b^4 F \frac{\epsilon_b a_s'}{1-F^2(1-\epsilon_b)(1-a_s')} + A_s\sigma T_c^4 F \frac{\epsilon_s a_b'}{1-F^2(1-\epsilon_b)(1-a_b)} - Y_c \quad (3.6)$$

The second term on the left-hand side and the second and third terms on the right-hand side of Eq. (3.6) can all be neglected since T_b and $T_c << T_s$. This introduces an error estimated at less than 1%. Also, $Y_c = Y_s$ and thus

$$Q_c = A_s \sigma T_s^4 F \frac{\epsilon_s a_b}{1-F^2(1-\epsilon_s)(1-a_b)} \tag{3.7}$$

The emittance, ϵ_s, can now be calculated since all the terms in Eq. (3.7) are known including a_b, which can be calculated using an iterative process and data obtained by substituting a blackbody radiator identical to the blackbody absorber for the sample. The emittance, or absorptance, of the blackbody from 145 to 560°R (80 to 311°K) was found to be 0.98 + 0.01.

Experimental Uncertainties The percentage maximum uncertainty in emittance values are calculated from

$$\delta(\epsilon) = \frac{\Delta(\epsilon)}{\epsilon} \times 100 = \left[4 \frac{\Delta(T)}{T} + \frac{\Delta(Q_c)}{Q_c} + \frac{\Delta(a_b)}{a_b} + \frac{\Delta(F)}{F} \right] \times 100 \tag{3.8}$$

Table 3-1 summarizes typical emittance measurement errors for gold and aluminum surfaces at sample temperatures of 100, 180, and 560°R (56, 100, and 311°K, respectively). For the Mylar surface the errors are 6.4, 5.1, and 3.5 percent for the above temperatures, respectively. As shown in the table, measurements at the lowest sample temperature are subject to the greatest uncertainty, principally because the ΔT between the blackbody absorber and the cryogen bath is approaching the same order of magnitude as the barometric pressure shifts at cryogenic liquid temperature. At the higher sample temperatures, the principal source of error is attributable to the ΔT's across the 2-1/2-in.-(6.35-cm-)diameter sample.

A source of error which was not listed in Table 3-1 but which can be very significant, is heat transfer to or from the blackbody absorber due to residual gas conduction. In the present experiments, great care was taken in designing and fabricating the experimental vacuum chamber so that a pressure of less than

Table 3-1

MAXIMUM UNCERTAINTIES IN TOTAL HEMISPHERICAL EMITTANCE DATA

Sample Temperature °R (°K)	Parameter	Nominal Parameter Value, N	Parameter Uncertainty, ΔN	Percent Error
100 (56)	Q_c, Btu/hr (w)	6.8×10^{-5} (2×10^{-5})	5.1×10^{-6} (1.5×10^{-6})	7.5
	T_s, °R (°K)	100 (56)	0.9 (0.5)	3.6
	a_b	0.98	0.01	1.0
	F	0.99	0.01	1.0
	ϵ	0.009	--	13.1
180 (100)	Q_c, Btu/hr (w)	5.5×10^{-4} (1.6×10^{-4})	5.1×10^{-6} (1.5×10^{-6})	1.0
	T_s, °R (°K)	180 (100)	1.2 (0.67)	2.7
	a_b	0.98	0.01	1.0
	F	0.99	0.01	1.0
	ϵ	0.011	--	5.7
560 (311)	Q_c, Btu/hr (w)	1.7×10^{-1} (5.1×10^{-2})	negligible	0
	T_s, °R (°K)	560 (311)	2.0 (1.1)	1.5
	a_b	0.98	0.01	1.0
	F	0.99	0.01	1.0
	ϵ	0.025	--	3.5

10^{-8} torr could be realized. At the lowest sample temperature, it can be shown that heat transfer by residual gas conduction is of the same order of magnitude as heat transferred by radiation if the chamber pressure is of the order of 10^{-5} torr.

3.1.3 Shield Reflectance Measurements

In order to check the consistency of emittance of the reflective shields used in the heat transfer test specimens, near normal infrared reflectance measurements were made on each shield. This was accomplished using a Gier Dunkle Instruments, Inc. Model DB100 Infrared Reflectometer. The instrument was standardized against a gold surface, and the reflectance data were compared against specimens of each shield material on which calormetric total hemispherical emittance measurements had been made at room temperature. Using this method, the reflectance of each shield relative to a standard was obtained. The total hemispherical emittance in turn is inferred by using the ratio of reflectance to total emittance for the standard.

The Gier Dunkle Reflectometer is a portable device, and the shield is placed on top of the measuring head. The sample surface is alternately irradiated by energy from two cavities at different temperatures. A vacuum thermocouple detector receives energy emitted by the sample and that reflected by the sample from each cavity. Only the reflected energy varies as the sample is alternately illuminated by the two cavities. Therefore, the measurement is independent of sample temperature.

Although the accuracy of the reflectance measurement is 1 percent, the reproducibility is 0.2 percent. For the high reflectance materials this represents a variation in reflectance of 0.002 for a reflectance of 0.98 which in turn corresponds to a reproducibility of $\pm$ 0.002 for the infrared shield emittance, or 7 to 10 percent for the aluminum and gold surfaces.

3.2 MATERIAL SPECIFICATIONS

Descriptions of the spacer and reflective shield materials used for fabrication of the test specimens investigated in this program are given in Table 3-2. Sufficient quantities of material were procured to accomplish all of the investigations in Tasks I and II as well as to insulate the 4-ft-(1.22-m-) diameter tank calorimeter used in Task III.

Table 3-2

INSULATION MATERIALS DESCRIPTION

Designation	Use	Source	Nominal Thickness, mils (mm)	Average Specific Weight, lbm/ft^2 (kg/m^2)
"Illusion Silk Net," approx. 1/16-in. (0.159-cm) Hexagonal Mesh	Spacer	John Heathcoat Co., New York, N.Y.	5 (0.13)	1.5×10^{-3} (7.3×10^{-3})
"Tissuglas," Style 60G	Spacer	Pallflex Products Co. Putnam, Conn.	0.6 (0.015)	8.0×10^{-4} (3.9×10^{-3})
Crinkled, single-aluminized 1/4-mil (0.0064-mm) Mylar*	Shield with integral spacer	National Metallizing Division, Standard Packaging Corp., Cranbury, N.J.	0.25 (0.0064)	1.9×10^{-3} (9.3×10^{-3})
Double-aluminized 1/4-mil (0.0064-mm) Mylar*	Shield	Same as above	0.25 (0.0064)	1.8×10^{-3} (8.8×10^{-3})
Double-goldized 1/4-mil (0.0064-mm) Mylar*	Shield	Same as above	0.25 (0.0064)	2.3×10^{-3} (1.1×10^{-2})

* E.I. DuPont

The space materials were ordered by the description given in Table 3-2. The sources listed are the only producers of these materials. A purchase specification, given in Appendix A, was prepared for the metallized Mylar materials, and it was sent to four vendors for quotation. A single source was then selected on the basis of agreement to comply with specifications in all respects, delivery, and price. The vendor's tests were conducted with a Lion Research Corporation Model 25 "Emissometer" using secondary standards furnished and calibrated by LMSC. The calibration was based upon total hemispherical emittance measurements and subsequent comparison with a Model 25 emissometer at LMSC. The vendor reported a purity of 99.78 percent for the aluminum used for evaporation. No purity was stated for the gold.

Upon receipt of the metallized Mylar material, nine samples were selected from each lot, and Lion emissometer measurements were made on each sample. These data are given in Table 3-3 together with the results of calorimetric total hemispherical emittance tests on one sample.

Adhesion tests were conducted on two specimens of each material. No removal of metal was visually observed in any case. The test was conducted by applying a 1/2-in.-(1.27-cm-) wide by 2-in.-(5.08-cm-) long piece of cellulose tape to the metal surface, covering an area 1/2-in. (1.27-cm) by 1-in. (2.54-cm). The tape was set by rubbing with a finger. The end of the tape was pulled at an angle approximately perpendicular to the film surface at a rate of 1 to 2 in. (2.54 to 5.08 cm) per minute.

The double-goldized Mylar material had numerous holes, which appeared to be due to melting of the substrate material, throughout the roll. These ranged in size from approximately 1/16-in. (0.159-cm) to 1/2-in. (1.27-cm) in diameter. Several tears were also present in the material. The locations and descriptions of these defects were recorded during the vendor's inspection procedure. All reflective shields were taken from area free from visible defects.

Table 3-3

REFLECTIVE SHIELD EMITTANCE INSPECTION RESULTS

Specimen Designation (a)	Side	ϵ_{Lion} (b)			ϵ_{TH} @ 540°R (300°K) (c)		
		DG	DA	SA	DG	DA	SA
-1	A	0.015	0.03	0.035			
	B	0.02	0.025	--			
-2	A	0.02	0.03	0.03			
	B	0.015	0.025	--			
-3	A	0.015	0.03	0.03			
	B	0.02	0.03	--			
-4	A	0.02	0.03	0.03			
	B	0.025	0.025	--			
-5	A	0.015	0.03	0.03	0.024	0.030	0.036
	B	0.02	0.025	--	0.022	0.029	--
-6	A	0.025	0.03	0.035			
	B	0.025	0.025	--			
-7	A	0.02	0.035	0.03			
	B	0.015	0.03	--			
-8	A	0.02	0.03	0.03			
	B	0.02	0.025	--			
-9	A	0.02	0.03	0.035			
	B	0.02	0.025	--			

Notes:

(a) Designation is DG-1, etc., for double-goldized Mylar, DA-1, etc., for double-aluminized Mylar, and SA-1, etc., for single-aluminized Mylar

(b) ± 0.005

(c) ± 0.001

3.3 INSULATION SPECIMEN PREPARATION

To assure uniformity in preparation of the test specimens for Tasks I and II, the following sample preparation and handling procedure was established:

1. Shield and spacer materials were visually inspected so that disks were cut from areas free from defects, large wrinkles, or creases.
2. The materials were cut to proper size using an electric shears and a template.
3. Total near-normal reflectance of each shield was measured at two points on each side. For the metallized surfaces the reflectance did not deviate from the average of all readings by more than 0.003 for more than 10 percent of the readings. No single reading deviated more than 0.005 from the average value.
4. To reduce any effects due to wrinkling caused by packaging of the double-coated Mylar and net spacers, they were stacked separately and subjected to a uniform compressive load of 1 psi (6.9×10^3 N/m^2) for 96 ± 24 hours prior to assembly of the test specimen. Two layers of smooth kraft type paper were placed between each shield or spacer so that a wrinkle in one layer would not be transferred to adjacent ones during the loading period. The load was applied through a 1/4-in.-(0.635-cm-) thick aluminum plate of the same diameter as the shield or spacer.
5. For the specimens having separate spacers, a spacer layer was included at each exterior boundary. For the crinkled, single-aluminized Mylar, the Flat Plate Calorimeter tests were conducted with the aluminized side facing out and in contact with the warm boundary.
6. The assembled specimen was weighed and the weight recorded.
7. The specimen was installed in the Flat Plate Calorimeter within one hour after preparation was completed.

At the conclusion of the calorimeter testing, the specimens were stored in the laboratory environment. One shield at or near the middle of the specimens was removed, and a sample prepared for room temperature calorimeter emittance tests.

3.4 FLAT PLATE CALORIMETER REPEATABILITY

A specimen was prepared from the double-aluminized Mylar and silk net materials for testing to evaluate the repeatability of the Flat Plate Calorimeter data. Ten sheets of Mylar and 22 sheets of net were used; each spacer layer consisted of two sheets of the netting. The test sequence consisted of equilibrium condition boiloff measurements using LN_2 for a 72-hr period with a single compressive load. The load was then relieved to zero for 8 hr. After this period the load was readjusted to the initial value, and the test continued until a 24-hr period of equilibrium boiloff was recorded. The data for these tests are presented in Table 3-4 for run number 1-A through 1-D. The average heat flux values for the first three 24-hr periods agreed to within 1.5 percent. After the load was removed and the original conditions reestablished the new values of heat flux was within 2 percent of the maximum value observed during the initial 72-hr period. These tests indicate that for moderate heat flux levels and compressive pressures the apparatus repeatability is 2 to 3 percent.

Testing was continued over a range of increasing and decreasing compressive loads. The cryogen was next changed to LH_2 and tests conducted for several additional conditions as shown in Table 3-4. For the two successive 24-hr equilibrium periods with LH_2, the heat flux data deviation was 2 percent which is consistent with the LN_2 data. This test was conducted with no external compressive load applied to the specimen so no loading variations are present in these results.

Table 3-4

FLAT PLATE CALORIMETER REPEATABILITY TEST DATA

Specimen No. 1, 10 Double-Aluminized Mylar Shields/22 Silk Net Spacers, Weight = 0.059 lbm (0.027 kg), Uncompressed Thickness = 0.15 in. (0.38 cm) (a)

Run No.	Measured Compressive Force(b) lbf	(N)	Equivalent Compressive Pressure psi	(N/m^2)	Measured Thickness(c) in.	(cm)	Boundary Temperatures $^{o}R\ T_H$ (^{o}K)	$^{o}R\ T_C$ (^{o}K)	Layer Density No./in.	(No./cm)	Measured Heat Flux Btu/hr/ft^2	(w/m^2)
1-A (First 24 Hrs)	1.0	(4.4)	5.0×10^{-3}	(30.45)	0.156	(0.396)	503 (279)	139 (77)	70.5	(27.8)	0.676	(2.13)
1-B (Second 24 Hrs)	1.0	(4.4)	5.0×10^{-3}	(30.45)	0.156	(0.396)	502 (279)	139 (77)	70.5	(27.8)	0.685	(2.16)
1-C (Third 24 Hrs)	1.0	(4.4)	5.0×10^{-3}	(30.45)	0.156	(0.396)	503 (279)	139 (77)	70.5	(27.8)	0.685	(2.16)
	0.059(d)	(0.26)	1.5×10^{-4}(d)	(1.0)	0.20	(0.51)	503 (279)	139 (77)	55.0	(21.7)	---	
1-D (Fourth 24 Hrs)	1.0	(4.4)	5.0×10^{-3}	(30.45)	0.154	(0.391)	504 (280)	139 (77)	71.4	(28.1)	0.670	(2.07)
2	6.4	(28.5)	3.2×10^{-2}	(220)	0.115	(0.292)	503 (279)	139 (77)	95.7	(37.7)	1.615	(5.20)
3	12.8	(56.9)	6.4×10^{-2}	(440)	0.109	(0.277)	502 (279)	139 (77)	100.8	(39.7)	2.085	(6.57)
4	2.0	(8.9)	1.0×10^{-2}	(69)	0.143	(0.363)	502 (279)	139 (77)	77.0	(30.3)	0.907	(2.86)
5	0.5	(2.2)	2.5×10^{-3}	(17)	0.150	(0.381)	500 (278)	139 (77)	73.3	(28.9)	0.555	(1.75)
6	1.9	(8.4)	9.3×10^{-3}	(64)	0.123	(0.312)	501 (278)	139 (77)	89.5	(35.2)	0.980	(3.09)
7	10.8	(48.0)	5.4×10^{-2}	(373)	0.108	(0.274)	501 (278)	139 (77)	101.8	(40.1)	1.840	(5.80)
8	25.0	(111.2)	1.25×10^{-1}	(863)	0.098	(0.249)	501 (278)	139 (77)	112.3	(44.2)	2.541	(8.02)
9	0.2	(0.9)	1.0×10^{-3}	(6.9)	0.155	(0.394)	500 (278)	139 (77)	71.0	(28.0)	0.384	(1.21)
10-A (First 24 Hrs)	0.059(d)	(0.26)	1.5×10^{-4}(d)	(1.0)	0.157	(0.399)	500 (278)	37 (20)	70.0	(27.6)	0.258	(0.81)
10-B (Second 24 Hrs)	0.059(d)	(0.26)	1.5×10^{-4}(d)	(1.0)	0.157	(0.399)	501 (278)	37 (20)			0.253	(0.79)
11	1.5	(6.7)	7.5×10^{-3}	(52)	0.126	(0.320)	501 (278)	37 (20)	87.3	(34.4)	0.743	(2.34)
12	11.0	(48.9)	6.0×10^{-2}	(414)	0.104	(0.264)	501 (278)	37 (20)	105.7	(41.6)	1.871	(5.90)
13	50.0	(222.4)	2.5×10^{-1}	(1727)	0.089	(0.226)	500 (278)	37 (20)	123.7	(48.7)	3.452	(10.86)

Notes: (a) Measured with a dial gage prior to installation in the FPC
(b) Force measurement accuracy = ± 0.1 lbf (± 0.4 N)
(c) Separation between hot and cold boundary surface plates
(d) Force = specimen weight; average pressure = $\frac{1}{2}$ weight/unit area (assumed)

Fig. 3-6 illustrates the heat flux data as a function of compressive load for all test conditions. No single point deviates more than 7 percent from the curve. The major portion of this deviation is probably due to the uncertainty in compressive load below $1x10^{-2}$ psi (69 N/m^2). At $1x10^{-3}$ psi (6.9 N/m^2) the maximum uncertainty in force is 50 percent. However, the resolution of the instrumentation to measure load cell output at this level is 10 percent, and the repeatability for this variable corresponds to this figure. On the basis of the data, the apparatus overall repeatability is estimated to be 12 percent at the lowest applied load. At pressures above $1x10^{-2}$ psi (69 N/m^2) the repeatability is 5 percent.

3.5 INSULATION REPRODUCIBILITY

A total of ten specimens were tested in the Flat Plate Calorimeter for the study of insulation reproducibility. Four were of double-aluminized 1/4-mil Mylar with two layers of silk net for each spacer, and six were of crinkled, single-aluminized 1/4-mil Mylar. Additional tests were conducted on this latter material to evaluate two-dimensional heat transfer effects in the Flat Plate Calorimeter apparatus for thick specimens. All tests were conducted with a hot boundary temperature of 500°R (278°K) and a cold boundary temperature of 37°R (20°K), and compressive loadings ranged from 1.5×10^{-4} psi (1.03 N/m^2) to 1×10^{-1} psi (690 N/m^2). Ambient pressure in the test apparatus was less than 8×10^{-7} torr for all tests.

3.5.1 Double-Aluminized Mylar/Silk Net

The heat transfer versus compressive loading characteristics of two specimens each of 10 shields and 22 layers of silk net and 20 shields and 42 layers of silk net were investigated. The data obtained for each specimen are presented in Table 3-5. Total hemispherical emittance data, measured at 540±5°R (300± 3°K), for the fifth shield (number 1 refers to shield adjacent to the hot boundary) of each specimen are shown in Table 3-6, together with a summary of the near-normal reflectance data on all shields in each specimen.

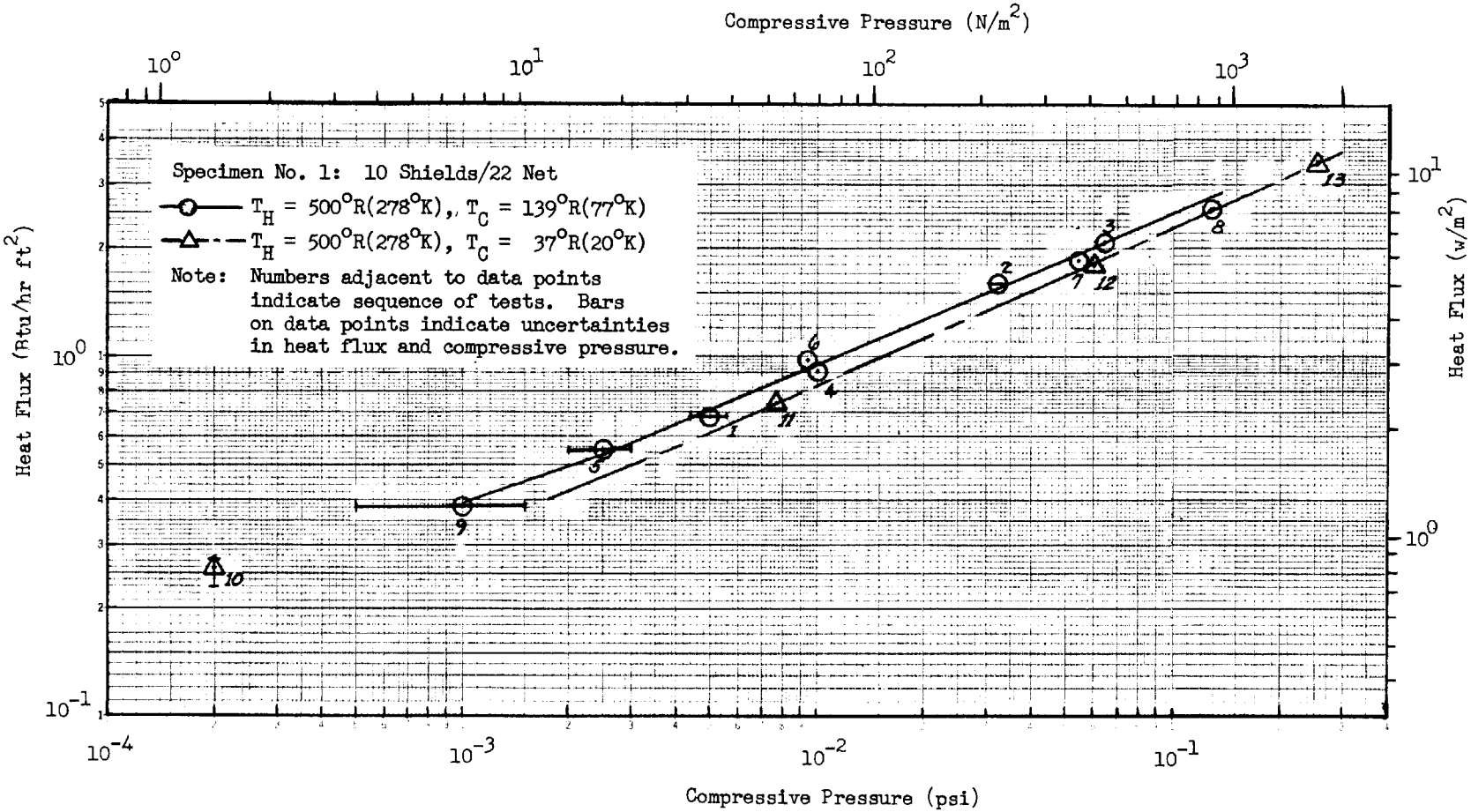

Fig. 3-6 Repeatability of FPC for Heat Flux as a Function of Compressive Pressure with Double-Aluminized Mylar/Silk Net

Table 3-5

FLAT PLATE CALORIMETER REPRODUCIBILITY TEST DATA WITH DOUBLE-ALUMINIZED MYLAR/SILK NET SPECIMENS (a)

Run No.	Measured Compressive Force(b) lbf	(N)	Equivalent Compressive Pressure psi	(N/m^2)	Measured Thickness(c) in.	(cm)	Layer Density No./in.	(No./cm)	Measured Heat Flux $Btu/hr\ ft^2$	(w/m^2)
Specimen No. 2, 10 shields/22 net, Weight = 0.061 lbm (0.028 kg) Uncompressed Thickness = 0.15 in. (0.38 cm)(d)										
1	0.061(e)	(0.27)	1.5×10^{-4}	(1.03)(e)	0.177	(0.450)	62.1	(24.4)	0.252	(0.795)
2	0.25	(1.1)	1.25×10^{-3}	(8.63)	0.139	(0.353)	79.2	(31.2)	0.378	(1.19)
3	0.70	(3.1)	3.5×10^{-3}	(24.1)	0.121	(0.307)	90.9	(35.8)	0.625	(1.97)
4	2.30	(10.2)	1.15×10^{-2}	(79.5)	0.110	(0.279)	100.0	(39.4)	1.10	(3.47)
5	1.0	(4.4)	5.0×10^{-3}	(34.5)	0.122	(0.310)	90.2	(35.5)	0.752	(2.37)
6	20.0	(89.0)	1.0×10^{-1}	(690)	0.095	(0.242)	115.7	(45.6)	2.34	(7.37)
7	1.7	(7.6)	8.5×10^{-3}	(58.5)	0.114	(0.290)	96.5	(38.0)	0.985	(3.11)
8	0.25	(1.1)	1.25×10^{-3}	(8.63)	0.132	(0.336)	83.3	(32.8)	0.366	(1.16)
9	0.061(e)	(0.27)	1.5×10^{-4}	(1.03)(e)	0.171	(0.435)	64.3	(25.3)	0.206	(0.650)
Specimen No. 3, 10 shields/22 net, Weight = 0.059 lbm (0.027 kg) Uncompressed Thickness = 0.14 in. (0.36 cm)(d)										
1	0.059(e)	(0.26)	1.5×10^{-4}	(1.03)(e)	0.417	(1.060)	26.4	(10.4)	0.282	(0.890)
2	0.059(e)	(0.26)	1.5×10^{-4}	(1.03)(e)	0.229	(0.582)	48.0	(18.9)	0.234	(0.738)
3	0.2	(0.9)	1.0×10^{-3}	(6.90)	0.158	(0.402)	69.5	(27.4)	0.295	(0.930)
4	0.4	(1.8)	2.0×10^{-3}	(13.80)	0.133	(0.338)	82.6	(32.5)	0.407	(1.28)
5	2.4	(10.7)	1.2×10^{-2}	(82.8)	0.110	(0.279)	100.0	(39.4)	0.989	(3.12)
6	5.0	(22.2)	2.5×10^{-2}	(172)	0.100	(0.254)	110.0	(43.3)	1.54	(4.85)
Specimen No. 4, 20 shields/42 net, Weight = 0.12 lbm (0.054 kg) Uncompressed Thickness = 0.31 in. (1.04 cm)(d)										
1	0.12 (e)	(0.53)	3.0×10^{-4}	(2.07)(e)	0.407	(1.030)	51.6	(20.3)	0.244	(0.77)
2	0.12 (e)	(0.53)	3.0×10^{-4}	(2.07)(e)	0.315	(0.800)	66.7	(26.3)	0.179	(0.565)
3	0.25	(1.1)	1.25×10^{-3}	(8.63)	0.260	(0.660)	80.8	(31.8)	0.214	(0.675)
4	1.0	(4.4)	3.0×10^{-3}	(20.7)	0.218	(0.554)	96.3	(37.9)	0.267	(0.842)
5	8.8	(39.1)	4.4×10^{-2}	(304)	0.173	(0.440)	121.5	(47.8)	0.872	(2.75)
6	21.0	(93.4)	1.05×10^{-1}	(725)	0.161	(0.409)	130.3	(51.3)	1.26	(3.97)
7	10.0	(44.5)	5.0×10^{-2}	(345)	0.175	(0.445)	120.0	(47.2)	0.937	(2.95)
8	1.0	(4.4)	5.0×10^{-3}	(34.5)	0.207	(0.526)	101.5	(40.0)	0.415	(1.31)
9	0.12 (e)	(0.53)	3.0×10^{-4}	(2.07)(e)	0.315	(0.800)	66.7	(26.3)	0.168	(0.530)
Specimen No. 5, 20 shields/42 net, Weight = 0.13 lbm (0.059 kg) Uncompressed Thickness = 0.27 in. (0.69 cm)(d)										
1	0.13 (e)	(0.58)	3.25×10^{-4}	(2.24)(e)	0.578	(1.47)	36.3	(14.3)	0.260	(0.820)
2	0.2	(0.9)	1.0×10^{-3}	(6.9)	0.315	(0.800)	66.7	(26.3)	0.203	(0.641)
3	0.5	(2.2)	2.5×10^{-3}	(17.2)	0.215	(0.547)	97.8	(38.5)	0.261	(0.824)
4	10.0	(44.5)	5.0×10^{-2}	(345)	0.179	(0.455)	117.2	(46.1)	0.835	(2.64)

Notes: (a) Data shown were obtained for a hot boundary temperature of 500°R (278°K) and a cold boundary temperature of 37°R (20°K)
(b) Force measurement accuracy = ± 0.1 lbf (± 0.4 N)
(c) Separation between hot and cold boundary surface plates
(d) Measured with a dial gage prior to installation in the FPC
(e) Force = Specimen weight; average pressure = ½ weight/unit area (assumed)

Measured heat flux as a function of the applied compressive load for the 10-shield and 20-shield specimens is shown by Figs. 3-7 and 3-8, respectively. Horizontal bars through some of the data points illustrate the effect of the maximum uncertainty in force on computed compressive load in the lower range. The lowest values shown are computed assuming that the pressure is equal to one-half the specimen weight per unit area (i.e. no external force applied to the system). For specimens 2 and 3 (Fig. 3-7), the thicknesses corresponding to the lowest pressure were greater than the values of uncompressed thickness measured prior to testing. For these points a definite separation exists between the cold surface of the apparatus and the coldest insulation layer. The spread in data between the two 10-shield specimens is approximately 15 percent at 1×10^{-3} psi ($6.9\ N/m^2$) decreasing to 10 percent at 1×10^{-2} psi ($69\ N/m^2$). This is nearly equal to the repeatability of the apparatus, discussed in Section 3.4, which was 12 and 5 percent for these two pressures, respectively. The flagged points for specimen No. 2 represent decreasing compressive load values after reaching a maximum load of 1×10^{-1} psi ($690\ N/m^2$). Some hysteresis appears to be evident at the lower pressures which might be attributed to a reduction in the total number of shield-to-spacer contacts after the specimen was subjected to the highest load value. However, no definite conclusion can be drawn in this regard as the differences are within the apparatus repeatability percentages. At 1.5×10^{-4} psi ($1.0\ N/m^2$), the boundary plate

Table 3-6

DOUBLE-ALUMINIZED MYLAR EMITTANCE AND REFLECTANCE DATA

Specimen No.	ϵ_{TH} (Calorimetric)	ρ_N	ϵ_{TH} from ρ_N (a)
2	0.0286 @ 552°R (307°K) 0.0279 @ 540°R (300°K)	$0.979 \pm {}^{.003}_{.005}$	0.028
3	0.0281 @ 570°R (316°K)	$0.977 \pm {}^{.003}_{.006}$	0.031
4	0.0275 @ 560°R (311°K)	$0.977 \pm {}^{.002}_{.004}$	0.031
5	0.0284 @ 541°R (300°K)	$0.980 \pm {}^{.003}_{.003}$	0.027

Note (a) ϵ_{TH} 1.33 x ϵ_{TN} (Ref. 5), ϵ_{TN} 1 - ρ_N

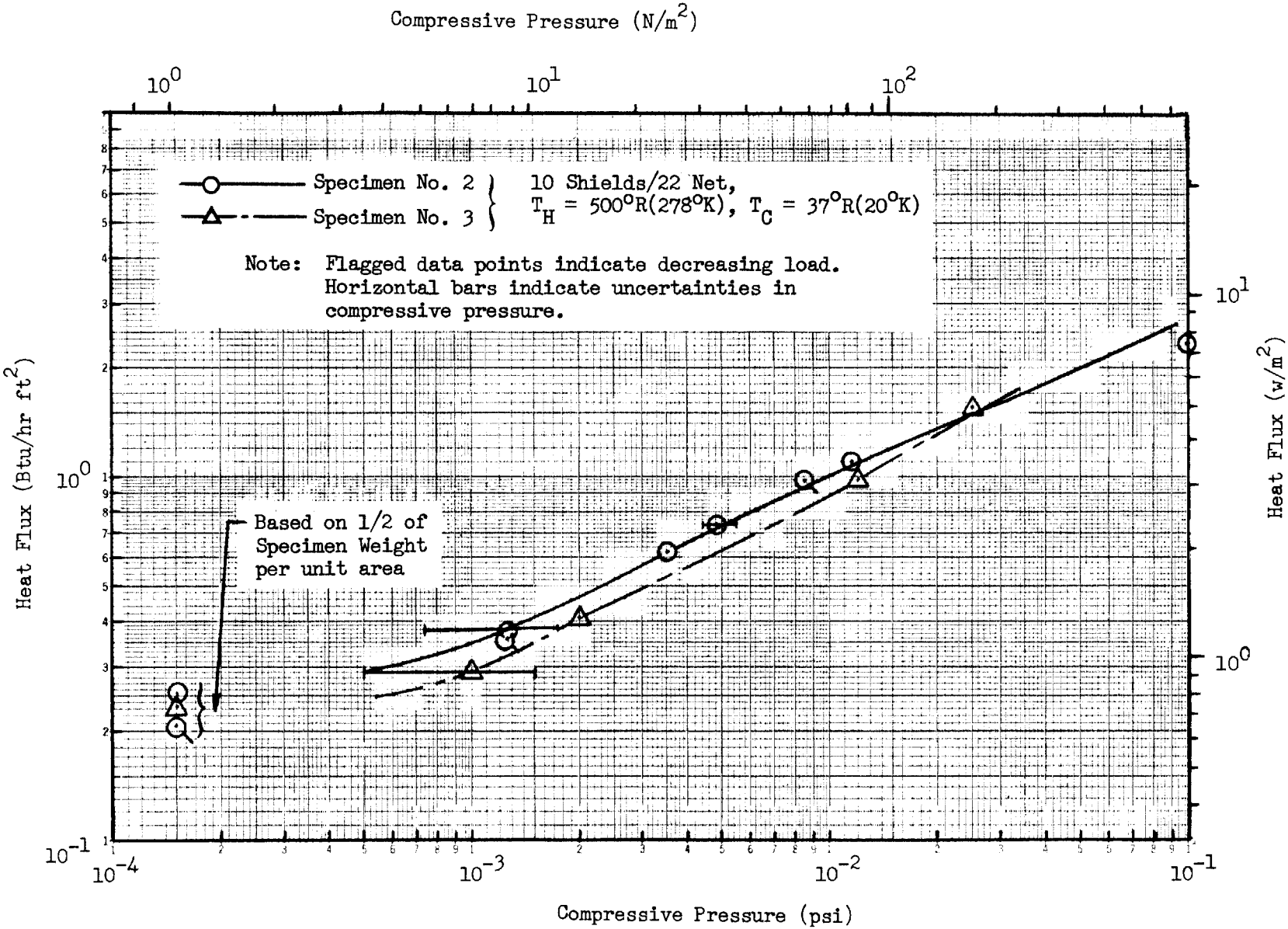

Fig. 3-7 Reproducibility of Heat Flux as a Function of Compressive Pressure for 10-Shield Specimens of Double-Aluminized Mylar/Silk Net

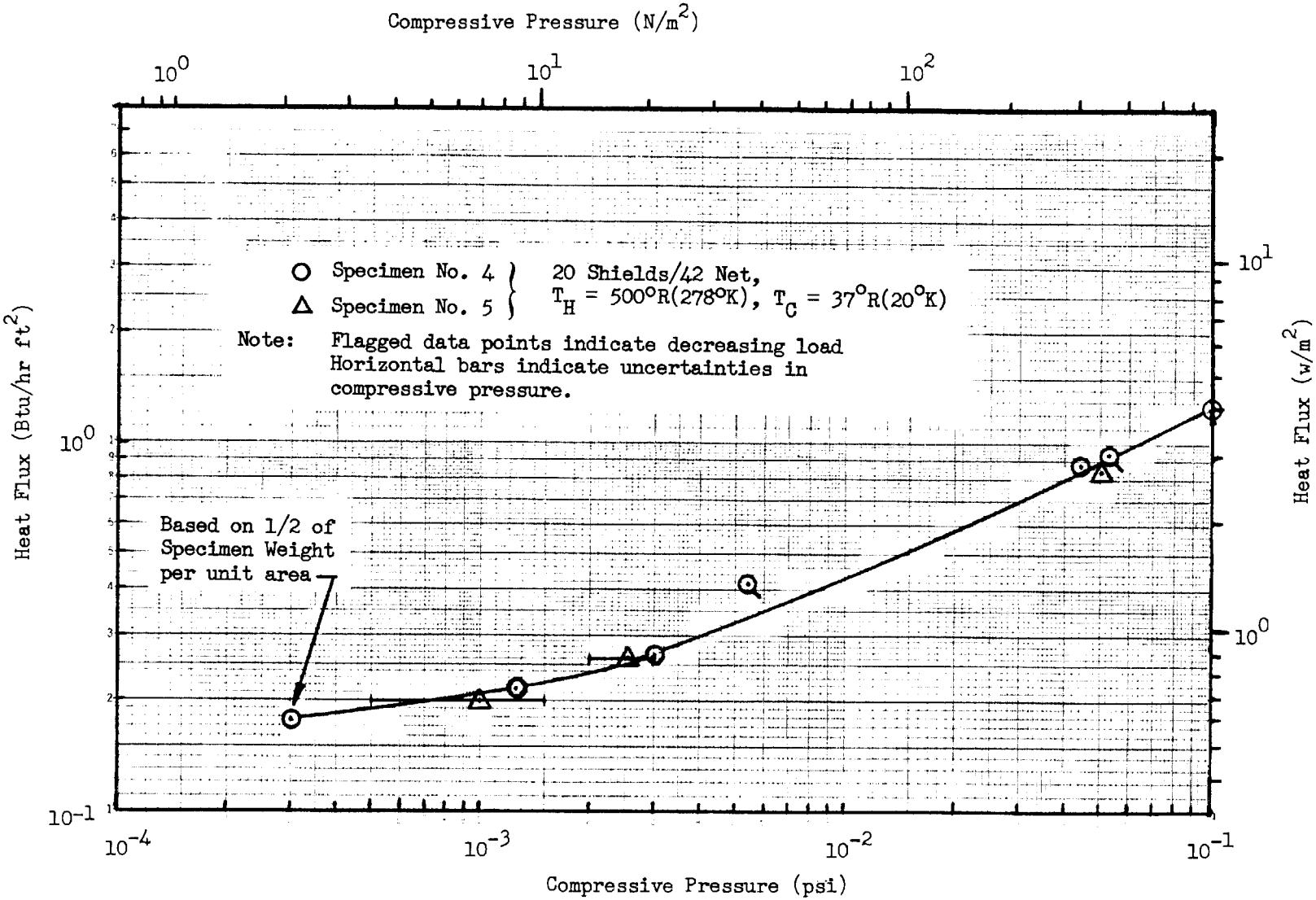

Fig. 3-8 Reproducibility of Heat Flux as a Function of Compressive Pressure for 20-Shield Specimens of Double-Aluminized Mylar/Silk Net

separation was greater than the initial thickness so that a discontinuity exists at the cold boundary interface. The effect of such a separation may increase or decrease the heat transfer. If the gap is sufficiently large, energy may be transferred parallel to the surface and into the calorimeter, resulting in an apparent increase in heat flux.

The data for the two 20-shield specimens are in excellent agreement as shown in Fig. 3-8. These are well within the apparatus repeatability. In comparing the performance of 10 shields (11 spacer layers) and 20 shields (21 spacer layers) the initial assumption is that the heat flux for the latter would be between 50 and 52 percent of that for the former. The data show that the heat flux for the 20-shield specimens is 63 percent of the average of that for the 10-shield specimens at 1×10^{-3} psi (6.9 N/m^2) and 47 and 53 percent at 1×10^{-2} psi (69 N/m^2) and 1×10^{-1} psi (690 N/m^2), respectively. This increased heat transfer in the low pressure region may be due to the greater initial pressure resulting from the increased weight of the 20-shield specimens. Consider that the heat flux through the solid portion of the insulation is proportional to some function of the compressive pressure as is discussed in Section 4.1; i.e., $q_s \propto a(P)^n$. For the case of no external forces applied to the system, the only pressure on the insulation layers is that due to the weight of the insulation itself. Thus, the insulation pressure for no external load, P_o, is proportional to the weight. The heat flux then becomes

$$(q_s)_o = f(W)$$

From the slopes of heat flux versus pressure in the high pressure region, where radiation becomes very small, the pressure proportionality approximates the 1/2 power. If this is valid at the lower pressures, and assuming that the pressure at any layer is equal to the weight per layer times the number of layers above the layer in question, the heat flux due to the insulation weight is approximated by $(1/2W)^{1/2}$. The solid contribution to the heat flux is then

$$q_s = a_o + a_1(P_a)^m$$

where $a_o \propto (1/2W)^{1/2}$ and the applied pressure is P_a. In the Flat Plate Calorimeter the load cell measures the weight of the sample plus the applied load so $P_a = (P - P_o)$ where P is based upon the load cell reading. At the low pressures where $P_o \approx P_a$, the heat flux ratio for the solid conduction of the 20-shield versus the 10-shield specimen is nearly 70 percent. If radiation and conduction are of equal magnitude, the resultant total heat flux for 20 shields approximates 60 percent of that for 10 shields.

The heat flux data for the 10- and 20-shield specimens were plotted as a function of layer density (see Fig. 3-9). The definition of layer density is the total number of layers (each layer is one shield or boundary surface plus two layers of silk net) divided by the separation between boundary plates. This corresponds to 11 layers for the 10-shield specimen and 21 layers for the 20-shield specimen in the Flat Plate Calorimeter apparatus. For a given layer density the ratio of heat flux between the 20- and 10-shield specimens varies from 0.65 at 70 layers/in. (27.6 layers/cm) to 0.30 at 110 layers/in. (43.3 layers/cm). Layer density versus compressive pressure data for the four specimens are presented in Fig. 3-10. At 110 layers/in., the 20-shield specimens correspond to a lower pressure and, therefore, a lower heat flux than do the 10-shield specimens. At the lower pressures, such as 80 layers/in., the pressure is nearly equal for all specimens at this layer density.

On the basis of heat flux versus compressive pressure data of Task I, this insulation system is reproducible to better than 10 percent. Similarly, good reproducibility was observed when comparing heat flux in terms of layer density. However, heat flux does not exhibit a constant proportionality to total number of layers. At the low pressures or layer densities, it is expected that a decreasing difference in performance will occur as the total number of layers is increased.

3.5.2 Crinkled, Single-Aluminized Mylar

Initially, the reproducibility tests of this type of insulation system were planned to include five specimens, three of 10 shields and two of 40 shields.

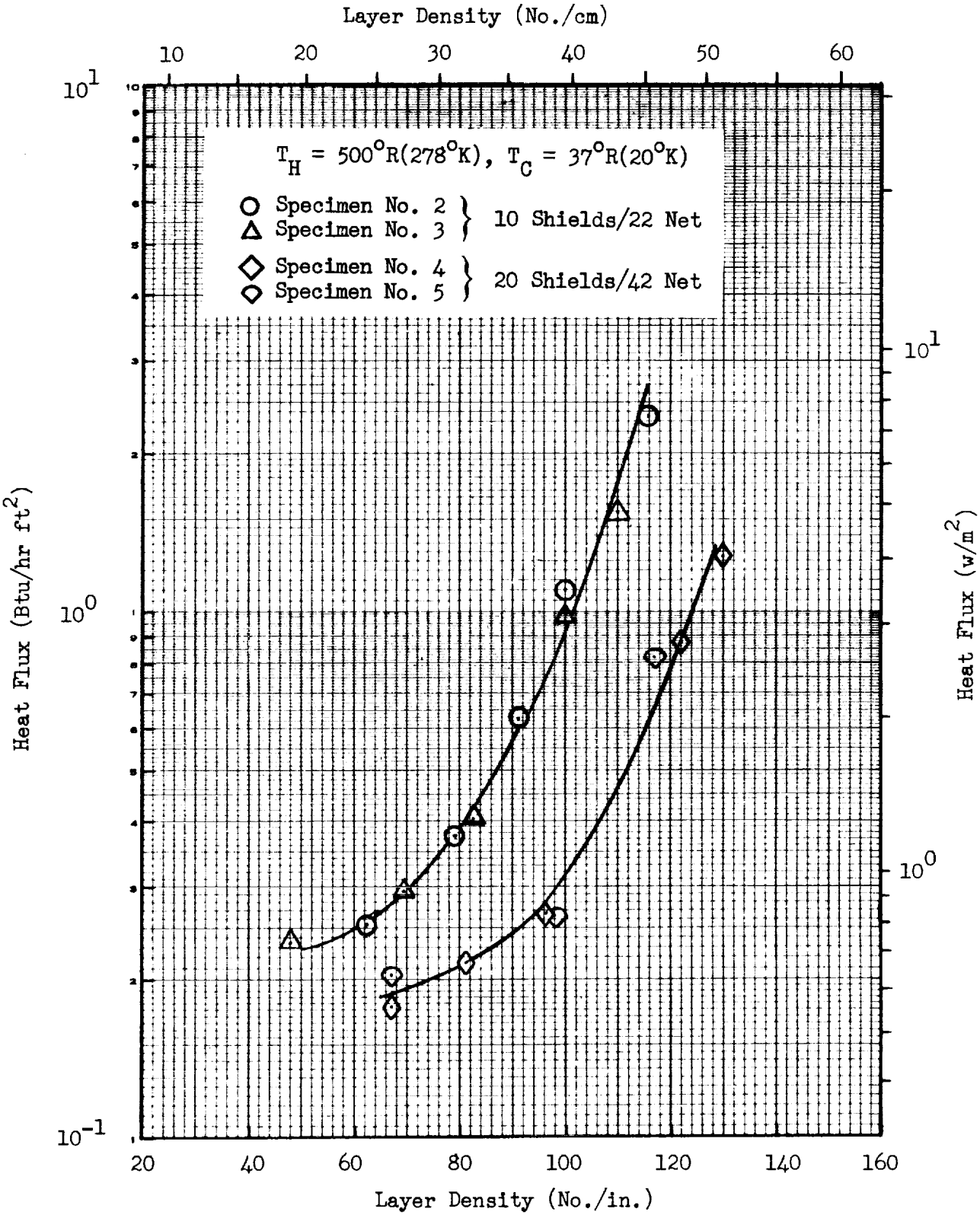

Fig. 3-9 Reproducibility of Heat Flux as a Function of Layer Density for Double-Aluminized Mylar/Silk Net

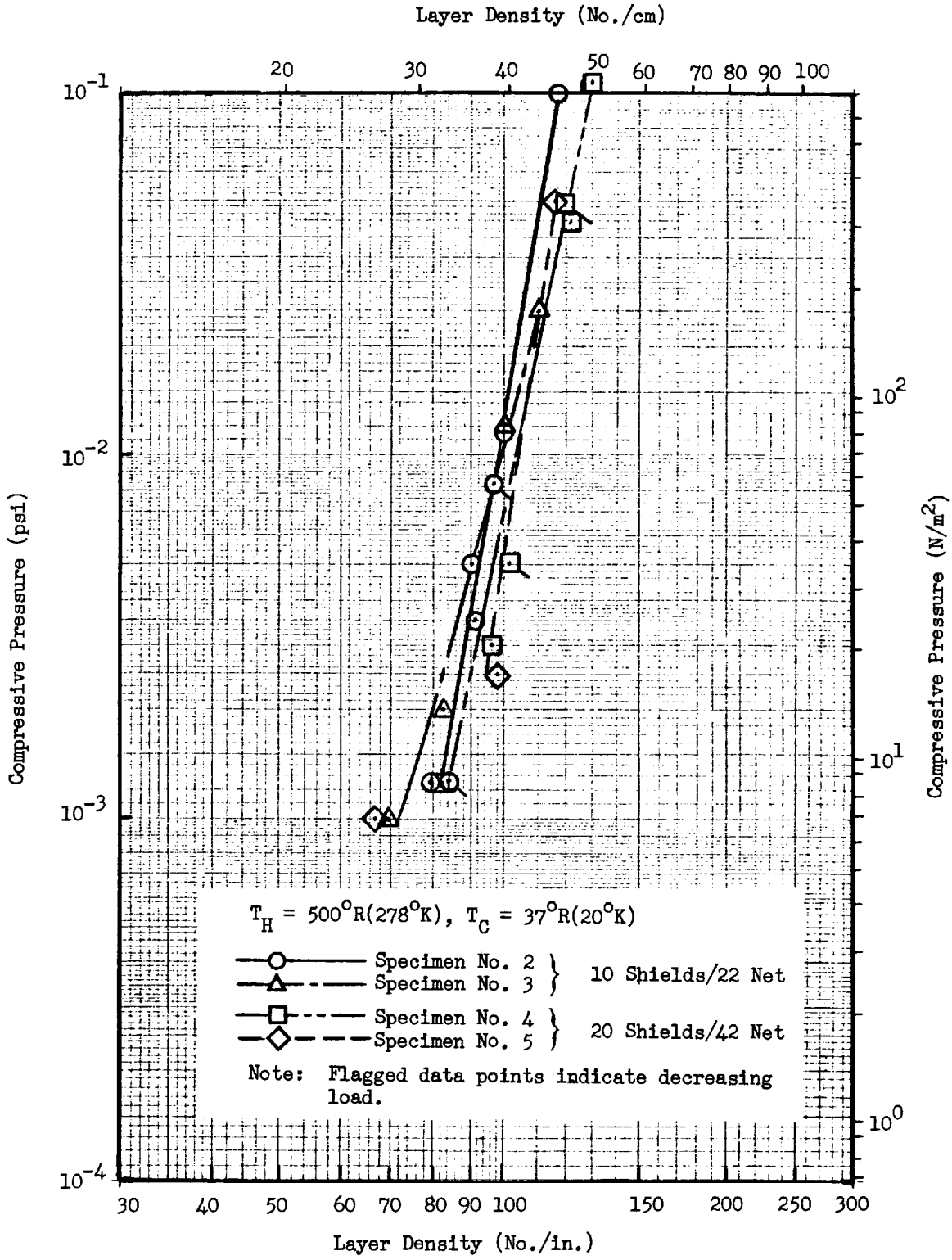

Fig. 3-10 Reproducibility of Compressive Pressure as a Function of Layer Density for Double-Aluminized Mylar/Silk Net

However, in view of the two-dimensional heat transfer effects observed during the 40-shield tests a sixth specimen was utilized to evaluate these effects in the Flat Plate Calorimeter. The preparation procedure of preloading the materials prior to assembly of a test specimen was not followed for this insulation system as it is believed this pre-treatment would have removed much of the crinkling, and the tests would, therefore, not be representative of this type of material. The individual shields were cut from the roll, and the specimen immediately assembled and placed into the Flat Plate Calorimeter apparatus. Room temperature calorimetric total hemispherical emittance data for single shields from representative heat transfer test specimens are presented in Table 3-7 together with a summary of the normal reflectance data. Calorimetric emittance measurements of the Mylar surface were made on only two specimens as the emittance of this surface is relatively high and small variations in it will have a negligible effect on the radiative transfer when compared to the effect of corresponding differences for the highly reflective aluminum surface.

The initial 10-shield specimen, No. 6, was assembled with the directions of the crinkles or striations oriented at 90° for adjacent layers. The remaining two 10-shield specimens, Nos. 7 and 8, were assembled with the crinkle direction parallel for all layers. The experimental data for these three specimens are presented in Table 3-8. Heat flux as a function of compressive pressure is shown by Fig. 3-11. Specimen No. 6, 90° crinkle orientation, initially showed a lower heat flux at compressive pressures in the $1x10^{-3}$ to $1x10^{-2}$ psi range (6.9 to 69 N/m^2). However, after loading to $1x10^{-1}$ psi (690 N/m^2) the heat flux markedly increased at decreasing pressures. This is attributed to an increase in contact area and/or number of contacts due to the high loading. The data for the two similarly oriented specimens (Nos. 7 and 8) agree to within 10 percent from $5x10^{-4}$ to $1.5x10^{-2}$ psi (3.45 to 103 N/m^2). The reproducibility of this system of 10 shields is within 10 percent for heat transfer on the basis of compressive pressure.

Table 3-7

CRINKLED, SINGLE-ALUMINIZED MYLAR EMITTANCE AND REFLECTANCE DATA

Specimen & Shield No.	ϵ_{TH} (Calorimetric)	ρ_N	ϵ_{TH} from ρ_N [a]
6 - 5, Al	0.0301	$0.975 \pm {}^{.004}_{.006}$	0.033
6 - 5 Mylar	--	$0.641 \pm {}^{.007}_{.004}$	0.38
7 - 5, Al	0.0322	$0.972 \; {}^{.005}_{.004}$	0.037
7 - 5 Mylar	--	--	--
9 - 21, Al	0.0341	$0.972 \pm {}^{.004}_{.007}$	0.037
9 - 21 Mylar	0.384	$0.619 \pm {}^{.005}_{.003}$	0.40
10 - 21, Al	0.0292	$0.977 \pm {}^{.003}_{.008}$	0.031
10 - 21 Mylar	0.375	$0.623 \pm {}^{.005}_{.007}$	0.40

Note: (a) $\epsilon_{TH} = 1.33\,\epsilon_{TN}$ for aluminum and $1.05\,\epsilon_{TN}$ for Mylar (Ref. 5)

$\epsilon_{TN} = 1 - \rho_N$

Data for the first 40-shield specimens (Nos. 9 and 10) are given in Table 3-8, and heat flux as a function of compressive pressure is shown by Fig. 3-12. Although the data for the two specimens are in good agreement for heat flux in terms of compressive pressure, the heat flux for the 40-shield specimens at 1×10^{-3} psi (6.9 N/m^2) is identical with that measured for the 10-shield specimens at this loading. As pressure increases, the heat flux difference increases and approaches a factor of four at 10^{-1} psi (690 N/m^2). The tests at the lower compressive pressures for the 40-shield specimens were conducted at thicknesses in the range of 0.4 to 1.0 in. (1.02 to 2.54 cm), and for highly anisotropic materials the two-dimensional heat transfer effects become significant in the 16-in.-(40.6-cm-) diameter Flat Plate Calorimeter. In order to

Table 3-8

FLAT PLATE CALORIMETER REPRODUCIBILITY TEST DATA WITH CRINKLED, SINGLE-ALUMINIZED MYLAR SPECIMENS

Run No.	Measured Compressive Force (b) lbf	(N)	Equivalent Compressive Pressure psi	(N/m^2)	Measured Thickness (c) in.	(cm)	Layer Density No./in.	(No./cm)	Measured Heat Flux $Btu/hr\ ft^2$	(w/m^2)
Specimen No. 6, 10 Shields, Weight = 0.023 lbm (0.0104 kg), Uncompressed Thickness = 0.35 in. (0.89 cm) (d) Crinkle Directions Oriented at 90° for Adjacent Layers										
1	0.023 (e)	(0.102)	$6x10^{-5}$ (e)	(0.41)	0.746	(1.893)	14.7	(5.8)	0.568	(1.79)
2	0.023 (e)	(0.102)	$6x10^{-5}$ (e)	(0.41)	0.364	(0.925)	30.2	(11.9)	0.406	(1.28)
3	0.5	(2.2)	$2.5x10^{-3}$	(17.3)	0.333	(0.845)	33.0	(13.0)	0.395	(1.24)
4	1.2	(5.3)	$6.0x10^{-3}$	(41.5)	0.234	(0.594)	47.0	(18.5)	0.540	(1.70)
5	3.0	(13.3)	$1.5x10^{-2}$	(103.5)	0.122	(0.310)	90.0	(35.4)	2.50	(7.88)
6	18.3	(81.4)	$9.1x10^{-2}$	(62.8)	0.067	(0.170)	164.0	(64.6)	20.05	(63.3)
7	1.0	(4.4)	$5.0x10^{-3}$	(34.5)	0.133	(0.338)	82.6	(32.5)	1.195	(3.77)
8	0.2	(0.9)	$1.0x10^{-3}$	(6.90)	0.169	(0.429)	65.1	(25.6)	0.650	(2.05)
9	0.023 (e)	(0.102)	$6x10^{-5}$ (e)	(0.41)	0.238	(0.605)	46.2	(18.2)	0.428	(1.35)
Specimen No. 7, 10 Shields, Weight = 0.0227 lbm (0.0103 kg), Uncompressed Thickness = 0.39 in. (0.99 cm) (d) Crinkled Directions Oriented Parallel in Adjacent Layers										
1	0.023 (e)	(0.102)	$6x10^{-5}$ (e)	(0.41)	0.631	(1.600)	17.4	(6.9)	0.563	(1.78)
2	0.1	(0.4)	$5.0x10^{-4}$	(3.45)	0.376	(0.955)	29.2	(11.5)	0.384	(1.21)
3	0.2	(0.9)	$1.0x10^{-3}$	(6.90)	0.313	(0.795)	35.1	(13.8)	0.467	(1.47)
4	0.25	(1.1)	$1.2x10^{-3}$	(8.29)	0.286	(0.726)	38.4	(15.1)	0.463	(1.46)
5	1.0	(4.4)	$5.0x10^{-3}$	(34.5)	0.156	(0.396)	70.5	(27.8)	0.880	(2.77)
6	2.5	(11.1)	$1.25x10^{-2}$	(86.3)	0.120	(0.305)	91.5	(36.0)	2.44	(7.70)
7	0.023 (e)	(0.102)	$6x10^{-5}$ (e)	(0.41)	0.433	(1.100)	25.4	(10.0)	0.318	(1.00)
Specimen No. 8, 10 Shields, Weight = 0.0236 lbm (0.0107 kg), Uncompressed Thickness = 0.28 in. (0.71 cm) (d) Crinkled Directions Oriented Same as Specimen No. 7										
1	0.024 (e)	(0.107)	$6x10^{-5}$ (e)	(0.41)	0.396	(1.005)	27.8	(10.9)	0.468	(1.47)
2	0.024 (e)	(0.107)	$6x10^{-5}$ (e)	(0.41)	0.282	(0.716)	39.0	(15.4)	0.425	(1.34)
3	0.1	(0.4)	$5.0x10^{-4}$	(3.45)	0.244	(0.620)	45.0	(17.7)	0.382	(1.20)
4	0.2	(0.9)	$1.0x10^{-3}$	(6.90)	0.200	(0.508)	55.0	(21.7)	0.382	(1.20)
5	0.6	(2.7)	$3.0x10^{-3}$	(20.7)	0.167	(0.424)	65.8	(25.9)	0.578	(1.82)
6	1.5	(6.7)	$7.5x10^{-3}$	(51.7)	0.125	(0.318)	87.9	(34.6)	1.15	(3.62)
7	2.0	(8.9)	$1.0x10^{-2}$	(6.90)	0.111	(0.282)	99.0	(39.0)	1.68	(5.29)
8	0.024 (e)	(0.107)	$6x10^{-5}$ (e)	(0.41)	0.203	(0.515)	54.2	(21.3)	0.385	(1.21)
Specimen No. 9, 40 Shields, Weight = 0.14 lbm (0.064 kg), Uncompressed Thickness = 1.02 in. (2.59 cm) (d) Crinkle Directions Oriented Parallel										
1	0.14 (e) (f)	(0.62)	$3.5x10^{-4}$ (e) $7.0x10^{-4}$ (f)	(2.40) (4.80)	0.780	(1.978)	52.5	(20.7)	0.365	(1.15)
2	0.14 (f)	(0.62)	$7.0x10^{-4}$ (f)	(4.80)	0.437	(1.100)	93.8	(36.9)	0.412	(1.30)
3	0.25	(1.1)	$1.25x10^{-3}$	(8.64)	0.400	(1.015)	102.5	(40.4)	0.514	(1.62)
4	1.0	(4.4)	$5.0x10^{-3}$	(34.5)	0.355	(0.902)	115.5	(45.5)	0.675	(2.13)
5	1.7	(7.6)	$8.5x10^{-3}$	(58.6)	0.315	(0.800)	130.0	(51.2)	0.770	(2.43)
6	2.2	(9.8)	$1.1x10^{-2}$	(75.9)	0.287	(0.729)	142.7	(56.2)	0.928	(2.93)
7	4.5	(20.0)	$2.25x10^{-2}$	(155)	0.226	(0.574)	181.1	(71.3)	1.64	(5.17)
8	10.0	(44.5)	$5.0x10^{-2}$	(345)	0.171	(0.435)	239.5	(94.3)	2.99	(9.44)
9	1.0	(4.4)	$5.0x10^{-3}$	(34.0)	0.355	(0.902)	115.5	(45.5)	0.470	(1.48)
10	0.25	(1.1)	$1.25x10^{-3}$	(8.64)	0.408	(1.037)	100.3	(39.5)	0.445	(1.40)
Specimen No. 10, 40 Shields, Weight = 0.14 lbm (0.064 kg), Uncompressed Thickness = 1.12 in. (2.84 cm) (d)										
1	0.14 (e) (e)	(0.62)	$3.5x10^{-4}$ (e) $3.5x10^{-4}$ (e)	(2.40) (2.40)	1.06	(2.592)	38.6	(15.2)	0.348	(1.10)
2	0.14 (f)	(0.62)	$7.0x10^{-4}$ (f)	(4.80)	1.00	(2.540)	41.0	(16.1)	0.310	(0.98)
3	0.14 (f)	(0.62)	$7.0x10^{-4}$ (f)	(4.80)	0.788	(2.000)	52.0	(20.5)	0.344	(1.09)
4	0.14 (f)	(0.62)	$7.0x10^{-4}$ (f)	(4.80)	0.665	(1.689)	61.7	(24.3)	0.367	(1.16)
5	0.14	(0.62)	$7.0x10^{-4}$ (f)	(4.80)	0.575	(1.460)	71.3	(28.1)	0.420	(1.32)
6	0.2	(0.9)	$1.0x10^{-3}$	(6.90)	0.445	(1.130)	92.2	(36.3)	0.525	(1.66)
7	0.5	(2.2)	$2.5x10^{-3}$	(7.2)	0.394	(1.000)	104.0	(40.9)	0.638	(2.01)
8	1.7	(7.6)	$8.5x10^{-3}$	(58.6)	0.315	(0.800)	130.0	(51.2)	0.820	(2.59)
9	3.0	(13.3)	$1.5x10^{-2}$	(103.5)	0.256	(0.650)	160.0	(63.0)	1.08	(3.40)

Notes: (a) Data shown were obtained for a hot boundary temperature of 500°R(278°K) and a cold boundary temperature of 37°R(20°K).
(b) Force measurement accuracy = ± 0.1 lbf (± 0.4 N).
(c) Separation between hot and cold boundary surface plates.
(d) Measured with a dial gage prior to installation in the FPC.
(e) Force = specimen weight; average pressure = 1/2 weight/unit area (assumed).
(f) Force = specimen weight; no gap; load cell indicated contact with specimen; average pressure = specimen weight/unit area (assumed).

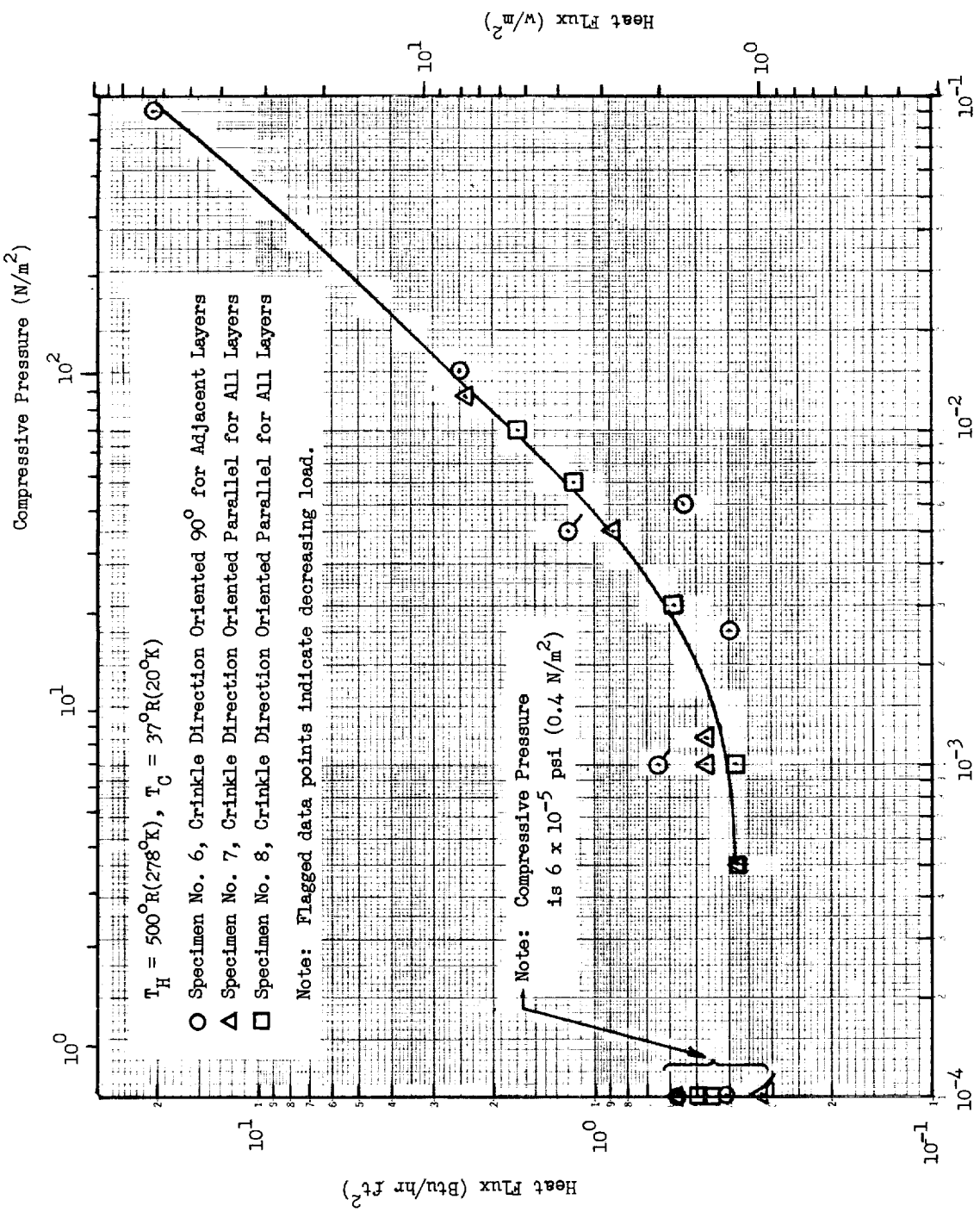

Fig. 3-11 Reproducibility of Heat Flux as a Function of Compressive Pressure for 10-Shield Specimens of Crinkled, Single-Aluminized Mylar

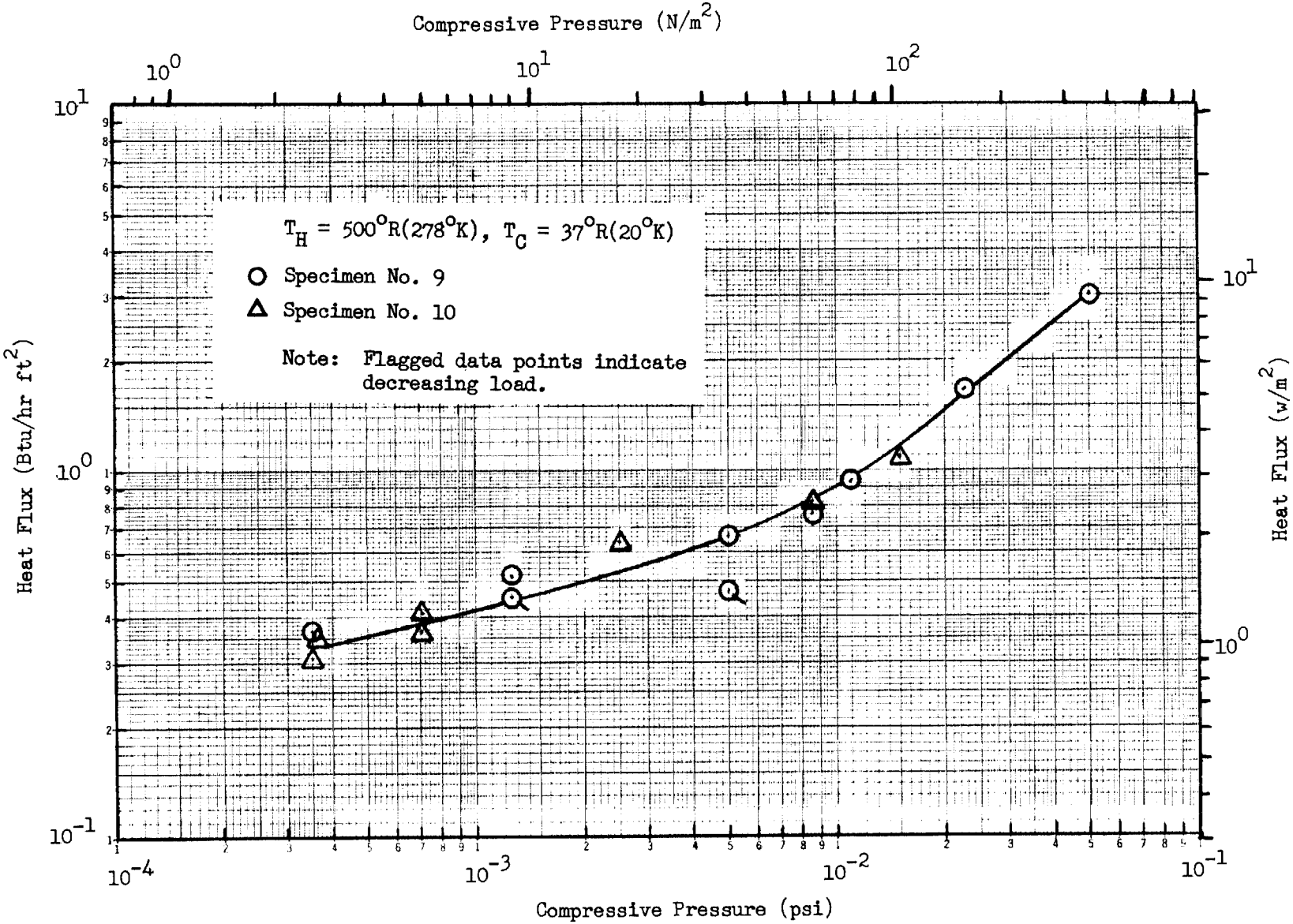

Fig. 3-12 Reproducibility of Heat Flux as a Function of Compressive Pressure for 40-Shield Specimens of Crinkled, Single-Aluminized Mylar

evaluate this effect for the crinkled, single-aluminized Mylar System, a two-dimensional heat transfer analysis was performed on the test configuration. A sixth specimen which was installed with a nearly isotropic intermediary insulation at the edge was also tested for comparison with the data for specimens 9 and 10. All heat flux tests were conducted using an edge boundary ring, spaced approximately 1/4 in. (0.635 cm) from the edge of the specimen. The edge ring was formed from a single layer of 1/2-mil-(0.013-mm-) thick by 1-in.-(2.54-cm-) wide Mylar, painted black on the interior surface and taped to the inner guard outer wall. Two thermocouples were cemented to the Mylar ring, 1/8 in. (0.318 cm) and 1/2 in. (1.27 cm) from the cold surface of the guard section. Temperatures measured by these thermocouples indicated the gradient from the cold guard to the lower edge of the ring was approximately linear, from 40 to 450°R (22 to 250°K). For the 3/4- to 1-in.-(1.91- to 2.54-cm-) thicknesses, the specimen edge viewed all of this edge ring. The linear gradient was chosen as it was felt this would produce the minimum in two-dimensional effects. However, at thicknesses greater than 3/8 in. (0.95 cm), it appears that the insulation anisotropy is sufficiently large that significant errors are introduced in the calorimeter heat flux.

The model employed to evaluate the two-dimensional effects consisted of a 1-radian segment of the test disk having a radius of 8 in. (20.3 cm). The network consisted of 8 radial columns, each 5 nodes deep, for a total of 40 nodal volumes. Three columns represent the test section, 3.125-in.-(7.938-cm-) radius. The outer edge of the disk is radiatively coupled to a ring consisting of five nodes of the same height as the disk nodes. Insulation edge and ring emittances were taken as 0.85. Each surface of the segment is bounded by two nodes which represent the test section and guard areas. These upper nodes are assumed to operate at the sink temperature and the lower ones at the source or hot boundary temperature. The output of the program consists of steady-state temperatures of each node, heat balances between each node, and the total heat transferred into test, guard, and edge areas.

For the analysis, the insulation and intermediary thermal properties were considered to be independent of temperature and pressure. The properties were

evaluated at the average insulation temperature, 270°R (150°K) and at a layer density of 70 to 80 layers/in. (27.6 to 31.5 layers/cm) which corresponds to a compressive pressure of approximately 2×10^{-3} psi (13.8 N/m^2). The thermal conductivity across the thickness for the single aluminized material was 1×10^{-5} Btu/hr ft°R (1.73×10^{-7} w/cm°K), and a conductivity of 3×10^{-2} Btu/hr ft°R (3.46×10^{-4} w/cm°K) was taken from Ref. 6 for the direction parallel to the layers. The intermediary, when used, was assumed to be isotropic and to have a thermal conductivity of 2×10^{-3} Btu/hr ft°R (3.46×10^{-5} w/cm°K). The edge node temperatures were set to conform to a linear gradient from 40 to 500°R (22 to 278°K). The conditions investigated were for 40-shield specimens with no intermediary and with a 2-in. (5.08-cm-)wide annular intermediary corresponding to the test conditions for specimen No. 11.

The results of the analytical studies are shown by Fig. 3-13 in which a ratio of measured heat flux to heat flux for the one-dimensional case, Q_c/Q_{1d}, is plotted as a function of specimen thickness. These data indicate that for thicknesses greater than 0.30 in. (0.76 cm) significant errors (>10 percent) will be present in the heat flux measurements for the case of no intermediary which corresponds to the test conditions for Specimens 6 through 10. The 2-in. (5.08-cm) intermediary increases the maximum acceptable insulation specimen thickness and also reduces the error at greater thicknesses. The sixth test specimen of this material was made up of 40 shields of the crinkled, single-aluminized Mylar cut to a 12-1/2 in. (31.8-cm) diameter. Two in. (5.08 cm), radially, of Dexiglas* paper were used as the intermediary. The Mylar was interleaved with the Dexiglas for a distance of approximately 1/4 in. (0.635 cm). The specimen edge, Dexiglas, radiated to the Mylar strip which produced a nearly linear gradient for the edge boundary. At the larger thicknesses, the midpoint of this ring was maintained at approximately the average of the hot and cold boundary temperatures; actual temperature was 270 to 285°R (150 to 158°K). No measurements of compressive pressure were made as a portion of the load was taken by the intermediary so no correlation could be obtained in this manner with the specimens tested previously.

* C. H. Dexter & Sons Paper Co.

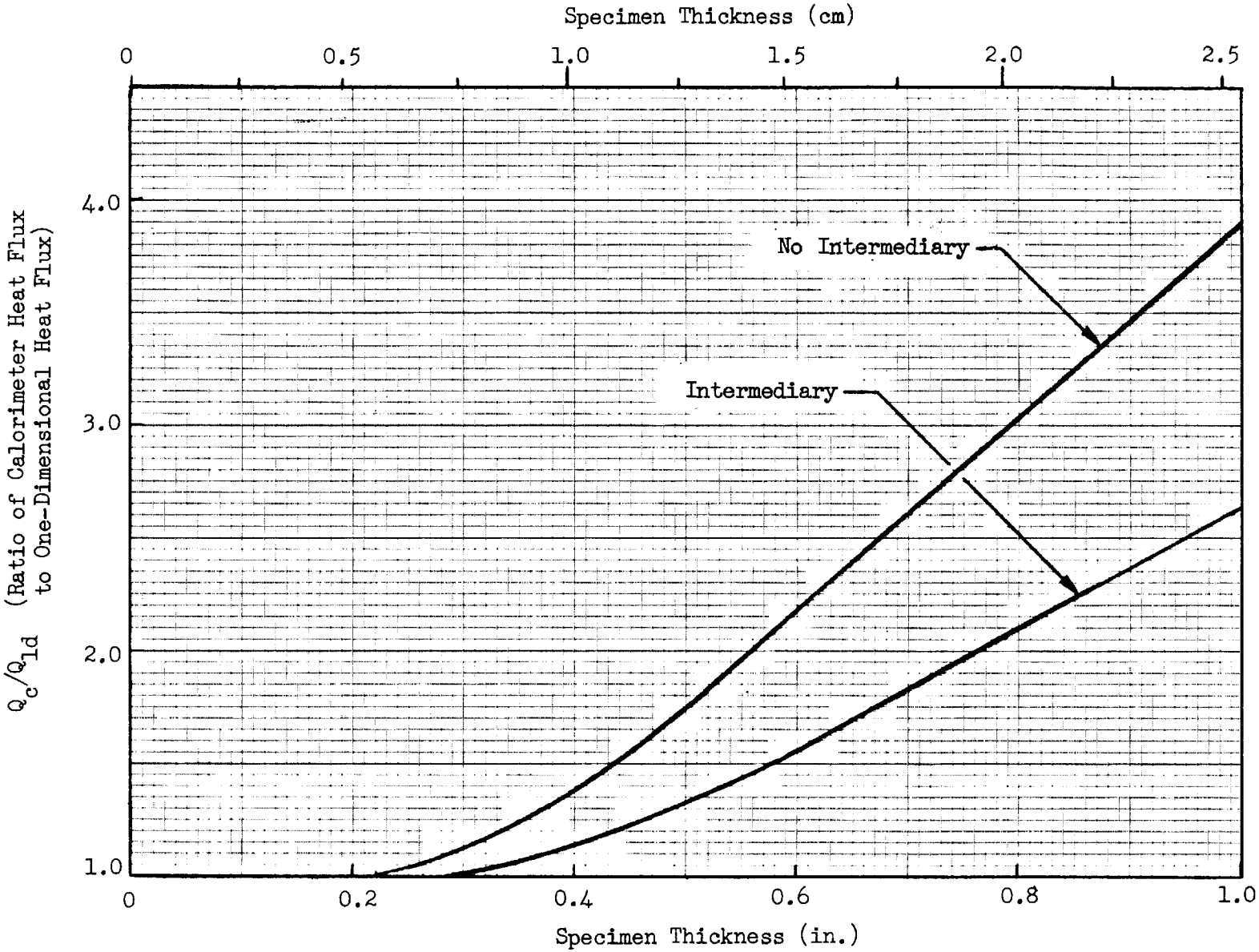

Fig. 3-13 Ratio of Calorimetric to One-Dimensional Heat Flux as a Function of Specimen Thickness

Heat flux was measured as a function of thickness which then was related to layer density. The data are given in Table 3-9.

Table 3-9

FLAT PLATE CALORIMETER REPRODUCIBILITY TEST DATA WITH A CRINKLED, SINGLE-ALUMINIZED MYLAR/DEXIGLAS INTERMEDIARY SPECIMEN (a)

Specimen No. 11, 40 Shields, 2-in.-(5.08-cm-) wide Dexiglass Intermediary

Run No.	Measured (b) Thickness in. (cm)	Layer Density No.in. (No./cm)	Measured Heat Flux Btu/hr ft^2 (w/m^2)	Corrected Heat Flux Btu/hr ft^2 (w/m^2)
1	0.891 (2.263)	46.0 (18.1)	0.214 (0.675)	0.092 (0.290)
2	0.894 (2.270)	45.8 (18.0)	0.210 (0.662)	0.090 (0.284)
3	0.750 (1.903)	34.7 (13.7)	0.235 (0.741)	0.120 (0.378)
4	0.627 (1.591)	65.4 (25.7)	0.270 (0.852)	0.168 (0.530)
5	0.500 (1.270)	82.0 (32.3)	0.335 (1.061)	0.256 (0.807)
6	0.410 (1.040)	100.0 (39.4)	0.510 (1.61)	0.447 (1.41)
7	0.250 (0.635)	164.0 (64.6)	1.07 (3.37)	1.07 (3.37)

Notes: (a) Data shown were obtained for a hot boundary temperature of 500°R (278°K) and a cold boundary temperature of 37°R (20°K)

(b) Separation between hot and cold boundary surface plates

(c) Correction taken from Fig. 3-13; i.e., Corrected Heat Flux = $\frac{\text{Measured Heat Flux}}{Q_c/Q_{1D}}$

The heat flux data for specimens 9, 10 and 11 are shown as a function of layer density in Fig. 3-14 for a comparison of the effect of the intermediary insulation on measured heat fluxes. At the lower layer densities, the use of the intermediary material reduces the measured heat flux by a factor of two over that for specimens 9 and 10. The curves of Fig. 3-13 were then employed to correct the measured heat flux values for specimens 7 through 11. In regard to the 10-shield specimens, the corrections were relatively small for the

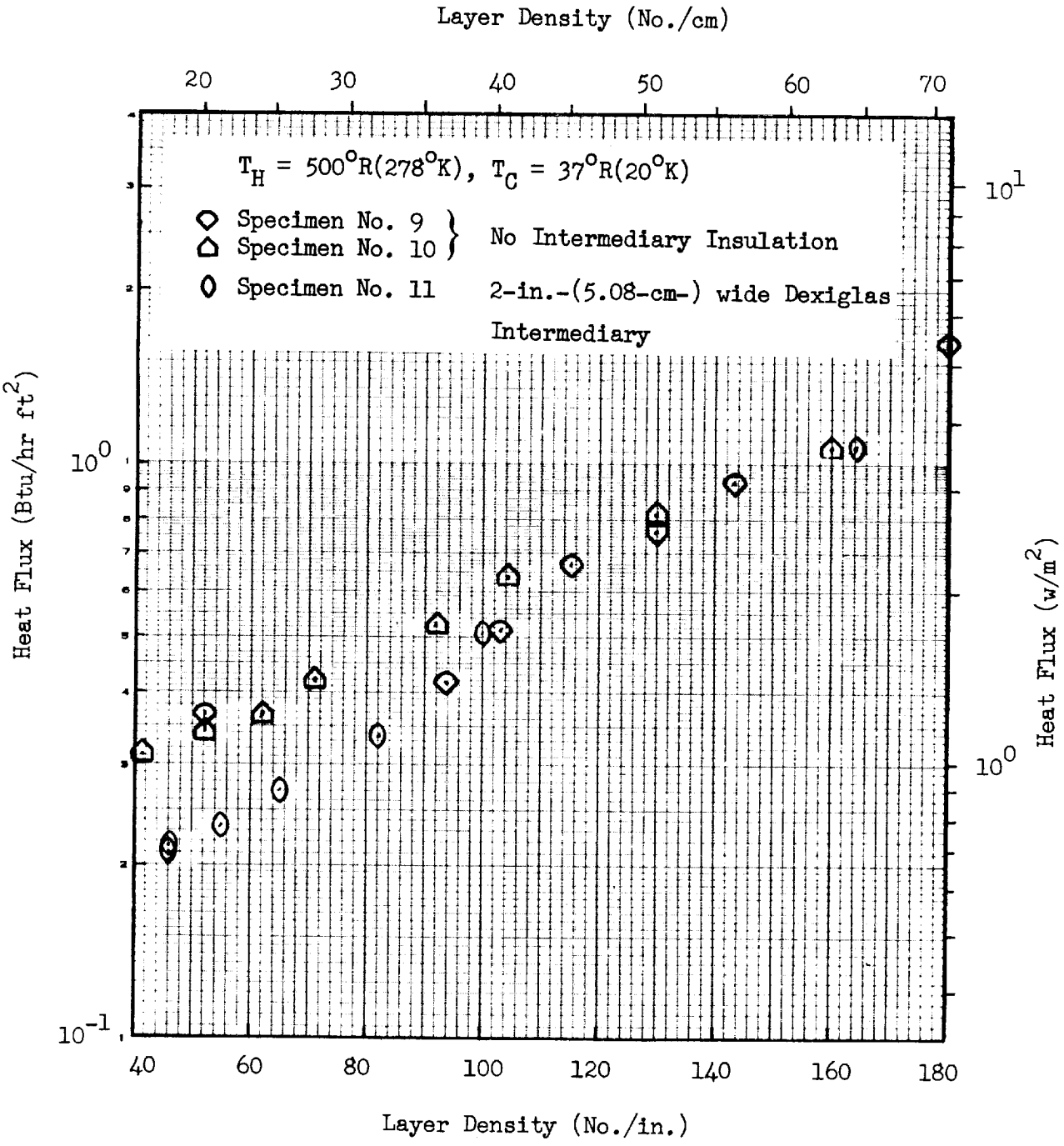

Fig. 3-14 Heat Flux as a Function of Layer Density for Crinkled, Single-Aluminized Mylar With and Without Intermediary Edge Insulation

greatest thicknesses. They ranged from 29 percent for No. 7 at 29.2 layers/in. (11.5 layers)cm) to 8 percent at 38.4 layers/in. (15.1 layers/cm) and from 3 to 8 percent for Specimen No. 8. The corrected values of heat flux are given in the last column of Table 3-9 for specimen No. 11. Heat flux data for the five specimens are plotted in Fig. 3-15 as a function of layer density. The corrected points are denoted by the vertical flags. Good agreement was achieved for the corrected values of all three of the 40-shield specimens. The data for the 10-shield specimens exhibit a relatively large difference between the individual specimens on the basis of layer density. Comparison of layer density versus compressive pressure data from Table 3-8 shows a similarly large deviation for specimens 7 and 8. This lack of reproducibility in the layer density/compressive pressure relationship results in the poor reproducibility of heat flux as a function of layer density for the 10-shield system.

Comparing the corrected heat flux data for the 40-shield specimens with an average for the 10-shield ones yields heat flux ratios for 40 to 10 shields of 0.16 at 100 layer/in. (39.4 layers/cm), 0.22 at 80 layers/in. (31.5 layers/cm), and 0.26 at 60 layers/in. (23.6 layers/cm). At the lowest layer density values, the corresponding heat flux ratios for 40 to 10 layers are 0.25 for radiation and 0.27 for conduction which are in good agreement with the corrected data. At the higher layer densities where conduction is the dominate mechanism the experimentally determined ratios are much less than theory would predict. This is apparently due to the differences in behavior of the layer density/pressure relationship. At 100 layers/in. (39.4 layers/cm) for the 10-shield specimens, the corresponding compressive pressure approximates 1×10^{-2} psi (69 N/m^2), whereas, for the 40-shield specimens the compressive pressure for the same layer density is 2×10^{-3} psi (13.8 N/m^2), as seen in Table 3-8.

In summary, the reproducibility of this type of insulation is 10 percent for heat flux versus compressive pressure. However, in terms of layer density it varies from 15 to nearly 80 percent depending upon the number of layers.

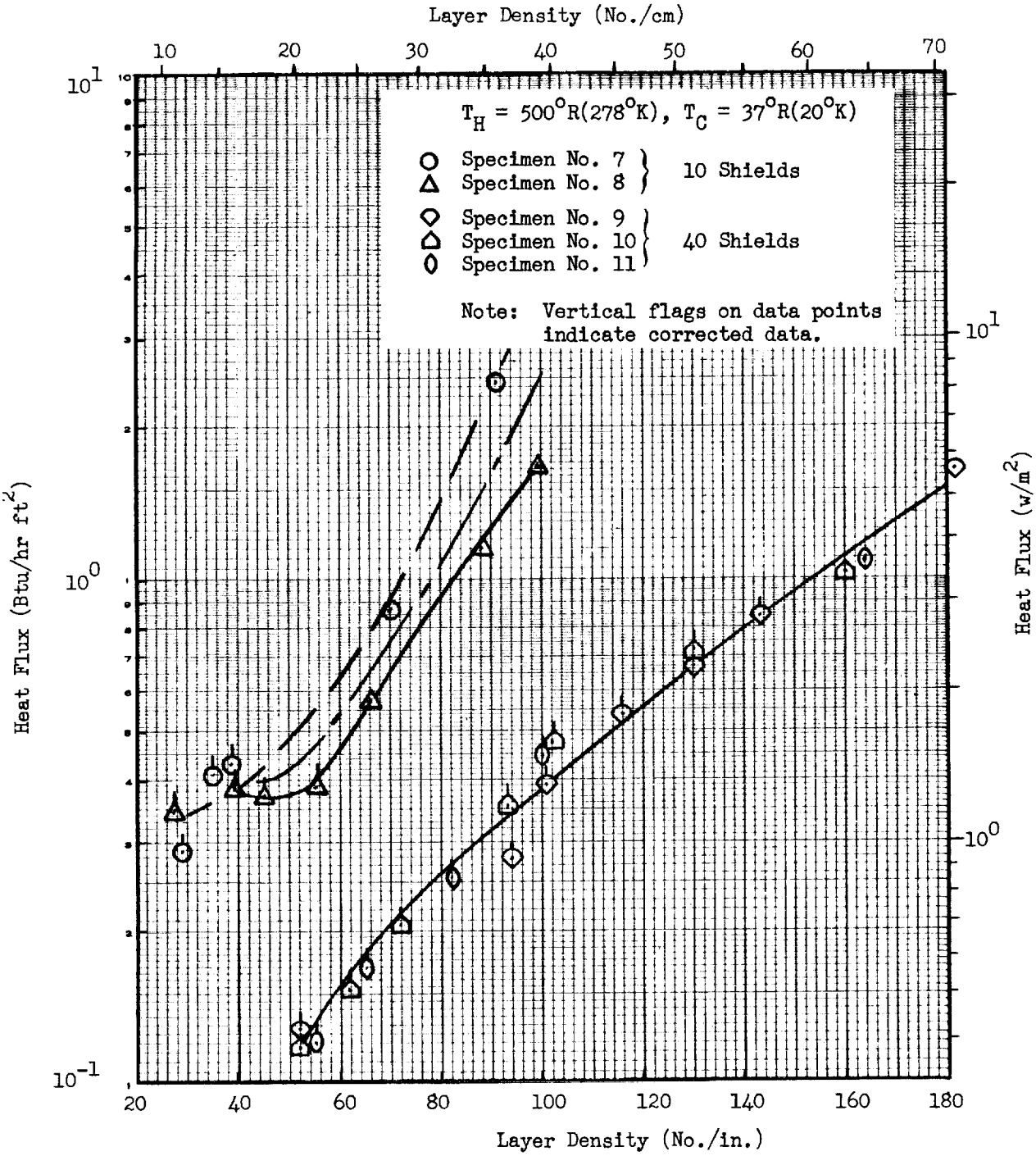

Fig. 3-15 Corrected Heat Flux as a Function of Layer Density for Crinkled, Single-Aluminized Mylar

Section 4

TASK II - MULTILAYER INSULATION PERFORMANCE

The primary objective of Task II was to develop a series of mathematical expressions which could be used to predict or to evaluate heat transfer characteristics for four specified multilayer insulation systems. In order to satisfy this objective, it was necessary to obtain experimental measurements of optical properties and total heat transfer for multiple specimens of each of the four systems. A second objective was to adapt the resulting heat transfer equation for one system selected from the four to predict its thermal performance when applied to a 4-ft-(1.22-m-) diameter tank calorimeter. The actual thermal performance of the selected system was subsequently verified by tests conducted in Task III.

The four multilayer insulation systems which were investigated are:

- Double-aluminized 1/4-mil (0.0064-mm) Mylar reflective shields with two 5-mil (0.13-mm) silk net spacers per shield
- Double-goldized 1/4-mil (0.0064-mm) Mylar reflective shields with two 5-mil (0.13-mm) silk net spacers per shield
- Crinkled, single-aluminized 1/4-mil (0.0064-mm) Mylar reflective shields
- Double-aluminized 1/4-mil (0.0064-mm) Mylar reflective shields with single 0.6-mil (0.015-mm) Tissuglas fiber paper spacers

Initially in the task, the form of a general heat transfer equation was developed. It was applicable to multilayer insulations operating with cryogenic cold boundary and space-ambient hot boundary temperatures. Then, equations of this general form were developed to describe the total heat transfer through each of the four insulation systems. Using these expressions, heat transfer can be predicted in terms of either compressive

pressure or layer density, boundary temperatures, and optical properties of the shields and spacers. The tests to provide experimental measurements of total heat transfer and total hemispherical emittance for each of the four insulation systems were conducted concurrently with the analysis. Heat transfer measurements for multiple specimens of each system were obtained on the Flat Plate Calorimeter as functions of the number of layers, compressive loading, and boundary temperatures. Total hemispherical emittance measurements for representative specimens of each shield material were obtained on the Calorimetric Emittance Apparatus as a function of shield temperature.

4.1 HEAT TRANSFER ANALYSIS

The goal of this portion of Task II was to develop a method of heat transfer analysis by which data from small scale laboratory tests, such as those performed on a flat plate calorimeter, could be used to predict the thermal performance of large scale insulation systems over a wide range of physical conditions. It was intended that this analytical method also would provide a tool by which an insulation system could be optimized for a specific mission through knowledge of the effects of temperature, pressure, and thermophysical properties of the material on overall system heat transfer.

4.1.1 Theoretical Background

Thermal energy transfer in multilayer insulations occurs through the simultaneous action of convection, conduction, and radiation processes. For application to long-term storage of cryogenic fluids in space, the convective mechanism can be neglected because the void dimensions of the insulation are small, and also because the gas pressure within the insulation must be less than 10^{-3} torr for the insulation to be sufficiently effective for such use. Conduction occurs through the solid insulation materials as well as through any residual gas present in the voids between radiation shields and spacers. In order to develop an analytical technique which is useful for both the evaluation of experimental data and the prediction of insulation system

performance for a wide range of space environments, the effect of interaction between the simultaneously acting radiation and conduction processes must first be examined. Once approximate limits regarding the geometry of the system, temperature conditions, and optical properties of the materials have been defined, the form of the appropriate solution for total heat transfer can be established.

Viskanta (Ref. 7) and Wang and Tien (Refs. 8 and 9) have investigated the problem of the interaction of radiation and conduction for the case of parallel walls separated by a conducting, absorbing, emitting, and scattering medium. The results of these investigations are in good agreement, but the solutions proposed by Wang and Tien are more easily applied to the analysis of multilayer insulations. All of the solutions are based upon a continuous isotropic layer separating the boundaries (reflective shields). Strictly, this applies only to the case of a continuous spacer (i.e., paper type) when the layers are highly compacted. At low layer densities even a paper type spacer is not continuous on a macroscopic scale because of the wavy nature of the shields and the spacers and the relatively small shield-to-spacer contact areas. However, when one considers that the space between the reflective shields is either a totally transparent medium (vacuum or gas at greatly reduced pressure) or a combination of this transparent medium and a nearly isotropic material, a good approximation is to treat the radiation process as did Wang and Tien. Similarly for conduction, the spacings between shields and the conducting media and between fibers in the spacer itself are small. Therefore, the temperature difference between adjacent solid portions is small compared to the absolute temperature, and the continuous media solution again is approximately correct.

With the method of Wang and Tien, three dimensionless parameters are used to define the problem in terms of the importance of the interaction between radiative and conductive transport mechanisms. These describe the ratio of the heat increments transferred by the conduction and the radiation processes, the optical thickness of the spacer, and whether true absorption or scattering of radiation dominates. They are defined, respectively, as

$$\eta = \frac{k\beta}{4\sigma T_1^3}, \quad \tau_o = \beta \ell, \text{ and } \lambda' = \frac{\epsilon}{\beta}$$

The conductivity term in the numerator of the first expression includes both solid-to-solid conduction and conduction through any residual gas. The basis for the use of this simplifying assumption in the identification of the applicable solution is that although the mechanisms are not physically identical, nor do they necessarily exhibit the same temperature dependence, the heat transfer used in each case may be expressed in terms of a conductivity and a local temperature gradient.

The optical thickness parameter, τ_o, is evaluated to determine whether or not the conditions fit the solution for the opaque limit for which $\tau_o \gg 1$, or the transparent limit for which $\tau_o \ll 1$. Examination of η, λ' and δ, with the latter defined as

$$\delta = \frac{\eta}{\lambda' \tau_o^2}$$

identifies whether or not radiation or conduction is predominant and whether or not these processes interact strongly or weakly. For the case where $\eta \ll 1$ and $\delta \ll 1$, the conduction and radiation process cannot be considered independently. Physically, this is typical of a high-temperature application for which the product of conductivity and extinction coefficient, $k\beta$, is small and $\tau_o > 1$, if absorption is dominant, or $\gg 1$, if scattering is dominant. An example of the latter would be a 0.4-in.(1-cm) thickness of a low density unbonded glass-fiber material exposed to an 1800°R (1000°K) vacuum environment. The total heat flux for such a case becomes

$$q = \frac{3/4\, k\beta(T_1 - T_2) + n^2\sigma(T_1^4 - T_2^4)}{3/4\,\tau_o + \left[3/8 + 1/3\,(1-\epsilon)\right]\left[\frac{1}{\eta + 2/3\epsilon} + \frac{\left(\frac{T_2}{T_1}\right)^3}{\frac{\eta}{\left(\frac{T_2}{T_1}\right)^3} + 2/3\epsilon}\right]} \tag{4.1}$$

For the optically thin case, where $\tau_o < 1$, when either $\eta \gg 1$ or $\delta \gg 1$, the appropriate total heat flux solution is

$$q = \frac{k}{\ell}(T_1 - T_2) + \frac{n^2\sigma(T_1^4 - T_2^4)}{3/4\,\tau_o}\left[\frac{3/4\,\tau_o\left(\frac{\epsilon}{2-\epsilon}\right) + 1/2\dfrac{\sqrt{3\lambda'}\tau_o}{\tanh\sqrt{3\lambda'}\tau_o} + 1/2\dfrac{\sqrt{3\lambda'}\tau_o}{\sinh\sqrt{3\lambda'}\tau_o} - 1}{3/4\,\tau_o\left(\frac{\epsilon}{2-\epsilon}\right) + 1/2\dfrac{\sqrt{3\lambda'}\tau_o}{\tanh\sqrt{3\lambda'}\tau_o} + 1/2\dfrac{\sqrt{3\lambda'}\tau_o}{\sinh\sqrt{3\lambda'}\tau_o}}\right] \quad (4.2)$$

This condition occurs for very small insulation thicknesses, i.e., on the order of 4×10^{-3} in. (0.01 cm), or for materials which have very low extinction coefficient values such that $\tau_o \ll 1$. At very low temperatures, $\eta \gg 1$. At higher temperatures such that $\eta < 1$, while τ_o remains $\ll 1$, δ becomes $\gg 1$. As discussed later, this corresponds to the case of multilayer insulations exposed to cryogenic temperature environments. The interaction increases total heat flux as can be seen by comparison of the second term on the right side of equation (4.2) with the pure radiation case. This effect becomes negligible where $\sqrt{3\lambda'}\tau_o \ll 1$, which is typical for a pure scattering case with $\lambda' = 0$, or for an optically thin case where $\tau_o \ll 1$, and equation (4.2) reduces to

$$q = \frac{k}{\ell}(T_1 - T_2) + \frac{n^2\sigma(T_1^4 - T_2^4)}{3/4\,\tau_o + \left(\frac{2}{\epsilon} - 1\right)} \quad (4.3)$$

Also, if $\sqrt{3\lambda'}\tau_o \gg 1$, which is typical for optically thick cases where $\tau_o \gg 1$, the solution becomes

$$q = \frac{k}{\ell}(T_1 - T_2) + \frac{n^2\sigma(T_1^4 - T_2^4)}{3/4\,\tau_o} \quad (4.4)$$

The three types of insultation systems studied in this program can be defined in terms of the parameters discussed above in order to select the type of heat flux solution appropriate to each case.

- Consider first the case of the crinkled, single-aluminized Mylar insulation where the space between adjacent shields is a totally transparent medium; i.e., it is evacuated or contains gas at a greatly reduced pressure. For this case, β and τ_o are both equal to zero. Equation (4.1) is meaningless because of the definition of η as applied to the basic

differential equation for heat flux. Heat is transferred by both radiation and conduction, but there are no interactions between the processes, and total heat flux is simply the sum of the individual fluxes as given by

$$q = \frac{k}{\ell}(T_1 - T_2) + \frac{\sigma(T_1^4 - T_2^4)}{\left(\frac{2}{\epsilon} - 1\right)} \qquad (4.5)$$

- The insulation with the open netting spacers presents a somewhat different problem than that for the case described above in that the netting is approximately 95% open area, but some absorption does occur in the solid area. On the basis of normal transmission measurements, the extinction coefficient, β, for the silk net is approximately 100 ft^{-1} (328 m^{-1}) for two layers of 5-mil-(0.13-mm)-thick material. The optical thickness, τ_o, is 7×10^{-2} which conforms to the transparent limit (optically thin case). Thus, Equation (4.2) applies. The absorption coefficient is not known for the silk material, but assuming it represents one-half of the total extinction coefficient, $\sqrt{3}\,\lambda' \tau_o \approx 0.09$, and Equation (4.3) describes the total heat flux. As $3/4\ \tau_o$ is negligible compared to $(\frac{2}{\epsilon} - 1)$, the heat flux is computed using Equation (4.5)

- A multilayer insulation which includes a fibrous, glass paperlike spacer was the final case that was examined. For the Tissuglass material, the absorption and extinction coefficients are 600 ft^{-1} (1970 m^{-1}) and 7000 ft^{-1} (22,970 m^{-1}), respectively (Ref. 10). The thickness is 0.6 mil (0.015 mm), $\lambda' = 9 \times 10^{-2}$, and $\tau_o = 0.35$. This places this system between the transparent and opaque limit cases. In a vacuum environment the effective conductivity of the solid phase may be as small as 1×10^{-6} Btu/hr ft °R (1.7×10^{-8} w/cm °K) at low layer densities, and η ranges from 5×10^{-3} to 1 for the room temperature to cryogenic temperature applications. The

value of δ varies from 0.4 to >>1 for these conditions. For $\delta > 1$, total heat flux is the sum of the conduction and radiation fluxes as computed from Equation (4.2). When $\delta = 0.4$ to 1.0, Equation (4.2) still presents an adequate prediction for the total heat flux as long as $r_o < 0.5$ and $\lambda' \rightarrow 0$. This is also in agreement with Viskanta's results (Ref. 7) for $r_o < 1$ in that conduction and radiation may be treated separately for engineering applications.

In summary, the total heat flux through all of the insulation systems investigated in this program can be treated as the sum of the components which result from individual conductive and radiation transport processes. For systems using the fibrous, paper-like spacers, the effect of interaction of conduction and radiation is to increase the radiative heat transfer over that of pure radiation alone.

4.1.2 Model Development

As shown in the preceding section, the properties of the insulation systems investigated in this program are such that total heat transfer through each of these systems can be evaluated by a summation of the conduction and radiation process components. The two-component equations derived in this task permit computation of heat flux in terms of temperature, number of layers, compression or layer density, and temperature dependent properties of spacers and reflective shields.

The equations were developed by treating the insulation as a continuous and homogenious medium. Consider first a single element of a multilayer composite. The physical model is depicted in Fig. 4-1 and consists of a single spacer or void layer bounded by shields having highly reflective surfaces. The reflective shield may be metallized on one or both surfaces, in which case the different optical properties of both boundaries are included. The spacer layers consist of either a second material or a void, as in the case of the crinkled, single-aluminized Mylar system. The general considerations and assumptions used in the analysis are as follows:

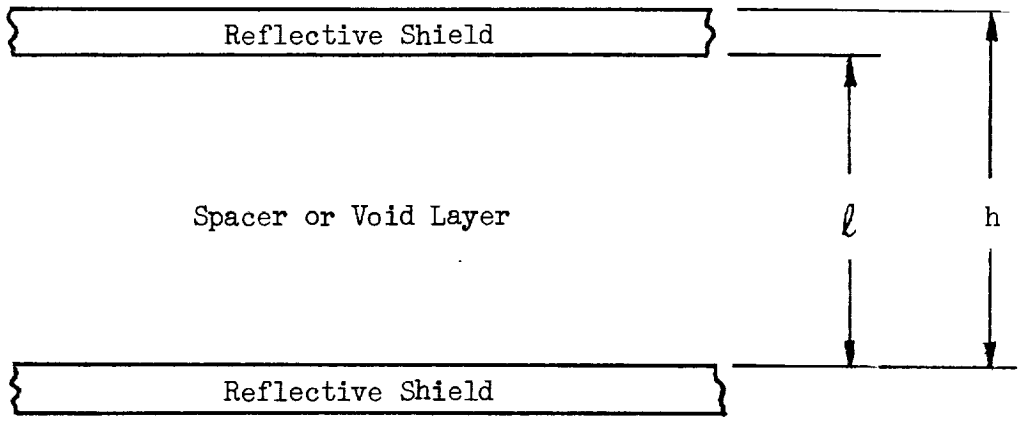

Fig. 4-1 Schematic of Physical Model for Single-Element Analysis

- Each radiation shield operates at a uniform temperature as its thermal resistance in the thickness direction is negligible compared to the resistance across the spacer layer. For example, the resistance of a 0.25-mil-(0.0064-mm-) thick plastic film is at least three orders of magnitude less than the equivalent shield-to-shield resistance in a typical multilayer insulation system.

- Radiation tunneling across the spacer or void layer may be neglected. Typical minimum spacer layer dimensions are on the order of 10^{-2} in (0.025 cm) so the tunneling effect is not a consideration above 40°R (22°K), as discussed in Ref. 11.

- The radiation and conduction mechanisms are independent and separable.

4.1.3 Characteristic Equations

Expressions describing the thermal performance of each of the four multilayer insulation systems investigated in this program were developed using

the solutions derived and presented in Appendix B. The coefficient and exponent of the solid conduction term for each system were evaluated from the experimental data of heat flux versus compressive pressure and layer density as a function of compressive pressure at constant boundary temperatures. Measurements of shield total hemispherical emittance as a function of temperature were obtained in order to formulate an expression for the temperature dependent emittance term for each type of reflective shield material. The assumptions which governed the analysis of these insulation systems are as follows:

- All tests were conducted at an ambient pressure of less than 1×10^{-6} torr. Conduction through the residual gas phase at this pressure is negligible and, therefore, the gas conduction term can be eliminated from the general heat transfer equation. For the typical path lengths between adjacent radiation shields in these multilayer insulations, $\ell < 2 \times 10^{-2}$ in.(0.051 cm), the effective gas phase thermal conductivity, k_g, was computed to be nearly two orders of magnitude less than the total effective conductivity of the insulation system.

- Refractive index of the spacer layer is unity for both the integral spacer and the net spacer. For the former, the void consists of a vacuum. For the latter, the index of the vacuum-silk fiber mixture is considered to be nearly the same as that of a vacuum because of the small fraction occupied by the silk material. Based upon the data of Caren (Ref. 12), the effective index of refraction for the fibrous glass paper spacer layer is 1.14.

- Temperature dependence for the conduction term is linear, and the coefficient is constant over several orders of magnitude of compressive pressure. The data of Ref. 10 show this to be a valid approximation for the conditions investigated in this program.

- For the layer densities investigated, $\ell \approx h$ as typical values of h are 2×10^{-2} to 5×10^{-3} in.(0.051 to 0.013 cm), whereas reflective shield thickness $(h-\ell)$ is 2.5×10^{-4} in.$(6.4 \times 10^{-4}$ cm).
- The boundary temperatures, denoted by subscripts 1 and 2, are the temperatures of the hot and cold external surfaces of the insulation composite, respectively.

With application of the above assumptions, Eq. (B.10) in the appendix reduces to:

$$q = \frac{P^m b_1}{2 N_c}\left(\frac{T_1^2 - T_2^2}{N_o}\right) + 4\left(\frac{b_4 b_5}{b_4 + b_5}\right)\frac{n^3\sigma}{(4+a_4)}\left(\frac{T_1^{4+a_4} - T_2^{4+a_4}}{N_o}\right) \qquad (4.6)$$

which is the fundamental equation used for analysis of the insulation system thermal performance. Setting $\frac{b_1}{2N_c} = a$, separating out $\frac{T_1 + T_2}{2} = T_m$, and substituting $b_4 = \frac{\epsilon_{TR4}}{(540)^{a_4}}$ and $b_5 = \frac{\epsilon_{TR5}}{(540)^{a_4}}$ in order to put the equation in a form using a room temperature value of total hemispherical emittance, ϵ_{TR}, Eq. (4.6) becomes

$$q = \frac{aP^m T_m (T_1 - T_2)}{N_o} + \frac{4\epsilon_{TR4}\,\epsilon_{TR5}\,n^3\sigma}{(4+a_4)(540)^{a_4}(\epsilon_{TR4}+\epsilon_{TR5})N_o}\left(T_1^{4+a_4} - T_2^{4+a_4}\right) \qquad (4.7)$$

As the Flat Plate Calorimeter experimental data is based upon measurement and control of the temperatures of the flat plate surfaces in contact with the specimen, and not the exterior surface temperatures of the insulation, it was necessary to modify Equation (4.7) further to include the thermal resistances between the insulation specimen and the boundary plates. Assuming that the boundary surface emittance values approach one ($\epsilon_b \approx 0.8$), the radiation term can be approximated by considering these surfaces to be equivalent to one additional reflective shield. This can be done because the radiant exchange factor between the shield of ϵ_1 and the boundary of $\epsilon_o \approx 1$ is equal to ϵ_1, whereas between adjacent shields it equals $\frac{\epsilon_1}{2}$. For the conduction term, the spacers between the exterior shields and the boundary

plates represent two additional resistances which increases the number of elements by two. Equation (4.7) was therefore modified to suit the flat plate calorimeter test conditions by substituting $(N_s + 1)$ for N_o in the first term, and N_s for N_o in the second term in the right side of the equation, where N_s is the number of radiation shields; and by substituting T_H and T_C (the hot and cold boundary plate surface temperatures) for T_1 and T_2, respectively. Evaluation of Equation (4.7) for each of the four multilayer insulations investigated, with n omitted for those systems where its value was found to be unity, thus results in the following:

Crinkled, Single-Aluminized Mylar

$$q = \frac{a' P^{m'} T_m}{N_s+1} (T_H - T_C) + \frac{4 \epsilon_{TRA} \epsilon_{TRM} \sigma}{(4+a_4)(540)^{a_4} (\epsilon_{TRA} + \epsilon_{TRM}) N_s} \left(T_H^{4+a_4} - T_C^{4+a_4} \right) \qquad (4.8)$$

Double-Aluminized Mylar/Silk Net

$$q = \frac{a'' P^{m''} T_m}{N_s+1} (T_H - T_C) + \frac{2 \epsilon_{TRA} \sigma}{(4+a_4)(540)^{a_4} N_s} \left(T_H^{4+a_4} - T_C^{4+a_4} \right) \qquad (4.9)$$

Double-Goldized Mylar/Silk Net

$$q = \frac{a''' P^{m'''} T_m}{N_s+1} (T_H - T_C) + \frac{2 \epsilon_{TRG} \sigma}{(4+a_4)(540)^{a_4} N_s} \left(T_H^{4+a_4} - T_C^{4+a_4} \right) \qquad (4.10)$$

Double-Aluminized Mylar/Tissuglas

$$q = \frac{a'''' P^{m''''} T_m}{N_s+1} (T_H - T_C) + \frac{2n^3 \epsilon_{TRA} \sigma}{(4+a_4)(540)^{a_4} N_s} \left(T_H^{4+a_4} - T_C^{4+a_4} \right) \qquad (4.11)$$

In these equations, the primed constants "a" and "m" denote coefficients and exponents peculiar to each insulation system. The values ϵ_{TRA}, ϵ_{TRM}, and ϵ_{TRG} refer to average room temperature emittance values for aluminized Mylar, Mylar, and goldized Mylar surfaces, respectively. For the two systems with double-aluminized Mylar shields, $\epsilon_{TR4} = \epsilon_{TR5} = \epsilon_{TRA}$. Similarly,

for the double-goldized Mylar shield system, $\epsilon_{TR4} = \epsilon_{TR5} = \epsilon_{TRG}$. For the range of Mylar substrate and metallized surface thicknesses investigated in this program, the temperature dependency exponent, $\alpha 4$, was found to be approximately constant and equal to 0.67 for both the aluminum and the Mylar surfaces. However, for the gold surfaces, this value varied with thickness over the range investigated. Complete results of the emittance measurements as a function of temperature are presented in Section 4.2.

In the analysis, the radiation heat transfer components of Equations (4.8) through (4.11) were computed using the room temperature emittance and temperature dependency values obtained from least-squares curve fits of the calorimetric emittance data. Subsequently, the radiation components were subtracted from the total measured heat flux for each flat plate calorimeter test to determine the solid conduction heat transfer components. The resultant solid conduction heat flux values were then evaluated as a function of compressive pressure to determine the constant coefficient and exponent values "a" and "m" for each of the four multilayer systems. This evaluation was accomplished by again using least-squares curve fits of the data. The process was repeated for each variation of number of layers and boundary temperatures that was investigated.

A second method was also used with limited success to determine coefficients and exponents of the heat transfer equations. This consisted of fitting the experimental heat flux versus compressive pressure data to an equation of the form

$$y = Ax^n + B$$

where B is the radiative heat transfer term, x is compressive pressure, and y is heat flux - all for a particular set of boundary temperatures. The advantage of this analysis method is that B is not computed separately, but rather from total heat flux data. These results can then be used to evaluate the type of solution proposed for the radiative transport term. Difficulty was encountered in using this method as a larger number of data points than were obtained for a single set of temperature conditions would be required to obtain accurate values of the coefficients and exponents.

Although compressive pressure is an important parameter in the study of the heat transfer process, it is not useful for insulation system design or for the prediction and analysis of tank performance. Rather, heat flux data as a function of the number of layers and total system thickness are required for these studies. Therefore, in the analysis, a consistent relationship between compressive pressure and layer density was needed so that a layer density term could be substituted for the pressure term in Equation (4.7). On the basis of the experimental data, the best approximation of the layer density-pressure relationship was found to be of the form

$$P = c(\overline{N})^n$$

Substitution of this pressure-layer density relationship into the heat transfer Equation (4.7) yields

$$q = \frac{a\left[c(\overline{N})^n\right]^m T_m}{N_s+1}(T_H-T_C)+\frac{4\epsilon_{TR4}\,\epsilon_{TR5}\,n^3\sigma}{(4+a_4)(540)^{a_4}(\epsilon_{TR4}+\epsilon_{TR5})N_s}\left(T_H^{4+a_4}-T_C^{4+a_4}\right) \quad (4.12)$$

Subsequent to completion of the flat plate calorimeter tests, the constant coefficients a and c and the constant exponents n and m were evaluated from the best fit of the data for solid conduction heat flux as a function of compressive pressure, and compressive pressure as a function of layer density. Results of these evaluations are presented in Sections 4.3.1, 4.3.2, 4.3.3, and 4.3.4 for the double-aluminized Mylar/silk net, double-goldized Mylar/silk net, crinkled single-aluminized Mylar, and double-aluminized Mylar/Tissuglas multilayer systems, respectively. Summarized below are the equations which result when the constant values of a, c, n, and m, evaluated independently for each of the multilayer systems, and the constant value of σ are substituted into Equation (4.12).

Crinkled, Single-Aluminized Mylar

$$q = \frac{1.65\times10^{-9}(\overline{N})^{2.32}T_m}{N_s+1}(T_H-T_C)+\frac{6.852\times10^{-9}\epsilon_{TRA}\,\epsilon_{TRM}}{(4+a_4)(540)^{a_4}(\epsilon_{TRA}+\epsilon_{TRM})N_s}\left(T_H^{4+a_4}-T_C^{4+a_4}\right) \quad (4.13)$$

where $\overline{N} < 87$ layers/in. (34.3 layers/cm)

and

$$q = \frac{8.57\times10^{-9}(\bar{N})^{2.02}T_m}{N_s + 1}(T_H - T_C) + \frac{6.852\times10^{-9}\epsilon_{TRA}\epsilon_{TRM}}{(4+a_4)(540)^{a_4}(\epsilon_{TRM}+\epsilon_{TRA})N_s}\left(T_H^{4+a_4} - T_C^{4+a_4}\right) \quad (4.14)$$

where $\bar{N} \geq 87$ layers/in. (34.3 layers/cm)

Double-Aluminized Mylar/Silk Net

$$q = \frac{7.46\times10^{-12}(\bar{N})^{3.56}T_m}{N_s + 1}(T_H - T_C) + \frac{3.426\times10^{-9}\epsilon_{TRA}}{(4+a_4)(540)^{a_4}N_s}\left(T_H^{4+a_4} - T_C^{4+a_4}\right) \quad (4.15)$$

Double-Goldized Mylar/Silk Net

$$q = \frac{4.37\times10^{-11}(\bar{N})^{3.27}T_m}{N_s + 1}(T_H - T_C) + \frac{3.426\times10^{-9}\epsilon_{TRG}}{(4+a_4)(540)^{a_4}N_s}\left(T_H^{4+a_4} - T_C^{4+a_4}\right) \quad (4.16)$$

Double-Aluminized Mylar/Tissuglas

$$q = \frac{1.13\times10^{-13}(\bar{N})^{3.91}T_m}{N_s + 1}(T_H - T_C) + \frac{3.426\times10^{-9}n^3\epsilon_{TRA}}{(4+a_4)(540)^{a_4}N_s}\left(T_H^{4+a_4} - T_C^{4+a_4}\right) \quad (4.17)$$

In using these equations, it should be remembered that each one represents the best fit of all of the data obtained during the program for that particular multilayer system. Consequently, comparison of the heat flux curve obtained from the equation for any one system with the test data obtained for any one specimen of that system will result, generally, in a poor correlation due to the relatively wide scatter of the heat flux and compressive pressure data as a function of layer density for specimens with different numbers of layers.

Best fits of the data for individual specimens and specimens of the same number of layers also were investigated for one of the four multilayer systems, double-goldized Mylar/silk net. Results of this investigation are presented and discussed in Section 4.4.

For all four of the multilayer systems investigated, the best fits of solid conduction heat flux data as a function of compressive pressure were obtained using a least-squares curve fitting process. In fitting compressive pressure data as a function of layer density for the double-goldized Mylar/silk net system, best fits were obtained using both least-squares and graphic fitting processes. It was found that the small additional precision afforded by the least-squares method was not justified, since the scatter of these data is relatively wide. Consequently, the data of compressive pressure as a function of layer density were fit graphically for each of the other multilayer systems.

4.2 REFLECTIVE SHIELD EMITTANCE MEASUREMENTS

Calorimetric total hemispherical emittance measurements were obtained as a function of temperature on specimens of each type of reflective shield material in order to evaluate the temperature-dependent emittance term in the heat transfer equation used for analysis and prediction of multilayer insulation thermal performance. Emittance determinations were also made at 540°R (300°K) on selected shields from the heat transfer test specimens so that the radiative transport component could be computed for each system at the various boundary temperatures. The apparatus used for these measurements is described in Section 3.1.2. The shield materials investigated were double-aluminized 1/4-mil Mylar, double-goldized 1/4-mil Mylar, and crinkled, single-aluminized 1/4-mil Mylar. Measurements were made on both the aluminum and the Mylar surfaces of the latter material. The results are presented in this section.

As the radiation shields used in this program are plastic films with thin vacuum-deposited metal coatings on one or both surfaces, it is important to understand the relationships of shield radiative properties to temperature and metal coating thickness. The first theoretical work on the radiation properties of thin metallic coatings (Ref. 13) was based upon the Drude single (or free) electron theory (DSE) of optical constants for bulk metals. However, later investigations (Ref. 14) showed that the anomalous skin effect theory (ASE), which was also initially derived for bulk metals, should be used for the cryogenic temperature range. Domoto (Ref. 15) has shown recently that the values of total hemispherical emittance predicted from the ASE

theory are nearly an order of magnitude greater than those predicted by the DSE theory at low temperatures. Also, it has been shown that when the metallic coating thickness becomes less than the electron mean free path, the electrical and thermal properties of the coating will differ from those of the bulk metal (Refs. 16 and 17).

From Ref. 15, for the cryogenic temperature range, the total normal emittance of metals including aluminum and gold can be approximated by

$$\epsilon_{TN} = C_1\left(3/4 + \sqrt{3}/\bar{\sigma}\right)\frac{A}{1+A} \tag{4.18}$$

where C_1 includes the Fermi velocity, the constant, $\bar{\sigma}$ is related to the electrical conductivity, and A is proportional to the absolute temperature to the two-thirds power. Total hemispherical emittance, which is the most suitable parameter for evaluation of heat transfer data, is given by $\epsilon_{TH} = 1.33\ \epsilon_{TN}$ (Ref. 5). For thin coatings, the electrical conductivity is proportional to the bulk metal electrical conductivity divided by the ratio of the electron mean free path to the film thichnesses (Ref. 17). As the thickness becomes less than the electron mean free path, the film conductivity decreases. This decrease in conductivity results in a corresponding increase in emittance.

Substituting $\bar{\sigma} \propto C_2\sigma_{(T)}$ and $A \propto C_3T^{2/3}$ into Equation (4.18) yields

$$\epsilon_{TN} \propto C_1\left[3/4 + \frac{\sqrt{3}}{C_2\sigma_{(T)}}\right]\left[\frac{C_3T^{2/3}}{1 + C_3T^{2/3}}\right] \tag{4.19}$$

where C_1, C_2, and C_3 are constants.

Except at very high temperatures, $C_3T^{2/3} \ll 1$, and the second term in parentheses on the right side of Equation (4.19) approaches C_3T^{β}. For higher temperatures, $\beta < 2/3$, and as temperature decreases, β approaches the value of two-thirds. For thin films, the $\frac{\sqrt{3}}{C_2\sigma_{(T)}}$ term becomes

$$\frac{\sqrt{3}}{C_2\sigma_b}\left(1 + \frac{C_2\sigma_b}{d}\right) = \frac{\sqrt{3}}{C_2C_4}\,T\left(1 + \frac{C_2C_4}{dT}\right) \propto T^{\alpha}$$

where d is the film thickness and σ_b is the bulk conductivity.

Thus the temperature dependence of emittance is given by

$$\epsilon_{TN(T)} \propto T^{(\alpha+\beta)}$$

The value of α increases with increasing d, whereas β is independent of d. Qualitatively, ($\alpha + \beta$) may be greater than or less than 0.67 for very large values of d, and as d becomes very small $(\alpha+\beta) < 0.67$. Thus, for the thin metallic coatings, the temperature dependence of emittance may be a function of the film thickness depending upon the properties of the particular metal.

4.2.1 Double-Aluminized 1/4-mil Mylar

Total hemispherical emittance data as a function of temperature from 110°R to 560°R (61°K to 311°K) for five specimens are shown in Fig. 4-2. The data fall into two well defined groups, both of which are in good agreement with the temperature dependence of $T^{2/3}$. The experimental data were fit using a least-squares method to evaluate the coefficients and exponents of the equations given in Fig. 4-2. The expression for the average emittance of all of the specimens of this material is $\epsilon_{TH} = 4.14 \times 10^{-4} (T)^{0.67}$ where the temperature is in °R. On the basis of emittance at 540°R (300°K), as used in the heat transfer equation, this expression yields a value of 0.0275. The measured values of emittance at this temperature ranged between 0.025 and 0.030, so the average is within $\pm$ 10 percent of the maximum and minimum values which were determined experimentally.

4.2.2 Double-Goldized 1/4-mil Mylar

The experimental data for six samples of this material are shown in Fig. 4-3. The value of total hemispherical emittance as a function of temperature as predicted by the ASE theory (Ref. 18) for the bulk metal is shown by the dashed line. The temperature dependence for this case is $T^{2/3}$. However, for the actual metalized shields used in the program, the temperature dependence is less than that predicted for the bulk material. This is believed to be due to the thickness effect on the exponent as discussed earlier.

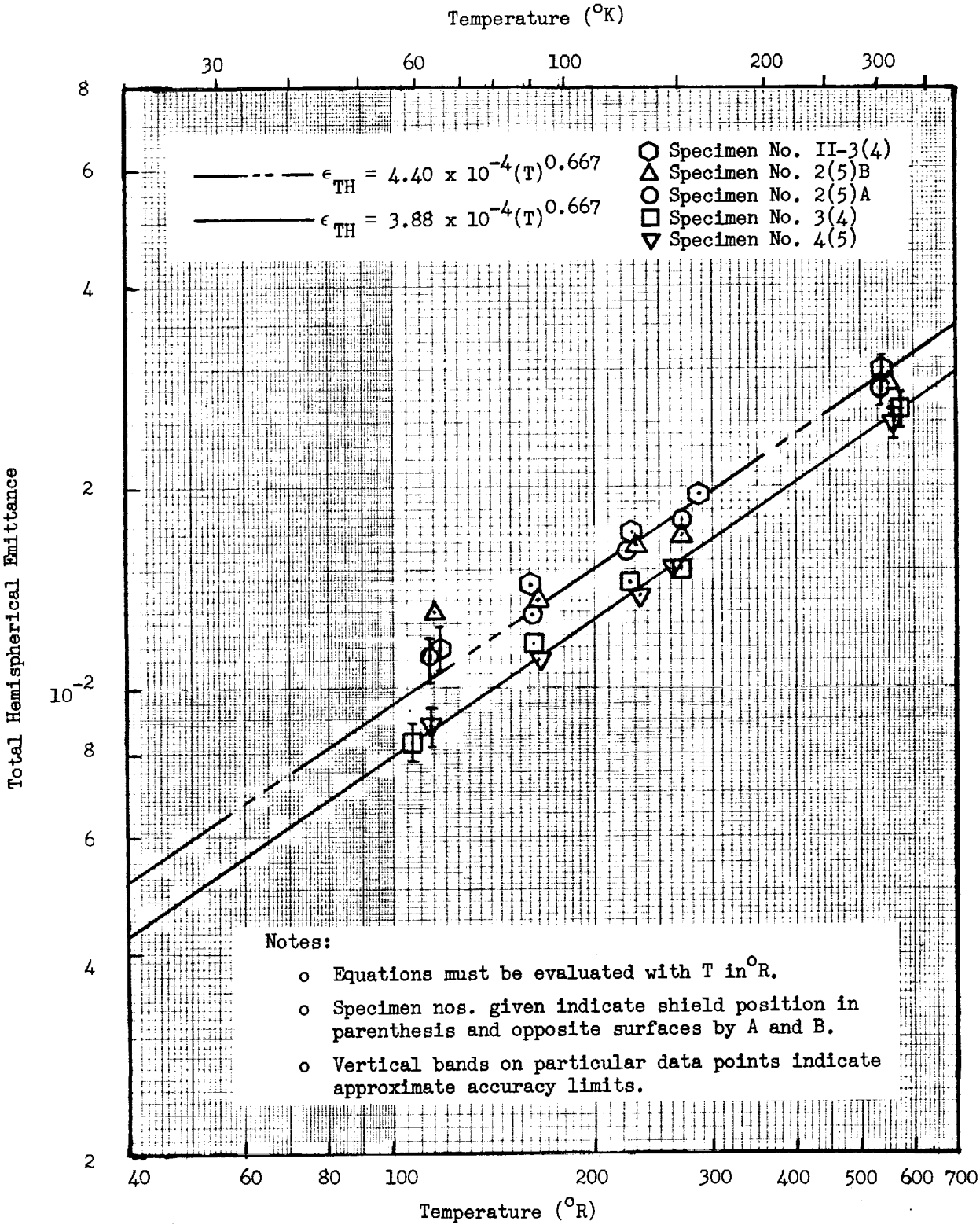

Fig. 4-2 Total Hemispherical Emittance of Double-Aluminized ¼-Mil Mylar As a Function of Temperature

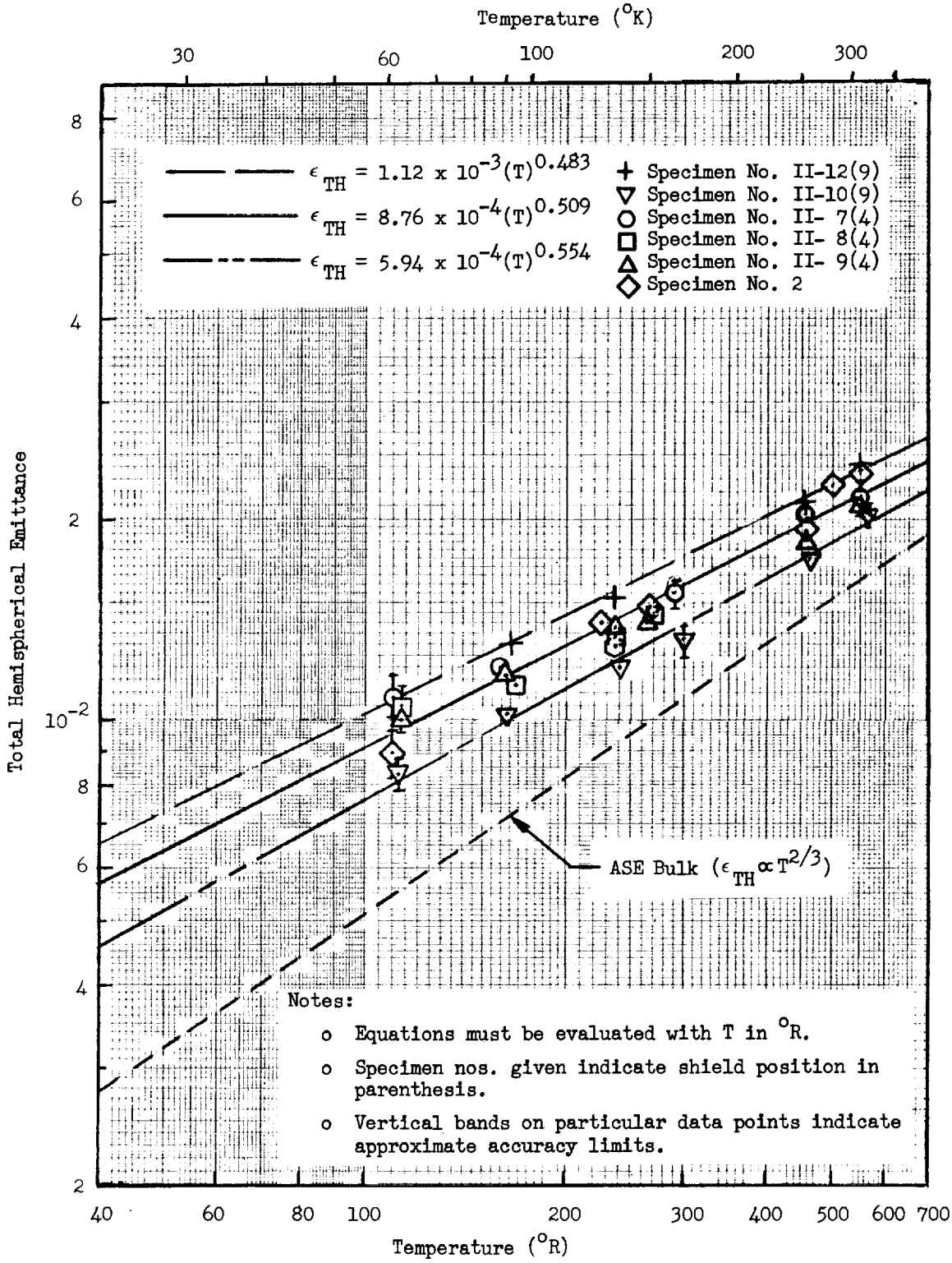

Fig. 4-3 Total Hemispherical Emittance of Double-Goldized ¼-Mil Mylar as a Function of Temperature

No accurate measurements were obtained of film thickness for these shields but from electrical resistance measurements of the coatings, the higher emittance samples exhibited higher resistances, which indicates less thickness than was indicated for the lower emittance specimens. Recent studies of gold coating on several substrates (Ref. 19) have shown this trend for gold thicknesses in the range of 400 to 700 Å. The goldized shields used in this program had coatings in this approximate thickness range.

The experimental data for specimens II-10 and II-12 were best fit by the equations corresponding to the broken lines shown in Fig. 4-3. For the other four specimens, the best fit is shown by the solid line which corresponds to the expression $\epsilon_{TH} = 8.76 \times 10^{-4} (T)^{0.509}$, where T is in °R. This expression also approximates the best fit of the data for all six specimens. At a temperature of 540°R (300°K), it yields an emittance value of 0.0215, and the range of measured values corrected to this temperature agrees within approximately $\pm$ 10 percent.

4.2.3 Crinkled, Single-Aluminized 1/4-mil Mylar

Measurements were obtained on three specimens of the Mylar side and on three specimens of the aluminum side of this material. The emittance data are shown in Figs. 4-4 and 4-5, respectively. Total hemispherical emittance of the Mylar side increases with increasing temperature in proportion to $T^{2/3}$. The experimental data are fit to within 10 percent by the equation

$$\epsilon_{TH} = 5.58 \times 10^{-3} (T)^{0.667}$$

over the temperature range of 115°R to 560°R (64°K to 311°K). Total hemispherical emittance of this surface is an order of magnitude higher than that for an aluminum surface over the temperature range investigated. A possible reason for this is that the absorption coefficient of the Mylar may be nearly constant over the wavelength range of 10 to 100 μ m.

The data for the aluminum side of this material do not appear to fit an equation of the simple temperature dependence form such as those derived

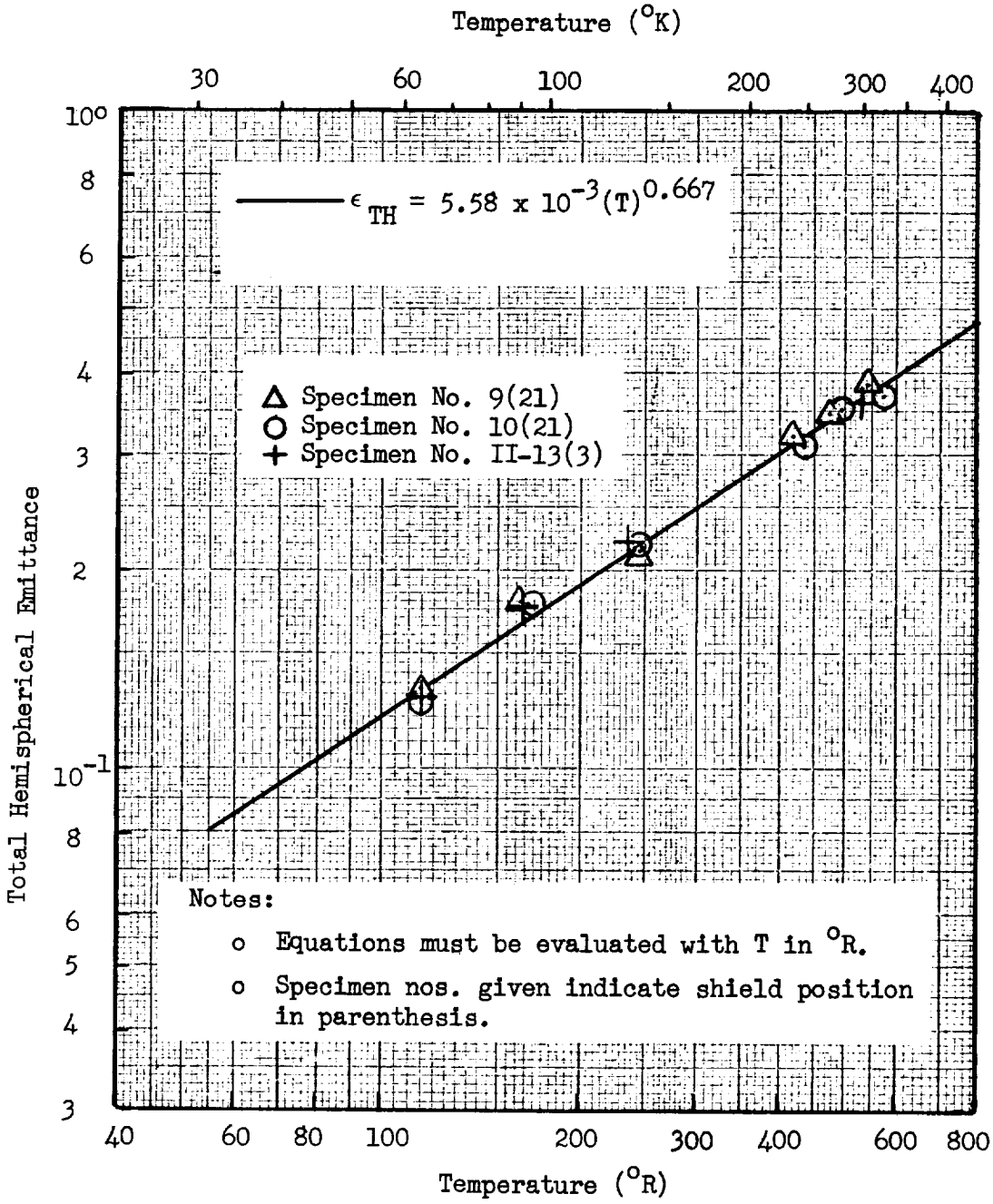

Fig. 4-4 Total Hemispherical Emittance of the Mylar Side of Crinkled, Single-Aluminized $\frac{1}{4}$-Mil Mylar as a Function of Temperature

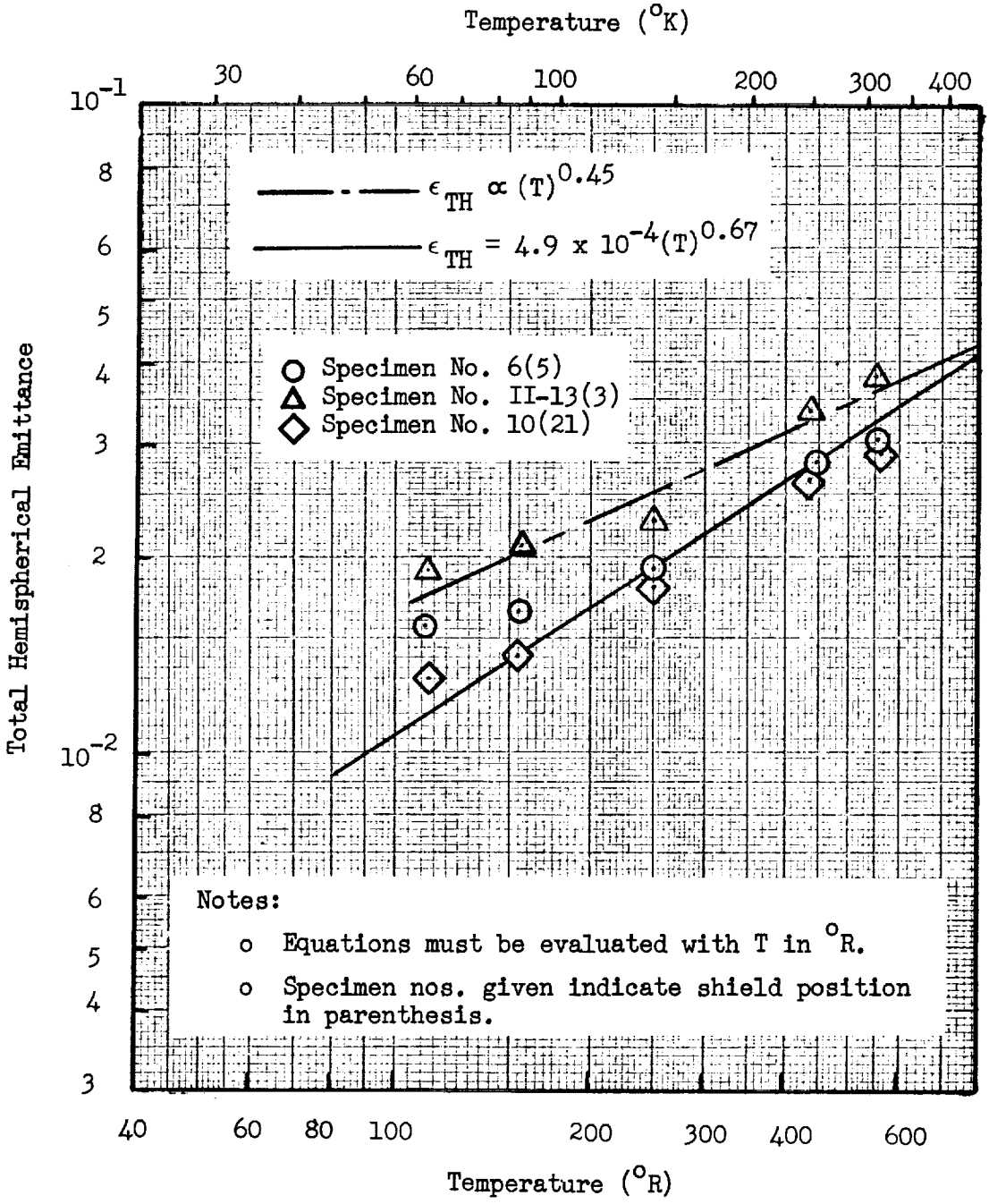

Fig. 4-5 Total Hemispherical Emittance of the Aluminium Side of Crinkled, Single-Aluminized ¼-Mil Mylar as a Function of Temperature

for the other metallic surfaces or for the Mylar side. The data would be best fit by a curved line - which at this time is unexplained. This apparent departure from the behavior exhibited by the double-aluminized material is particularly curious in view of the agreement of the data from the Mylar side of the crinkled, single-aluminized material with the simple temperature dependence function. From 200°R to 540°R (111°K to 300°K), the data are in reasonably good agreement with $\epsilon \propto T^{2/3}$ as shown by the solid line in Fig. 4-5. However, at lower temperatures the departure from this line is significant and it appears to increase with decreasing temperature. A better approximation to all of the data is obtained using a temperature-dependence exponent of 0.45 as shown by the dashed line in the figure. However, the agreement is still poor over the entire temperature range.

For the analysis of the heat transfer data presented in Section 4.3, the $T^{2/3}$ expression was used, since this provides the best fit of the data at the higher temperatures. At the lower temperatures, radiation heat transfer is small compared to that by conduction, and any inaccuracy introduced by an underestimation of the true emittance is very small.

4.3 HEAT TRANSFER TESTS

Flat plate calorimeter tests were conducted for a total of twenty specimens of multilayer insulation during the Task II effort. Of these, six specimens each of the double-aluminized Mylar/silk net, double-goldized Mylar/silk net, and double-aluminized Mylar/Tissuglas systems were tested. In addition, two specimens of the crinkled, single-aluminized Mylar system were investigated.

During the tests, heat flux measurements based on equilibrium boiloff flowrates of the test cryogens were obtained as functions of applied compressive force, specimen thickness, and the boundary temperatures imposed. Equivalent compressive pressures corresponding to the applied forces ranged from 1.5×10^{-4} psi (1.04 N/m^2), the compression due to specimen weight only, to approximately 5×10^{-1} psi (3450 N/m^2). Four discrete combinations of boundary temperatures were imposed with hot boundary temperatures of 500°R and 610°R (278°K and 339°K) and with cold boundary temperatures of 140°R and 37°R (77°K and 20°K). Ambient gas pressures within the test apparatus were reduced to less than 8×10^{-7} torr for all of the tests.

Results of the Task II flat plate calorimeter tests are presented in this section.

4.3.1 Double-Aluminized Mylar/Silk Net

Heat transfer characteristics of this material system were investigated for a total of six specimens. Of these, two specimens each were composed of 5 shields with 6 double net spacers, 10 shields with 11 double net spacers, and 20 shields with 21 double net spacers.

A tabulation of the experimental data obtained for all six specimens is presented in Table 4-1. For each data point, the tabulated values include measured compressive force, measured thickness based on separation of the hot and cold boundary plate surfaces, and the boundary temperatures imposed. Also included are computed values of equivalent compressive pressure, layer density, and heat flux for each data point.

Plots of heat flux as a function of compressive pressure for the six specimens tested are shown in Figs. 4-6 and 4-7. All of the data appear to fit a general expression for heat flux where the conduction component is proportional to pressure to a power. This relationship can be expressed for constant boundary temperatures as

$$q = a(P)^m + b$$

where b is the radiation term. The data plots shown a slight upward curvature which is due to the radiation component. The curvature is more pronounced for the 610°R (339°K) hot boundary as the radiative term for this condition is more than twice that for the 500°R (278°K) hot boundary.

The ratios of heat flux measured for the 5-, 10-, and 20-shield specimens are in good agreement with calculated values obtained using inverse ratios of the number of layers. A comparison of the ratios of experimental heat flux for the 5- and 10-shield specimens to those for the 20-shield specimens is shown in Table 4-2. On the basis of the number of layers, the predicted heat flux ratio for 5- to 20-shield specimens is 3.50, and for 10- to 20-shield specimens is 1.91. Inspection of the table shows that the ratios determined from the experimental data are in agreement with the predicted ratios to within approximately $\pm$ 10 percent.

Table 4-1

FLAT PLATE CALORIMETER TEST DATA FOR DOUBLE-ALUMINIZED MYLAR/SILK NET

Run No.	Measured Compressive Force[a] lbf	(N)	Equivalent Compressive Pressure psi	(N/m^2)	Measured Thickness[b] in.	(cm)	Boundary Temperatures T_h °R	(°K)	T_c °R	(°K)	Layer Density No./in.	(No./cm)	Measured Heat Flux Btu/hr ft^2	(w/m^2)
Specimen No. II-1, 10 shields/22 net, Weight 0.06 lb (0.027 Kg), Uncompressed Thickness = 0.15 in. (0.38 cm) [e]														
1	0.06[c]	(0.27)	1.5×10^{-4}[c]	(1.0)	0.238	(0.605)	500	(278)	37	(20)	46.2	(18.2)	0.378	(1.19)
1	0.06[c]	(0.27)	1.5×10^{-4}[c]	(1.0)	0.236	(0.599)	610	(339)	37	(20)	46.6	(18.4)	0.572	(1.80)
2	0.06[d]	(0.27)	3.0×10^{-4}[d]	(2.1)	0.185	(0.470)	610	(339)	37	(20)	59.5	(23.4)	0.419	(1.32)
2	0.06[d]	(0.27)	3.0×10^{-4}[d]	(2.1)	0.185	(0.470)	500	(278)	37	(20)	59.5	(23.4)	0.251	(0.79)
3	0.25	(1.11)	1.25×10^{-3}	(8.6)	0.169	(0.429)	500	(278)	37	(20)	65.2	(25.7)	0.444	(1.40)
3	0.25	(1.11)	1.25×10^{-3}	(8.6)	0.171	(0.434)	610	(339)	37	(20)	64.4	(25.4)	0.722	(2.28)
4	0.4	(1.8)	2.0×10^{-3}	(13.8)	0.153	(0.389)	610	(339)	37	(20)	72.0	(28.4)	0.821	(2.59)
4	0.4	(1.8)	2.0×10^{-3}	(13.8)	0.154	(0.391)	500	(278)	37	(20)	71.5	(28.2)	0.520	(1.64)
5	0.7	(3.1)	3.5×10^{-3}	(24.1)	0.134	(0.340)	500	(278)	37	(20)	82.2	(32.4)	0.650	(2.05)
5	0.7	(3.1)	3.5×10^{-3}	(24.1)	0.134	(0.340)	610	(339)	37	(20)	82.2	(32.4)	1.030	(3.25)
6	1.5	(6.7)	7.5×10^{-3}	(51.7)	0.112	(0.284)	610	(339)	37	(20)	98.3	(38.7)	1.390	(4.38)
6	1.5	(6.7)	7.5×10^{-3}	(51.7)	0.112	(0.284)	500	(278)	37	(20)	98.3	(38.7)	0.883	(2.78)
7	10.5	(46.7)	5.25×10^{-2}	(362)	0.0945	(0.240)	500	(278)	37	(20)	116.5	(45.9)	1.790	(5.64)
7	10.5	(46.7)	5.25×10^{-2}	(362)	0.0945	(0.240)	610	(339)	37	(20)	116.5	(45.9)	2.730	(8.61)
8	0.7	(3.1)	3.5×10^{-3}	(24.1)	0.128	(0.325)	610	(339)	37	(20)	86.0	(33.9)	1.112	(3.51)
8	0.7	(3.1)	3.5×10^{-3}	(24.1)	0.128	(0.325)	500	(278)	37	(20)	86.0	(33.9)	0.710	(2.24)
9	0.25	(1.11)	1.25×10^{-3}	(8.6)	0.157	(0.399)	500	(278)	37	(20)	70.0	(27.6)	0.481	(1.52)
9	0.25	(1.11)	1.25×10^{-3}	(8.6)	0.157	(0.399)	610	(339)	37	(20)	70.0	(27.6)	0.753	(2.37)
Specimen No. II-2, 10 shields/22 net, Weight 0.06 lb (0.027 Kg), Uncompressed Thickness = 0.14 in. (0.36 cm) [e]														
1	0.06[c]	(0.27)	1.5×10^{-4}[c]	(1.0)	0.236	(0.599)	500	(278)	140	(77)	46.6	(18.4)	0.324	(1.02)
1	0.06[c]	(0.27)	1.5×10^{-4}[c]	(1.0)	0.236	(0.599)	610	(339)	140	(77)	46.6	(18.4)	0.450	(1.42)
2	0.2	(0.9)	1.0×10^{-3}	(6.9)	0.171	(0.434)	610	(339)	140	(77)	64.4	(25.4)	0.750	(2.36)
2	0.2	(0.9)	1.0×10^{-3}	(6.9)	0.171	(0.434)	500	(278)	140	(77)	64.4	(25.4)	0.435	(1.37)
3	0.3	(1.3)	1.5×10^{-3}	(10.3)	0.150	(0.381)	500	(278)	140	(77)	73.3	(28.9)	0.475	(1.50)
3	0.3	(1.3)	1.5×10^{-3}	(10.3)	0.150	(0.381)	610	(339)	140	(77)	73.3	(28.9)	0.812	(2.56)
4	0.7	(3.1)	3.5×10^{-3}	(24.1)	0.130	(0.330)	610	(339)	140	(77)	84.7	(33.4)	1.140	(3.59)
4	0.7	(3.1)	3.5×10^{-3}	(24.1)	0.130	(0.330)	500	(278)	140	(77)	84.7	(33.4)	0.690	(2.18)
5	1.0	(4.4)	5.0×10^{-3}	(34.5)	0.112	(0.284)	500	(278)	140	(77)	98.3	(38.7)	0.820	(2.59)
5	1.0	(4.4)	5.0×10^{-3}	(34.5)	0.112	(0.284)	610	(339)	140	(77)	98.3	(38.7)	1.370	(4.32)
6	13.0	(57.8)	6.5×10^{-2}	(448)	0.0945	(0.240)	610	(339)	140	(77)	116.5	(45.9)	3.08	(9.71)
6	13.0	(57.8)	6.5×10^{-2}	(448)	0.0945	(0.240)	500	(278)	140	(77)	116.5	(45.9)	1.990	(6.27)
7	1.0	(4.4)	5.0×10^{-3}	(34.5)	0.107	(0.272)	500	(278)	140	(77)	102.7	(40.5)	0.863	(2.72)
7	1.0	(4.4)	5.0×10^{-3}	(34.5)	0.106	(0.269)	610	(339)	140	(77)	103.6	(40.8)	1.480	(4.67)
8	0.2	(0.9)	1.0×10^{-3}	(6.9)	0.157	(0.399)	610	(339)	140	(77)	70.0	(27.6)	0.810	(2.55)
8	0.2	(0.9)	1.0×10^{-3}	(6.9)	0.157	(0.399)	500	(278)	140	(77)	70.0	(27.6)	0.490	(1.54)
Specimen No. II-3, 5 shields/12 net, Weight 0.03 lb (0.014 Kg), Uncompressed Thickness = 0.09 in. (0.23 cm) [e]														
1	0.03[d]	(0.13)	1.5×10^{-4}[d]	(1.0)	0.110	(0.279)	500	(278)	140	(77)	54.5	(21.5)	0.522	(1.65)
1	0.03[d]	(0.13)	1.5×10^{-4}[d]	(1.0)	0.110	(0.279)	610	(339)	140	(77)	54.5	(21.5)	1.100	(3.47)
2	0.4	(1.8)	2.0×10^{-3}	(13.8)	0.0867	(0.220)	610	(339)	140	(77)	69.2	(27.3)	1.720	(5.42)
2	0.4	(1.8)	2.0×10^{-3}	(13.8)	0.0867	(0.220)	500	(278)	140	(77)	69.2	(27.3)	0.955	(3.01)
3	2.0	(8.9)	1.0×10^{-2}	(69)	0.071	(0.180)	500	(278)	140	(77)	84.5	(33.3)	1.650	(5.20)
3	2.0	(8.9)	1.0×10^{-2}	(69)	0.071	(0.180)	610	(339)	140	(77)	84.5	(33.3)	3.160	(9.96)
4	8.0	(35.6)	4.0×10^{-2}	(276)	0.059	(0.150)	610	(339)	140	(77)	101.5	(40.0)	4.910	(15.48)
4	8.0	(35.6)	4.0×10^{-2}	(276)	0.059	(0.150)	500	(278)	140	(77)	101.5	(40.0)	2.730	(8.61)
5	20	(89.0)	2.0×10^{-1}	(1380)	0.047	(0.119)	500	(278)	140	(77)	127.7	(50.3)	6.270	(19.76)

Notes: (a) Force measurement accuracy ±0.1 lb (± 0.4 N)
(b) Separation between hot and cold boundary surface plates
(c) Force = specimen weight; average pressure = 1/2 weight/unit area (assumed)
(d) Force = specimen weight; no gap; load cell indicated contact with specimen; average pressure = specimen weight/unit area (assumed)
(e) Measured with a dial gage prior to installation in the FPC

Table 4-1 (Cont'd)

Run No.	Measured Compressive Force[a] lbf	(N)	Equivalent Compressive Pressure psi	(N/m^2)	Measured Thickness[b] in.	(cm)	Boundary Temperatures Th ^oR (^oK)	Tc ^oR (^oK)	Layer Density No./in.	(No./cm)	Measured Heat Flux Btu/hr ft^2	(w/m^2)
Specimen No. II-4, 5 shields/12 net, Weight = 0.03 lb (0.014 Kg), Uncompressed Thickness = 0.10 in. (0.25 cm)[e]												
1	0.03[d]	(0.13)	1.5×10^{-4}[d]	(1.0)	0.120	(0.305)	610 (339)	37 (20)	50.0	(19.7)	0.920	(2.90)
1	0.03[d]	(0.13)	1.5×10^{-4}[d]	(1.0)	0.120	(0.305)	500 (278)	37 (20)	50.0	(19.7)	0.462	(1.46)
2	0.3	(1.3)	1.5×10^{-3}	(10.3)	0.100	(0.254)	500 (278)	37 (20)	60.0	(23.6)	0.943	(2.97)
2	0.3	(1.3)	1.5×10^{-3}	(10.3)	0.100	(0.254)	610 (339)	37 (20)	60.0	(23.6)	1.77	(5.58)
3	3.0	(13.3)	1.5×10^{-2}	(103)	0.0716	(0.182)	610 (339)	37 (20)	83.8	(33.0)	3.58	(11.28)
3	3.0	(13.3)	1.5×10^{-2}	(103)	0.0710	(0.180)	500 (278)	37 (20)	84.5	(33.3)	2.30	(7.25)
4	46.0	(205)	2.3×10^{-1}	(1590)	0.0531	(0.135)	500 (278)	37 (20)	113.0	(44.5)	5.83	(18.38)
4	46.0	(205)	2.3×10^{-1}	(1590)	0.0531	(0.135)	610 (339)	37 (20)	113.0	(44.5)	9.87	(31.11)
5	2.5	(11.1)	1.25×10^{-2}	(86.2)	0.0650	(0.165)	610 (339)	37 (20)	92.5	(36.4)	3.36	(10.59)
5	2.5	(11.1)	1.25×10^{-2}	(86.2)	0.0650	(0.165)	500 (278)	37 (20)	92.5	(36.4)	2.10	(6.62)
6	0.15	(0.67)	7.5×10^{-4}	(5.2)	0.0945	(0.240)	500 (278)	37 (20)	63.5	(25.0)	0.750	(2.36)
6	0.15	(0.67)	7.5×10^{-4}	(5.2)	0.0945	(0.240)	610 (339)	37 (20)	63.5	(25.0)	1.305	(4.11)
Specimen No. II-5, 20 shields/42 net, Weight = 0.12 lb (0.054 Kg), Uncompressed Thickness = 0.25 in. (0.64 cm)[e]												
1	0.12[c]	(0.53)	3.0×10^{-4}[c]	(2.1)	0.429	(1.090)	500 (278)	140 (77)	49.0	(19.3)	0.480	(1.51)
1	0.12[c]	(0.53)	3.0×10^{-4}[c]	(2.1)	0.429	(1.090)	610 (339)	140 (77)	49.0	(19.3)	0.610	(1.92)
2	0.2	(0.9)	1.0×10^{-3}	(6.9)	0.288	(0.732)	610 (339)	140 (77)	72.9	(28.7)	0.388	(1.22)
2	0.2	(0.9)	1.0×10^{-3}	(6.9)	0.288	(0.732)	500 (278)	140 (77)	72.9	(28.7)	0.224	(0.706)
3	1.0	(4.4)	5.0×10^{-3}	(34.5)	0.221	(0.561)	500 (278)	140 (77)	95.0	(37.4)	0.426	(1.34)
3	1.0	(4.4)	5.0×10^{-3}	(34.5)	0.221	(0.561)	610 (339)	140 (77)	95.0	(37.4)	0.610	(1.92)
4	4.75	(21.1)	2.3×10^{-2}	(159)	0.200	(0.508)	610 (339)	140 (77)	105.0	(41.4)	1.105	(3.48)
4	5.0	(22.2)	2.5×10^{-2}	(159)	0.200	(0.508)	500 (278)	140 (77)	105.0	(41.4)	0.645	(2.03)
5	500	(2224)	2.5	(17,200)	0.124	(0.315)	500 (278)	140 (77)	169.2	(66.7)	4.15	(13.08)
5	500	(2224)	2.5	(17,200)	0.124	(0.315)	610 (339)	140 (77)	169 2	(66.7)	6.55	(20.65)
6	0.1	(0.4)	5.0×10^{-4}	(3.4)	0.286	(0.726)	610 (339)	140 (77)	73.4	(28.9)	0.410	(1.29)
6	0.1	(0.4)	5.0×10^{-4}	(3.4)	0.286	(0.726)	500 (278)	140 (77)	73.4	(28.9)	0.276	(0.870)
Specimen No. II-6, 20 shields/42 net, Weight = 0.12 lb (0.054 Kg), Uncompressed Thickness = 0.29 in. (0.74 cm)[e]												
1	0.12[c]	(0.53)	3.0×10^{-4}[c]	(2.1)	0.407	(1.034)	500 (278)	37 (20)	51.6	(20.3)	0.339	(1.07)
1	0.12[c]	(0.53)	3.0×10^{-4}[c]	(2.1)	0.407	(1.034)	610 (339)	37 (20)	51.6	(20.3)	0.408	(1.29)
2	0.2	(0.9)	1.0×10^{-3}	(6.9)	0.358	(0.909)	610 (339)	37 (20)	58.7	(23.1)	0.385	(1.21)
2	0.2	(0.9)	1.0×10^{-3}	(6.9)	0.358	(0.909)	500 (278)	37 (20)	58.7	(23.1)	0.225	(0.709)
3	0.8	(3.6)	4.0×10^{-3}	(27.6)	0.255	(0.648)	500 (278)	37 (20)	82.4	(32.5)	0.355	(1.12)
3	0.8	(3.6)	4.0×10^{-3}	(27.6)	0.255	(0.648)	610 (339)	37 (20)	82.4	(32.5)	0.570	(1.80)
4	1.8	(8.0)	9.0×10^{-3}	(62.1)	0.222	(0.564)	610 (339)	37 (20)	94.7	(37.3)	0.740	(2.33)
4	2.0	(8.9)	1.0×10^{-2}	(69.0)	0.222	(0.564)	500 (278)	37 (20)	94.7	(37.3)	0.480	(1.51)
5	8.0	(35.6)	4.0×10^{-2}	(276)	0.181	(0.460)	500 (278)	37 (20)	116.0	(45.7)	0.802	(2.53)
5	8.0	(35.6)	4.0×10^{-2}	(276)	0.181	(0.460)	610 (339)	37 (20)	116.0	(45.7)	1.27	(4.00)
6	32.0	(142)	1.6×10^{-1}	(1100)	0.157	(0.399)	610 (339)	37 (20)	133.8	(52.7)	2.24	(7.06)
6	32.0	(142)	1.6×10^{-1}	(1100)	0.157	(0.399)	500 (278)	37 (20)	133.8	(52.7)	1.52	(4.79)
7	1.0	(4.4)	5.0×10^{-3}	(34.5)	0.242	(0.615)	500 (278)	37 (20)	86.8	(34.2)	0.428	(1.35)
7	1.0	(4.4)	5.0×10^{-3}	(34.5)	0.242	(0.615)	610 (339)	37 (20)	86.8	(34.2)	0.650	(2.05)

Notes: (a) Force measurement accuracy ±0.1 lb (± 0.4 N)
(b) Separation between hot and cold boundary surface plates
(c) Force = specimen weight; average pressure = 1/2 weight/unit area (assumed)
(d) Force = specimen weight; no gap; load cell indicated contact with specimen; average pressure = specimen weight/unit area (assumed)
(e) Measured with a dial gage prior to installation in the FPC

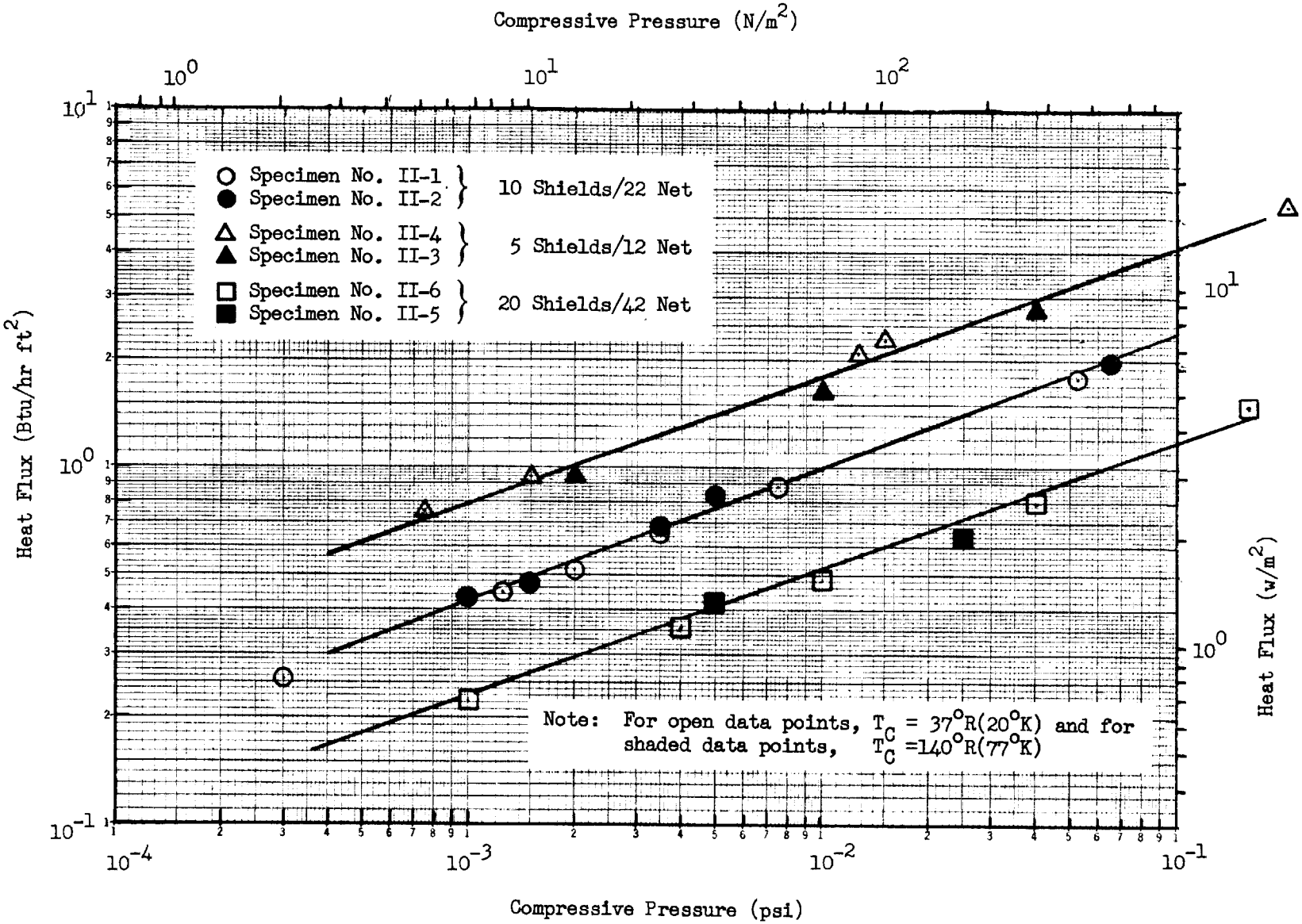

Fig. 4-6 Heat Flux as a Function of Compressive Pressure for Double-Aluminized Mylar/Silk Net With $T_H = 500^{\circ}R(278^{\circ}K)$

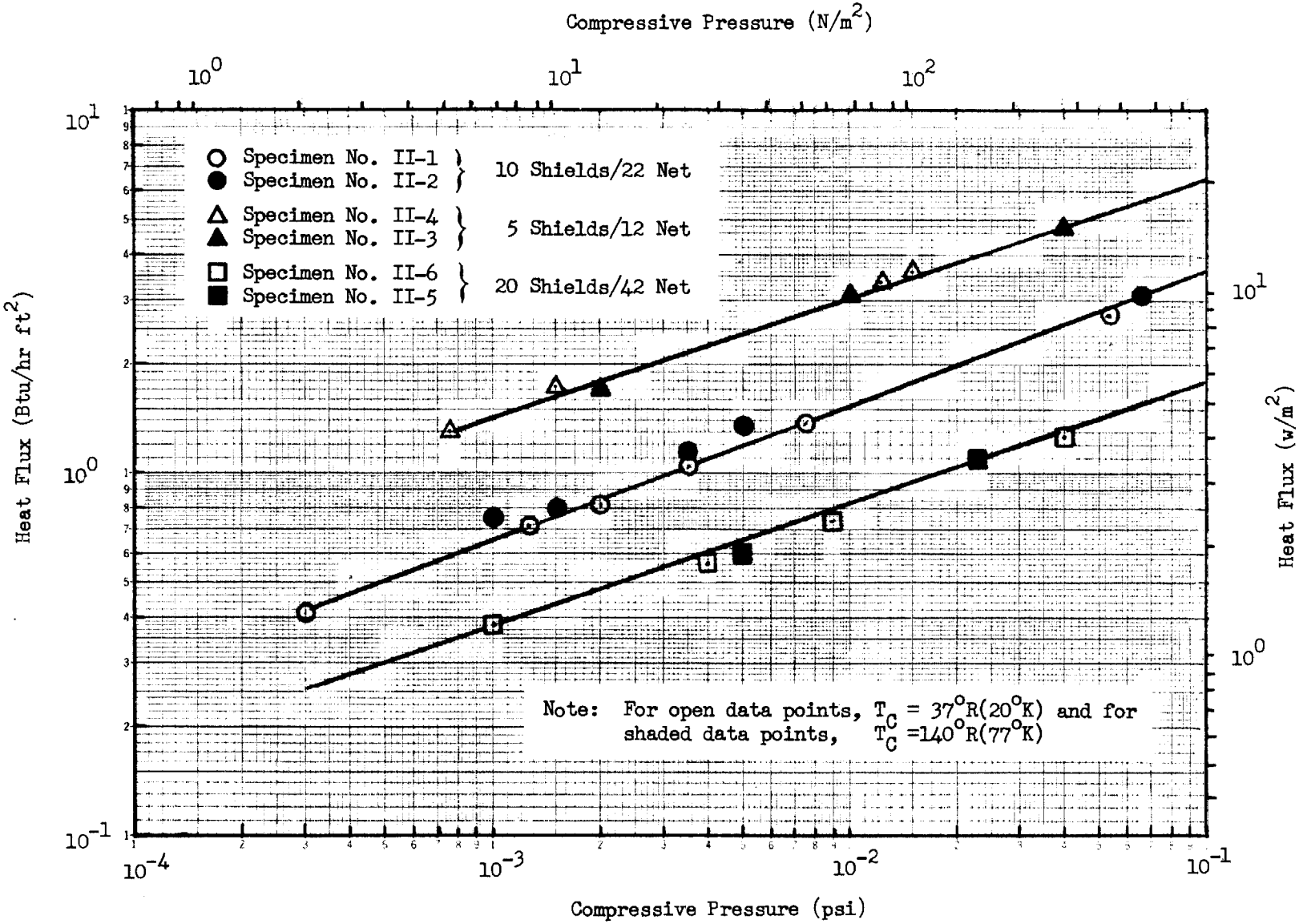

Fig. 4-7 Heat Flux as a Function of Compressive Pressure for Double-Aluminized Mylar/Silk Net with T_H = 610°R(339°K)

Table 4-2

VARIATION OF HEAT FLUX WITH NUMBER OF LAYERS

Hot Boundary Temperature ^{o}R (^{o}K)	Heat Flux Ratio	Compressive Pressure		
		1×10^{-3} psi (6.9 N/m^2)	1×10^{-2} psi (69 N/m^2)	1×10^{-1} psi (690 N/m^2)
500 (278)	q_5/q_{20}	3.50	3.54	3.47
	q_{10}/q_{20}	1.82	1.95	2.03
610 (339)	q_5/q_{20}	3.75	3.93	3.61
	q_{10}/q_{20}	1.78	1.92	1.98

The effect of hot boundary temperature on heat flux can be evaluated by comparing heat flux ratios for specimens with the same number of layers, and with the same applied compressive pressures, for the two hot boundary temperatures imposed during the tests. For example, at a compressive pressure of 1×10^{-3} psi (6.9 N/m^2), the ratio of heat flux for $610^{o}R$ ($339^{o}K$) to that for $500^{o}R$ ($278^{o}K$) ranges from approximately 1.64 to 1.80, depending upon the number of layers in the specimen. At a compressive pressure of 1×10^{-2} psi (69 N/m^2), the corresponding ratios range from approximately 1.55 to 1.75, and at a compressive pressure of 1×10^{-1} psi (690 N/m^2), they range from approximately 1.49 to 1.59.

Extending this comparison a step further, the ratio of the predicted solid conduction heat flux component for $610^{o}R$ ($339^{o}K$) to that for $500^{o}R$ ($278^{o}K$), based on the assumption that the conduction components are proportional to the product of average temperature and temperature difference (Ref. Eq. 4.7), ranges from 1.49 to 1.53 depending upon the cold boundary temperature selected. Similarly, the ratio of the predicted radiation heat flux component for $610^{o}R$ ($339^{o}K$) to that for $500^{o}R$ ($278^{o}K$) is 2.53, based on the assumption that the radiation components are proportional to $T_H^{4.67} - T_C^{4.67}$.

When similar heat flux ratios were evaluated for the two cold boundary temperatures imposed during the tests, it was found that the influence of these temperatures was overshadowed by minor specimen-to-specimen variations (system reproducibility) and small data inaccuracies (calorimeter repeatability). This was expected since the ratios of predicted solid conduction heat flux for 37°R (20°K) to those for 140°R (77°K) are only 1.08 for the 500°R (278°K) hot boundary, and 1.05 for the 610°R (339°K) hot boundary.

The same heat flux ratio comparisons which were presented above to show the effect of hot boundary temperature on heat flux also can be used to qualitatively evaluate the relative influences of the solid conduction and radiation heat transfer mechanisms. For this multilayer system, the proportion of the total heat flux due to each of these mechanisms varied widely at different applied compressive pressures and at different hot boundary temperatures. For example, at the high compressive pressure value of 1×10^{-1} psi (690 N/m^2), the radiation heat transfer component was found to be relatively small compared to that for conduction. For this case, the ratio of total experimental heat flux for 610°R (339°K) to that for 500°R (278°K) ranged from 1.49 to 1.59 depending upon the number of layers in the specimen. This ratio range agrees very well with the predicted range of 1.49 to 1.53 for solid conduction alone, indicating that the influence of radiation was indeed small. However, at lower compressive pressures the influence of radiation was much greater, and the total experimental heat flux ratios increased accordingly, i.e., 155 to 1.75 at 1×10^{-2} psi (69 N/m^2), and 1.64 to 1.80 at 1×10^{-3} psi (6.9 N/m^2).

The relationship of heat flux with layer density for this multilayer system is shown in Figs. 4-8 and 4-9 for 500°R (278°K) and 610°R (339°K) hot boundary temperatures, respectively. For the 10- and 20-shield specimens, the data fall within a ±20 percent band which is consistent with the results obtained in Task I for this system (Ref. Section 3.5). For the 5-shield specimens, however, the variations of discrete data points with respect to a curve fit through the data are large compared to those where the curves were fit as a function of compressive pressure. This is primarily because the compressive pressure/layer density relationships of the two 5-shield specimens were quite different, whereas for the two 10-shield and the two 20-shield specimens,

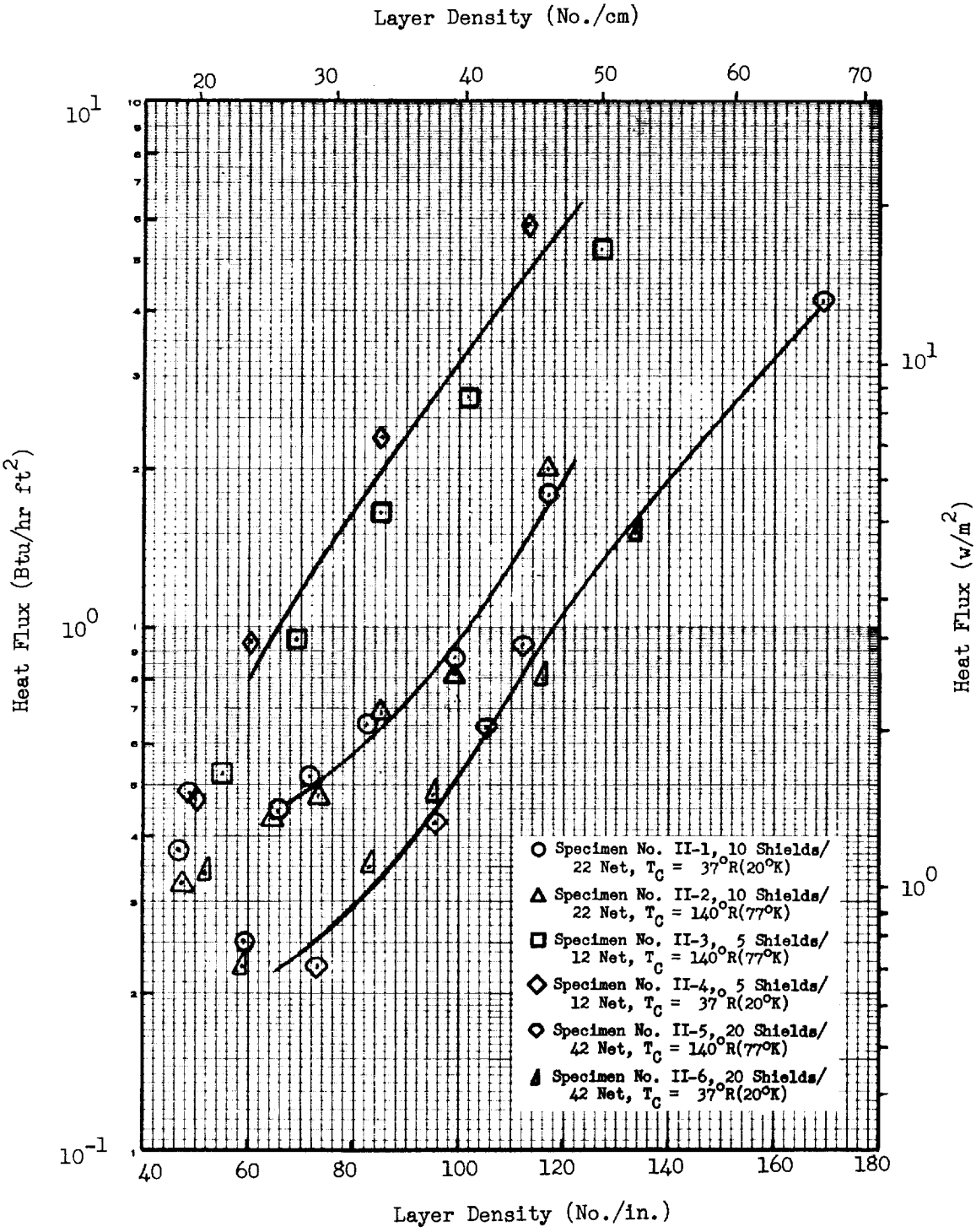

Fig. 4-8 Heat Flux as a Function of Layer Density for Double-Aluminized Mylar/Silk Net with T_H = 500°R(278°K)

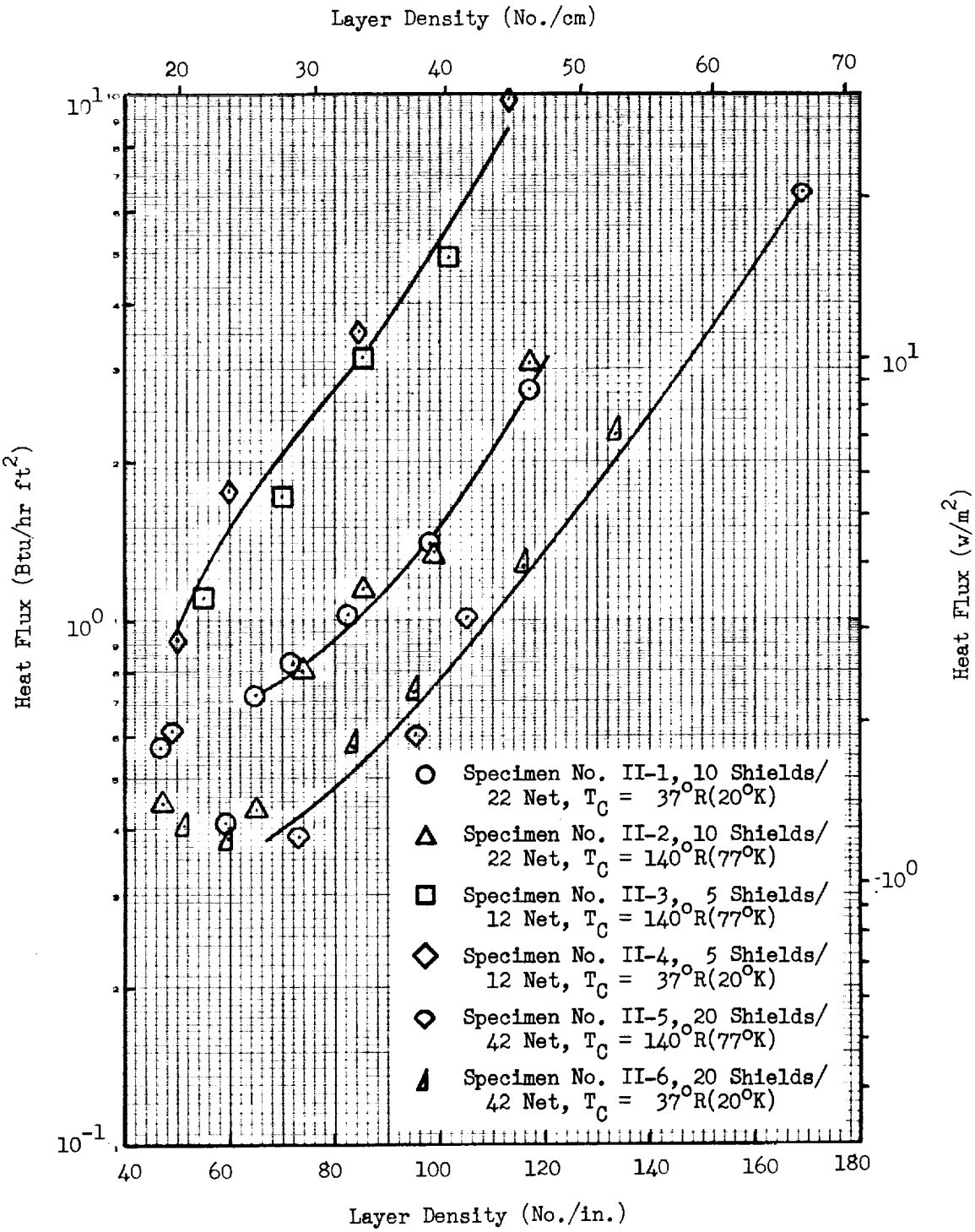

Fig. 4-9 Heat Flux as a Function of Layer Density for Double-Aluminized Mylar/Silk Net with T_H = 610°R(339°K)

these relationships were quite similar. Figs. 4-10 and 4-11 show these relationships for the specimens tested at 140°R (77°K) and 37°R (20°K), respectively. The differences noted for the two 5-shield specimens are probably due to geometrical and physical differences in the specimens rather than temperature, however, since no similar differences were noted for the 10- and 20-shield specimens.

At constant layer density values, the ratios of heat flux for the 5- and 10-shield specimens differ significantly from those at constant compressive pressures (Ref. Table 4-2). For example, at 90 layers/in. (35.4 layers/cm), the ratios of the heat flux for the 5-shield specimens to those for the 10-shield specimens (Figs. 4-8 and 4-9) are approximately 3.2 in each case. The corresponding ratios are approximately 2.0 and 1.8 at constant compressive pressures of 1×10^{-3} psi (6.9 N/m^2) and 1×10^{-1} (690 N/m^2), respectively. This characteristic results from the fact that the compressive pressure for the 5-shield specimens is significantly greater than that for the 10-shield specimens at any particular layer density value. However, ratios of heat flux for the 10- and 20-shield specimens, based upon constant layer density and constant compressive pressure, respectively, agree more closely since the compressive pressure/layer density relationships for these specimens are nearly identical (Ref. Figs. 4-10 and 4-11).

Analysis of the heat transfer data was accomplished using Eq. (4.9). The radiative term was computed for the average shield emittance (temperature dependence of emittance is 0.67), boundary temperature, and number of shields. The average room temperature emittance values used for these computations are given in Table 4-3. The radiation contribution to heat flux was computed and then subtracted from the total heat flux data for each data point to yield the conduction heat flux as a function of compressive pressure. This value was then normalized for boundary temperatures and the number of layers as indicated by the expression

$$\Phi = \frac{(q_{total} - q_{rad})(N_s+1)}{(T_H-T_C)(T_m)}$$

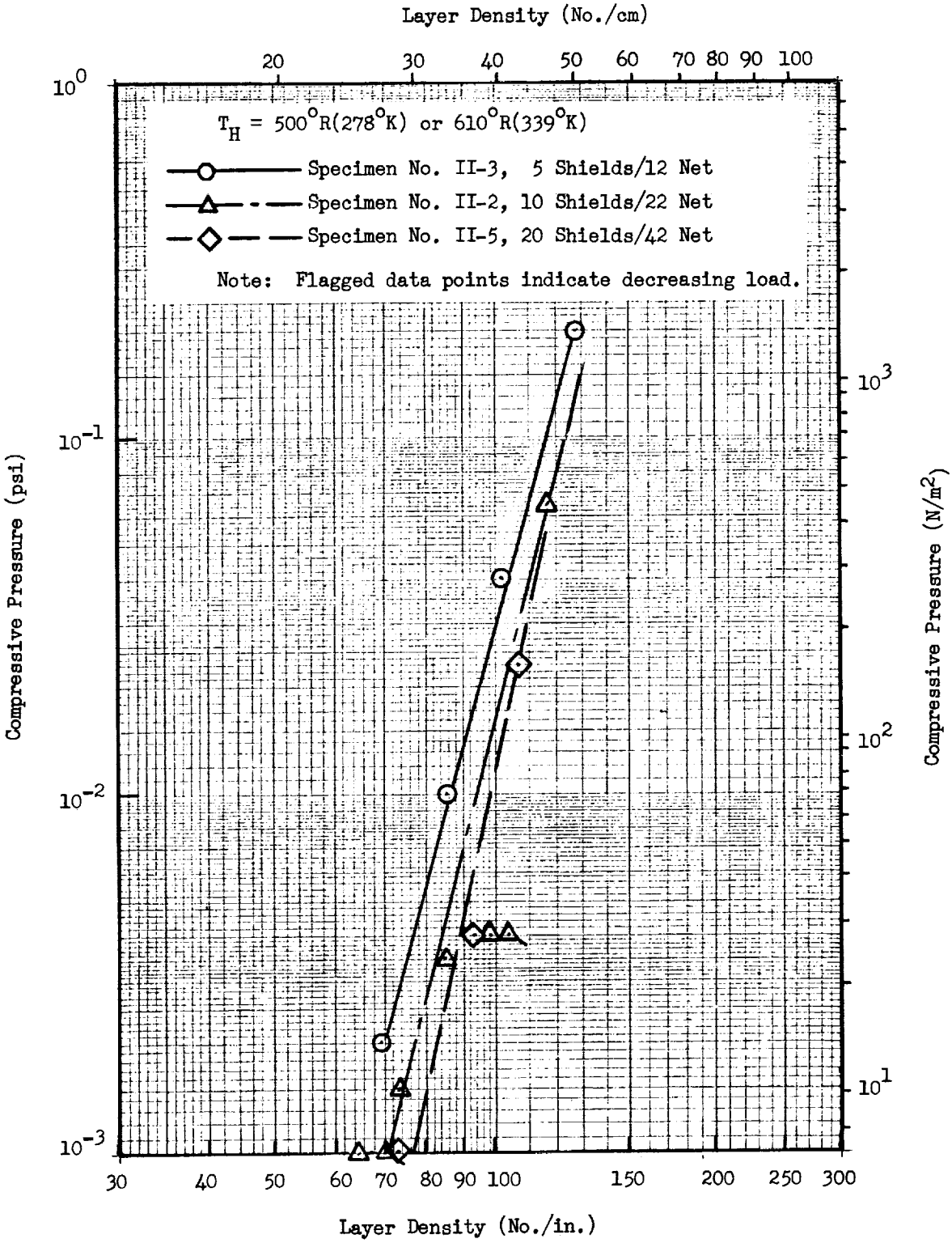

Fig. 4-10 Compressive Pressure as a Function of Layer Density for Double-Aluminized Mylar/Silk Net with T_C = 140°R(77°K)

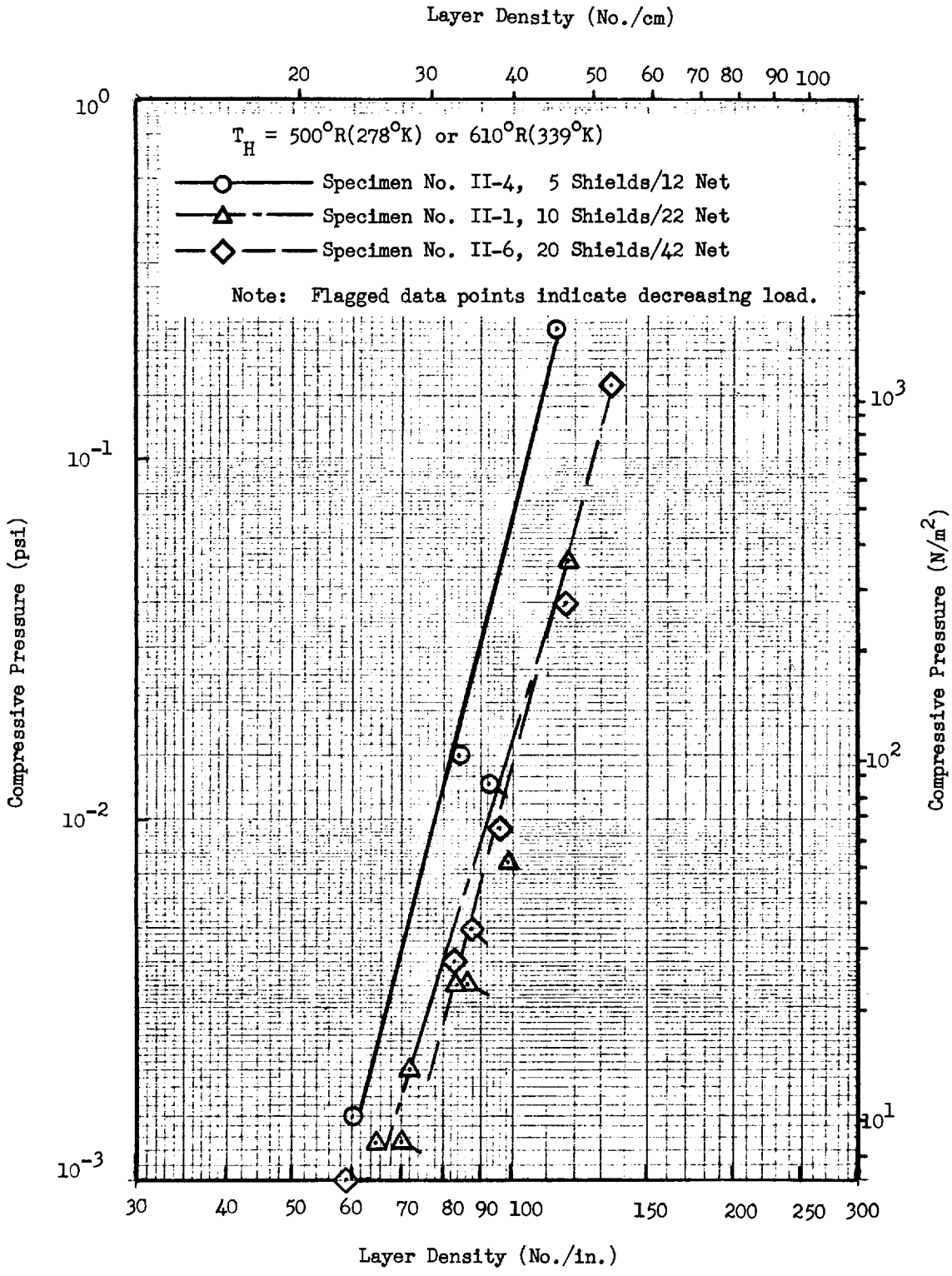

Fig. 4-11 Compressive Pressure as a Function of Layer Density for Double-Aluminized Mylar/Silk Net with T_C = 37°R(20°K)

Table 4-3

EMITTANCE VALUES FOR DOUBLE-ALUMINIZED MYLAR/SILK NET

Specimen No.	Average Value of ϵ_{Th}* at 540°R (300°K)
II-1	0.030
II-2	0.028
II-3	0.029
II-4	0.028
II-5	0.027
II-6	0.028

*Based upon ρ_N measurements for all shields and ϵ_{TH} for a single shield where $\epsilon_{TH} = 1.33\,\epsilon_{TN}$ (Ref. 5), and $\epsilon_{TN} = 1 - \rho_N$

and the parameter Φ was plotted as a function of compressive pressure in order to evaluate the conduction term coefficient and exponent. As the pressure determined from the load cell measurements includes the load due to the specimen weight, the applied pressure term was evaluated as

$$P_a = (P - P_o)$$

where P_a is the applied compressive pressure, P is the pressure from the load cell data, and P_o is the pressure due to the specimen weight per unit area. The correlation of Φ with $(P-P_o)$ is shown in Fig. 4-12. A least-squares method fit of the data resulted in the expression

$$\Phi = 5.45 \times 10^{-4} (P-P_o)^{0.437}$$

where pressure is in psi (N/m^2) and Φ is Btu/hr ft^2 $°R^2$ (w/m^2 $°K^2$). The broken lines in the figure represent ±15 percent deviations from the equation. Of the 53 data points plotted all but 6 fall within this band. The resulting equation for prediction of total heat flux for this material system, based upon the Task II data, is

$$q = \frac{5.45\times10^{-4}(P-P_o)^{0.437}T_m}{N_s + 1}(T_H - T_C) + \frac{1.10\times10^{-11}\epsilon_{TR}}{N_s}\left(T_H^{4.67} - T_C^{4.67}\right) \qquad (4.20)$$

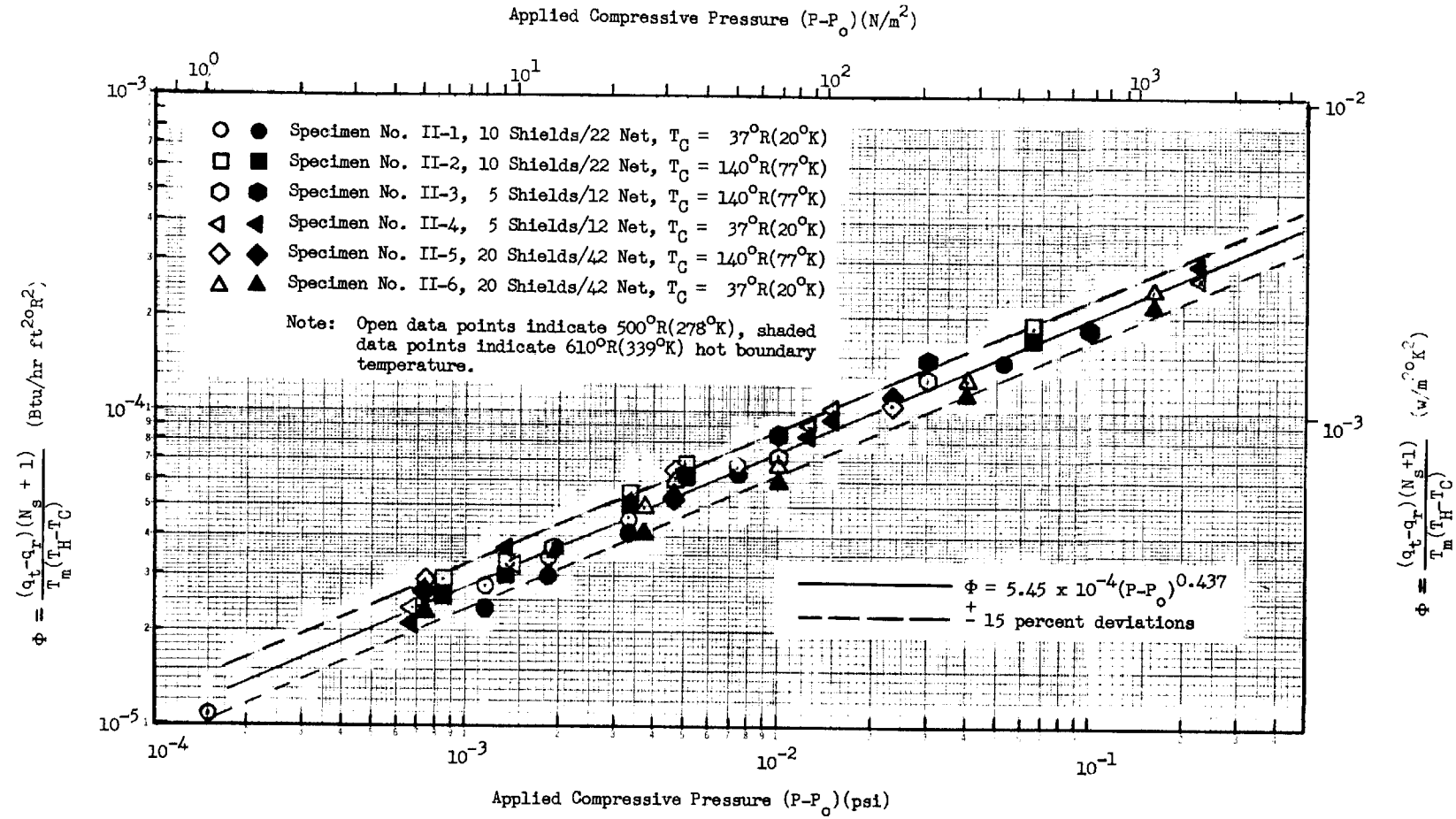

Fig. 4-12 Normalized Solid Conduction Heat Flux (Task II Data) as a Function of Applied Compressive Pressure for Double-Aluminized Mylar/Silk Net

where ϵ_{TR} is the total hemispherical emmittance at 540°R (300°K).

Similar data for the specimens investigated in Task I are shown in Fig. 4-13. The best fit to these data shows a slightly different coefficient and exponent. These differences are due to the fact that only 10- and 20-shield specimens were investigated in Task I, and the coefficient and exponent varied slightly with the total number of layers. Also, the correlation in Fig. 4-12 is based upon more data points. Therefore, best fits were obtained independently for the 5-, 10- and 20-shield specimen data. The results for two specimens each of 5, 10, and 20 shields are as follows:

$$5 \text{ shields}, \Phi = 6.6 \times 10^{-4} (P-P_o)^{0.47}$$
$$10 \text{ shields}, \Phi = 5.4 \times 10^{-4} (P-P_o)^{0.43}$$
$$20 \text{ shields}, \Phi = 4.9 \times 10^{-4} (P-P_o)^{0.40}$$

In addition, variations were observed for the four individual specimens of 10 and 20 shields each. For example, for the 20 shield specimens, the coefficient varied from 4.48×10^{-4} to 5.19×10^{-4} and the exponent varied from 0.394 to 0.414. The least-squares fit based upon 83 data points obtained in Tasks I and II for the conduction heat flux yielded

$$q_s = \frac{5.79 \times 10^{-4} (P-P_o)^{0.45} T_m}{N_s + 1} (T_H - T_C)$$

By substitution of the above expression for solid conduction heat flux into Eq. (4.20), the euqation for prediction of heat flux in terms of compressive pressure, based upon all of the data obtained for this system, is

$$q = \frac{5.79 \times 10^{-4} (P-P_o)^{0.45} T_m}{N_s + 1} (T_H - T_C) + \frac{1.10 \times 10^{-11} \epsilon_{TR}}{N_s} \left(T_H^{4.67} - T_C^{4.67} \right) \qquad (4.21)$$

Finally, compressive pressure was evaluated as a function of layer density for this multilayer system using the relationship $P-P_o = c (\bar{N})^n$ discussed previously in Section 4.1.3. Values of c and n were determined for the best fit of the data obtained for all six of the Task II specimens and substituted into equation (4.21). The resulting expression is

$$q = \frac{7.46 \times 10^{-12} (\bar{N})^{3.56} T_m}{N_s + 1} (T_H - T_C) + \frac{1.10 \times 10^{-11} \epsilon_{TR}}{N_s} \left(T_H^{4.67} - T_C^{4.67} \right) \qquad (4.22)$$

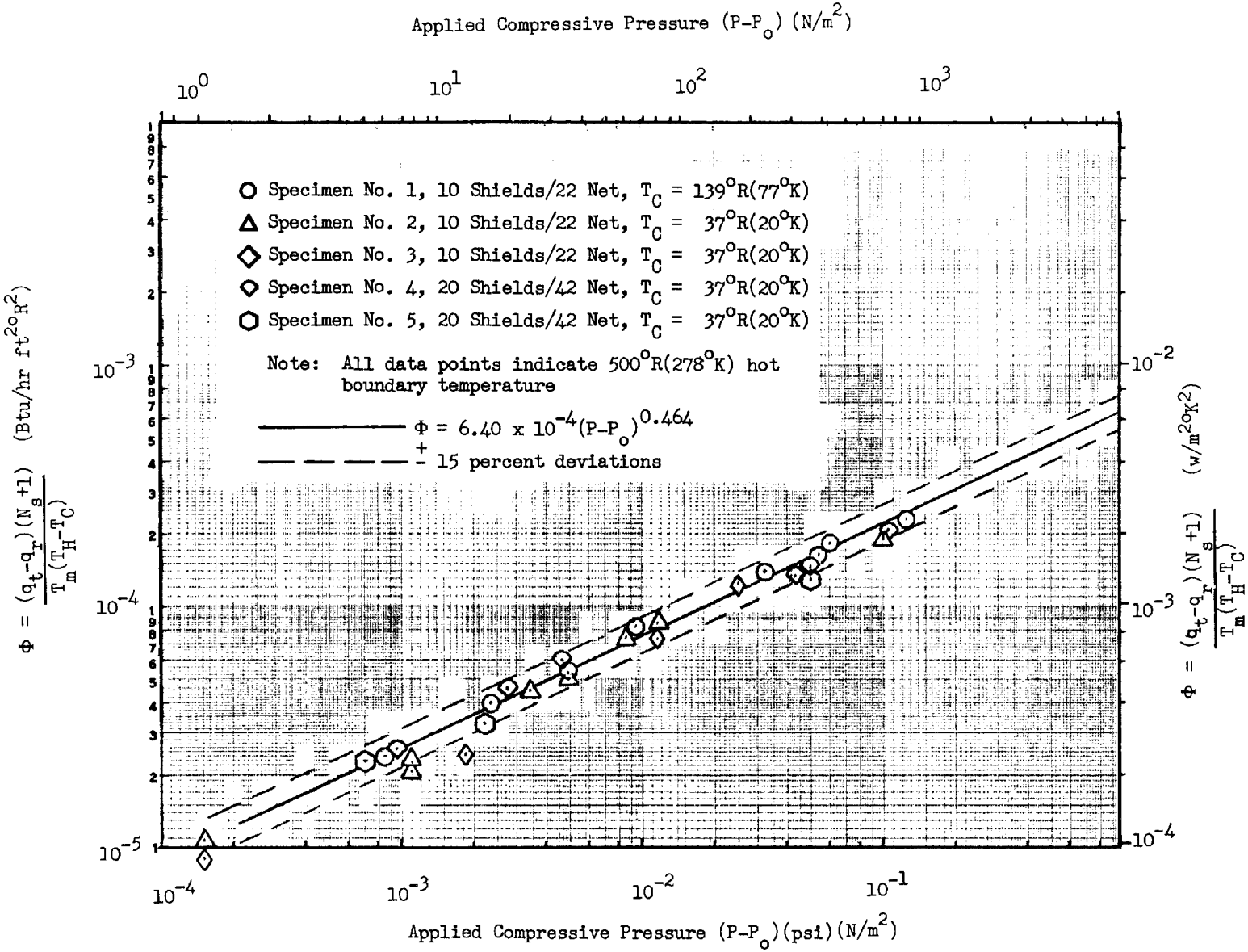

Fig. 4-13 Normalized Solid Conduction Heat Flux (Task I Data) as a Function of Applied Compressive Pressure for Double-Aluminized Mylar/Silk Net

4.3.2 Double-Goldized Mylar/Silk Net

A total of six specimens of this multilayer composite were tested on the Flat Plate Calorimeter in Task II. Of these, two specimens each were composed of 5 shields with 6 double net spacers, two additional specimens each consisted of 10 shields with 11 double net spacers, and the two final specimens each were assembled using 20 shields with 21 double net spacers.

Data obtained from these tests is presented in Table 4-4. The tabulated values include measured compressive force, computed equivalent compressive pressure, measured specimen thickness, boundary temperatures, and heat flux computed from boiloff flowrates for each data point.

The data for heat flux as a function of compressive pressure are summarized in Figs. 4-14 and 4-15 for 500°R (278°K) and 610°R (339°K) hot boundary temperatures, respectively. These data show that the thermal performance of this system is similar to that of the double-aluminized Mylar/silk net composite. At the higher hot boundary temperature, and for low compressive pressures, the total heat flux values are approximately 10 percent less than those measured for the aluminized Mylar specimens with the same number of layers. This improvement in thermal performance is due to the lower emittance of the gold surface in the compressive pressure/temperature region where radiation heat transfer is a more significant proportion of the total. As the compressive pressure value increases, the difference in total heat flux decreases for equivalent goldized Mylar and aluminized Mylar specimens. Also, for the 500°R (278°K) hot boundary temperature, the radiation component is less than one-half of that for 610°R (339°K), and the difference in total heat flux between the goldized Mylar and the aluminized Mylar specimens is less than the variation due to material reproducibility. Consequently, the effect of the lower emittance of the gold surface is less apparent at high compressive pressures or at the low hot boundary temperature. At compressive pressures below 8×10^{-4} psi ($5.5\ N/m^2$), the data points in Figs. 4-14 and 4-15 correspond to spacings between the flat plate apparatus surfaces that are greater than the uncompressed

Table 4-4

FLAT PLATE CALORIMETER TEST DATA FOR DOUBLE-GOLDIZED MYLAR/SILK NET

Run No	Measured Compressive Force (a) lbf	(N)	Equivalent Compressive Pressure Psi	(N/m^2)	Measured Thickness (b) in.	(cm)	Boundary Temperatures T_h °R(°K)	T_c °R(°K)	Layer Density No./in.	(No./cm)	Measured Heat Flux BTU/hr ft^2	(w/m^2)
Specimen No. II-7, 10 shields / 22 net, Weight = 0.076 lb (0.034 Kg), Uncompressed thickness = 0.20 in. (0.51 cm) (c)												
1	0.076 (c)	(0.34)	1.9×10^{-4} (c)	(1.3)	0.248	(0.630)	500	(278) 140 (77)	44.4	(17.5)	0.535	(1.69)
1	0.076 (c)	(0.34)	1.9×10^{-4} (c)	(1.3)	0.248	(0.630)	610	(339) 140 (77)	44.4	(17.5)	0.776	(2.45)
2	0.7	(3.1)	3.5×10^{-3}	(24.1)	0.166	(0.422)	610	(339) 140 (77)	66.3	(26.1)	1.04	(3.28)
2	0.7	(3.1)	3.5×10^{-3}	(24.1)	0.166	(0.422)	500	(278) 140 (77)	66.3	(26.1)	0.645	(2.03)
3	1.2	(5.3)	6.0×10^{-3}	(41.4)	0.143	(0.363)	500	(278) 140 (77)	76.9	(30.3)	0.858	(2.70)
3	1.2	(5.3)	6.0×10^{-3}	(41.4)	0.143	(0.363)	610	(339) 140 (77)	76.9	(30.3)	1.42	(4.48)
4	2.0	(8.9)	1.0×10^{-2}	(69)	0.120	(0.305)	610	(339) 140 (77)	91.7	(36.1)	1.72	(5.42)
4	2.0	(8.9)	1.0×10^{-2}	(69)	0.120	(0.305)	500	(278) 140 (77)	91.7	(36.1)	1.17	(3.69)
5	80.0	(356)	4.0×10^{-1}	(2760)	0.0805	(0.204)	500	(278) 140 (77)	136.6	(53.8)	4.80	(15.1)
5	86.0	(383)	4.3×10^{-1}	(2970)	0.080	(0.203)	610	(339) 140 (77)	137.5	(54.1)	7.53	(23.7)
6	3.3	(14.7)	1.65×10^{-2}	(114)	0.111	(0.282)	610	(339) 140 (77)	99.1	(39.0)	2.03	(6.40)
7	1.6	(7.1)	8.0×10^{-3}	(55.2)	0.120	(0.305)	610	(339) 140 (77)	91.7	(36.1)	1.50	(4.73)
8	0.3	(1.3)	1.5×10^{-3}	(10.3)	0.167	(0.424)	610	(339) 140 (77)	65.9	(25.9)	0.715	(2.25)
8	0.3	(1.3)	1.5×10^{-3}	(10.3)	0.167	(0.424)	500	(278) 140 (77)	65.9	(25.9)	0.564	(1.78)
Specimen II-8, 10 shields/22 net, Weight = 0.076 lb (0.034 Kg), Uncompressed thickness = 0.18 in. (0.48 cm) (e)												
1	0.076 (c)	(0.34)	1.9×10^{-4} (c)	(1.3)	0.232	(0.589)	500	(278) 37 (20)	47.4	(18.7)	0.583	(1.84)
1	0.076 (c)	(0.34)	1.9×10^{-4} (c)	(1.3)	0.232	(0.589)	610	(339) 37 (20)	47.4	(18.7)	0.777	(2.45)
2	0.5	(2.2)	2.5×10^{-3}	(17.2)	0.157	(0.399)	610	(339) 37 (20)	70.1	(27.6)	0.902	(2.84)
2	0.5	(2.2)	2.5×10^{-3}	(17.2)	0.157	(0.399)	500	(278) 37 (20)	70.1	(27.6)	0.657	(2.07)
3	0.8	(3.6)	4.0×10^{-3}	(27.6)	0.142	(0.361)	500	(278) 37 (20)	77.5	(30.5)	0.720	(2.27)
3	0.8	(3.6)	4.0×10^{-3}	(27.6)	0.142	(0.361)	610	(339) 37 (20)	77.5	(30.5)	1.04	(3.28)
4	2.0	(8.9)	1.0×10^{-2}	(69)	0.121	(0.307)	610	(339) 37 (20)	90.9	(35.8)	1.52	(4.79)
4	2.0	(8.9)	1.0×10^{-2}	(69)	0.121	(0.307)	500	(278) 37 (20)	90.9	(35.8)	1.05	(3.31)
5	25.0	(111)	1.25×10^{-1}	(862)	0.095	(0.241)	500	(278) 37 (20)	115.8	(45.6)	2.58	(8.13)
6	80.0	(356)	4.0×10^{-1}	(2760)	0.081	(0.206)	610	(339) 37 (20)	135.8	(53.5)	6.68	(21.1)
7	2.0	(8.9)	1.0×10^{-2}	(69)	0.110	(0.279)	610	(339) 37 (20)	100.0	(39.4)	1.58	(4.98)
7	2.0	(8.9)	1.0×10^{-2}	(69)	0.112	(0.284)	500	(278) 37 (20)	98.2	(38.7)	1.02	(3.22)
8	0.4	(1.8)	2.0×10^{-3}	(13.8)	0.158	(0.401)	500	(278) 37 (20)	69.6	(27.4)	0.475	(1.50)
8	0.4	(1.8)	2.0×10^{-3}	(13.8)	0.158	(0.401)	610	(339) 37 (20)	69.6	(27.4)	0.760	(2.40)
Specimen II-9, 5 shields / 12 net, Weight = 0.04 lb (0.018 Kg), Uncompressed thickness = 0.10 in. (0.25 cm) (e)												
1	0.04 (c)	(0.18)	1.0×10^{-4} (c)	(0.69)	0.124	(0.315)	500	(278) 140 (77)	48.4	(19.1)	0.633	(2.00)
1	0.04 (c)	(0.18)	1.0×10^{-4} (c)	(0.69)	0.124	(0.315)	610	(339) 140 (77)	48.4	(19.1)	0.970	(3.06)
2	0.2	(0.9)	1.0×10^{-3}	(6.9)	0.0965	(0.245)	610	(339) 140 (77)	62.2	(24.5)	1.32	(4.16)
2	0.2	(0.9)	1.0×10^{-3}	(6.9)	0.0965	(0.245)	500	(278) 140 (77)	62.2	(24.5)	0.850	(2.68)
3	0.3	(1.3)	1.5×10^{-2}	(103)	0.067	(0.170)	500	(278) 140 (77)	89.6	(35.3)	2.20	(6.93)
3	0.3	(1.3)	1.5×10^{-2}	(103)	0.067	(0.170)	610	(339) 140 (77)	89.6	(35.3)	3.82	(12.0)
4	60.0	(267)	3.0×10^{-1}	(2070)	0.055	(0.140)	610	(339) 140 (77)	109.1	(43.0)	10.40	(32.8)
4	60.0	(267)	3.0×10^{-1}	(2070)	0.055	(0.140)	500	(278) 140 (77)	109.1	(43.0)	7.03	(22.2)
5	0.6	(2.7)	2.0×10^{-3}	(13.8)	0.0866	(0.220)	500	(278) 140 (77)	69.3	(27.3)	0.893	(2.81)
5	0.6	(2.7)	2.0×10^{-3}	(13.8)	0.0866	(0.220)	610	(339) 140 (77)	69.3	(27.3)	1.70	(5.36)
6	0.04 (d)	(0.18)	2.0×10^{-4} (d)	(1.4)	0.0985	(0.250)	610	(339) 140 (77)	60.9	(24.0)	1.27	(4.00)
6	0.04 (d)	(0.18)	2.0×10^{-4} (d)	(1.4)	0.0985	(0.250)	500	(278) 140 (77)	60.9	(24.0)	0.815	(2.57)

NOTES:

(a) Force measurement accuracy $\pm$ 0.1 lb ($\pm$ 0.4 N)

(b) Separation between hot and cold boundary surface plates

(c) Force = specimen weight; Average pressure = 1/2 weight/unit area (assumed)

(d) Force = specimen weight; No gap; Load cell indicated contact with specimen; Average pressure = specimen weight/unit area (assumed)

(e) Measured with a dial gage prior to installation in the FPC

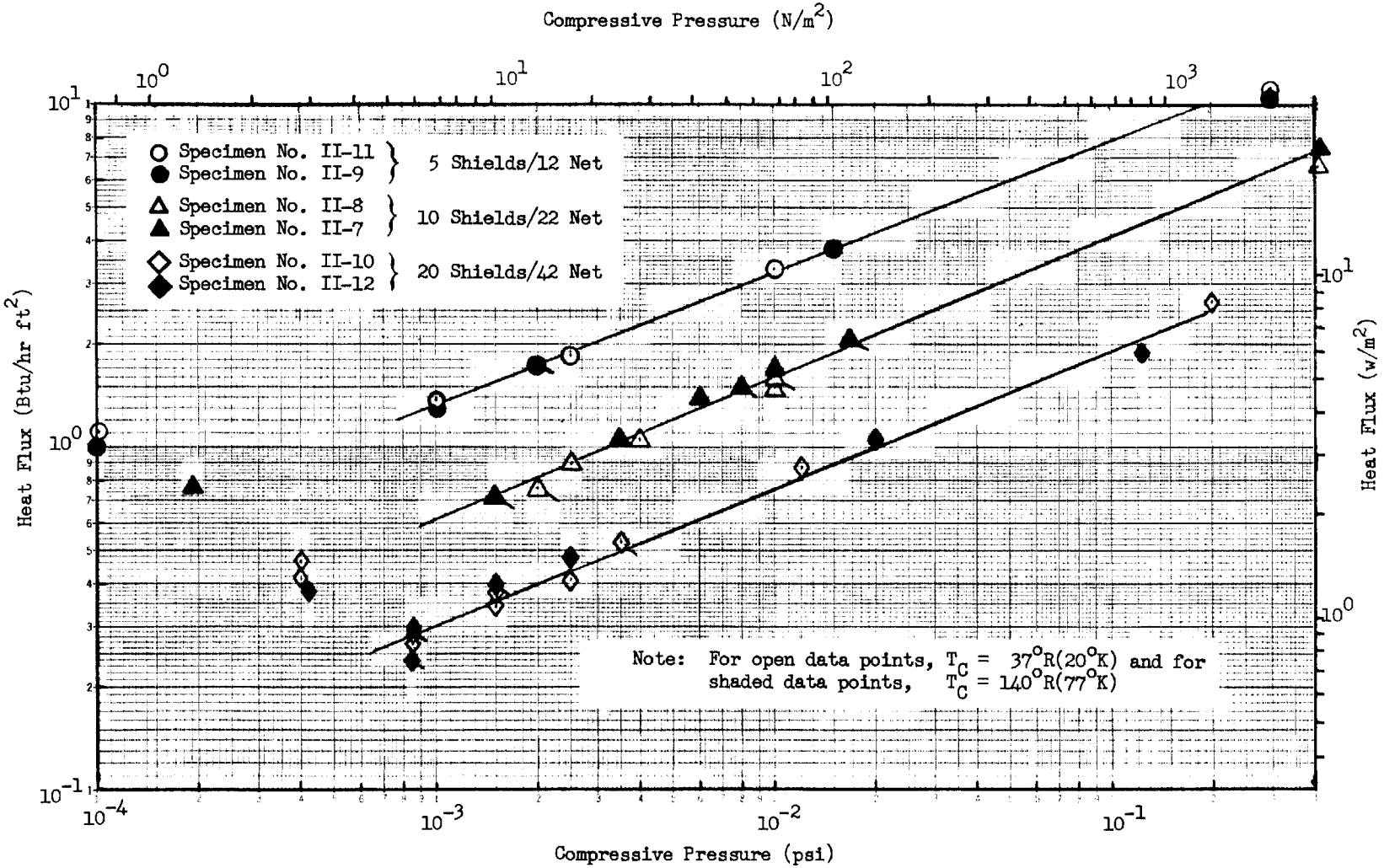

Fig. 4-15 Heat Flux as a Function of Compressive Pressure for Double-Goldized Mylar/Silk Net with $T_H = 610^{\circ}R(339^{\circ}K)$

specimen thicknesses, and the apparent increase in heat transfer is due to energy exchange between the calorimeter test section and the edge of the apparatus through the gap at the cold boundary.

The heat flux versus compressive pressure data for this multilayer system are consistent for similar specimens within approximately ±15 percent at any particular compressive pressure and hot boundary temperature. The basic reproducibility of the material, allowing for variations due to the repeatability of the apparatus, is therefore approximately ±10 percent in terms of compressive pressure.

From the data presented in Figs. 4-14 and 4-15, it can be seen that the radiation heat transfer component is generally a smaller proportion of the total for the double-goldized Mylar/silk net system than was the case for the double-aluminized Mylar/silk net composite. Therefore, in the general form of the heat transfer equation given by $q = a(P)^m + b$, values of the radiation component b are relatively small, and the curves drawn through the data points are very nearly straight lines.

For this multilayer system, the increase in measured heat flux for specimens with fewer layers is in reasonably good agreement with that calculated using the inverse ratio of the number of layers. Over the range of compressive pressures investigated for both hot boundary temperatures, the measured and predicted ratios based on the number of layers generally agree within +20 percent to -10 percent. For example, the ratio of the measured heat flux for a 5-shield specimen to that for a 20-shield specimen, for a compressive pressure of 1×10^{-3} psi ($6.9\ N/m^2$) and a 610°R (339°K) hot boundary temperature, is 4.20. The predicted value for this ratio is 3.50 based on the number of layers. Therefore, the ratio of the measured values is approximately 20 percent higher than that predicted.

The effect of hot and cold boundary temperatures on heat flux for the double-goldized Mylar/silk net system based on ratios of the measured values obtained is also in good engineering agreement with that calculated using the analytical model. For example, the ratio of the measured heat flux for a 5-shield specimen at a compressive pressure of 1×10^{-3} psi (6.9 N/m^2), for a hot boundary temperature of 610°R (339°K) compared to that for 500°R (278°K), is 1.56. Based on the product of mean temperature and temperature difference, the calculated solid conduction heat flux ratio for these two hot boundary temperatures ranges from 1.49 to 1.53 depending upon the cold boundary temperature selected. The ratio of the radiation heat flux components calculated for these two hot boundaries approaches 2.50, the exact value depending upon the temperature dependency exponent value derived for Eq. (4.10).

The variation of heat flux with layer density for this multilayer system is shown in Figs. 4-16 and 4-17 for 500°R (278°K) and 610°R (339°K) hot boundary temperatures, respectively. For specimens with the same number of layers, these data generally agree within approximately ±25 percent. However, the data for the two 5-shield specimens agree within approximately ±5 percent. This trend is exactly opposite to that observed for the double-aluminized Mylar/silk net system where the greatest variation of data occurred for the 5-shield specimens. There is no apparent reason for this trend, and the close correlation of the double-goldized Mylar/silk net specimen data appears to be simply fortuitous.

The relationship of compressive pressure and layer density for the double-goldized Mylar/silk net system is illustrated in Figs. 4-18 and 4-19 for the specimens tested at 140°R (77°K) and 37°R (20°K),respectively. As expected, this material behaved very much like the double-aluminized Mylar/silk net composite. However, for the double-goldized Mylar/silk net system, curves drawn through the data points cross at a layer density value of approximately 75 layers/in. (29.5 layers/cm), whereas they did not cross in the range of layer densities investigated for the material with the aluminized Mylar shields.

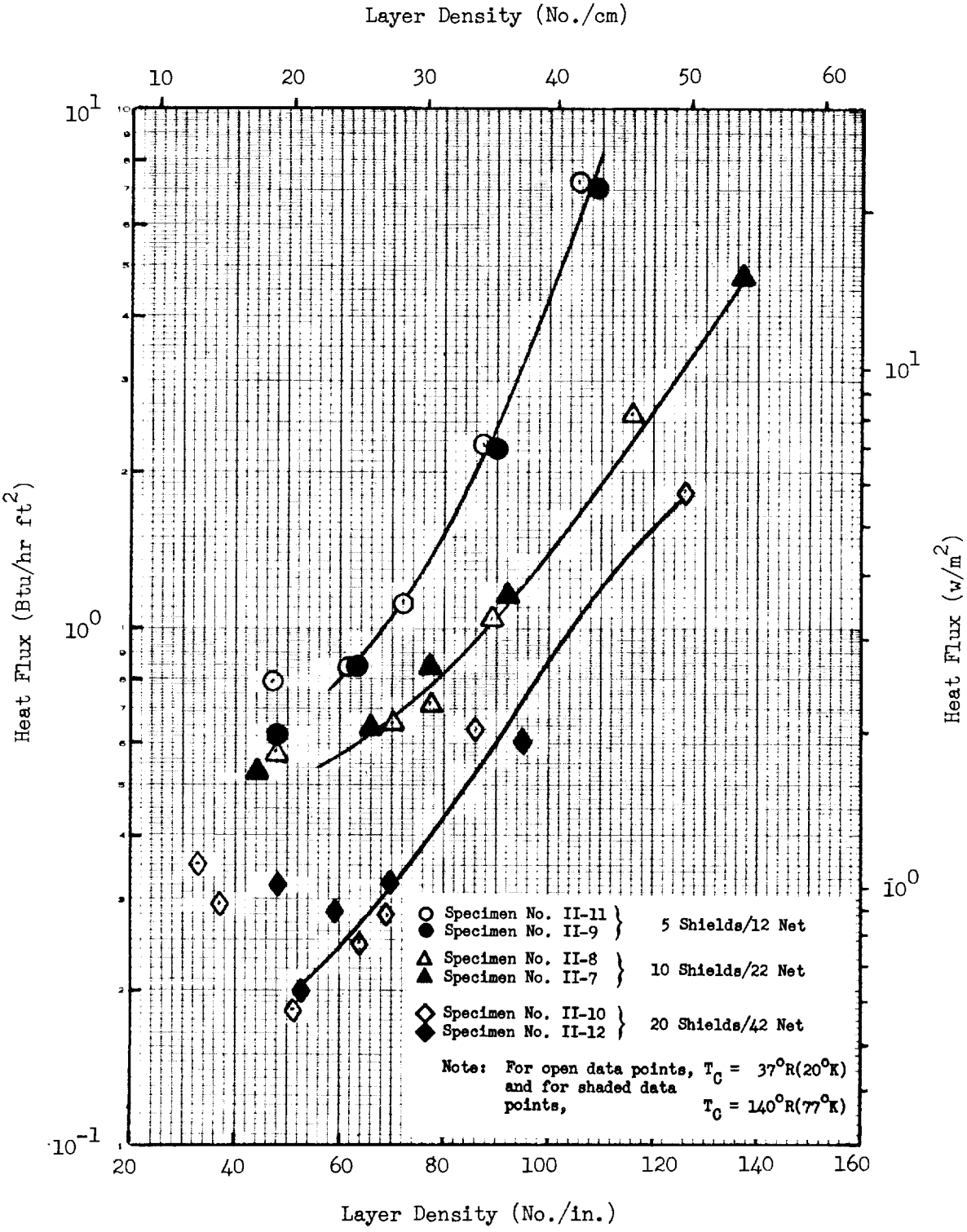

Fig. 4-16 Heat Flux as a Function of Layer Density for Double-Goldized Mylar/Silk Net with T_H = 500°R(278°K)

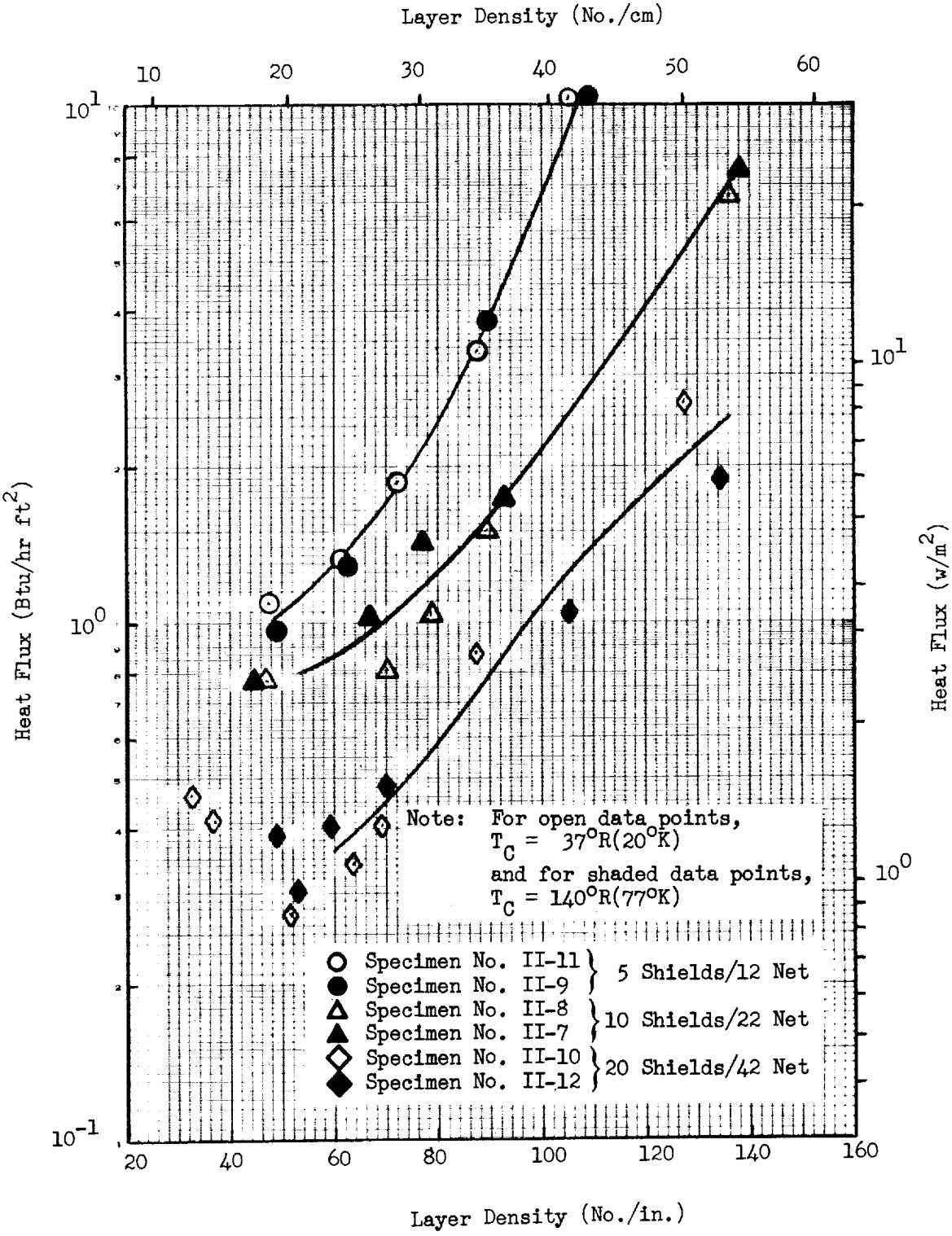

Fig. 4-17 Heat Flux as a Function of Layer Density for Double-Goldized Mylar/Silk Net with T_H = 610°R(339°K)

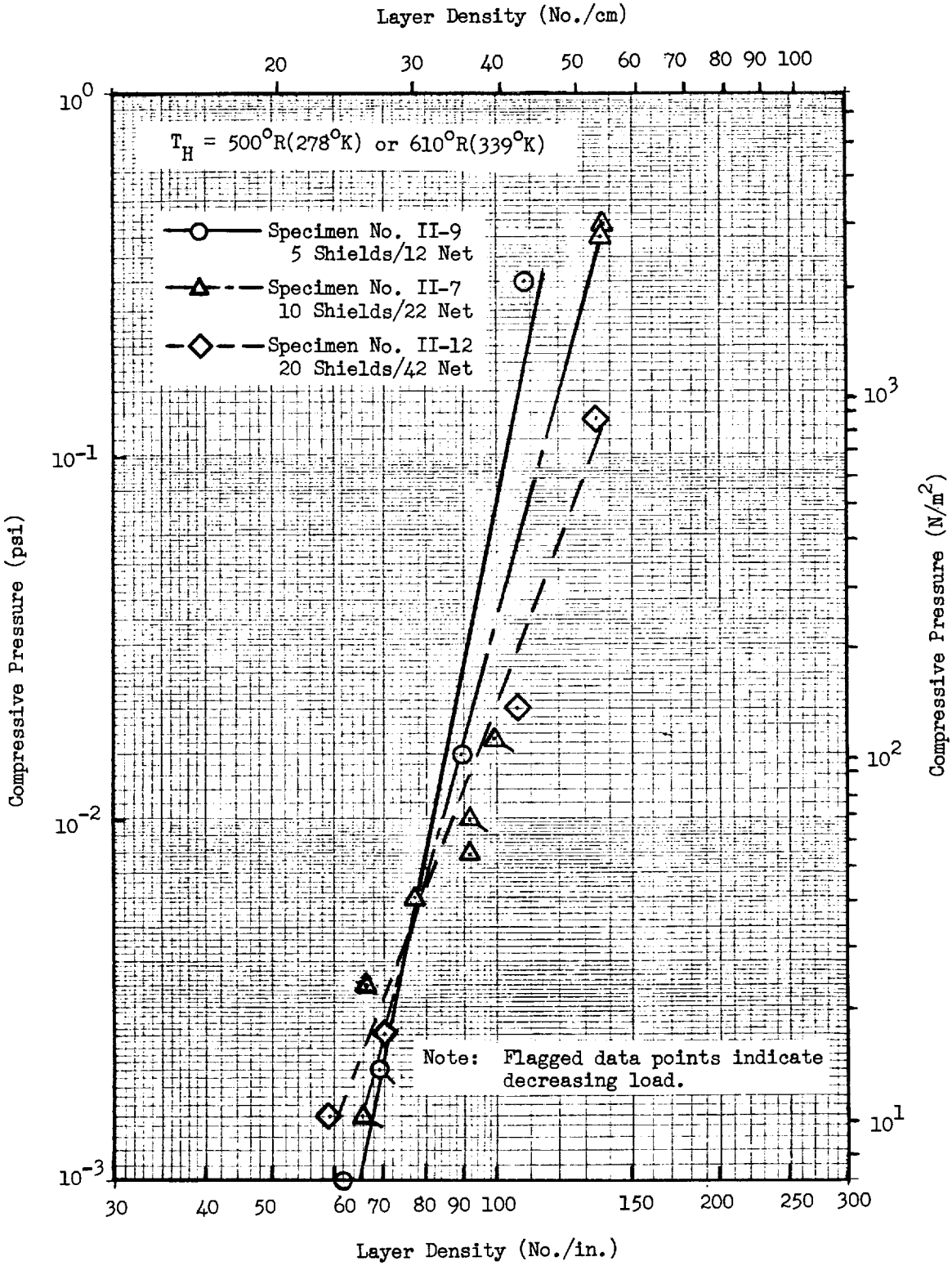

Fig. 4-18 Compressive Pressure as a Function of Layer Density for Double-Goldized Mylar/Silk Net with T_C = 140°R(77°K)

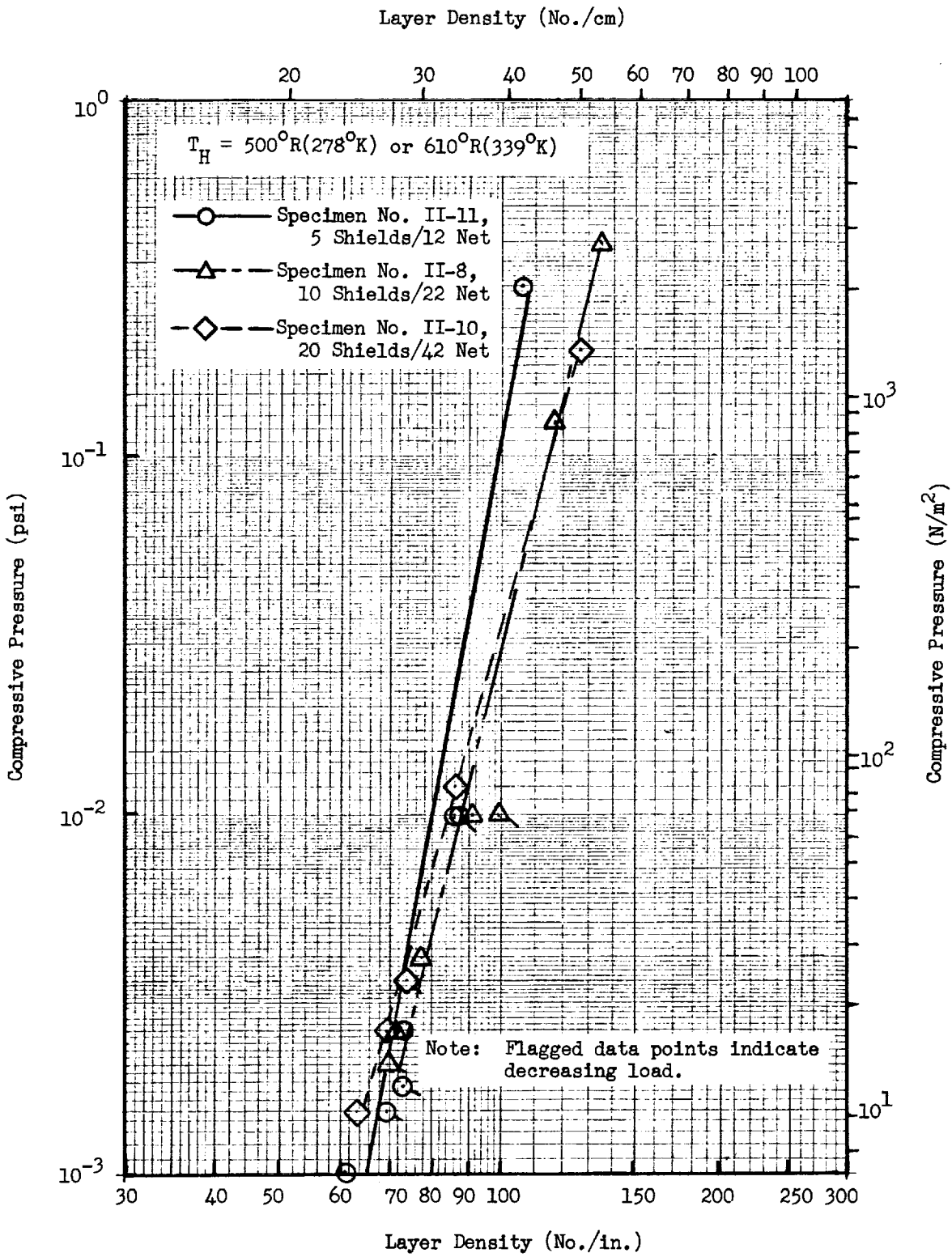

Fig. 4-19 Compressive Pressure as a Function of Layer Density for Double-Goldized Mylar/Silk Net with T_C = 37°R(20°K)

Because the compressive pressure/layer density relationship is similar in the region of approximately 65 to 85 layers/in. (25.6 to 33.5 layers/cm), heat flux ratios at constant values of layer density for 5-, 10-, and 20-shield specimens are quite similar to the corresponding ratios for constant values of compressive pressure.

Eq. (4.10) was used in the analysis of the heat transfer data for this multilayer system. Evaluation of the compressive pressure dependency coefficient and exponent for the conduction term was accomplished using the same technique that was discussed earlier for the double-aluminized Mylar composite system. Emittance values and the corresponding temperature dependency exponents obtained from measurements of emittance or normal reflectance for six double-goldized Mylar specimens are presented in Table 4-5. An average emittance value $\epsilon_{TR} = 0.0215$, and the corresponding value of the temperature dependence exponent, $\alpha_4 = 0.51$, were used to compute the radiation heat flux for each data point obtained in the flat plate calorimeter tests. Solid conduction heat flux values were then computed and normalized for boundary temperatures and the number of layers to obtain values of the parameter Φ which are shown as a function of compressive pressure in Fig. 4-20. The solid line in the figure represents the equation obtained from a least-squares curve fit to the resulting data, and the broken lines show ±15 percent deviations from the equation. Data based on

Table 4-5

EMITTANCE VALUES FOR DOUBLE-GOLDIZED MYLAR/SILK NET

Specimen Number	Average ϵ_{TH} at 540°R(300°K)*	Temperature Exponent
II-7	0.021	0.509
II-8	0.022	0.509
II-9	0.021	0.509
II-10	0.020	0.554
II-11	0.021	0.509
II-12	0.024	0.483

*$\epsilon_{TH} = 1.33\ \epsilon_{TN}$ (Ref. 5), and $\epsilon_{TN} = 1-\rho_N$

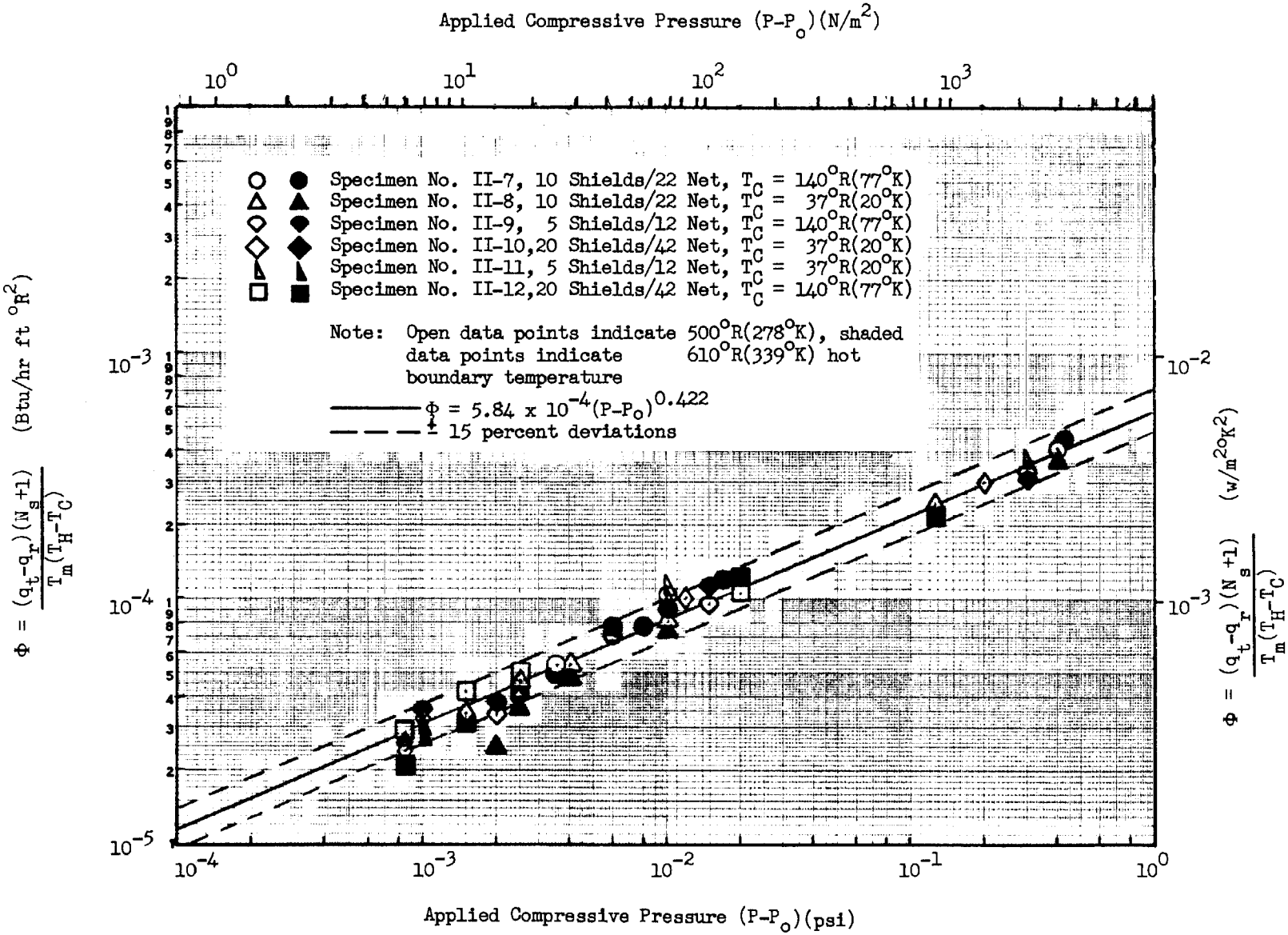

Fig. 4-20 Normalized Solid Conduction Heat Flux as a Function of Applied Compressive Pressure for Double-Goldized Mylar/Silk Net

specimen weight, where the cold boundary plate was not in contact with the specimen, were not included in the analysis. As shown, the majority of the data points fall within the ± 15 percent band. Eq. (4.10), with the co-efficients and exponents evaluated for this multilayer system, is

$$q = \frac{5.84\times10^{-4}(P-P_o)^{0.422}T_m}{N_s+1}(T_H-T_C)+\frac{3.426\times10^{-9}\epsilon_{TR}}{(4+a_4)(540)^{a_4}N_s}\left(T_H^{4+a_4}-T_C^{4+a_4}\right) \quad (4.23)$$

When compressive pressure was evaluated as a function of layer density, using all of the data obtained for this multilayer system, and the results were substituted into Eq. (4.23), the resulting expression is

$$q = \frac{4.37\times10^{-11}(\bar{N})^{3.27}T_m}{N_s+1}(T_H-T_C)+\frac{3.426\times10^{-9}\epsilon_{TR}}{(4+a_4)(540)^{a_4}N_s}\left(T_H^{4+a_4}-T_C^{4+a_4}\right) \quad (4.24)$$

Eq. (4.10) was evaluated for individual specimens, and for specimen pairs composed of an equal number of layers. These results are presented and discussed in Section 4.4.

4.3.3 Crinkled, Single-Aluminized Mylar

The data obtained for this multilayer material in Task I showed poor reproductibility for heat flux as a function of layer density. (Ref. Section 3.5.2). Because of this characteristic, and because of the two-dimensional heat flow problem encountered in Task I for testing of thick specimens in the flat plate apparatus, the decision was made to test only two additional specimens of this system, and then to investigate a fourth multilayer composite, double-aluminized Mylar/Tissuglas, in addition.

Since, in the Task I tests, the crinkled, single-aluminized Mylar system characteristically exhibited large changes in thickness for relatively small increments of compressive pressure within the practical layer density range, it was desirable to conduct tests on specimens with a larger number of layers. However, it was clear from the Task I results that practical specimens were limited to less than 40 shields if the use of an intermediary at the edge of the specimen and correction of heat flux measurements for two-dimensional heat transfer effects were to be avoided. The use of an intermediary would, of course, preclude the determination of compressive pressure since an indeterminate portion of any applied compressive force would be reacted by the intermediary. Consequently, the two specimens tested in the Task II effort consisted of 5 and 20 shields of the crinkled material. Both specimens were tested with a cold boundary temperature of 37°R (20°K). Results of the tests are presented and compared with Task I results for this material in this section.

Tabulated data for the two specimens are presented in Table 4-6. Average room temperature total hemispherical emittance values which were measured for the Mylar surfaces were 0.39 and 0.38 and for the aluminum surfaces were 0.035 and 0.33, respectively, for specimens II-13 and II-14. Heat flux as a function of compressive pressure for the 5- and 20-shield specimens with a 500°R (278°K) hot boundary temperature is shown in Fig. 4-21. The Task I data for 10 shields is also plotted for comparison. The behavior of the

Table 4-6

FLAT PLATE CALORIMETER TEST DATA FOR CRINKLED SINGLE-ALUMINIZED MYLAR

Run No	Measured Compressive Force[a] lbf	(N)	Equivalent Compressive Pressure psi	(N/m^2)	Measured Thickness[b] in	(cm)	Boundary Temperatures T_h °R (°K)	T_c °R (°K)	Layer Density No/in	(No/cm)	Measured Heat Flux Btu/hr ft^2	(w/m^2)
Specimen No. II-13, 5 crinkled shields Weight = 0.015 lb (0.0068 Kg), Uncompressed thickness = 0.14 in.(0.36 cm)[c]												
1	0.015[c]	(0.067)	5.0×10^{-5}[c]	(0.34)	0.158	(0.401)	500(278)	37(20)	37.9	(14.9)	0.760	(2.40)
1	0.015[c]	(0.067)	5.0×10^{-5}[c]	(0.34)	0.158	(0.401)	610(339)	37(20)	37.9	(14.9)	1.43	(4.51)
2	0.1	(0.4)	5.5×10^{-4}	(3.8)	0.127	(0.323)	610(339)	37(20)	47.3	(18.6)	1.61	(5.07)
2	0.1	(0.4)	5.5×10^{-4}	(3.8)	0.127	(0.323)	500(278)	37(20)	47.3	(18.6)	0.810	(2.55)
3	0.3	(1.3)	1.7×10^{-3}	(11.7)	0.110	(0.279)	500(278)	37(20)	54.6	(21.5)	0.970	(3.06)
3	0.3	(1.3)	1.7×10^{-3}	(11.7)	0.110	(0.279)	610(339)	37(20)	54.6	(21.5)	1.85	(5.83)
4	0.65	(2.9)	3.7×10^{-3}	(25.5)	0.087	(0.221)	610(339)	37(20)	69.0	(27.2)	2.35	(7.41)
4	0.65	(2.9)	3.7×10^{-3}	(25.5)	0.087	(0.221)	500(278)	37(20)	69.0	(27.2)	1.32	(4.16)
5	1.2	(5.3)	6.8×10^{-3}	(46.9)	0.067	(0.170)	500(278)	37(20)	89.5	(35.2)	2.13	(6.71)
5	1.2	(5.3)	6.8×10^{-3}	(46.9)	0.067	(0.170)	610(339)	37(20)	89.5	(35.2)	3.57	(11.3)
6	3.9	(17.3)	2.2×10^{-2}	(152)	0.0473	(0.120)	610(339)	37(20)	127.0	(50.0)	11.8	(37.2)
6	3.9	(17.3)	2.2×10^{-2}	(152)	0.0473	(0.120)	500(278)	37(20)	127.0	(50.0)	7.45	(23.5)
7	0.3	(1.3)	1.7×10^{-3}	(11.7)	0.089	(0.226)	500(278)	37(20)	67.5	(26.6)	0.990	(3.12)
7	0.3	(1.3)	1.7×10^{-3}	(11.7)	0.086	(0.218)	610(339)	37(20)	69.8	(27.5)	1.78	(5.61)
8	0.015[d]	(0.067)	1.0×10^{-4}[d]	(0.69)	0.107	(0.272)	610(339)	37(20)	56.0	(22.0)	1.44	(4.54)
8	0.015[d]	(0.067)	1.0×10^{-4}[d]	(0.69)	0.107	(0.272)	500(278)	37(20)	56.0	(22.0)	0.643	(2.03)
Specimen No. II-14, 20 crinkled shields, Weight = 0.08 lb (0.036 Kg), Uncompressed thickness = 0.4 in (1.02 cm)[c]												
1	0.08[c]	(0.36)	2.2×10^{-4}[c]	(1.5)	0.498	(1.26)	500(278)	37(20)	42.2	(16.6)	0.253	(0.797)
1	0.08[c]	(0.36)	2.2×10^{-4}[c]	(1.5)	0.498	(1.26)	610(339)	37(20)	42.2	(16.6)	0.430	(1.36)
2	0.08[d]	(0.36)	4.5×10^{-4}[d]	(3.1)	0.401	(1.02)	610(339)	37(20)	52.3	(20.6)	0.348	(1.10)
2	0.08[d]	(0.36)	4.5×10^{-4}[d]	(3.1)	0.401	(1.02)	500(278)	37(20)	52.3	(20.6)	0.208	(0.656)
3	0.3	(1.3)	1.7×10^{-3}	(11.7)	0.331	(0.841)	500(278)	37(20)	63.4	(25.0)	0.308	(0.971)
3	0.3	(1.3)	1.7×10^{-3}	(11.7)	0.331	(0.841)	610(339)	37(20)	63.4	(25.0)	0.475	(1.50)
4	0.4	(1.8)	2.25×10^{-3}	(15.5)	0.285	(0.724)	610(339)	37(20)	73.6	(29.0)	0.480	(1.51)
4	0.4	(1.8)	2.25×10^{-3}	(15.5)	0.285	(0.724)	500(278)	37(20)	73.6	(29.0)	0.325	(1.02)
5	0.9	(4.0)	5.1×10^{-3}	(35.2)	0.242	(0.615)	500(278)	37(20)	86.8	(34.2)	0.456	(1.44)
5	0.9	(4.0)	5.1×10^{-3}	(35.2)	0.242	(0.615)	610(339)	37(20)	86.8	(34.2)	0.707	(2.23)
6	1.5	(6.7)	8.5×10^{-3}	(58.6)	0.200	(0.508)	610(339)	37(20)	105.0	(41.3)	0.974	(3.07)
6	1.5	(6.7)	8.5×10^{-3}	(58.6)	0.200	(0.508)	500(278)	37(20)	105.0	(41.3)	0.678	(2.14)
7	2.5	(11.1)	1.4×10^{-2}	(96.5)	0.154	(0.391)	500(278)	37(20)	136.3	(53.7)	1.33	(4.19)
7	2.5	(11.1)	1.4×10^{-2}	(96.5)	0.154	(0.391)	610(339)	37(20)	136.3	(53.7)	1.73	(5.45)
8	10.0	(44.5)	5.65×10^{-2}	(390)	0.091	(0.231)	610(339)	37(20)	231.0	(90.9)	7.32	(23.1)
8	10.0	(44.5)	5.65×10^{-2}	(390)	0.091	(0.231)	500(278)	37(20)	231.0	(90.9)	5.21	(16.4)
9	0.9	(4.0)	5.1×10^{-3}	(35.2)	0.207	(0.526)	500(278)	37(20)	101.5	(40.0)	0.464	(1.46)
9	0.9	(4.0)	5.1×10^{-3}	(35.2)	0.207	(0.526)	610(339)	37(20)	101.5	(40.0)	0.699	(2.20)
10	0.08[d]	(0.36)	4.5×10^{-4}[d]	(3.1)	0.324	(0.823)	610(339)	37(20)	64.9	(25.6)	0.350	(1.10)
10	0.08[d]	(0.36)	4.5×10^{-4}[d]	(3.1)	0.324	(0.823)	500(278)	37(20)	64.9	(25.6)	0.223	(0.703)
11	0.08[c]	(0.36)	2.2×10^{-4}[c]	(1.5)	0.400	(1.02)	500(278)	37(20)	52.5	(20.7)	0.163	(0.514)
11	0.08[c]	(0.36)	2.2×10^{-4}[c]	(1.5)	0.400	(1.02)	610(339)	37(20)	52.5	(20.7)	0.274	(0.864)

NOTES:
(a) Force measurement accuracy ± 0.1 lb (± 0.4 N)
(b) Separation between hot and cold boundary surface plates
(c) Force = specimen weight; Average pressure = 1/2 weight/unit area (assumed)
(d) Force = specimen weight; No gap; Load cell indicated contact with specimen; Average pressure = specimen weight/unit area (assumed)
(e) Measured with a dial gage prior to installation in the FPC

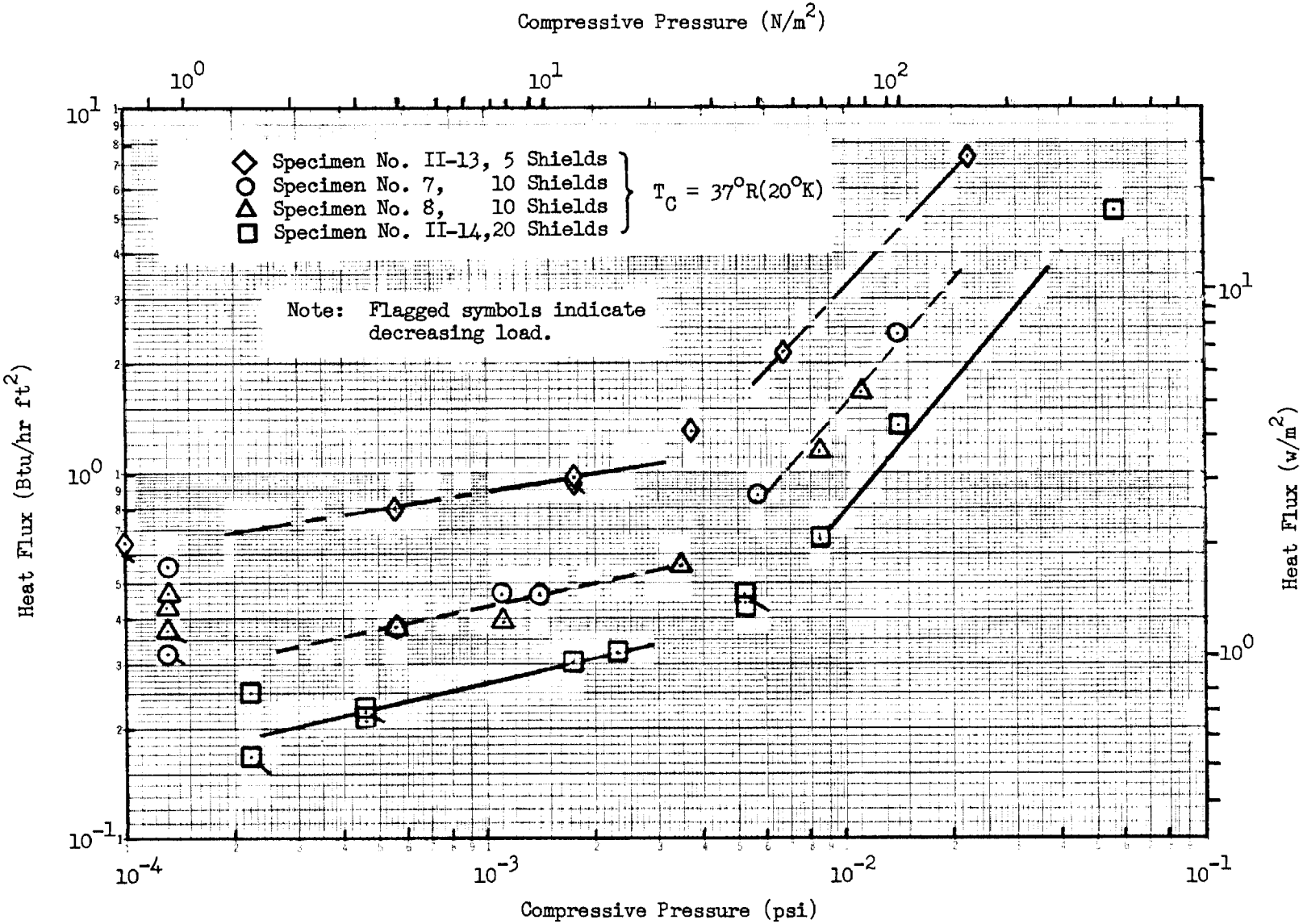

Fig. 4-21 Heat Flux as a Function of Compressive Pressure for Crinkled, Single-Aluminized Mylar with $T_H = 500°R(278°K)$

material under compressive loading did not exhibit a uniform relationship of heat flux with compressive pressure over the range of compressive pressure investigated. However, a good approximation of the true relationship was obtained by considering that a discontinuity occurred in the region of 5×10^{-3} psi (34.5 N/m^2), and then by using two different equations to fit the data on either side of this value. The curves in Fig. 4-21 indicate the different equations and fit the experimental data within ±15 percent.

In the region of low compressive pressure, the heat flux for the 20-shield specimen is greater than would be calculated using the 10-shield specimen data multiplied by the inverse ratio of the number of layers. On that basis, the ratio of the 20-shield specimen heat flux to that for the 10-shield specimen should be 0.52. However, the ratio of the heat flux values computed from the experimental dated is 0.62 for a compressive pressure of 1×10^{-3} psi (6.9 N/m^2). This is indicative of a "self-compression" effect due to the weight of the additional shields. Comparison of heat flux values for the 5- and 10-shield specimens at a compressive pressure of 1×10^{-3} psi (6.9 N/m^2) shows that the ratio, $q_{10}/q_5 = 0.48$, is in good agreement with a calculated ratio of 0.55 based on the inverse ratio of the number of layers. In the high compressive pressure region, i.e., 1×10^{-2} psi (69 N/m^2) and above, the self-compression effect was not observed and the measured heat flux ratios for specimens with a different number of layers were in good agreement with those calculated using the inverse ratio of the number of layers.

Fig. 4-22 shows a comparison of the experimental heat flux data for the 5- and 20-shield specimens for hot boundary temperatures of 500°R (278°K) and 610°R (339°K). The effect of the hot boundary temperature on heat flux can be evaluated by comparing ratios of the experimental heat flux for these two temperatures at constant values of compressive pressure. For example, the ratios of the heat flux for 610°R (339°K) to that for 500°R (278°K) are 1.93 and 1.60 for the 5- and 20-shield specimens, respectively, at a compressive

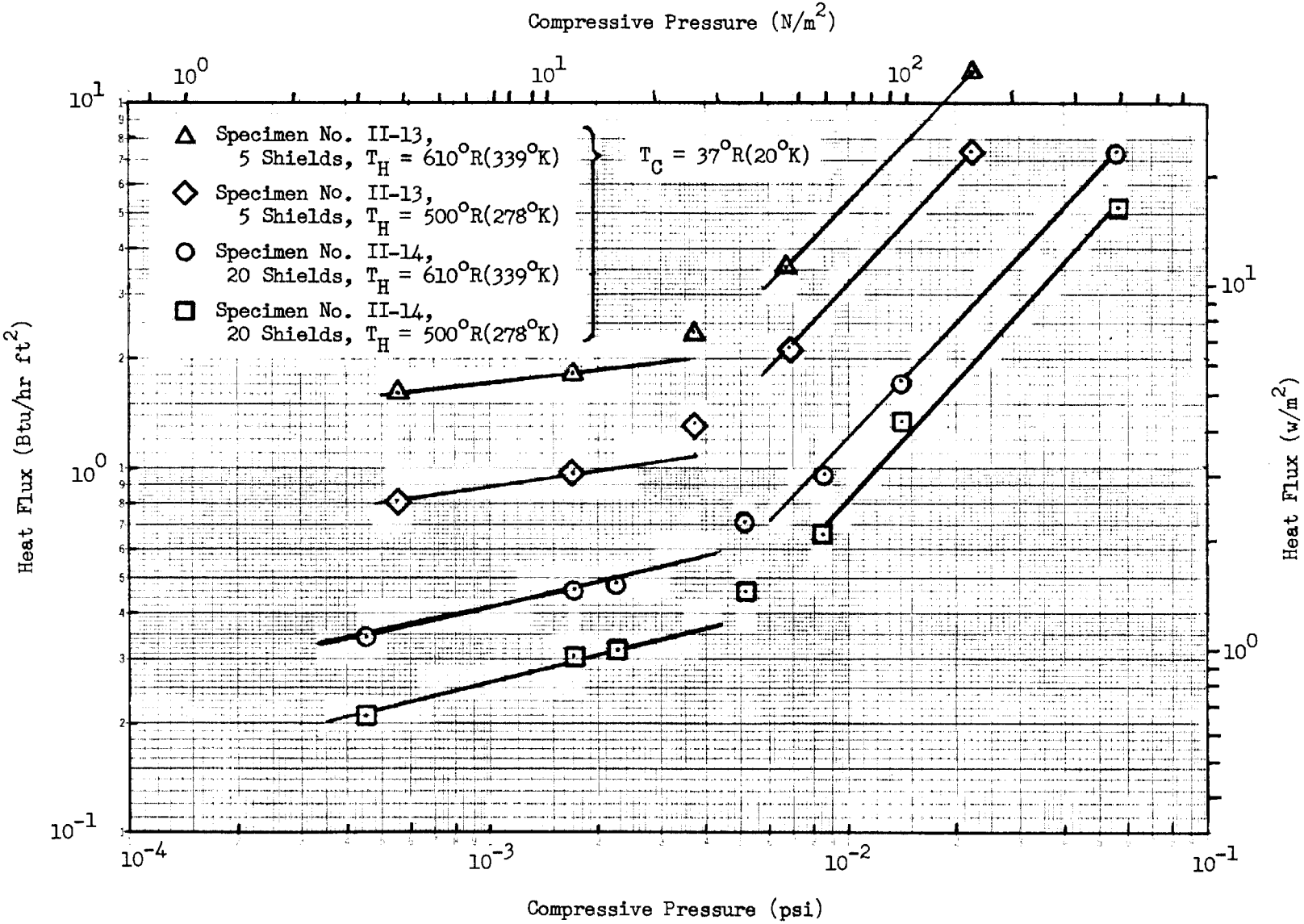

Fig. 4-22 Heat Flux as a Function of Compressive Pressure for Crinkled, Single-Aluminized Mylar with T_H = 500°R(278°K) and 610°R(339°K)

pressure of $1x10^{-3}$ psi (6.9 N/m^2). Similarly, the corresponding ratios are 1.65 and 1.47 at a compressive pressure of $1x10^{-2}$psi (69 N/m^2). Based on the analytical model described by Eq. (4.8), the ratio of calculated solid conduction heat flux values at a constant compressive pressure can be computed as the ratio of the products of mean temperature and temperature difference for the two hot boundary temperatures in combination with a particular cold boundary temperature. This ratio varies from 1.49 to 1.53 depending upon the cold boundary temperature selected (Ref. Section 4.3.1) The ratio of predicted radiation heat flux values is 2.53, computed as the value of $T_H^{4.67} - T_C^{4.67}$ for 610°R (339°K) compared to that for 500°R (278°K). For the radiation component, the effect of the cold boundary temperature is negligible. Comparison of the ratios obtained from the experimental heat flux values with those from predicted values shows that radiation heat transfer is a greater proportion of the total for this multilayer system than it was for the metallized Mylar/silk net systems discussed earlier.

Heat flux as a function of layer density is shown in Fig. 4-23 for 5-, 10-, and 20-shield specimens. The curve representing the 40-shield data, corrected for two-dimensional effects, is also shown for comparison. These data show that the predictability and reproducibility of this system are very poor in terms of layer density. The scatter in the 10-shield specimen data is such that no conclusions can be drawn regarding the performance of the 5- and 20-shield specimens in comparison to the 10-shield specimen. For specimen No. 7, a curve drawn through the data (not shown) would cross that for the 5-shield specimen at approximately 90 layers/in. (35.4 layers/cm). Yet at 70 layers/in. (27.6 layers/cm) it would approach that for a similar 10-shield specimen, No. 8. Comparing the 20- and 40-shield specimen data at low layer densities, i.e., 60 to 80 layers/in.(23.6 to 31.5 layers/cm), the ratio of the heat flux for 20 shields to that for 40 is approximately 75 percent of that predicted from the ratio of the number of layers.

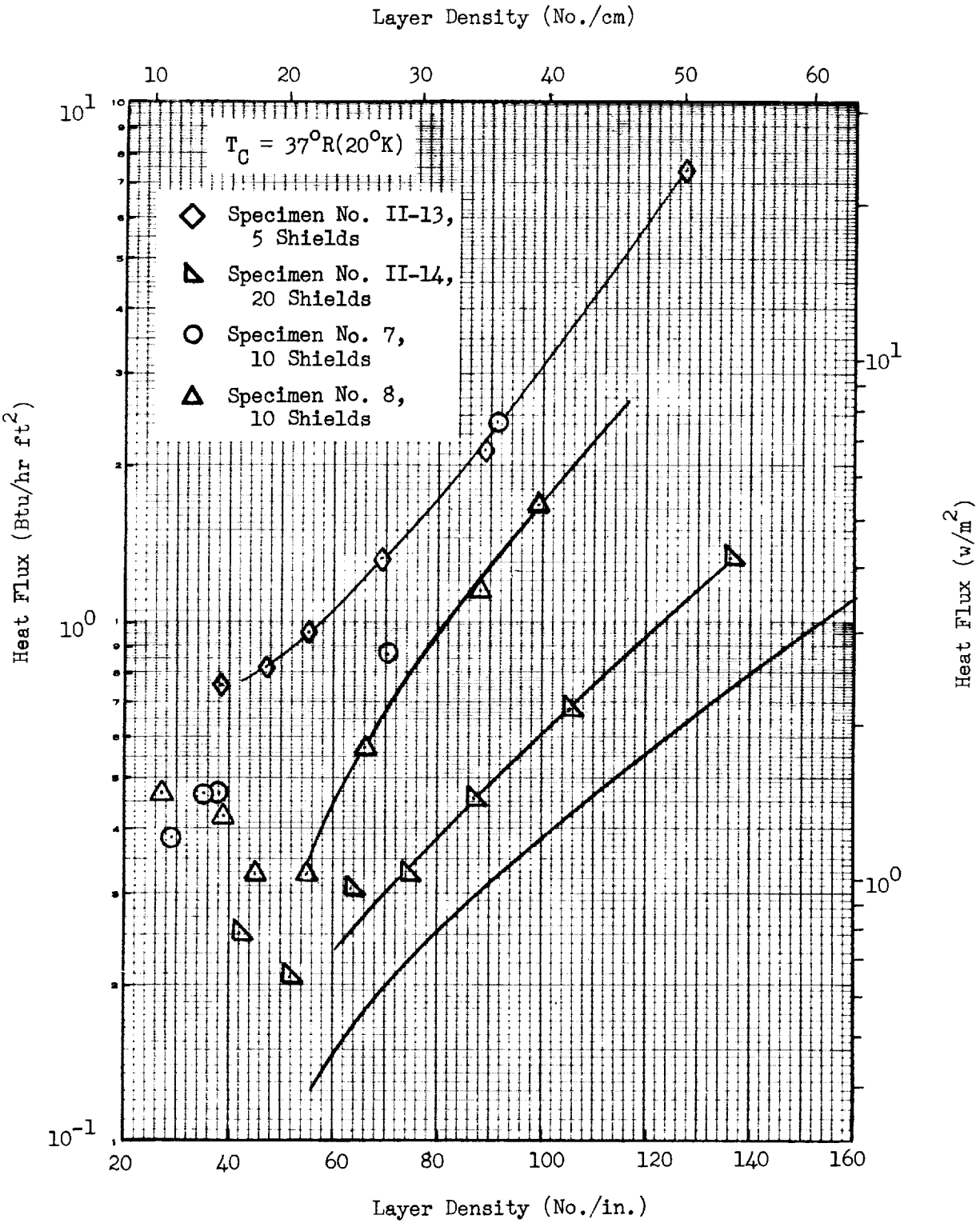

Fig. 4-23 Heat Flux as a Function of Layer Density for Crinkled, Single-Aluminized Mylar with T_H = 500°R(278°K)

Compressive pressure as a function of layer density is shown in Fig. 4-24 for the 5-, 10-, 20-, and 40-shield specimens. Over the entire range investigated, the compressive pressure values obtained for the 10-shield specimens at any particular layer density value show very poor predictability and reproducibility characteristics with respect to those obtained for the 5- and 20-shield specimens. The predictability and reproducibility are improved for the 20- and 40-shield specimens, except at very low values of compressive pressure. These data clearly indicate that this multilayer system is significantly less reproducible than the metallized Mylar/silk net systems discussed earlier with respect to the compressive pressure/layer density relationship. Moreover, for applications in which the system would be subjected to acceleration loads, the self-compression effects observed at layer densities below approximately 100 layers/in. (39.4 layers/cm) could significantly degrade the thermal performance of this material.

The broken lines shown in Fig. 4-24 represent the limits of scatter for data points (not shown) obtained at room temperature for duplicate specimens of 20, 40, and 80 shields. These data were measured using a compression testing machine for which the load versus deflection characteristics were continuously recorded during the tests. Specimens for these tests were 16 in.(40.6 cm) in diameter, and were compressed between flat rigid steel plates.

In view of the poor reproducibility as evidenced by the scatter of data obtained for the 10 shield specimens, and the inconsistencies noted for predicting the influence of the number of layers, this multilayer system would be characterized by very large uncertainties in the prediction of thermal performance with the system applied to a cryogenic storage vessel. The "self-compression" tendency would further increase the uncertainity for use of Flat Plate Calorimeter data to predict thermal performance as installed on a tank or structure. For example, the heat transfer characteristics for

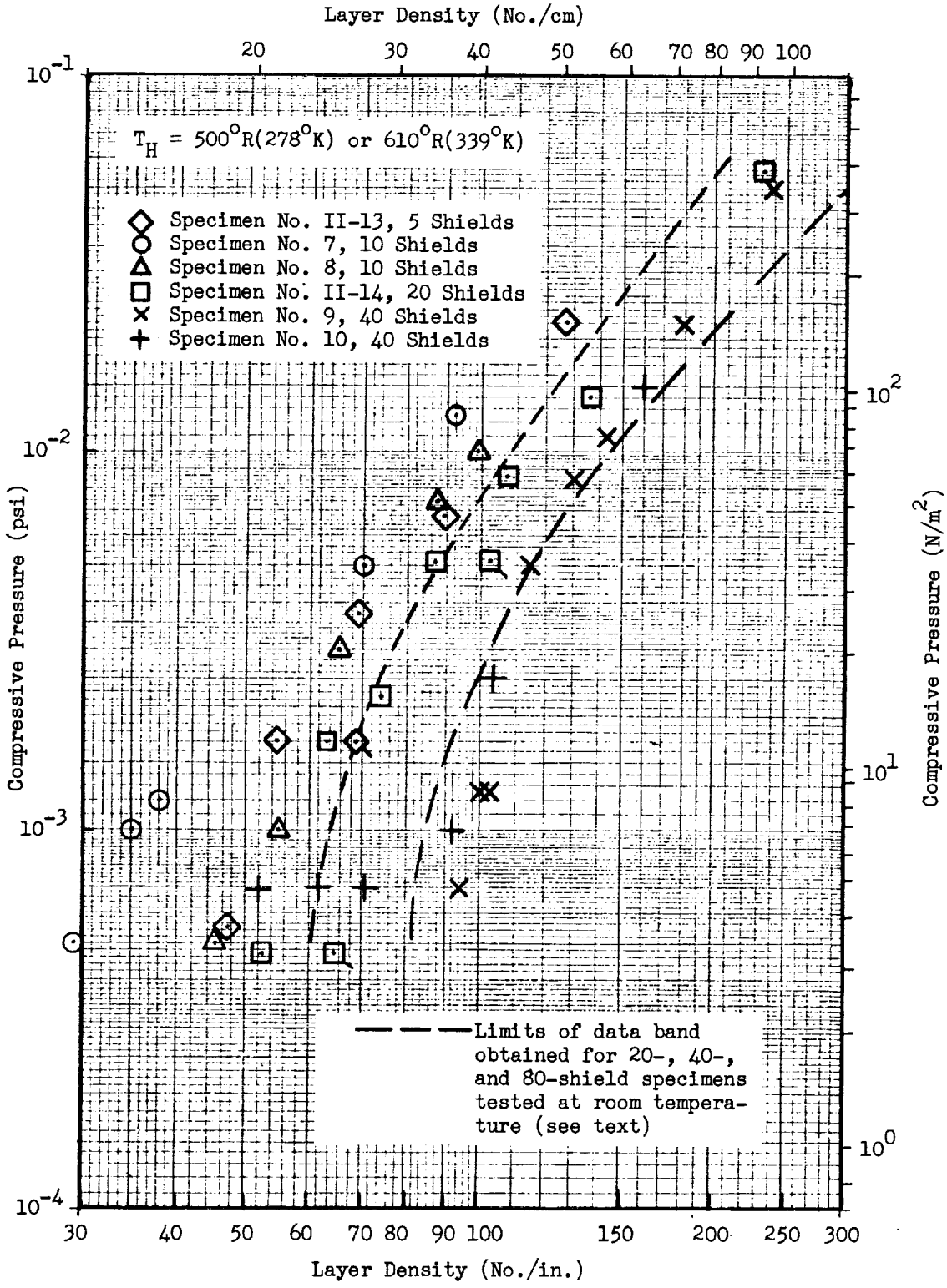

Fig. 4-24 Compressive Pressure as a Function of Layer Density for Crinkled, Single-Aluminized Mylar with T_C = 37°R(20°K)

this material where it is installed on a vertical surface in a gravity environment should be entirely different from those where it is installed on a horizontal surface.

Because of the poor reproducibility of this system, only a cursory analysis was conducted of the heat transfer mechanisms. Fig. 4-25 illustrates the computed values of the conduction term normalized for the number of layers. The radiation heat flux component was computed as discussed earlier, and was then subtracted from the measured total heat flux values. The normalized data were fit graphically to determine the coefficient and exponent of the compressive pressure function. For compressive pressures less than $4\text{x}10^{-3}$ psi (27.6 N/m^2), the expression that resulted is

$$q_s = \frac{7.04\text{x}10^{-4}(P-P_o)^{0.495}T_m}{N_s + 1}(T_H-T_C)$$

For compressive pressures greater than $5\text{x}10^{-3}$ psi (34.5 N/m^2), the resulting expression is

$$q_s = \frac{5.08\text{x}10^{-3}(P-P_o)^{0.813}T_m}{N_s + 1}(T_H-T_C)$$

Substituting the above expressions together with optical property values presented earlier into Eq. (4.8), the equations which result for prediction or evaluation of thermal performance for this system are

$$q = \frac{7.04\text{x}10^{-4}(P-P_o)^{0.495}T_m}{N_s + 1}(T_H-T_C) + \frac{2.22\text{x}10^{-11}\epsilon_{TRA}\epsilon_{TRM}}{(\epsilon_{TRA}+\epsilon_{TRM})N_s}\left(T_H^{4.67}-T_C^{4.67}\right) \quad (4.25)$$

and

$$q = \frac{5.08\text{x}10^{-3}(P-P_o)^{0.813}T_m}{N_s + 1}(T_H-T_C) + \frac{2.22\text{x}10^{-11}\epsilon_{TRA}\epsilon_{TRM}}{(\epsilon_{TRA}+\epsilon_{TRM})N_s}\left(T_H^{4.67}-T_C^{4.67}\right) \quad (4.26)$$

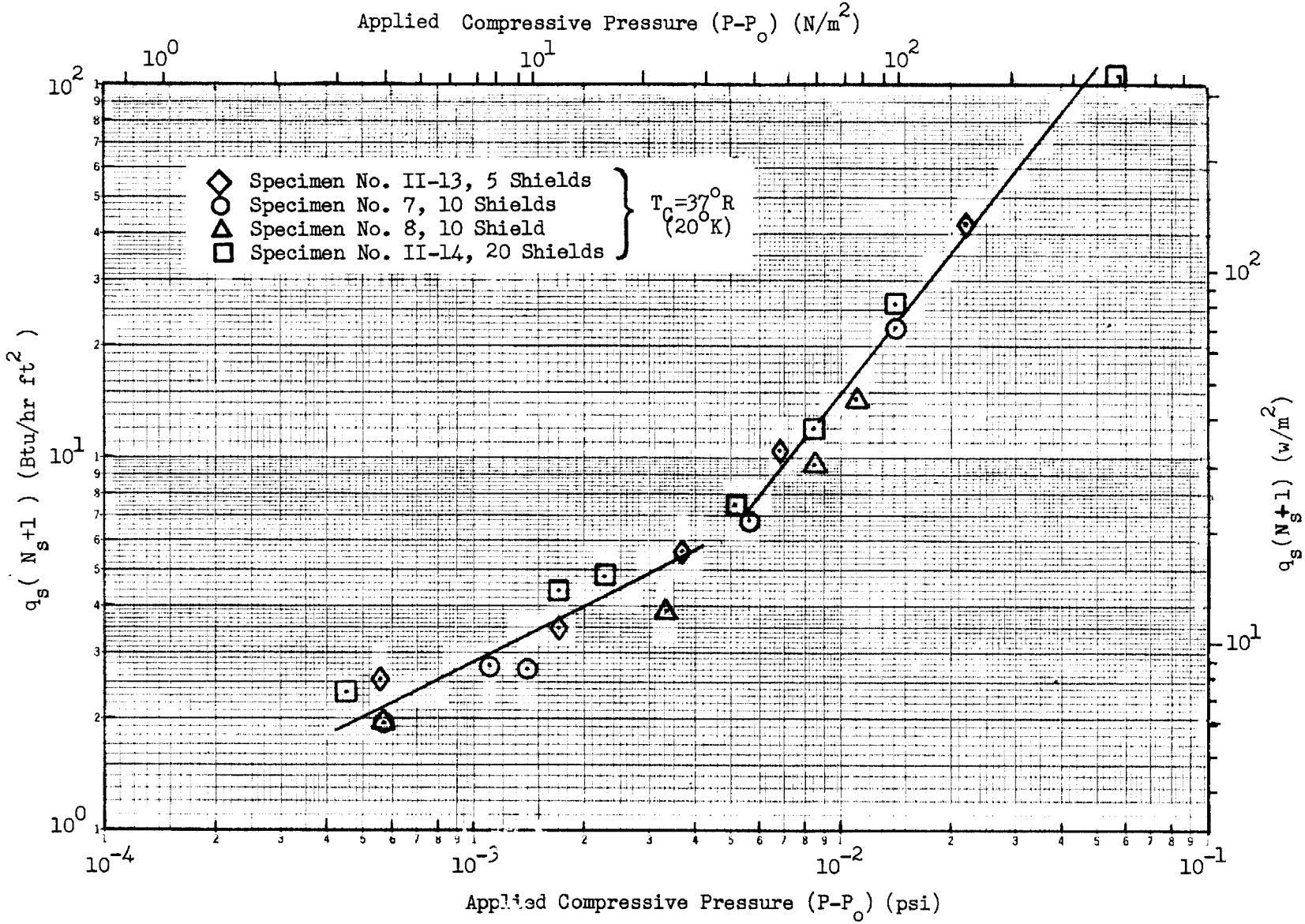

Fig. 4-25 Normalized Solid Conduction Heat Flux as a Function of Applied Compressive Pressure for Crinkled, Single-Aluminized Mylar

for compressive pressure values less than 4×10^{-3} psi (27.6 N/m^2) and greater than 5×10^{-3} psi (34.5 N/m^2), respectively.

With evaluation of compressive pressure as a function of layer density, using all of the data obtained for this multilayer system, these expressions become

$$q = \frac{1.65 \times 10^{-9} (\bar{N})^{2.32} T_m}{N_s + 1} (T_H - T_C) + \frac{2.22 \times 10^{-11} \epsilon_{TRA} \epsilon_{TRM}}{(\epsilon_{TRA} + \epsilon_{TRM}) N_s} \left(T_H^{4.67} - T_C^{4.67} \right) \quad (4.27)$$

and

$$q = \frac{8.57 \times 10^{-9} (\bar{N})^{2.02} T_m}{N_s + 1} (T_H - T_C) + \frac{2.22 \times 10^{-11} \epsilon_{TRA} \epsilon_{TRM}}{(\epsilon_{TRA} + \epsilon_{TRM}) N_s} \left(T_H^{4.67} - T_C^{4.67} \right) \quad (4.28)$$

for layer density values less than or greater than 87 layers/in. (34.3 layers/cm), respectively.

4.3.4 Double-Aluminized Mylar/Tissuglas

For this multilayer composite, heat transfer characteristics were investigated for two specimens each of 10 shields with 11 spacers, 20 shields with 21 spacers, and 40 shields with 41 spacers.

The experimental data obtained for all six specimens are presented in Table 4-7. These data include measured values of compressive force, specimen thickness, and boundary temperatures as well as computed values of equivalent compressive pressure, layer density, and heat flux for each data point.

Figs. 4-26 and 4-27 show the variation of heat flux with compressive pressure for 500°F (278°K) and 610°R (339°K) hot boundary temperatures, respectively. In general, these data appear to fit the expression $q = a(P)^m + b$ discussed earlier (Ref. Section 4.3.1). For this composite system, the curves drawn through the data points are very nearly straight lines since the radiation heat transfer component is a small part of the total heat transfer at the higher values of compressive pressure. The data for heat flux as a function of compressive pressure are reproducible within approximately $\pm$ 10 percent for this material.

Table 4-7

FLAT PLATE CALORIMETER TEST DATA FOR DOUBLE-ALUMINIZED MYLAR/TISSUGLAS

Run No.	Measured Compressive Force (a) lbf	(N)	Equivalent Compressive Pressure psi	(N/m^2)	Measured Thickness (b) in.	(cm)	Boundary Temperatures T_h $^oR(^oK)$	T_c $^oR(^oK)$	Layer Density No./in.	(No./cm)	Measured Heat Flux $Btu/hr\ ft^2$	(w/m^2)
Specimen No. II-15, 20 shields/21 spacers, Weight = 0.068 lb (0.031 Kg), Uncompressed thickness = 0.21 in. (0.53 cm)(e)												
1	0.068(c)	(0.30)	1.7×10^{-4}(c)	(1.2)	0.201	(0.511)	500(278)	140(77)	104.5	(41.1)	0.291	(0.917)
1	0.068(c)	(0.30)	1.7×10^{-4}(c)	(1.2)	0.201	(0.511)	610(339)	140(77)	104.5	(41.1)	0.372	(1.17)
2	0.2	(0.9)	1.0×10^{-3}	(6.9)	0.133	(0.338)	610(339)	140(77)	157.9	(62.2)	0.382	(1.20)
2	0.2	(0.9)	1.0×10^{-3}	(6.9)	0.133	(0.338)	500(278)	140(77)	157.9	(62.2)	0.290	(0.914)
3	0.4	(1.8)	2.0×10^{-3}	(13.8)	0.121	(0.307)	500(278)	140(77)	173.6	(68.3)	0.415	(1.31)
3	0.4	(1.8)	2.0×10^{-3}	(13.8)	0.121	(0.307)	610(339)	140(77)	173.6	(68.3)	0.684	(2.16)
4	1.0	(4.4)	5.0×10^{-3}	(34.5)	0.106	(0.269)	610(339)	140(77)	198.1	(78.0)	1.01	(3.18)
4	1.0	(4.4)	5.0×10^{-3}	(34.5)	0.106	(0.269)	500(278)	140(77)	198.1	(78.0)	0.700	(2.21)
5	6.0	(26.7)	3.0×10^{-2}	(207)	0.082	(0.208)	500(278)	140(77)	256.1	(101)	1.84	(5.80)
5	6.0	(26.7)	3.0×10^{-2}	(207)	0.082	(0.208)	610(339)	140(77)	256.1	(101)	2.69	(8.48)
Specimen No. II-16, 20 shields/21 spacers, Weight = 0.069 lb (0.031 Kg), Uncompressed thickness = 0.19 in. (0.48 cm)(e)												
1	0.069(c)	(0.31)	1.7×10^{-4}(c)	(1.2)	0.252	(0.640)	500(278)	37(20)	83.5	(32.9)	0.258	(0.813)
1	0.069(c)	(0.31)	1.7×10^{-4}(c)	(1.2)	0.252	(0.640)	610(339)	37(20)	83.5	(32.9)	0.388	(1.22)
2	0.069(c)	(0.31)	1.7×10^{-4}(c)	(1.2)	0.191	(0.485)	610(339)	37(20)	109.9	(43.3)	0.330	(1.04)
2	0.069(c)	(0.31)	1.7×10^{-4}(c)	(1.2)	0.191	(0.485)	500(278)	37(20)	109.9	(43.3)	0.202	(0.637)
3	0.1	(0.4)	5.0×10^{-4}	(3.4)	0.167	(0.424)	500(278)	37(20)	125.7	(49.5)	0.247	(0.779)
3	0.1	(0.4)	5.0×10^{-4}	(3.4)	0.167	(0.424)	610(339)	37(20)	125.7	(49.5)	0.371	(1.17)
4	0.2	(0.9)	1.0×10^{-3}	(6.9)	0.138	(0.351)	610(339)	37(20)	152.2	(59.9)	0.465	(1.47)
4	0.2	(0.9)	1.0×10^{-3}	(6.9)	0.138	(0.351)	500(278)	37(20)	152.2	(59.9)	0.299	(0.942)
5	1.0	(4.4)	5.0×10^{-3}	(34.5)	0.099	(0.251)	500(278)	37(20)	212.1	(83.5)	0.721	(2.27)
5	1.0	(4.4)	5.0×10^{-3}	(34.5)	0.099	(0.251)	610(339)	37(20)	212.1	(83.5)	1.09	(3.44)
6	6.0	(26.7)	3.0×10^{-2}	(207)	0.079	(0.201)	610(339)	37(20)	265.8	(105)	2.91	(9.17)
6	6.0	(26.7)	3.0×10^{-2}	(207)	0.079	(0.201)	500(278)	37(20)	265.8	(105)	1.94	(6.11)
7	0.069(c)	(0.31)	1.7×10^{-4}(c)	(1.2)	0.199	(0.505)	500(278)	37(20)	105.5	(41.5)	0.287	(0.905)
7	0.069(c)	(0.31)	1.7×10^{-4}(c)	(1.2)	0.255	(0.648)	610(339)	37(20)	82.4	(32.4)	0.298	(0.939)
Specimen No. II-17, 40 shields/41 spacers, Weight = 0.131b (0.059 Kg), Uncompressed thickness = 0.28 in. (0.71 cm)(e)												
1	0.13(d)	(0.58)	6.6×10^{-4}(d)	(4.6)	0.281	(0.714)	500(278)	140(77)	145.9	(57.4)	0.171	(0.539)
1	0.13(d)	(0.58)	6.6×10^{-4}(d)	(4.6)	0.281	(0.714)	610(339)	140(77)	145.9	(57.4)	0.212	(0.668)
2	0.2	(0.9)	8.3×10^{-4}	(5.7)	0.265	(0.673)	610(339)	140(77)	154.7	(60.9)	0.210	(0.662)
2	0.2	(0.9)	8.3×10^{-4}	(5.7)	0.265	(0.673)	500(278)	140(77)	154.7	(60.9)	0.153	(0.482)
3	0.6	(2.7)	2.8×10^{-3}	(19.3)	0.222	(0.564)	500(278)	140(77)	184.7	(72.7)	0.274	(0.864)
3	0.6	(2.7)	2.8×10^{-3}	(19.3)	0.222	(0.564)	610(339)	140(77)	184.7	(72.7)	0.371	(1.17)
4	0.8	(3.6)	3.8×10^{-3}	(26.2)	0.206	(0.523)	610(339)	140(77)	199.0	(78.3)	0.451	(1.42)
4	0.8	(3.6)	3.8×10^{-3}	(26.2)	0.206	(0.523)	500(278)	140(77)	199.0	(78.3)	0.302	(0.952)
5	1.6	(7.1)	7.8×10^{-3}	(53.8)	0.168	(0.427)	500(278)	140(77)	244.0	(96.1)	0.493	(1.55)
5	1.6	(7.1)	7.8×10^{-3}	(53.8)	0.168	(0.427)	610(339)	140(77)	244.0	(96.1)	0.758	(2.39)
6	4.1	(18.2)	2.0×10^{-2}	(138)	0.147	(0.373)	610(339)	140(77)	278.9	(109.8)	1.29	(4.07)
6	4.1	(18.2)	2.0×10^{-2}	(138)	0.147	(0.373)	500(278)	140(77)	278.9	(109.8)	0.843	(2.66)
7	0.6	(2.7)	2.8×10^{-3}	(19.3)	0.236	(0.599)	500(278)	140(77)	173.7	(68.4)	0.263	(0.829)
7	0.6	(2.7)	2.8×10^{-3}	(19.3)	0.236	(0.599)	610(339)	140(77)	173.7	(68.4)	0.354	(1.12)

NOTES:
(a) Force measurement accuracy $\pm$ 0.1 lb ($\pm$ 0.4 N)
(b) Separation between hot and cold boundary surface plates
(c) Force = specimen weight; Average pressure = 1/2 weight/unit area (assumed)
(d) Force = specimen weight; No gap; Load cell indicated contact with specimen; Average pressure = specimen weight/unit area (assumed)
(e) Measured with a dial gage prior to installation in the FPC

Table 4-7 (Cont'd)

FLAT PLATE CALORIMETER TEST DATA FOR DOUBLE-ALUMINIZED MYLAR/TISSUGLAS

Run No.	Measured Compressive Force (a) lbf	(N)	Equivalent Compressive Pressure psi	(N/m^2)	Measured Thickness (b) in.	(cm)	Boundary Temperatures T_h $^oR(^oK)$	T_c $^oR(^oK)$	Layer Density No./in.	(No./cm)	Measured Heat Flux Btu/hr ft^2	(w/m^2)
Specimen No. II-18, 40 shields/41 spacers, Weight = 0.13 lb (0.059 Kg), Uncompressed thickness = 0.29 in. (0.74 cm)(d)												
1	0.2	(0.9)	1.0×10^{-3}	(6.9)	0.374	(0.950)	500(278)	37(20)	109.6	(43.1)	0.164	(0.517)
1	0.2	(0.9)	1.0×10^{-3}	(6.9)	0.374	(0.950)	610(339)	37(20)	109.6	(43.1)	0.207	(0.652)
2	0.4	(1.8)	2.0×10^{-3}	(13.8)	0.251	(0.638)	610(339)	37(20)	163.3	(64.3)	0.290	(0.914)
2	0.4	(1.8)	2.0×10^{-3}	(13.8)	0.251	(0.638)	500(278)	37(20)	163.3	(64.3)	0.225	(0.709)
3	0.8	(3.6)	4.0×10^{-3}	(27.6)	0.202	(0.513)	500(278)	37(20)	203.0	(79.9)	0.321	(1.01)
3	0.8	(3.6)	4.0×10^{-3}	(27.6)	0.202	(0.513)	610(339)	37(20)	203.0	(79.9)	0.446	(1.41)
4	1.0	(4.4)	5.0×10^{-3}	(34.5)	0.188	(0.478)	610(339)	37(20)	218.1	(85.9)	0.515	(1.62)
4	1.0	(4.4)	5.0×10^{-3}	(34.5)	0.188	(0.478)	500(278)	37(20)	218.1	(85.9)	0.385	(1.21)
5	2.4	(10.7)	1.2×10^{-2}	(82.7)	0.165	(0.419)	500(278)	37(20)	248.5	(97.8)	0.629	(1.98)
5	2.4	(10.7)	1.2×10^{-2}	(82.7)	0.165	(0.419)	610(339)	37(20)	248.5	(97.8)	0.898	(2.83)
6	5.0	(22.2)	2.5×10^{-2}	(172)	0.149	(0.378)	610(339)	37(20)	275.2	(108)	1.24	(3.91)
6	5.0	(22.2)	2.5×10^{-2}	(172)	0.149	(0.378)	500(278)	37(20)	275.2	(108)	0.892	(2.81)
Specimen No. II-19, 10 shields/11 spacers, Weight = 0.034 lb (0.015 Kg), Uncompressed thickness = 0.08 in. (0.20 cm)(d)												
1	0.1	(0.4)	7.0×10^{-4}	(4.8)	0.082	(0.208)	500(278)	140(77)	134.1	(52.8)	0.448	(1.41)
1	0.1	(0.4)	7.0×10^{-4}	(4.8)	0.082	(0.208)	610(339)	140(77)	134.1	(52.8)	0.640	(2.02)
2	0.3	(1.3)	1.5×10^{-3}	(10.3)	0.069	(0.175)	610(339)	140(77)	159.4	(62.8)	0.945	(2.98)
2	0.3	(1.3)	1.5×10^{-3}	(10.3)	0.069	(0.175)	500(278)	140(77)	159.4	(62.8)	0.695	(2.19)
3	1.8	(8.0)	9.0×10^{-3}	(62.1)	0.059	(0.150)	500(278)	140(77)	186.4	(73.4)	1.89	(5.96)
3	1.8	(8.0)	9.0×10^{-3}	(62.1)	0.059	(0.150)	610(339)	140(77)	186.4	(73.4)	2.86	(9.01)
4	14.0	(62.3)	7.0×10^{-2}	(483)	0.049	(0.124)	610(339)	140(77)	224.5	(88.4)	8.98	(28.3)
4	14.0	(62.3)	7.0×10^{-2}	(483)	0.049	(0.124)	500(278)	140(77)	224.5	(88.4)	6.26	(19.7)
5	0.8	(3.6)	4.0×10^{-3}	(27.6)	0.062	(0.157)	500(278)	140(77)	177.4	(69.8)	1.10	(3.47)
5	0.8	(3.6)	4.0×10^{-3}	(27.6)	0.062	(0.157)	610(339)	140(77)	177.4	(69.8)	1.63	(5.14)
6	0.2	(0.9)	1.1×10^{-3}	(7.6)	0.071	(0.180)	610(339)	140(77)	154.9	(61.0)	0.837	(2.64)
6	0.2	(0.9)	1.1×10^{-3}	(7.6)	0.071	(0.180)	500(278)	140(77)	154.9	(61.0)	0.543	(1.71)
Specimen No. II-20, 10 shields/11 spacers, Weight = 0.034 lb (0.015 Kg), Uncompressed thickness = 0.11 in. (0.28 cm)(d)												
1	0.034(c)	(0.15)	1.7×10^{-4}(c)	(1.2)	0.117	(0.297)	500(278)	37(20)	94.0	(37.0)	0.305	(0.961)
1	0.034(c)	(0.15)	1.7×10^{-4}(c)	(1.2)	0.117	(0.297)	610(339)	37(20)	94.0	(37.0)	0.465	(1.47)
2	0.1	(0.4)	3.3×10^{-4}	(2.3)	0.096	(0.244)	610(339)	37(20)	114.6	(45.1)	0.516	(1.63)
2	0.1	(0.4)	3.3×10^{-4}	(2.3)	0.096	(0.244)	500(278)	37(20)	114.6	(45.1)	0.322	(1.01)
3	0.2	(0.9)	1.1×10^{-3}	(7.6)	0.078	(0.198)	500(278)	37(20)	141.0	(55.5)	0.582	(1.83)
3	0.2	(0.9)	1.1×10^{-3}	(7.6)	0.078	(0.198)	610(339)	37(20)	141.0	(55.5)	0.885	(2.79)
4	0.5	(2.2)	2.6×10^{-3}	(17.9)	0.066	(0.168)	610(339)	37(20)	166.7	(65.6)	1.522	(4.80)
4	0.5	(2.2)	2.6×10^{-3}	(17.9)	0.066	(0.168)	500(278)	37(20)	166.7	(65.6)	0.903	(2.85)
5	1.5	(6.7)	7.6×10^{-3}	(52.4)	0.059	(0.150)	500(278)	37(20)	186.4	(73.4)	1.77	(5.58)
5	1.5	(6.7)	7.6×10^{-3}	(52.4)	0.059	(0.150)	610(339)	37(20)	186.4	(73.4)	2.85	(8.98)
6	15.0	(66.7)	7.5×10^{-2}	(517)	0.049	(0.124)	610(339)	37(20)	224.5	(88.4)	9.41	(29.7)
6	15.0	(66.7)	7.5×10^{-2}	(517)	0.049	(0.124)	500(278)	37(20)	224.5	(88.4)	6.02	(19.0)
7	0.5	(2.2)	2.6×10^{-3}	(17.9)	0.065	(0.165)	500(278)	37(20)	169.2	(66.6)	0.838	(2.64)
7	0.5	(2.2)	2.6×10^{-3}	(17.9)	0.065	(0.165)	610(339)	37(20)	169.2	(66.6)	1.263	(3.98)
8	0.2	(0.9)	1.1×10^{-3}	(7.6)	0.077	(0.196)	610(339)	37(20)	142.9	(56.3)	0.702	(2.21)
8	0.2	(0.9)	1.1×10^{-3}	(7.6)	0.077	(0.196)	500(278)	37(20)	142.9	(56.3)	0.445	(1.40)

NOTES:
(a) Force measurement accuracy $\pm$ 0.1 lb ($\pm$ 0.4 N)
(b) Separation between hot and cold boundary surface plates
(c) Force = specimen weight; No gap; Load cell indicated contact with sepecimen; Average pressure = specimen weight/unit area (assumed)
(d) Measured with a dial gage prior to installation in the FPC

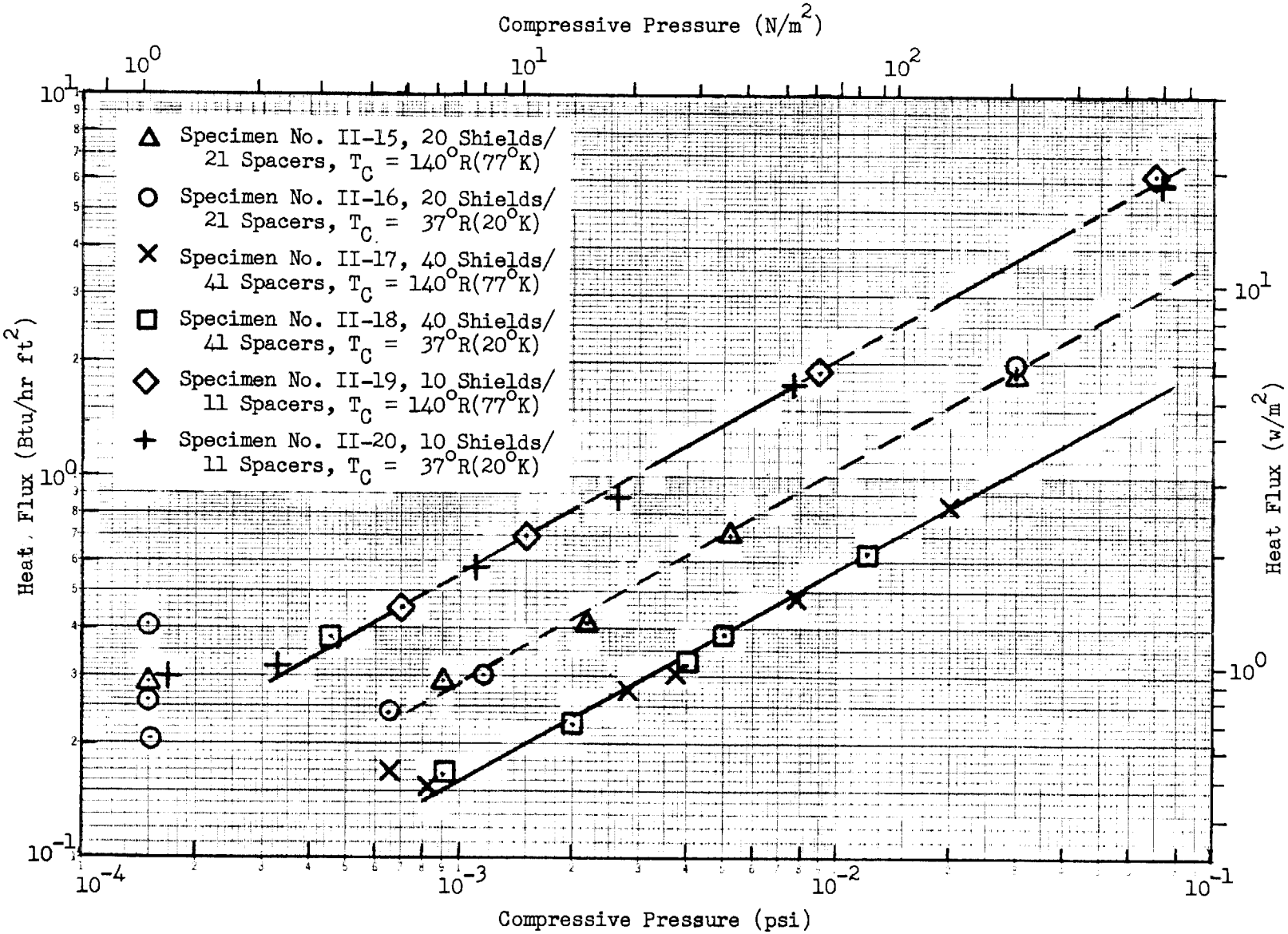

Fig. 4-26 Heat Flux as a Function of Compressive Pressure for Double-Aluminized Mylar/Tissuglas with $T_H = 500^\circ R(278^\circ K)$

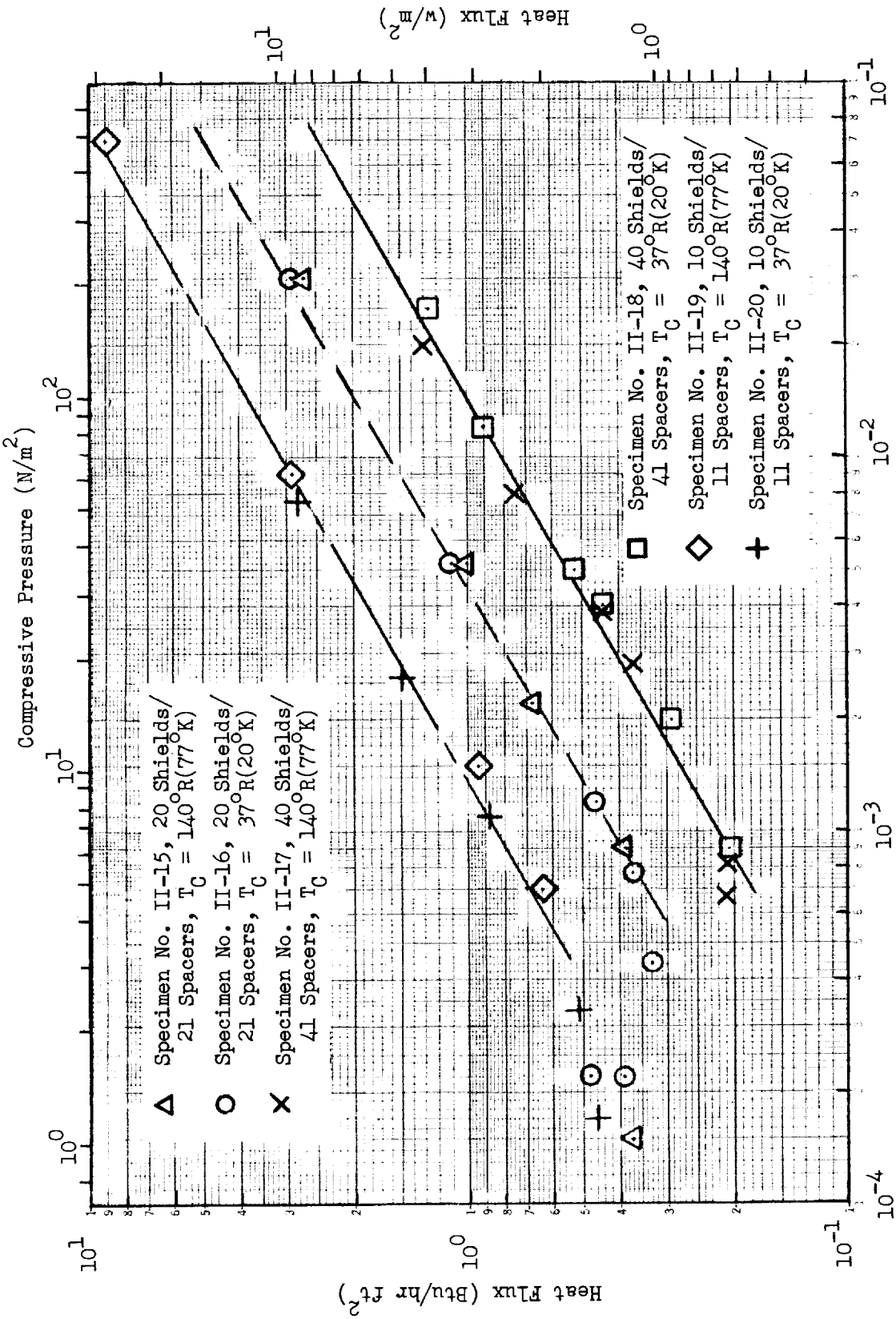

Fig. 4-27 Heat Flux as a Function of Compressive Pressure for Double-Aluminized Mylar/Tissuglas with a T_H = 610°R(339°K)

Ratios of measured heat flux values for the 10-, 20-, and 40-shield specimens at constant values of compressive pressure and for the same boundary temperatures are in excellent agreement with calculated values based on the inverse ratio of the number of layers. For example, at a compressive pressure of 1×10^{-3} psi (6.9 N/m^2) for a 500°R (278°K) hot boundary temperature, the ratio of the measured heat flux for the 10-shield specimens to that for the 40-shield specimens is 3.49. The inverse ratio of the number of layers for these specimens is 3.73 which is approximately 7 percent greater than the ratio of the measured heat flux values. At a compressive pressure of 1×10^{-2} psi (69 N/m^2) for a 610°R (339°K) hot boundary temperature, the ratio of measured heat flux values is 3.88 compared to the calculated ratio of 3.73 for the same specimens. In this case the calculated ratio is approximately 4 percent less than the measured value ratio.

The effect of hot and cold boundary temperatures on heat flux for the double-aluminized Mylar/Tissuglas system is in good agreement with that predicted from the analytical model only at high values of compressive pressure. For example, at a compressive pressure of 1×10^{-2} psi (69 N/m^2) for 10-shield specimens, the ratio of the measured heat flux value for a 610°R (339°K) hot boundary compared to that for a 500°R (278°K) hot boundary is 1.55. The ratio of the product of mean temperature and temperature difference, which is used to predict the solid conduction heat flux component, ranges from 1.49 to 1.53 for these two hot boundary temperatures depending upon the cold boundary temperature selected. The ratio of the expression $T_H^{4.67} - T_C^{4.67}$, which is used in the prediction of the radiation heat flux components, is 2.53 for the same two hot boundary temperatures. It can be seen by comparing the ratios of measured and predicted heat flux components given above that solid conduction is the dominant heat transfer mechanism for this particular case as would be expected. However, at a compressive pressure of 1×10^{-3} psi (6.9 N/m^2) for the 10-shield specimens, the ratio of the measured heat flux values for 610°R (339°K) and 500°R (278°K) hot boundary temperatures, respectively, is 1.52. Since this ratio is less than the 1.55 ratio obtained at a compressive pressure of 1×10^{-2} psi (69 N/m^2), it appears that the

solid conduction component becomes more dominant with decreasing compressive pressure. This characteristic is contrary to that predicted by the analytical model and observed for the other multilayer systems investigated where the proportion of the total heat flux contributed by the solid conduction mechanism increases with increasing compressive pressure. It might have been due to an interaction between the conduction and radiation mechanisms, but this could not be verified conclusively from the data obtained.

Figs. 4-28 and 4-29 show the data for heat flux as a function of layer density for the 10-, 20-, and 40-shield specimens for 500°R(278°K) and 610°R (339°K) hot boundary temperatures, respectively. These data show a reproducibility within approximately $\pm$ 15 percent for the specimens with the same number of layers. Ratios of the data at constant values of layer density are in good general agreement with the inverse ratio of the number of layers (i.e., within $\pm$ 20 percent) for the 20- and 40-shield specimens throughout the range of layer density values investigated. For example, at a layer density value of 125 layers/in. (49.2 layers/cm) and for a hot boundary temperature of 610°R (339°K), the ratio of the heat flux for the 20-shield specimen compared to that for the 40-shield specimen is 1.74, whereas the inverse ratio of the number of layers is 1.95. At a layer density value of 225 layers/in. (88.6 layers/cm) for the same hot boundary temperature, the corresponding ratio of the experimental heat flux values is 2.33.

The same general agreement was observed for the 10-shield specimens compared to either the 20- or 40-shield specimens at layer density values below approximately 150 layers/in. (59.1 layers/cm). However, at layer density values above 150 layers/in. (59.1 layers/cm), the heat flux values for the 10-shield specimens are from two to four times greater than those corresponding to the inverse ratio of the number of layers. At a layer density value of 225 layers/in. (88.6 layers/cm) for the 610°R (339°K) hot boundary temperature, for example, the ratio of the heat flux value for the 10-shield specimen compared to that for the 40-shield specimen is 14.75. For these same specimens, the inverse ratio of the number of layers is only 3.73. This characteristic is indicative

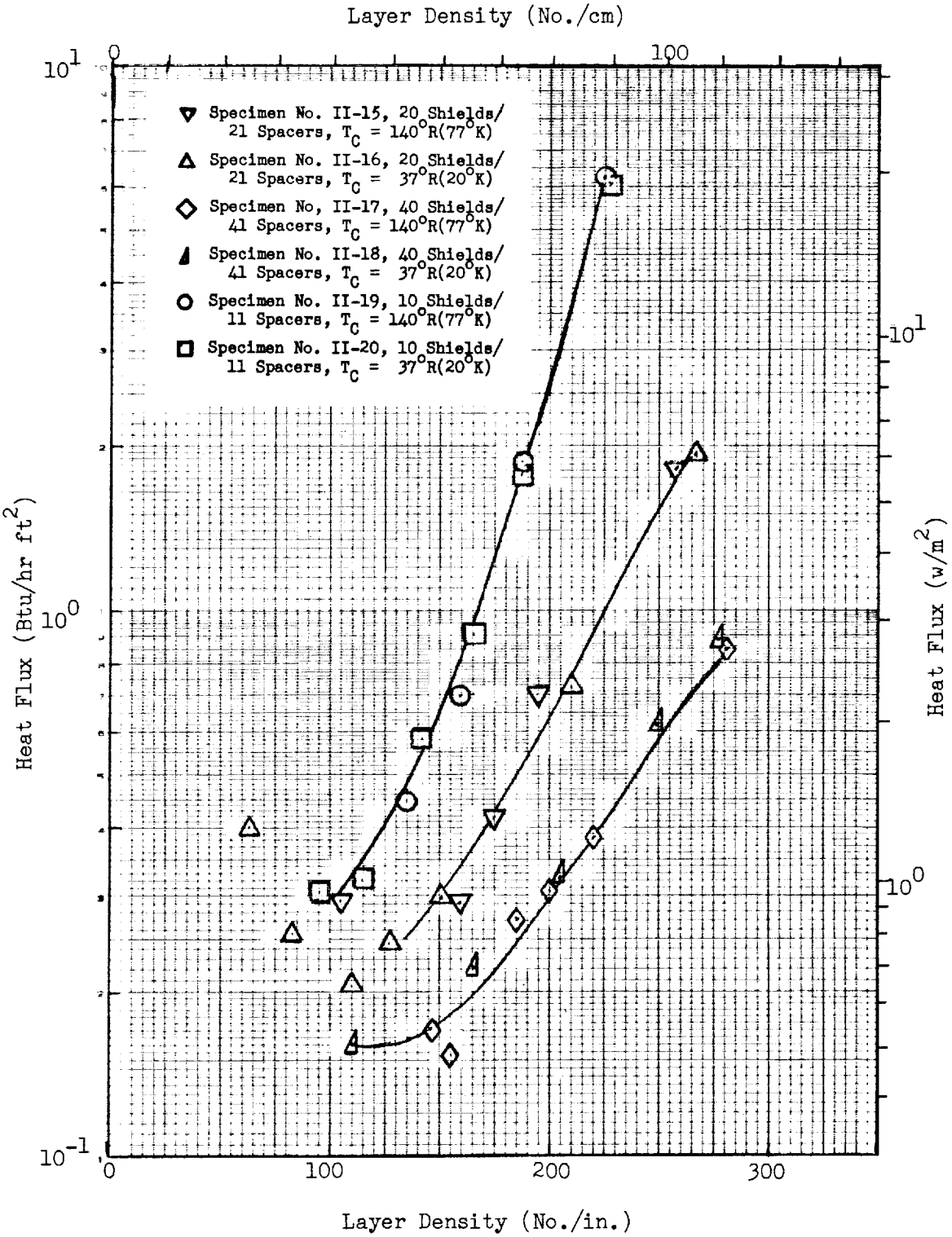

Fig. 4-28 Heat Flux as a Function of Layer Density for Double-Aluminized Mylar/Tissuglas with T_H=500°R(278°K)

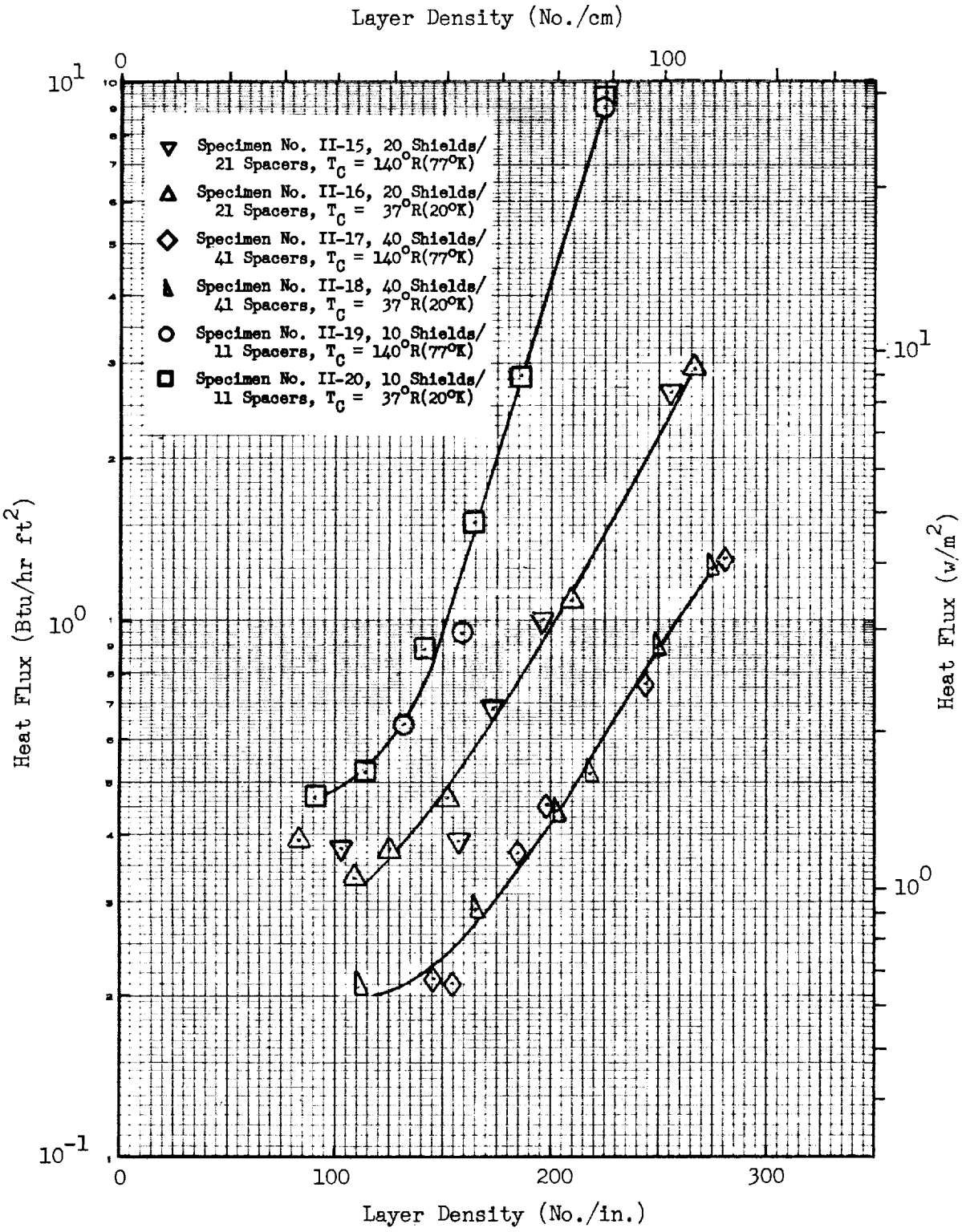

Fig. 4-29 Heat Flux as a Function of Layer Density for Double-Aluminized Mylar/Tissuglas with T_H = 610°R(339°K)

of the relationship of compressive pressure with layer density for the 10-, 20-, and 40-shield specimens. Figs. 4-30 and 4-31 illustrate this relationship for specimens tested at 140°R (77°K) and 37°R (20°K) cold boundary temperatures, respectively. At constant layer density values, the compressive pressure for the 10-shield specimens ranges from two to ten times greater than that for the 20- and 40-shield specimens.

Analysis and evaluation of the data obtained for the double-aluminized Mylar/Tissuglas composite were accomplished using Eq. (4.11). Radiation heat flux components were computed for each data point using an average room temperature emittance value of 0.0285 and a temperature dependency exponent value of 0.67 obtained from measurements of emittance and normal reflectance for six double-aluminized Mylar specimens taken from the flat plate calorimeter test specimens. The average room temperature emittance for each of the six specimens is presented in Table 4-8. A refractive index value, n, of 1.14 (Ref. 12) was used in the computation of the radiation heat flux components.

Solid conduction heat flux components were computed as the difference between the total heat flux based on boiloff measurements and the computed radiation components, i.e., the same technique used for each of the other multilayer systems investigated. The conduction parameter, Φ, normalized for boundary temperatures and number of layers, is shown as a function of compressive pressure in Fig. 4-32. The equation obtained from a least-squares fit of these data is illustrated by the solid line in the figure, and $\pm$ 15 percent deviations are shown by the broken lines. For values of compressive pressure above 1×10^{-3} psi (6.9 N/m^2), the data generally fit within the $\pm$ 15 percent band.

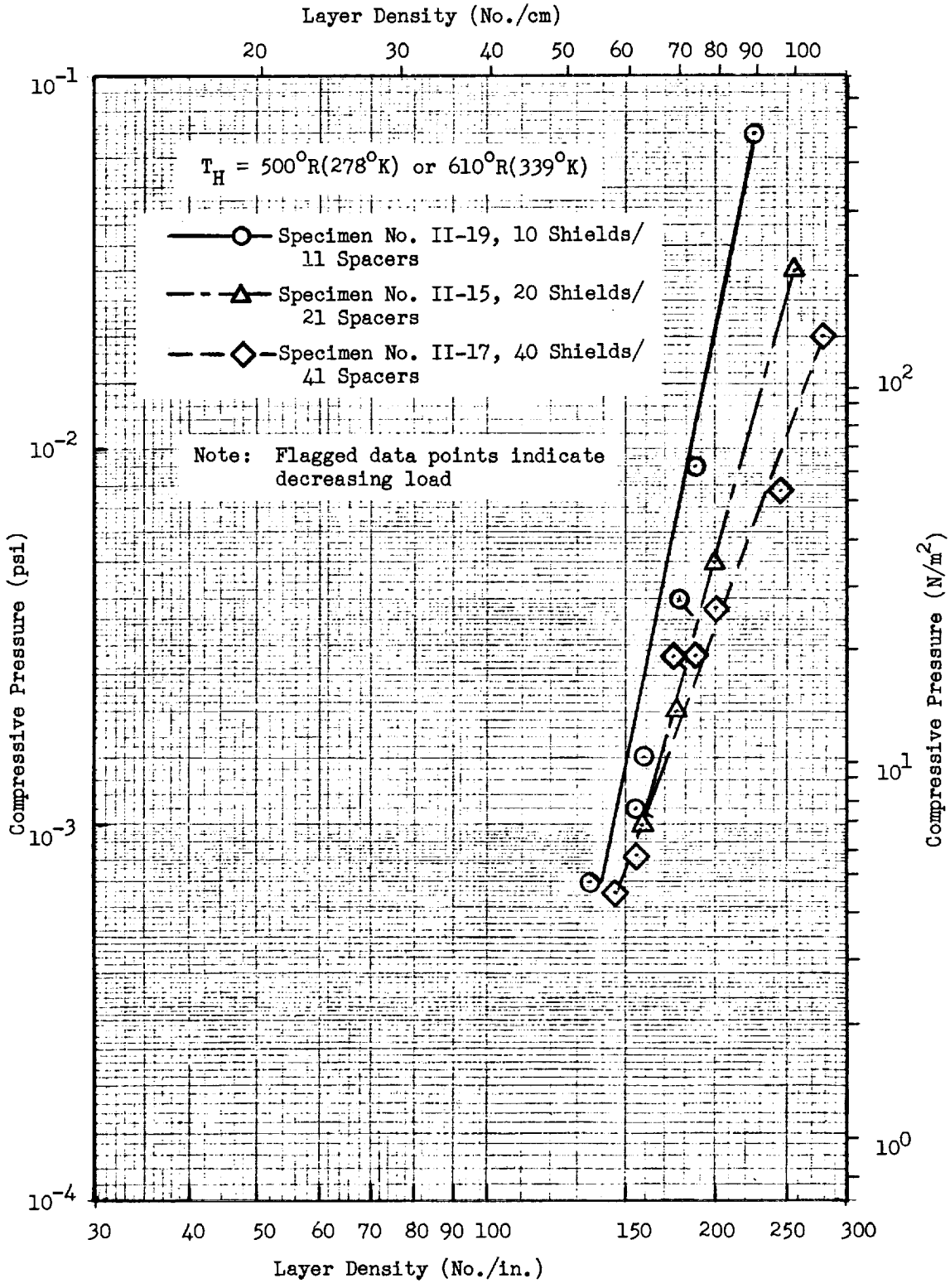

Fig. 4-30 Compressive Pressure as a Function of Layer Density for Double-Aluminized Mylar/Tissuglas with T_C = 140°R (77°K)

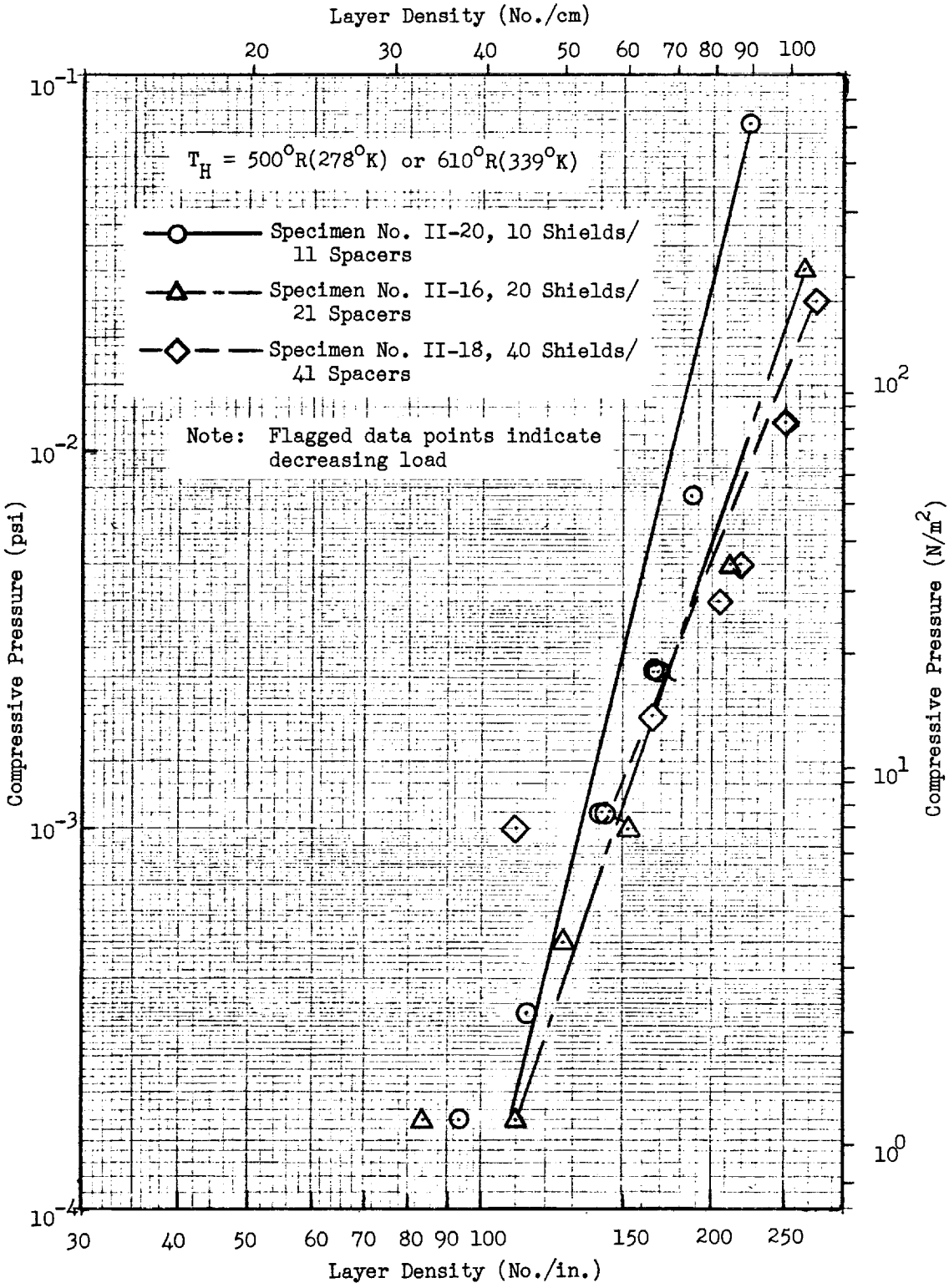

Fig. 4-31 Compressive Pressure as a Function of Layer Density for Double-Aluminized Mylar/Tissuglas with T_C = 37°R(20°K)

Table 4-8

EMITTANCE VALUES FOR DOUBLE-ALUMINIZED MYLAR/TISSUGLAS

Specimen No.	Average ϵ_{TH} @ 540°R (300°K)*
II-15	$0.029 \pm .002$
II-16	$0.029 \pm .003$
II-17	$0.029 \pm \begin{matrix} .003 \\ .004 \end{matrix}$
II-18	$0.028 \pm .004$
II-19	$0.027 \pm .002$
II-20	$0.028 \pm \begin{matrix} .002 \\ .003 \end{matrix}$

* Based upon ρ_N measurements for all shields and ϵ_{TH} for a single shield, where $\epsilon_{TH} = 1.33\ \epsilon_{TN}$ (Ref. 5), and $\epsilon_{TN} = 1-\rho_N$

Evaluation of Eq. (4.11) for this multilayer system yields

$$q = \frac{2.74\text{x}10^{-3}(P-P_o)^{0.633}T_m}{N_s + 1}(T_H-T_C) + \frac{1.63\text{x}10^{-11}\epsilon_{TR}}{N_s}\left(T_H^{4.67}-T_C^{4.67}\right) \qquad (4.29)$$

where ϵ_{TR} is the total hemispherical emittance of the shields at 540°R (300°K).

When compressive pressure is evaluated as a function of layer density for this multilayer system, Eq. (4.29) becomes

$$q = \frac{1.13\text{x}10^{-13}(\bar{N})^{3.91}T_m}{N_s + 1}(T_H-T_C) + \frac{1.63\text{x}10^{-11}\epsilon_{TR}}{N_s}\left(T_H^{4.67}-T_C^{4.67}\right) \qquad (4.30)$$

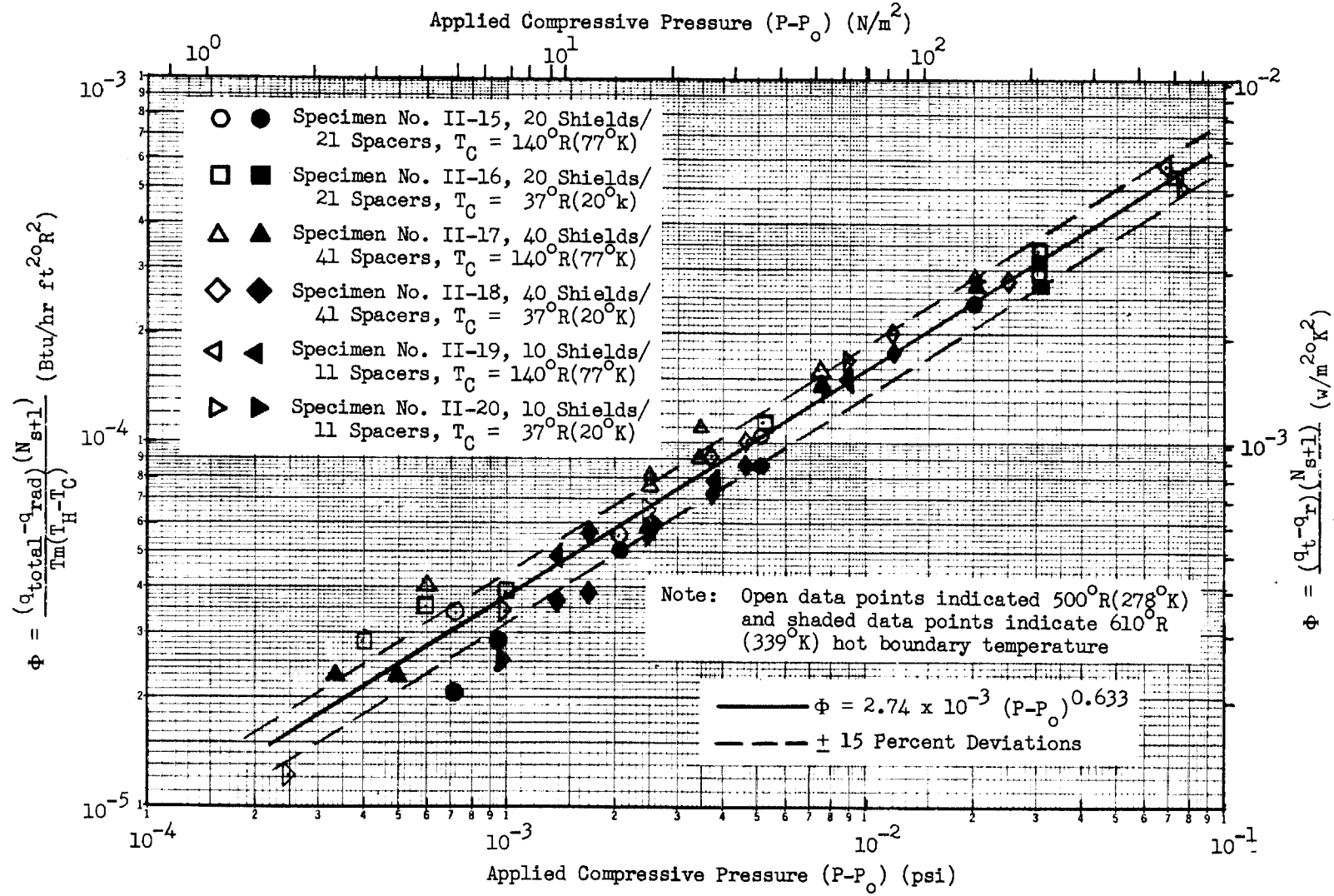

Fig. 4-32 Normalized Solid Conduction Heat Flux as a Function of Applied Compressive Pressure for Double-Aluminized Mylar/Tissuglas

4.4 INSULATION PERFORMANCE PREDICTIONS

A major objective of this program was to develop an analytical technique for using flat plate calorimeter heat transfer data to predict the thermal performance of a tank-installed multilayer insulation system. Such a technique was developed in Task II for the double-goldized Mylar/silk net system. The resulting equations and data correlations are presented and discussed in this section. Results of additional boiloff tests which were subsequently conducted in Task III to verify predicted thermal performance of the system as installed on a 4 -ft-(1.22-m-) diameter tank calorimeter will be presented in the final report.

The double-goldized Mylar/silk net insulation system was selected for development of the prediction technique and for the Task III tank tests primarily because the flat plate calorimeter test data obtained for this system exhibited good reproductibility characteristics and correlated well with the analytical model. In addition, it was found that Mylar shields and silk net spacers could be fit readily and applied to the compound curved surfaces of the tank calorimeter without introducing significant joint or seam discontinuities.

Using the same technique developed for the double-goldized Mylar/silk net composite, similar equations were developed for the other multilayer systems investigated using the flat plate calorimeter data available (Ref. Section 4.1.3). However, the predictability range of each of the other systems were not verified by independent tests such as those performed for the double-goldized Mylar/silk net system using the tank calorimeter.

The analytical expression derived from the data obtained in Task II for six specimens of the double-goldized Mylar/silk net system, Eq. (4.23), is

$$q = \frac{5.84\times10^{-4}(P-P_o)^{0.422}T_m}{N_s+1}(T_H-T_C)+\frac{3.426\times10^{-9}\epsilon_{TR}}{(4+\alpha_4)(540)^{\alpha_4}N_s}\left(T_H^{4+\alpha_4}-T_C^{4+\alpha_4}\right)$$

Using the average value of room temperature total hemispherical emittance for all of the specimens tested, $\epsilon_{TR} = 0.0215$, and the corresponding temperature dependency exponent, $\alpha_4 = 0.51$, the above equation reduces to

$$q = \frac{5.84\text{x}10^{-4}(P-P_o)^{0.422}T_m}{N_s + 1}(T_H-T_C) + \frac{6.70\text{x}10^{-13}}{N_s}\left(T_H^{4.51}-T_C^{4.51}\right) \qquad (4.31)$$

This form of the equation is used to predict thermal performance for typical installations of the double-goldized Mylar/silk net system where the ϵ_{TR} and α_4 values for the actual shields are not readily available.

In order for the prediction equation to be of practical use for tank-installed insulation systems, it is necessary to convert the conduction term to a function of layer density. The "as installed" layer density can be determined from local measurements of insulation thickness at one or more points over the tank surface. The prediction equation can be modified by substituting an expression for compressive pressure, $P-P_o$, as a function of layer density, $\bar{N}$, into the basic expression.

Analysis of the data obtained from the flat plate calorimeter tests for each of the multilayer systems investigated shows that the relationship of compressive pressure with layer density for each can be approximated by

$$(P - P_o) = c(\bar{N})^n$$

The constant coefficient, c, and the constant exponent, n, can be evaluated from a least-squares curve fit of the experimental data for compressive pressure as a function of layer density. Substitution of this relationship into Eq. (4.23) yields

$$q = \frac{5.84\text{x}10^{-4}\left[c(\bar{N})^n\right]^{0.422}T_m}{N_s + 1}(T_H-T_C) + \frac{3.426\text{x}10^{-9}\epsilon_{TR}}{(4+\alpha_4)(540)^{\alpha_4}N_s}\left(T_H^{4+\alpha_4}-T_C^{4+\alpha_4}\right) \qquad (4.32)$$

Eq. (4.32) was evaluated for the double-goldized Mylar/silk net insulation system by performing least-squares curve fits of the data for compressive pressure as a function of layer density (Figs. 4-18 and 4-19). Initially, for the two 20-shield specimens, the constants c and n were evaluated for each specimen individually. The resulting expressions are $(P-P_o) = 2.58\text{x}10^{-17}(\bar{N})^{7.56}$ for Specimen No. II-10 and $(P-P_o) = 1.50\text{x}10^{-13}(\bar{N})^{5.50}$ for Specimen No. II-12. Since the relationships for these two specimens were quite different, Eq. (4.32) was evaluated independently for each. Also, since these particular specimens included shields which exhibited the greatest variations of emittance for any of the double-goldized Mylar shields investigated (Ref. Section 4.2.2), the corresponding values of room temperature emittance and the temperature dependency exponent were used in the evaluations. The resulting equations are

$$q = \frac{5.62\text{x}10^{-11}(\bar{N})^{3.19}T_m}{N_s + 1}(T_H - T_C) + \frac{4.47\text{x}10^{-13}}{N_s}\left(T_H^{4.554} - T_C^{4.554}\right) \qquad (4.33)$$

and

$$q = \frac{2.24\text{x}10^{-9}(\bar{N})^{2.32}T_m}{N_s + 1}(T_H - T_C) + \frac{8.58\text{x}10^{-13}}{N_s}\left(T_H^{4.483} - T_C^{4.483}\right) \qquad (4.34)$$

for Specimen Nos. II-10 and II-12, respectively. For Specimen No. II-10, Eq. (4.33), values of $\epsilon_{TR} = 0.0193$ and $a_4 = 0.554$ were used, whereas for Specimen No. II-12, Eq. (4.34), the values were $\epsilon_{TR} = 0.0235$ and $a_4 = 0.0483$ (Ref. Fig. 4-3).

Using Eqs. (4.33) and (4.34), heat flux was computed as a function of layer density for the boundary temperatures imposed on each specimen in Task II. The results are shown in Figs. 4-33 and 4-34 for Specimen Nos. II-10 and II-12, respectively. As shown, the correlation of the predictions with experimental data is within $\pm$ 20 percent except for a single data point for Specimen No. II-12.

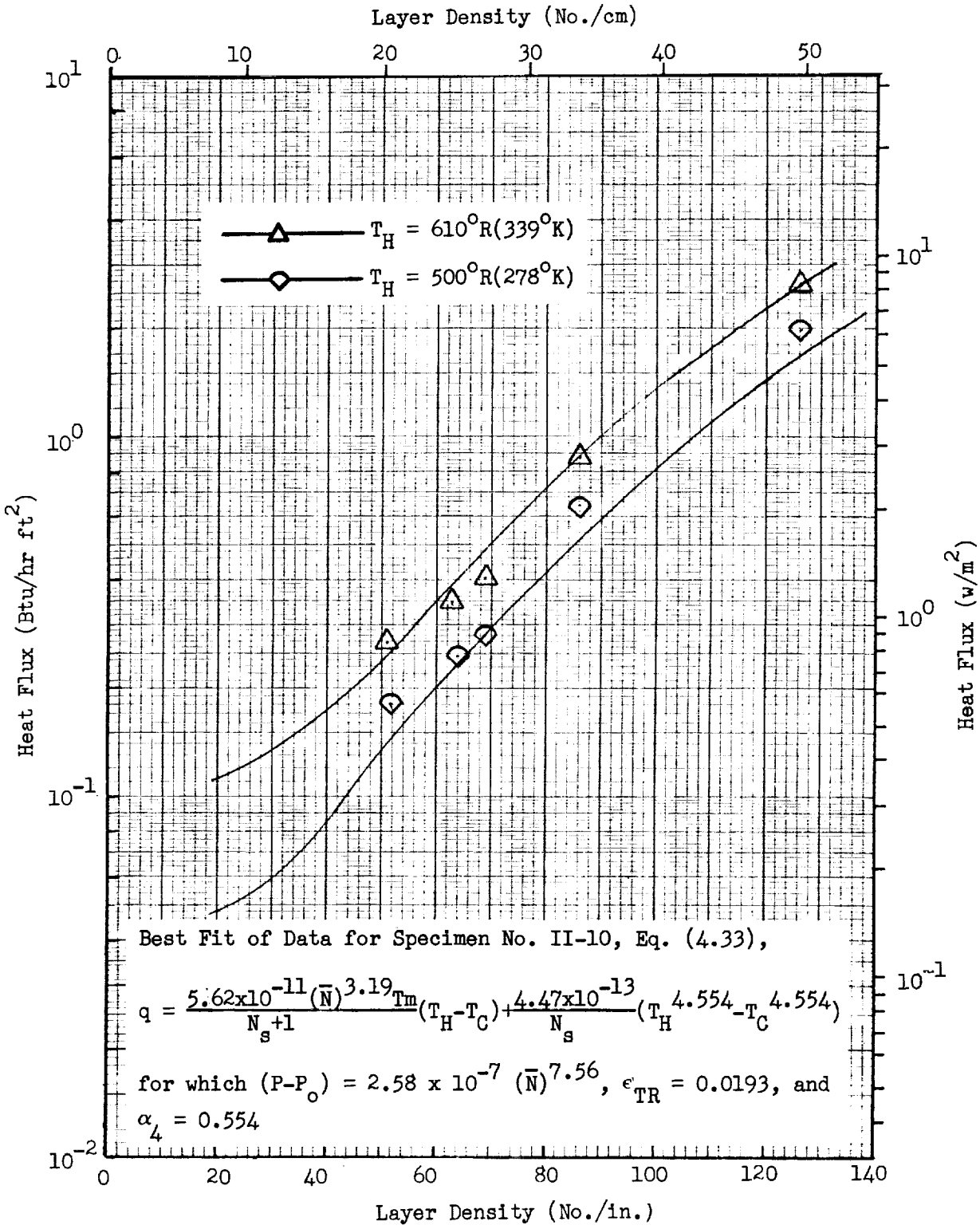

Fig. 4-33 Predicted and Measured Heat Fluxes as a Function of Layer Density for Double-Goldized Mylar/Silk Net with $T_C = 37°R(20°k)$

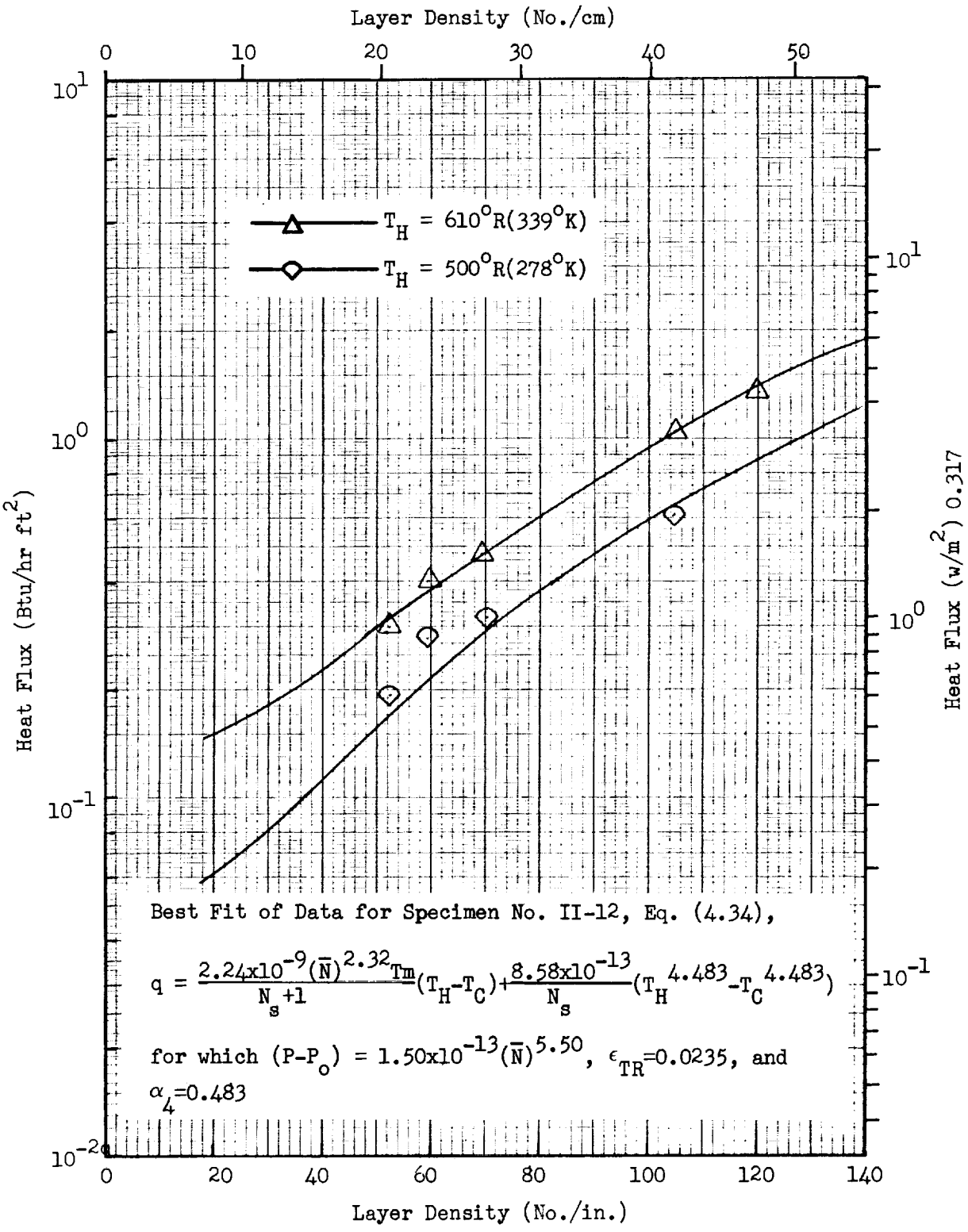

Fig. 4-34 Predicted and Measured Heat Fluxes as a Function of Layer Density for Double-Goldized Mylar/Silk Net with T_C = 140°R(77°K)

Evaluation of compressive pressure as a function of layer density for both 20-shield specimens results in

$$(P-P_o) = 3.17 \times 10^{-15}(\bar{N})^{6.44}$$

Substituting this expression together with the average room temperature emittance value, $\epsilon_{TR} = 0.0215$, and the average temperature dependency exponent, $a_4 = 0.51$, into Eq. (4.32) yields

$$q = \frac{4.35\times10^{-10}(\bar{N})^{2.72}T_m}{N_s + 1}(T_H-T_C) + \frac{6.70\times10^{-13}}{N_s}\left(T_H^{4.51}-T_C^{4.51}\right) \qquad (4.35)$$

The results obtained when Eq. (4.35) was used to compute heat flux for a 20-shield system are presented in Fig. 4-35. For this case, the predicted heat flux correlated with the experimental data points within $\pm$ 25 percent.

Similar computations were performed to obtain the equations for predicting thermal performance of the 10- and 5-shield specimens. These results are presented in Fig. 4-36 for the two 10-shield specimens and in Fig. 4-37 for the two 5-shield specimens. The average room temperature emittance, $\epsilon_{TR} = 0.0215$, and the corresponding temperature dependency exponent, $a_4 = 0.51$, were again used for these computations. The resulting equations are

$$q = \frac{7.92\times10^{-11}(\bar{N})^{3.12}T_m}{N_s + 1}(T_H-T_C) + \frac{6.70\times10^{-13}}{N_s}\left(T_H^{4.51}-T_C^{4.51}\right) \qquad (4.36)$$

and

$$q = \frac{1.42\times10^{-10}(\bar{N})^{2.99}T_m}{N_s + 1}(T_H-T_C) + \frac{6.70\times10^{-13}}{N_s}\left(T_H^{4.51}-T_C^{4.51}\right) \qquad (4.37)$$

for the 10- and 5-shield specimens, respectively.

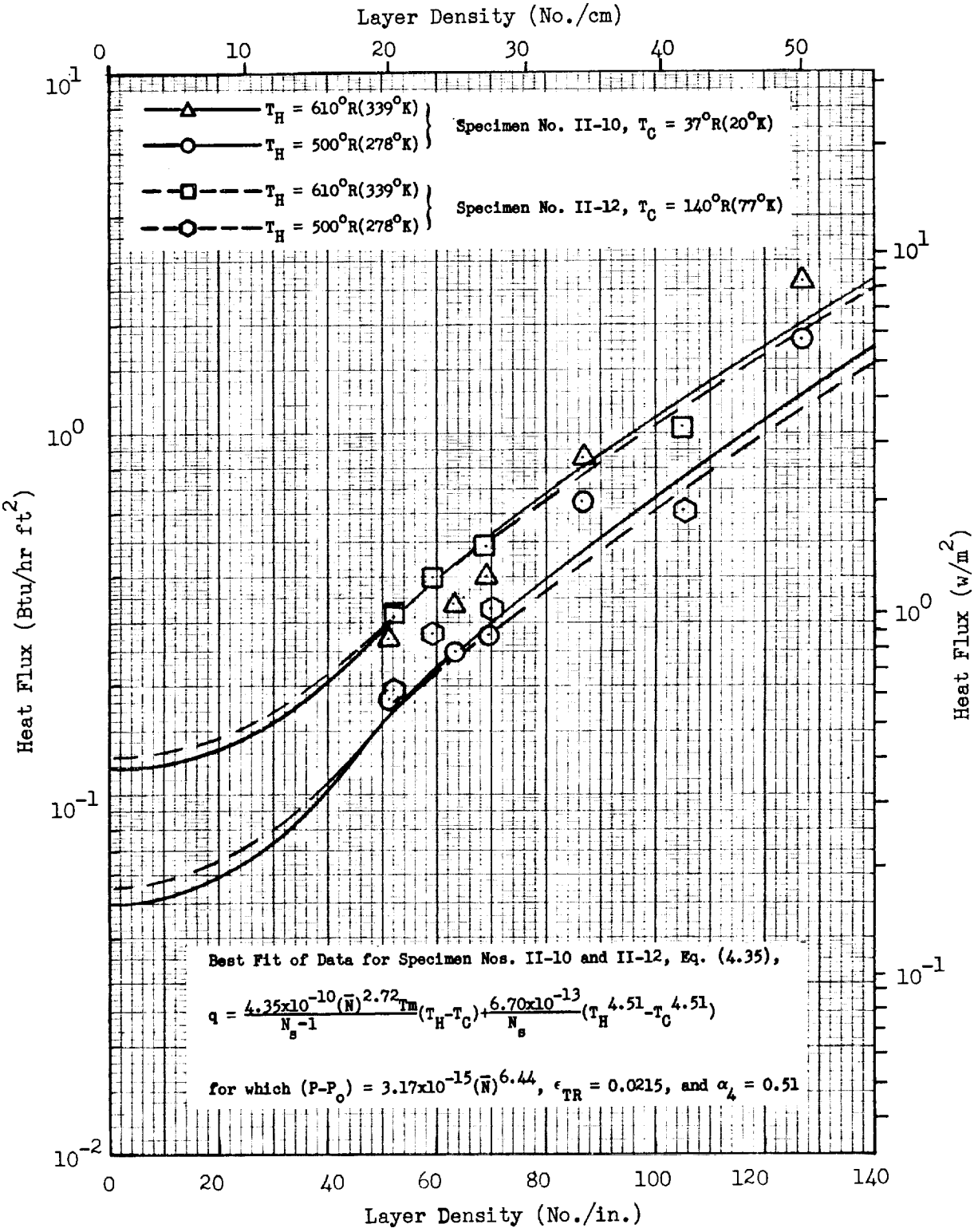

Fig. 4-35 Predicted and Measured Heat Fluxes as a Function of Layer Density for Two 20-Shield Specimens of Double-Goldized Mylar/ Silk Net

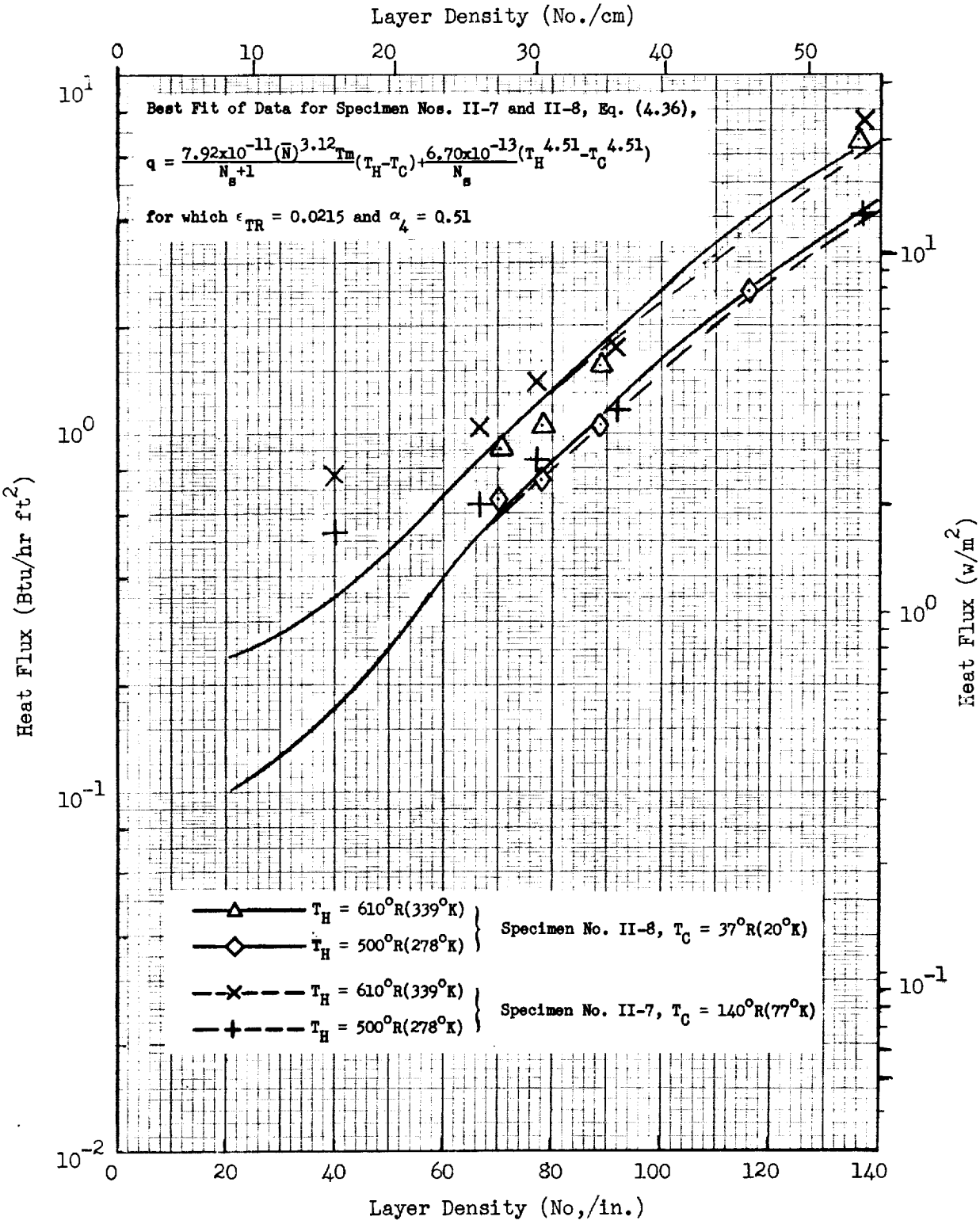

Fig. 4-36 Predicted and Measured Heat Fluxes as a Function of Layer Density for Two 10-Shield Specimens of Double-Goldized Mylar/Silk Net

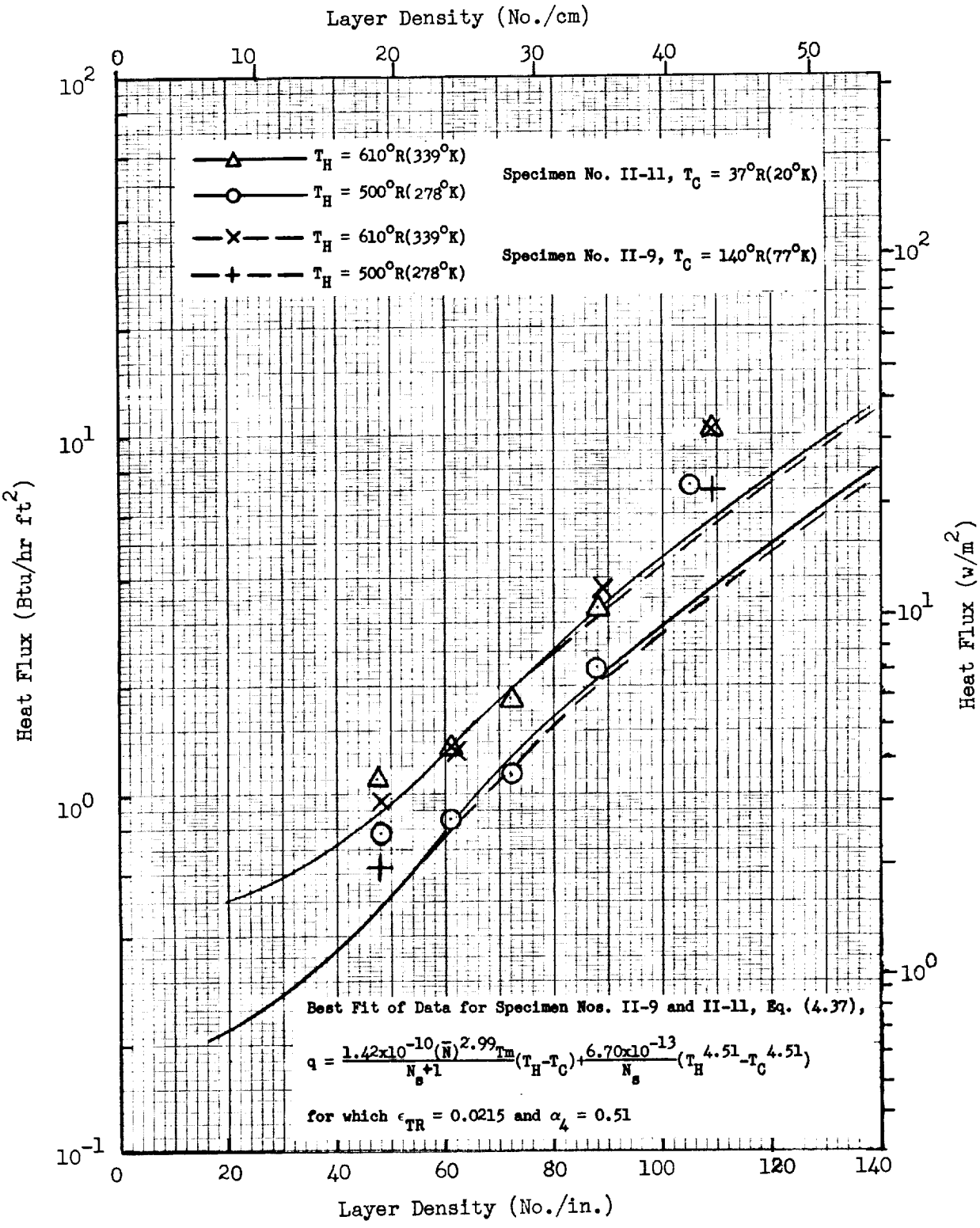

Fig. 4-37 Predicted and Measured Heat Fluxes as a Function of Layer Density for Two 5-Shield Specimens of Double-Goldized Mylar/Silk Net.

Finally, the data for all six double-goldized Mylar/silk net specimens were analyzed in order to evaluate the heat flux equation for a single expression of layer density as a function of compressive pressure. The expression which characterizes all of the data is

$$(P-P_o) = 1.42 \times 10^{-17}(\bar{N})^{7.75}$$

Substitution of this expression together with the average room temperature emittance, $\epsilon_{TR} = 0.0215$, and the corresponding temperature dependency exponent, $a_4 = 0.51$, into Eq. (4.32) yields

$$q = \frac{4.37\times10^{-11}(\bar{N})^{3.27}T_m}{N_s + 1}(T_H-T_C) + \frac{6.70\times10^{-13}}{N_s}\left(T_H^{4.51}-T_C^{4.51}\right) \qquad (4.38)$$

For each of the four boundary temperature combinations investigated in Task II, heat flux was computed as a function of layer density for 5-, 10-, and 20-shield systems using Eq. (4.38). Figs. 4-38 through 4-41 show these results correlated with the experimental data. The correlation is generally poor as was expected since the relationship of compressive pressure with layer density varies significantly for specimens with different numbers of layers.

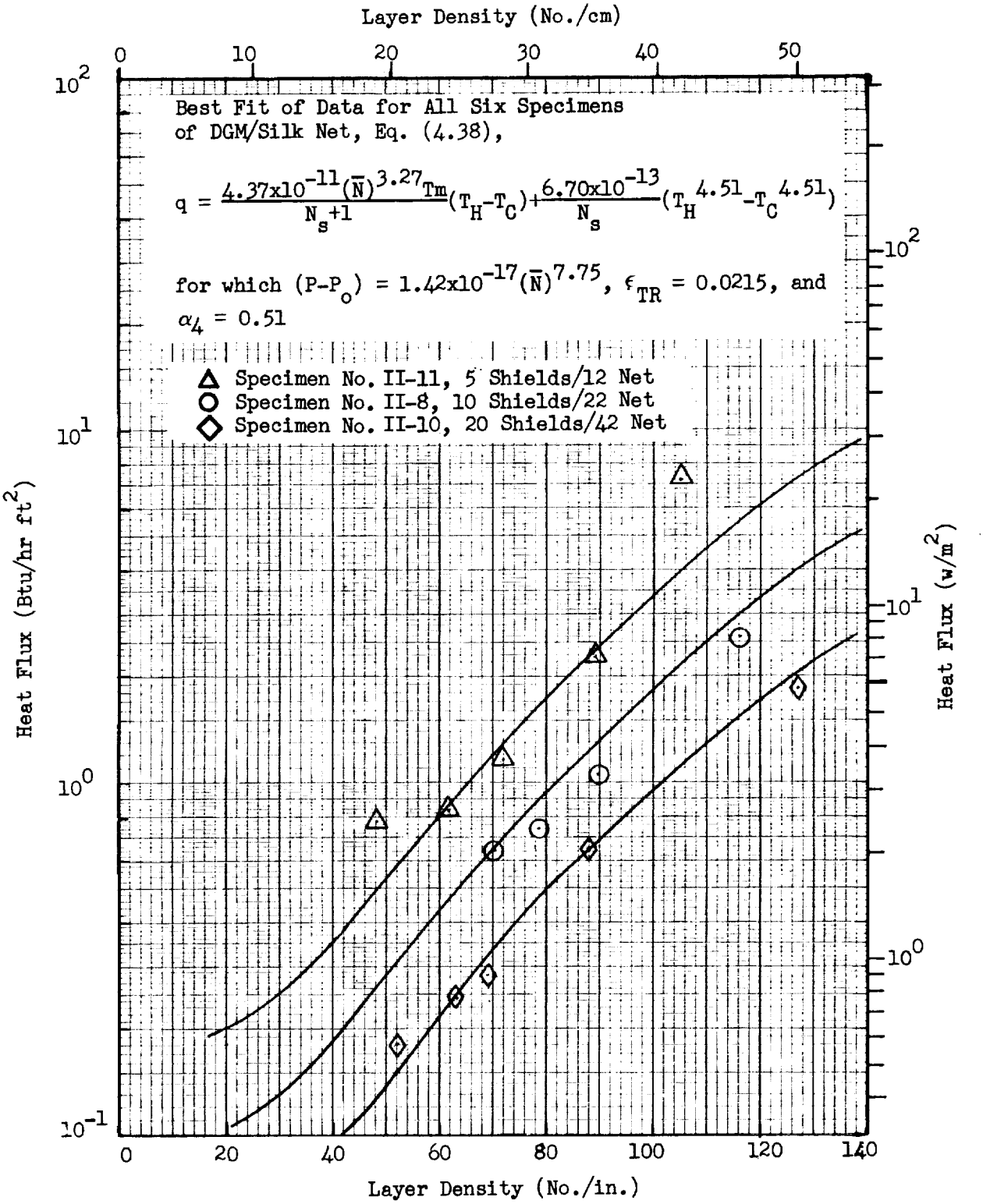

Fig. 4-38 Predicted and Measured Heat Fluxes as a Function of Layer Density for Double-Goldized Mylar/Silk Net with $T_H = 500^\circ R(278^\circ K)$ and $T_C = 37^\circ R(20^\circ K)$

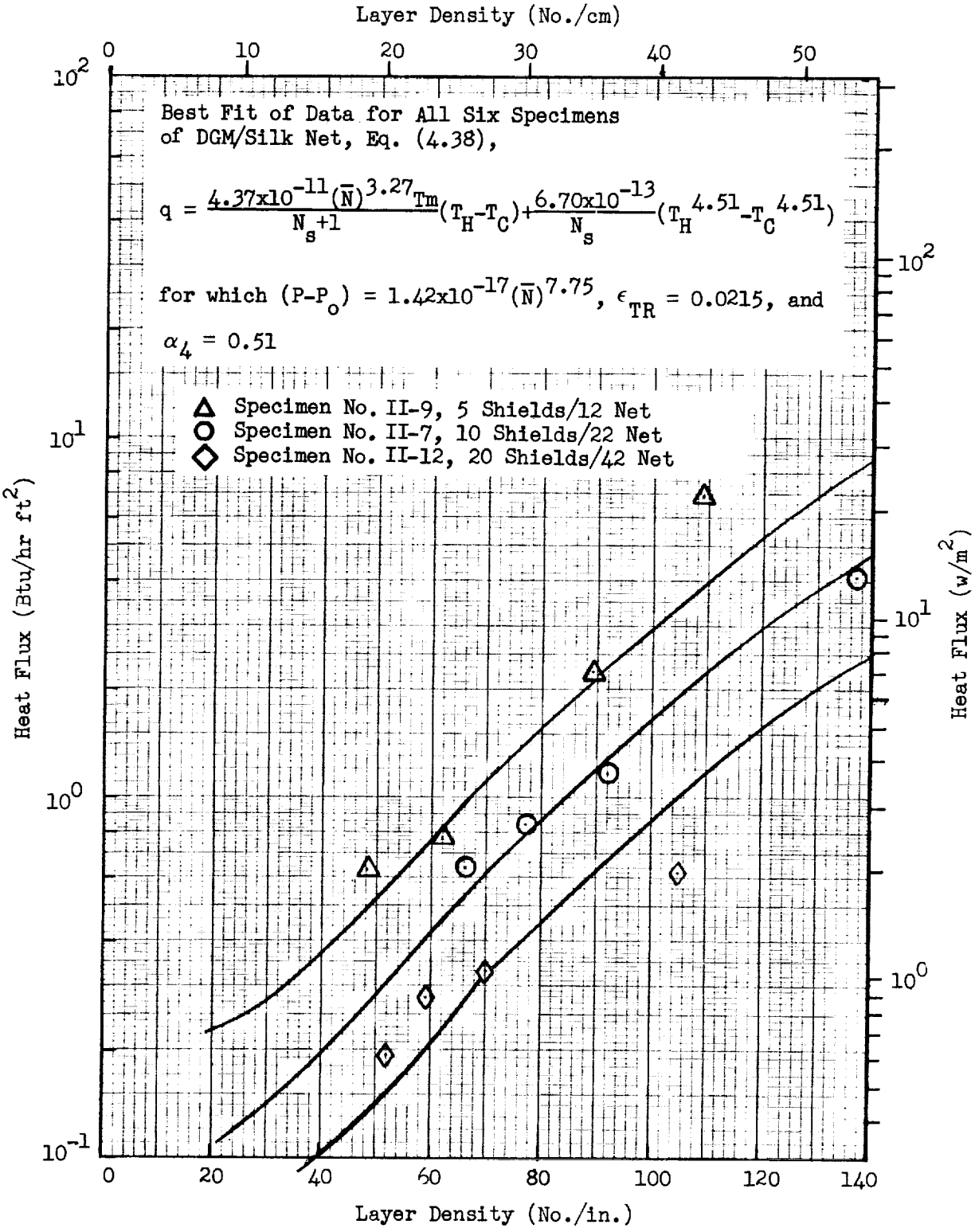

Fig. 4-39 Predicted and Measured Heat Fluxes as a Function of Layer Density for Double-Goldized Mylar/Silk Net with $T_H = 500^oR(278^oK)$ and $T_C = 140^oR(77^oK)$

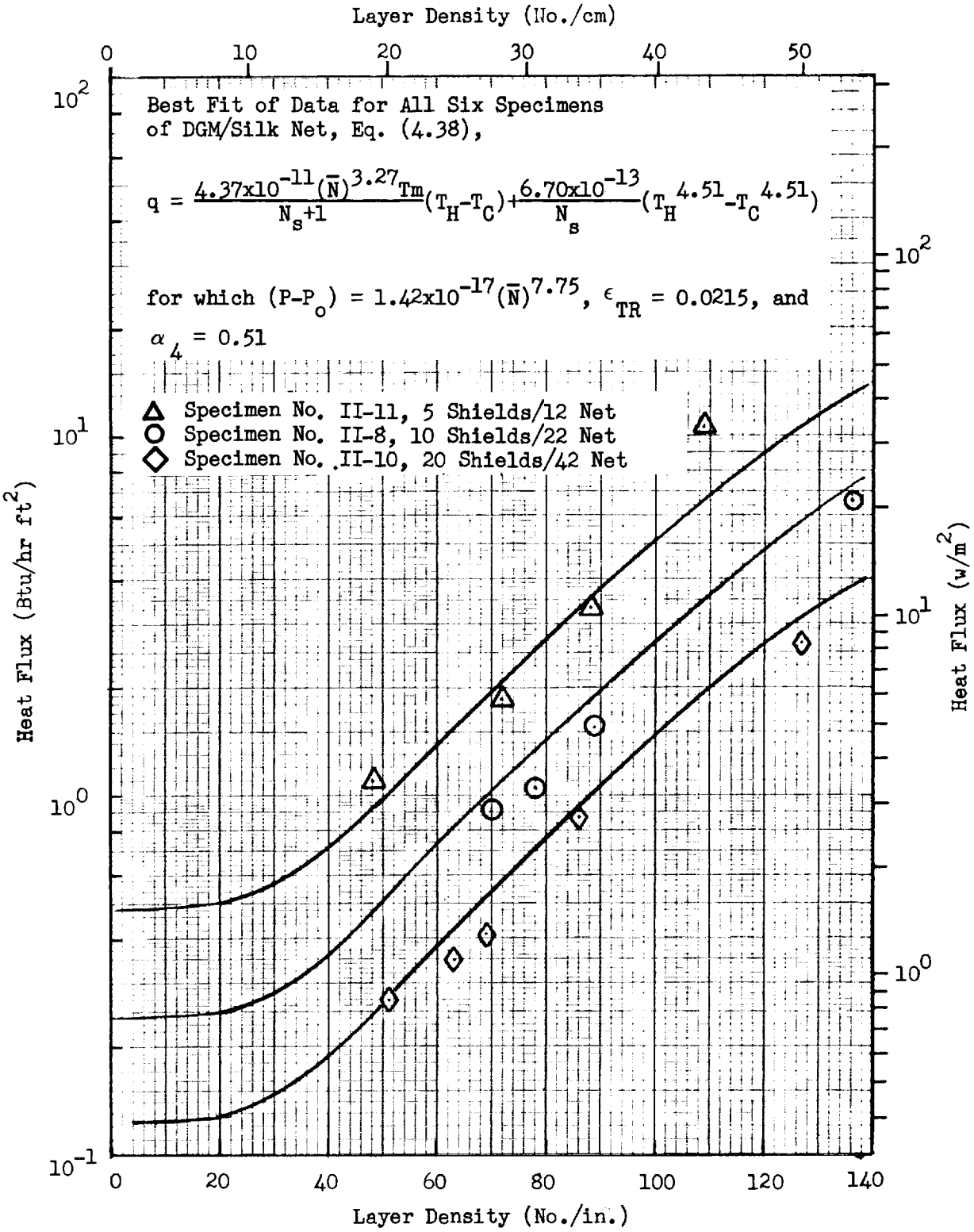

Fig. 4-40 Predicted and Measured Heat Fluxes as a Function of Layer Density for Double-Goldized Mylar/Silk Net with $T_H = 610^oR(339^oK)$ and $T_C = 37^oR(20^oK)$

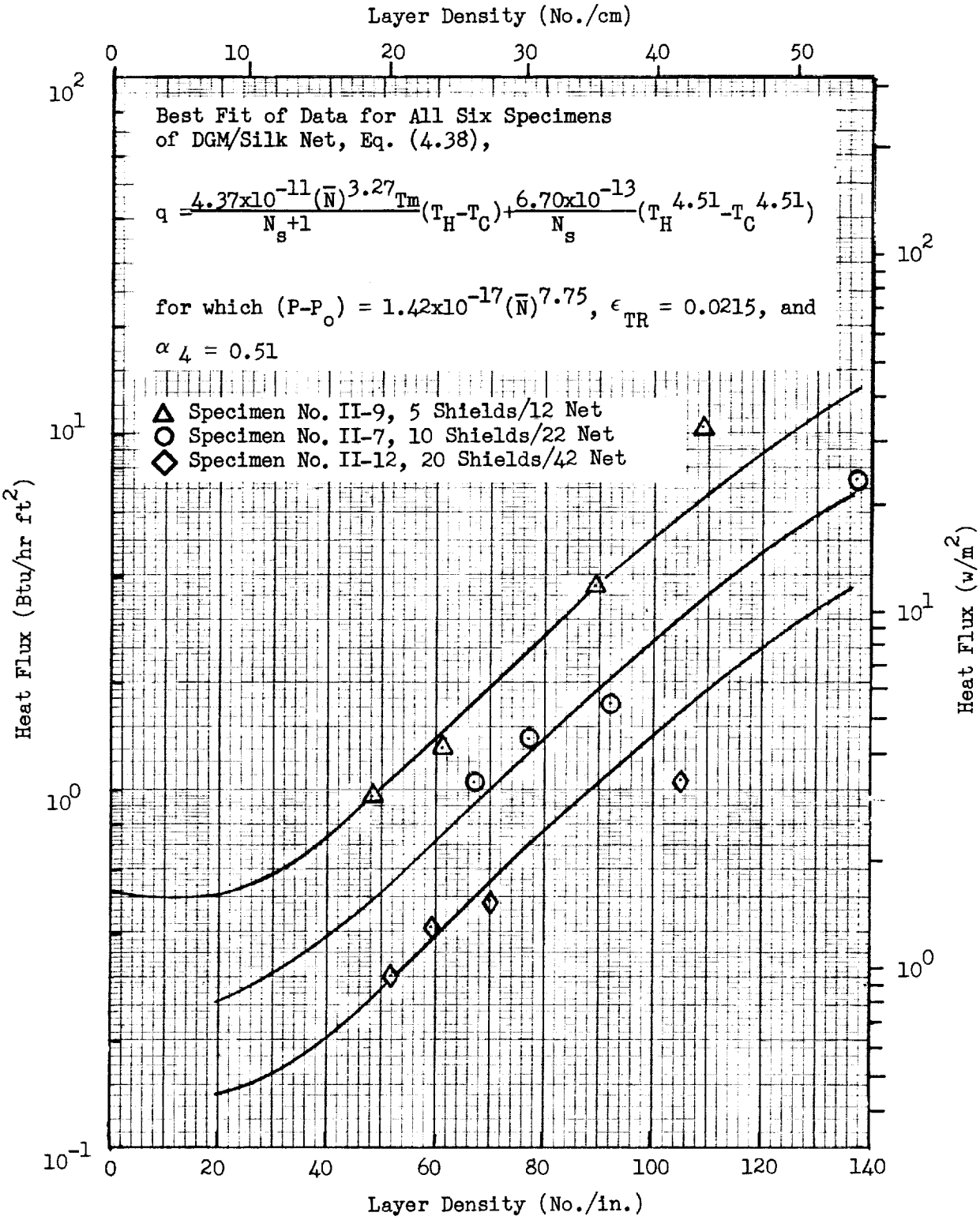

Fig. 4-41 Predicted and Measured Heat Fluxes as a Function of Layer Density for Double-Goldized Mylar/Silk Net with T_H 610°R(339°K) and T_C = 140°K(77°K)

Section 5

DISCUSSION OF RESULTS

All of the Task I and Task II program objectives described in previous sections of this report were achieved. Initially in Task I, the absolute accuracies of experimental data obtained from Flat Plate Calorimeter (FPC) measurements were determined. These data include heat rate based on measured cryogen boiloff, compressive pressure based on measured compressive load, layer density based on measured specimen thickness, and measured boundary temperatures. Subsequent to the determination of experimental accuracies, the basic repeatability of heat rate measurements obtained from the FPC also was determined from a series of tests performed on a single specimen of double-aluminized Mylar/silk net insulation. Finally in Task I, the basic reproducibility of two multilayer systems, double-aluminized Mylar/silk net and crinkled, single-aluminized Mylar, was determined from tests performed on several specimens of each.

In Task II, characteristic thermal performance data were obtained for four different multilayer systems for a wide range of compressive loads, specimen thicknesses, and boundary temperatures. These data include both the system characteristics from FPC measurements and optical properties from shield emittance and reflectance measurements. Concurrently, an analysis was conducted to evaluate the experimental data obtained from Tasks I and II. In the analysis characteristic equations were developed to predict and correlate the thermal performance of each of the four multilayer insulations tested. Finally in Task II, the equation developed for one selected multilayer system, double-goldized Mylar/silk net, was evaluated to predict the thermal performance of 20-, 10-, and 5-shield layups of this insulation installed on a 4-ft-(1.22-m-) diameter tank calorimeter.

For the insulations investigated in this program, the maximum uncertainty in heat rate measurements was found to be ± 4.5 percent for a heat rate of

0.100 Btu/hr ft^2 (0.315 w/m^2). This uncertainty decreased to ±3.0 percent for a heat rate an order of magnitude greater. A maximum inaccuracy of ±0.10 lbf(±0.44 N) in compressive forces measured on the FPC was found for forces ranging from 0 to 100 lbf(0 to 445 N). For the nominal surface area of the specimens tested in the FPC, this force inaccuracy is equivalent to an uncertainty of $\pm 5.0 \times 10^{-4}$ psi (± 3.4 N/m^2) in compressive pressure. For compressive forces of 100 to 400 lbf(445 to 1780 N), the maximum uncertainties were found to be ±0.20 lbf(±0.89 N) in compressive force and $\pm 1.0 \times 10^{-3}$ psi (6.9 N/m^2) in compressive pressure. These uncertainties in compressive pressure are equivalent to ±50 percent at a compressive pressure of 1.0×10^{-3} psi (6.9 N/m^2) and ±2.5 percent at a compressive pressure of 1.0×10^{-1} psi (690 N/m^2). The maximum error in specimen thickness measurements was found to be $\pm 1.0 \times 10^{-3}$ in. ($\pm 2.5 \times 10^{-3}$ cm), which resulted in a ±9 percent deviation in layer density for the 5-shield specimens at maximum layer density values decreasing to less than ±1 percent for the 20- and 40- shield specimens at the lowest values of layer density. Maximum inaccuracy of the boundary temperature measurements was found to be $\pm 1.0^{\circ}R$ ($\pm 0.6^{\circ}K$).

From the series of tests conducted in Task I on a single specimen of double-aluminized Mylar/silk net, the repeatability of the FPC heat flux measurements as a function of compressive pressure was determined to be ±12 percent at a compressive pressure of 1.0×10^{-3} psi (6.9 N/m^2) decreasing to ±5 percent at a compressive pressure of 1.0×10^{-1} psi (690 N/m^2).

Reproducibility of heat flux measurements as a function of compressive pressure for multiple specimens of each of the four insulations investigated in the program was found to range between 10 and 20 percent. Based on layer density, however, the reproducibility of heat flux measurements for the four insulations was found to vary much more widely; e.g., up to 80 percent for the crinkled, single-aluminized Mylar system. The insulations using double silk net spacers exhibited better reproducibility than did either the crinkled, single-aluminized Mylar on the double-aluminized Mylar/Tissuglas insulations.

On the basis of the heat flux data obtained as a function of compressive pressure in Task I, both the double-aluminized Mylar/silk net and the crinkled, single-aluminized Mylar systems were found to be reproducible within ±10 percent. On the basis of heat flux as a function of layer density from the same Task I data, the reproducibility of the double-aluminized Mylar/silk net system was found to vary from ±10 to ±20 percent, while that for the crinkled, single-aluminized Mylar system varied from ±15 to ±80 percent depending upon the number of layers tested and the layer density. In general, specimens with the fewest layers showed the poorest reproducibility.

Optical properties of the three reflective shield materials investigated in the program were thoroughly characterised by measurements of emittance and reflectance as a function of shield temperature obtained in Tasks I and II. Typical values of total hemispherical emittance for these shield materials are summarized in Table 5-1.

Table 5-1

SUMMARY OF TOTAL HEMISPHERICAL EMITTANCE DATA FOR ¼-MIL MYLAR REFLECTIVE SHIELDS

MATERIAL	TEMPERATURE $^{\circ}R$	TEMPERATURE ($^{\circ}K$)	ϵ_{TH}
Double-Aluminized Mylar	540 300 115	(300) (167) (64)	0.028 0.018 0.010
Single-Aluminized Mylar, Aluminum Side	540 300 115	(300) (167) (64)	0.035 0.025 0.015
Single-Aluminized Mylar, ¼-Mil Mylar Side	540 300 115	(300) (167) (64)	0.37 0.25 0.13
Double-Goldized Mylar	540 300 115	(300) (167) (64)	0.022 0.016 0.009

As expected, the gold-coated surface exhibited the lowest values of total hemispherical emittance. The aluminized surface of the crinkled, single-aluminized material showed the highest emittance of the metal surfaces investigated, and the temperature dependence of the emittance deviated from that of the double-aluminized material.

From the heat transfer tests conducted in Task II, it was found that use of the insulations with double silk net spacers resulted in the lowest values of heat flux for a given value of compressive pressure and for a given number of shields. For the same value of compressive pressure, and for the same number of shields, the crinkled, single-aluminized Mylar and the Tissuglas spacer systems yielded somewhat higher heat fluxes in that order. Typical data of heat flux at two different compressive pressures for 5-, -10, and 20-shield systems are presented in Table 5-2. These data show that an increase in compressive pressure from 1.0×10^{-3} psi ($6.9\ N/m^2$) to 1.0×10^{-2} psi ($69\ N/m^2$) resulted in the least increase in heat flux for the double silk net spacer systems; i.e., a factor of approximately 2.1 to 2.3 for the double-aluminized Mylar/silk net system and a factor of approximately 2.4 to 2.6 for the double-goldized Mylar/silk net system. For a corresponding increase in compressive pressure, the heat flux values increased by a factor of approximately 2.9 to 3.6 for the crinkled, single-aluminized Mylar system, and by a factor of approximately 3.6 to 3.8 for the double-aluminized Mylar/Tissuglas system. At the low compressive pressure, 1.0×10^{-3} psi ($6.9\ N/m^2$), and with the $610^{\circ}R$ ($339^{\circ}K$) hot boundary temperature, the heat flux for the double-goldized Mylar/silk net system was 10 to 15 percent lower than that for the double-aluminized Mylar/silk net composite. However, at the higher compressive pressure the trend was reversed, probably due to the difference in compression response for the goldized Mylar and the aluminized Mylar material systems. For 10-shield specimens and a $500^{\circ}R$ ($278^{\circ}K$) hot boundary temperature, the rate of change of heat flux with compressive pressure varies as shown in Fig. 5-1 for the four multilayer systems tested. At compressive pressure values below 4.0×10^{-3} psi ($27.6\ N/m^2$), the crinkled, single-aluminized system exhibits the least increase of heat flux with compressive pressure, while the double-

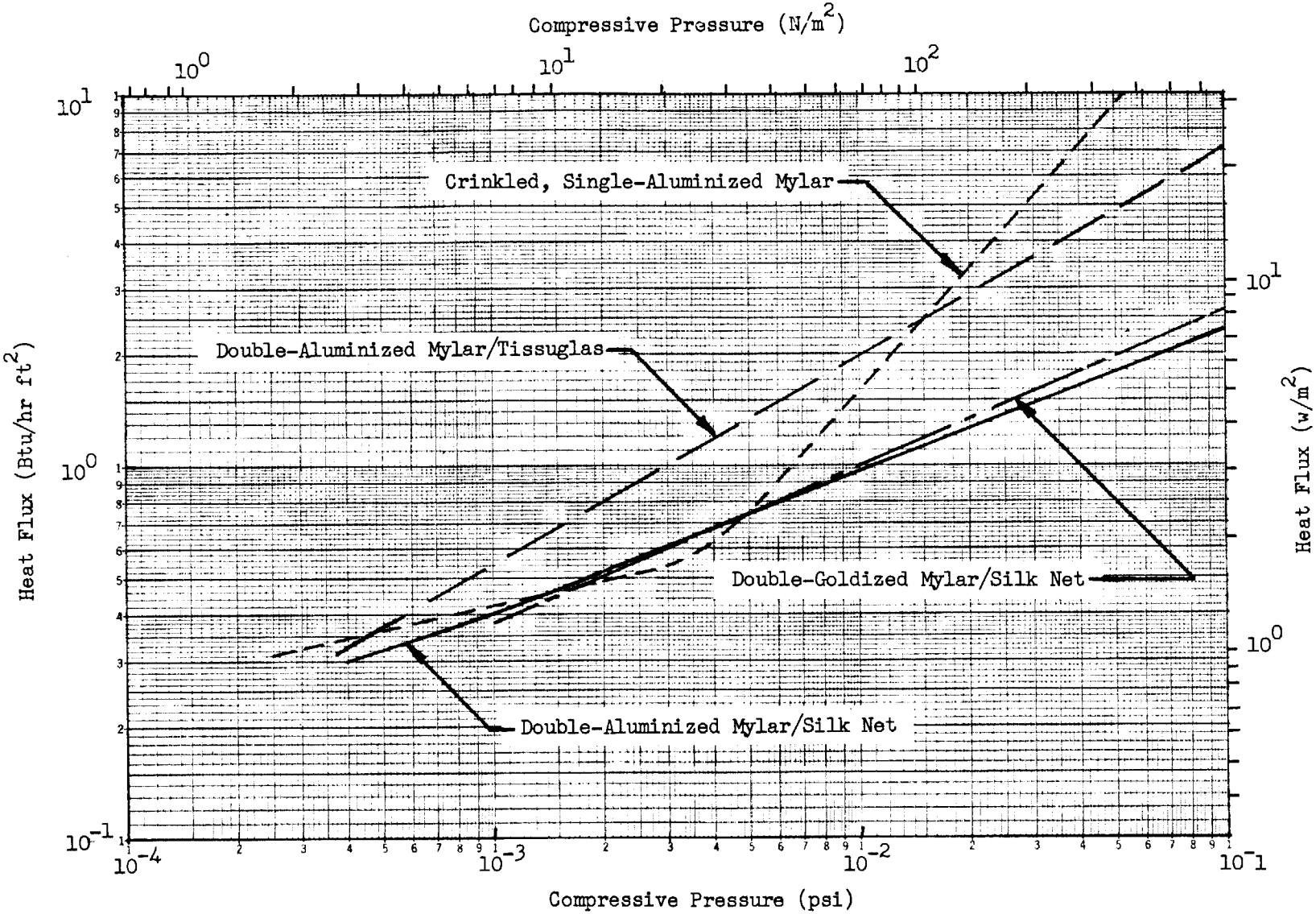

Fig. 5-1 Heat Flux as a Function of Compressive Pressure for Four Multilayer Insulations with $T_H = 500^\circ R(278^\circ K)$

aluminized Mylar/Tissuglas system shows the greatest increase. At compressive pressure values above 4.0×10^{-3} psi (27.6 N/m^2), the silk net spacer composites show the least increase in heat flux with compressive pressure whereas the crinkled, single-aluminized Mylar system shows the greatest increase.

Table 5-2

COMPARISON OF HEAT FLUX MEASURED AT TWO TEMPERATURES AND AT TWO COMPRESSIVE PRESSURES FOR FOUR INSULATIONS

PRESSURE		TEMPERATURE		NUMBER OF SHIELDS	HEAT FLUX, Btu/hr ft^2 (w/m^2), FOR THESE INSULATIONS							
					Double-Al Mylar/Silk Net		Double-Goldized Mylar/Silk Net		Crinkled, Single-Al Mylar		Double-Al Mylar/Tissuglas	
psi	(N/m^2)	°R	(°K)									
1×10^{-3}	(6.9)	500	(278)	5	0.79	(2.49)	0.86	(2.71)	0.89	(2.81)	-	-
				10	0.41	(1.29)	0.39	(1.23)	0.43	(1.36)	0.56	(1.77)
				20	0.23	(0.72)	0.21	(0.66)	0.26	(0.82)	0.29	(0.91)
		610	(339)	5	1.42	(4.48)	1.32	(4.16)	1.72	(5.42)	-	-
				10	0.68	(2.14)	0.62	(1.95)	-	-	0.85	(2.68)
				20	0.38	(1.20)	0.32	(1.01)	0.42	(1.32)	0.42	(1.32)
1×10^{-2}	(69)	500	(278)	5	1.75	(5.52)	1.88	(5.93)	3.20	(10.1)	-	-
				10	0.96	(3.03)	1.00	(3.15)	1.55	(4.89)	2.01	(6.34)
				20	0.49	(1.54)	0.54	(1.70)	0.82	(2.58)	1.04	(3.28)
		610	(339)	5	3.07	(9.68)	3.22	(10.1)	5.30	(16.7)	-	-
				10	1.50	(4.73)	1.60	(5.04)	-	-	3.10	(9.77)
				20	0.78	(2.46)	0.77	(2.43)	1.20	(3.78)	1.58	(4.98)

The experimental data shows that the cold boundary temperature exerted little influence on the heat flux measured for a given warm boundary temperature. This characteristic is as predicted by the analytical model since the conduction term is proportional to the temperature difference multiplied by the average temperature which is nearly a constant for the two cold boundary temperatures investigated in the program. Also, the radiation heat transport is governed by the hot boundary temperature for cases where the temperature difference is large as it was in the program investigations since this component is proportional to $T_H^{4+a_4} - T_C^{4+a_4}$.

Heat flux as a function of layer density is shown in Fig. 5-2 for 10-shield specimens of each of the four insulations tested for a 500°R (278°K) hot boundary temperature. The lowest heat flux values obtained were those for crinkled, single-aluminized Mylar for the uncompressed stacking layer density value. Slightly higher heat flux values were observed for the uncompressed stacking layer density values for double-aluminized Mylar/Tissuglas, double-aluminized Mylar/silk net, and double-goldized Mylar/silk net systems, in that order.

The average uncompressed stacking layer density values for each of these systems were derived from the uncompressed thickness data presented in Tables 3-8, 4-1, 4-4, 4-6, and 4-7. The data used were based on both the pretest thickness measurements (obtained with a dial gage after layup of each specimen) and FPC thickness measurements (obtained by observing the initial contact of the cold boundary plate with the specimen). The average uncompressed stacking layer density values derived for each system reflect measurements made for all specimens of that system regardless of the number of layers. This was done because the values obtained for individual specimens scattered widely, and no consistent relationship as a function of the number of layers could be found. Consequently, minimum heat flux values for 10-shield specimens, both above and below those shown in Fig. 5-2, can be found in the tables.

Bulk density as a function of layer density is shown in Fig. 5-3 for each of the four insulations tested during the program. These data were computed using the weight/unit area data presented in Table 3-2. It can be seen that the bulk density values, within the range of practical designs for each system, are comparable for the double-aluminized Mylar/silk net, double-goldized Mylar/silk net, and double-aluminized Mylar/Tissuglas systems, although each system exhibits different practical layer density ranges. Bulk density for the crinkled single-aluminized Mylar system is significantly less than that for any of the other systems throughout its range of practical layer density values.

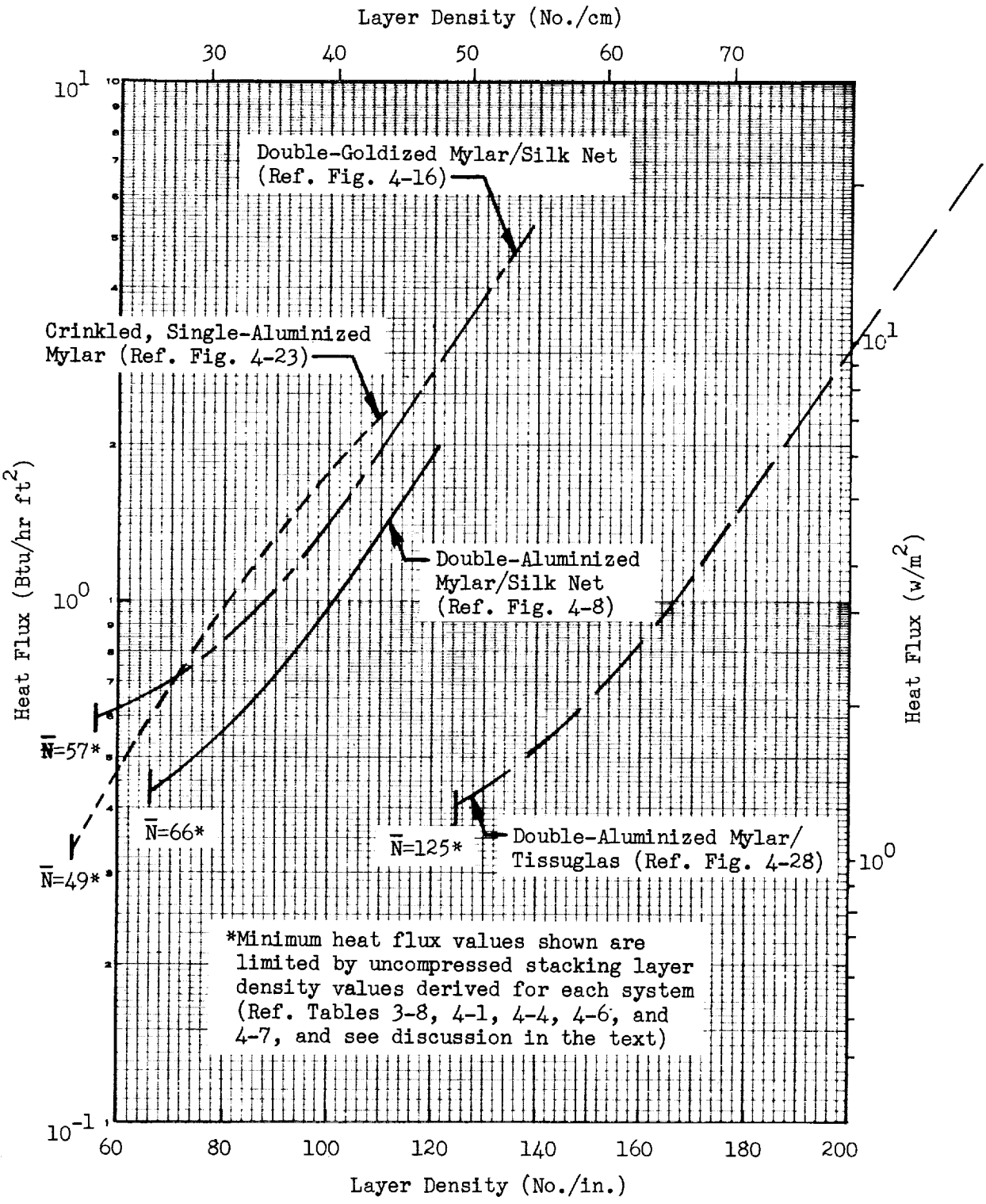

Fig. 5-2 Heat Flux as a Function of Layer Density for Four Multilayer Insulations with $T_H = 500^{\circ}R$ ($278^{\circ}K$)

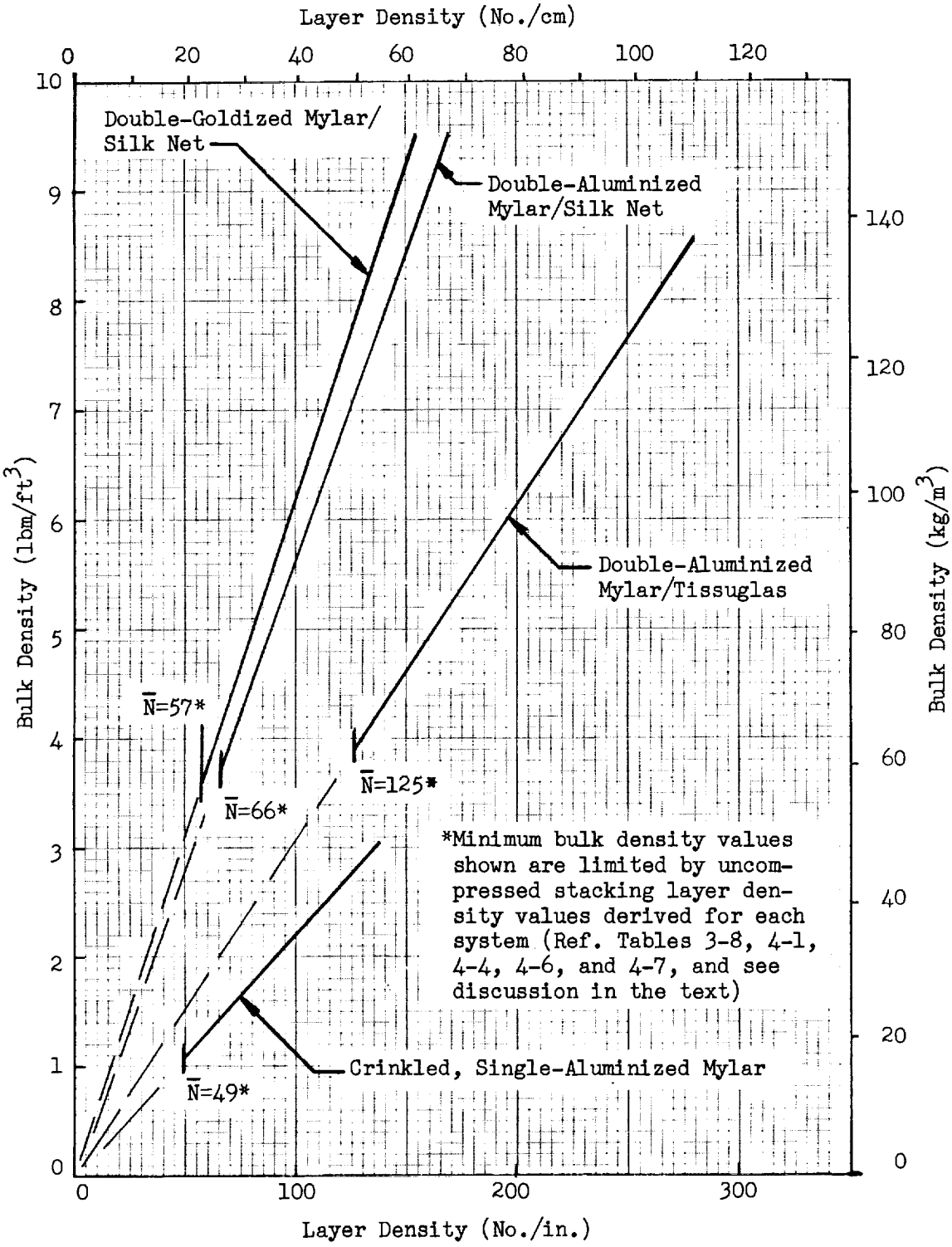

Fig. 5-3. Bulk Density as a Function of Layer Density for Four 1/4-Mil Mylar Multilayer Insulations

An indication of the relative overall efficiencies of the four insulations investigated in the program can be obtained by plotting the product of heat flux and weight/unit area as a function of layer density for each. Such a plot is presented in Fig. 5-4 for 10-shield specimens with a 500°R (278°K) hot boundary temperature. As shown in the figure, the very low unit weight of the crinkled, single-aluminized Mylar material reduces the heat flux-unit weight product so that this system shows a better overall efficiency than any of the other systems. Based on this measure of efficiency, the double-aluminized Mylar/Tissuglas, double-aluminized Mylar/silk net, and double-goldized Mylar/silk net systems, in that order, exhibit higher values of the heat flux-unit weight product.

Insulation unit weights as a function of heat flux for a 500°R (278°K) hot boundary temperature are presented in Figs. 5-5 through 5-8 for each of the four insulations investigated in the program. These data were compiled using the best fit of the data of heat flux, layer density, and specimen thickness for each composite system (Ref. Tables 3-8, 4-1, 4-4, 4-6 and 4-7) together with the bulk density data from Fig. 5-3. For each system, the data shown is limited by the average uncompressed stacking density of the specimens tested, since this represents a minimum practical design condition. The data shown in these figures can be used to compare idealized system weights (no allowance included for attachment or installation penalties) for designs with the same thermal performance. For example, consider the typical design cases noted in Figs. 5-5 through 5-8. In each case, the designs were selected to yield a nominal heat flux value of 0.300 Btu/hr ft^2 (0.946 w/m^2) using the minimum practical layer density (uncompressed stacking density) for each system. The resulting layer density values, number of shields, insulation thickness, and insulation unit weights are summarized in the figures.

The comparison described above can be extended to show the relative total unit weights for each insulation system (i.e., insulation weight plus propellant boiloff weight per unit of insulation surface area). Such a comparison was made assuming that each system was applied to storage of liquid hydrogen in space for a 30-day mission duration. The results are presented in

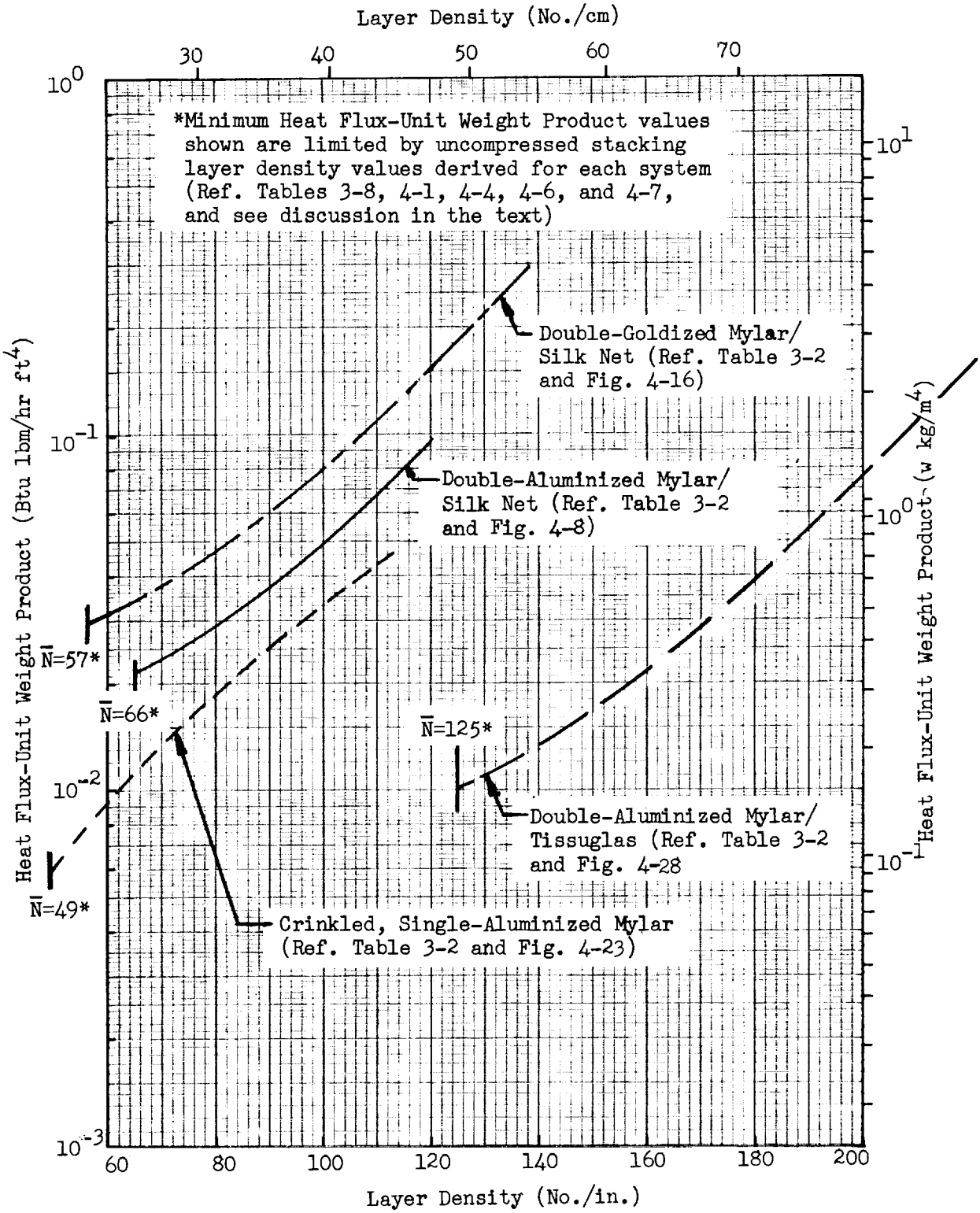

Fig. 5-4 Product of Heat Flux and Unit Weight as a Function of Layer Density for Four Multilayer Insulations with $T_H = 500^{\circ}R$ ($278^{\circ}K$)

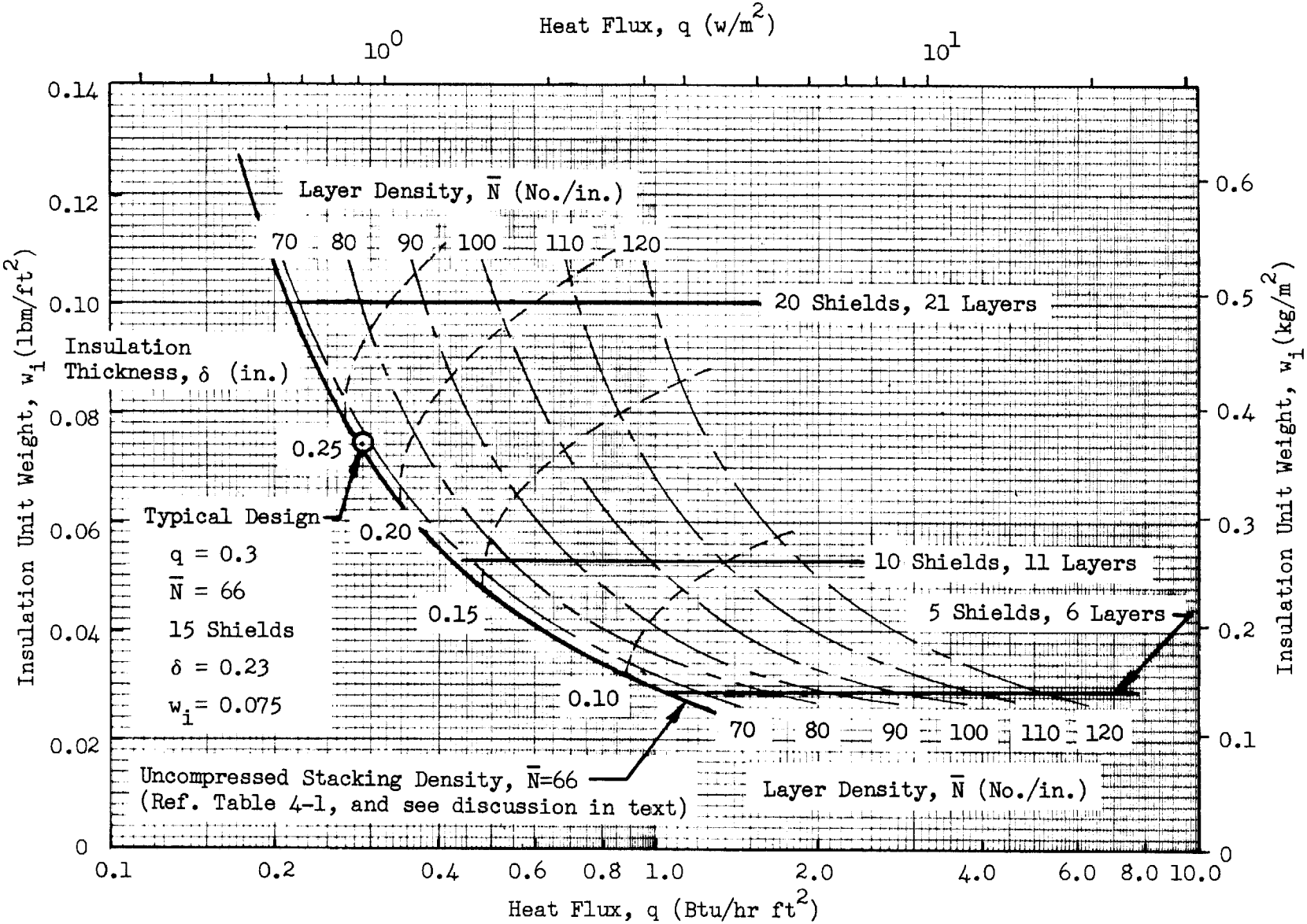

Fig. 5-5 Insulation Unit Weight as a Function of Heat Flux for the Double-Aluminized Mylar/Silk Net Composite System with $T_H = 500^{\circ}R(278^{\circ}K)$

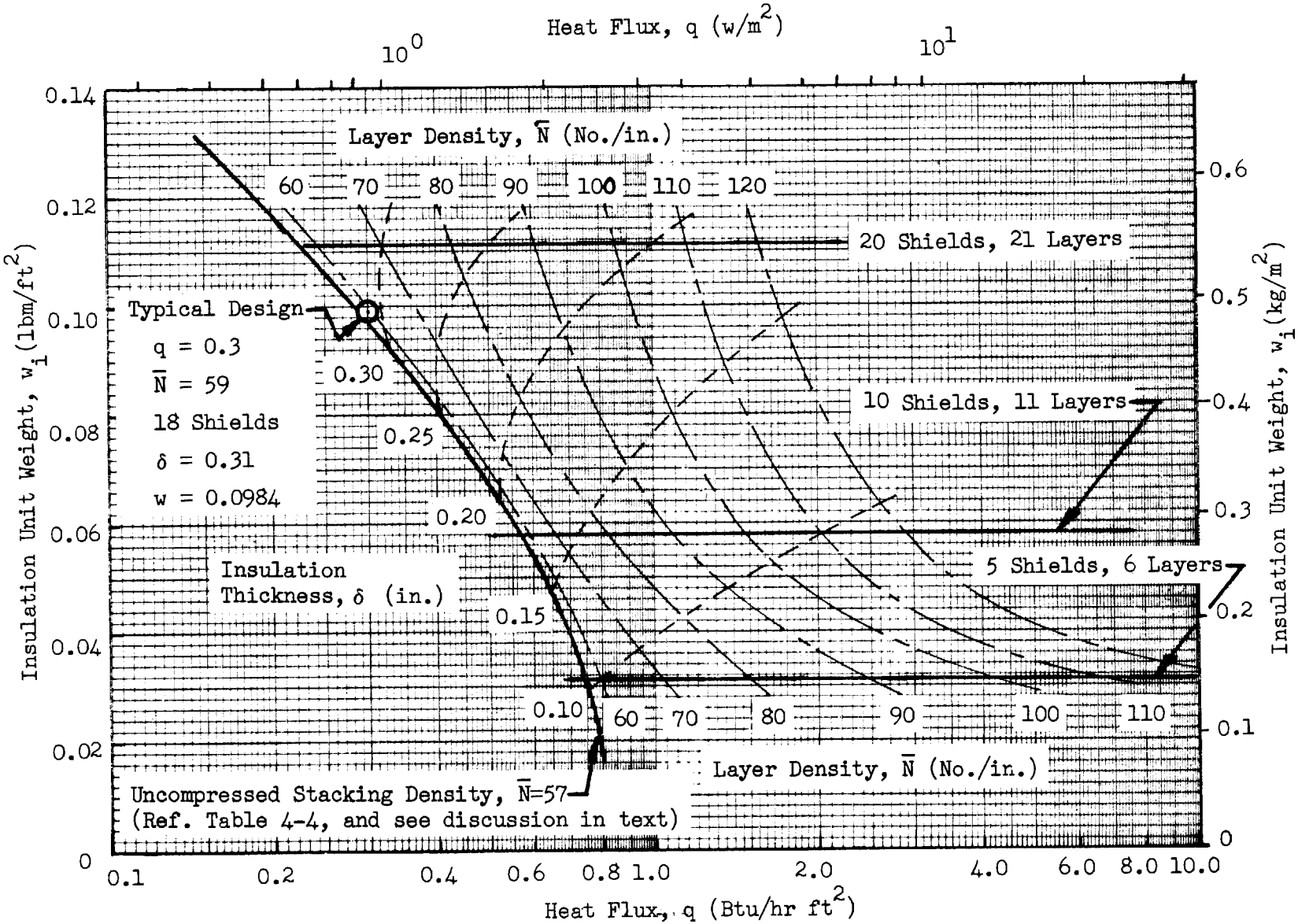

Fig. 5-6 Insulation Unit Weight as a Function of Heat Flux for the Double-Goldized Mylar/Silk Net Composite System with $T_H = 500^{\circ}R(278^{\circ}K)$

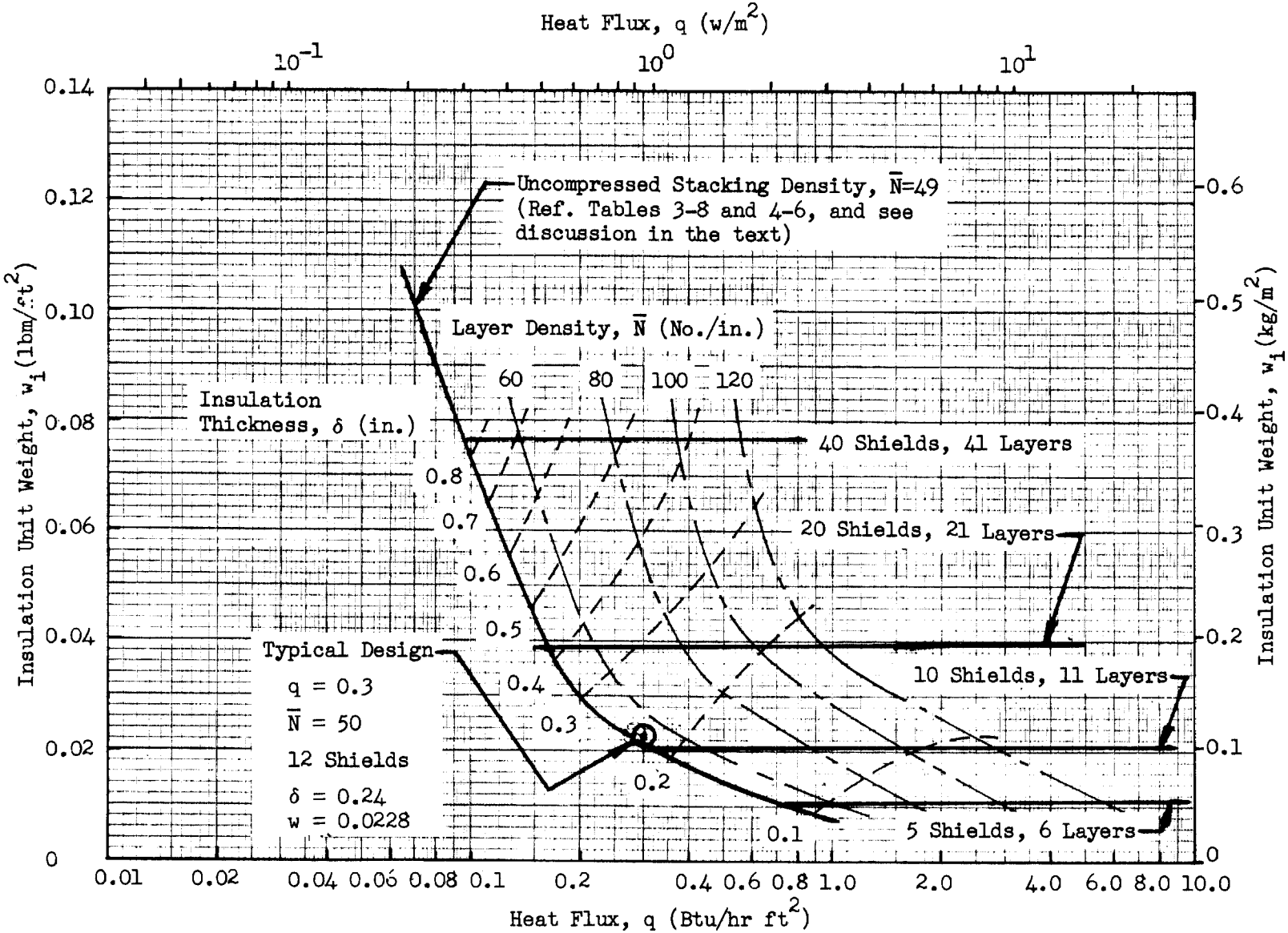

Fig. 5-7 Insulation Unit Weight as a Function of Heat Flux for the Crinkled, Single-Aluminized Mylar System with $T_H = 500^{\circ}R(278^{\circ}K)$

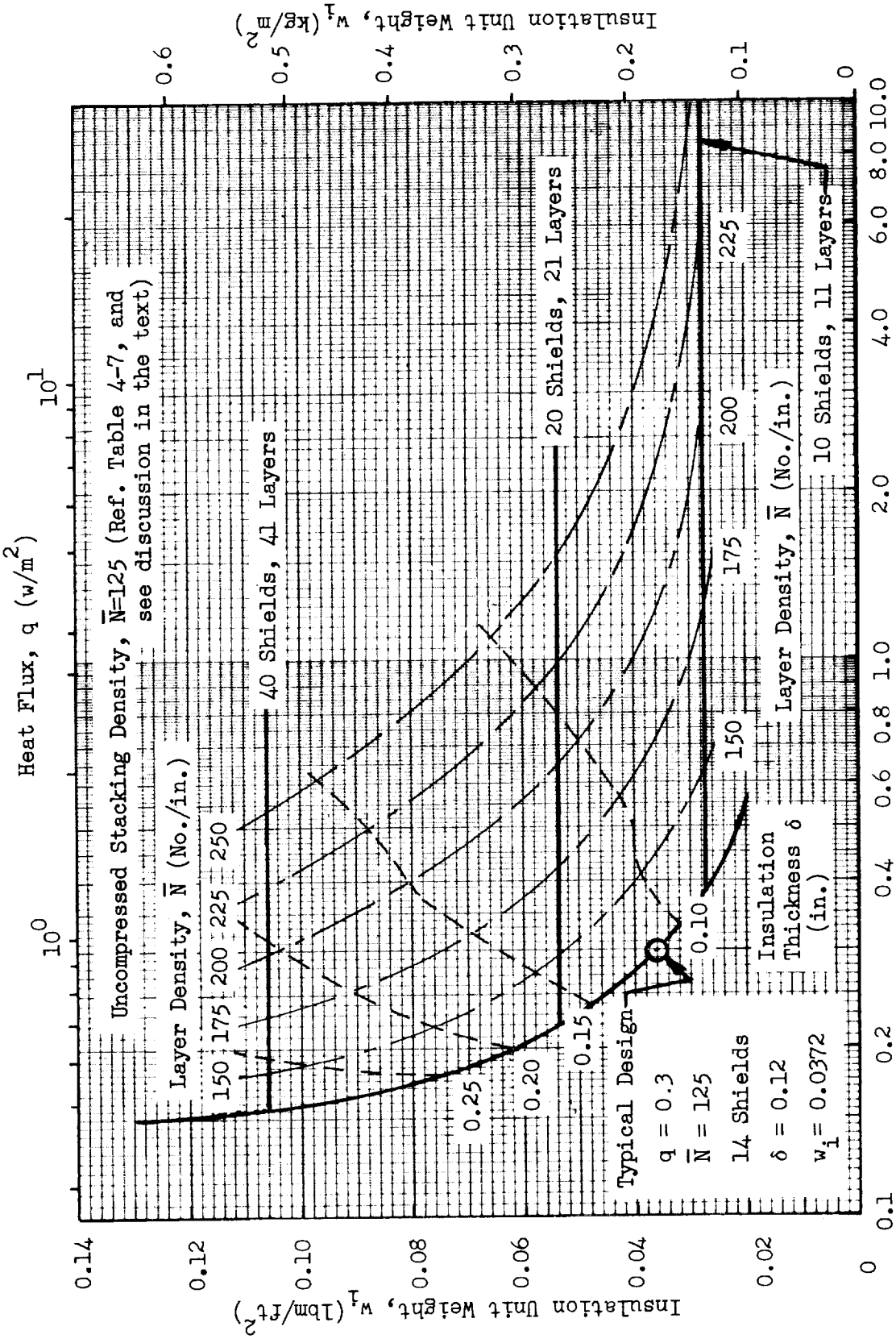

Fig. 5-8 Insulation Unit Weight as a Function of Heat Flux for the Double-Aluminized Mylar/Tissuglas Composite System with $T_H = 500^{\circ}R(278^{\circ}K)$

Fig. 5-9 which shows total unit weights as a function of actual-to-design nominal layer density values for each insulation. In the figure, the data which represent the best fit of the FPC measurements are shown as the lower boundary of the data band for each insulation. The unit weight penalties which could result from increased heat fluxes (greater than the design nominals) due to the maximum reproducibility uncertainty of the data are shown as the upper boundary of each data band. The reproducibility penalty values of heat flux as a function of layer density which were derived from the Task II data and discussed in earlier sections of this report were used to compute the heat flux penalties. The nominal design layer density values, design heat flux, and the maximum reproducibility penalties used in the calculations are summarized in the figure.

It can be seen by inspection of the data presented in Fig. 5-9 that the total unit weights are approximately equal for each of the four insulations investigated if the nominal design layer density values are achieved and if the best-fit data are correct. However, considering the maximum heat flux values based on reproducibility data, the total unit weights begin to diverge as shown. For this case, the minimum total unit weight of approximately 1.34 lbm/ft^2 (6.54 kg/m^2) is exhibited by the double-aluminized Mylar/Tissuglas composite.

The systems with double silk net spacers show a slightly higher total unit weight of approximately 1.45 lb/ft^2 (7.08 kg/m^2) and the crinkled, single-aluminized Mylar system shows the highest total unit weight of approximately 2.06 lb/ft^2 (10.1 kg/m^2). If the actual layer densities achieved are 20 percent higher than the design nominal values, and again considering maximum heat flux values, the relative total unit weights for each system are somewhat different. For this case, the minimum total unit weight value of approximately 1.81 lb/ft^2 (8.84 kg/m^2) is exhibited by the double-aluminized Mylar/silk net system. The total unit weights for the double-goldized Mylar/silk net and the double-aluminized Mylar/Tissuglas systems are slightly higher, and that for the crinkled, single-aluminized Mylar system is again the

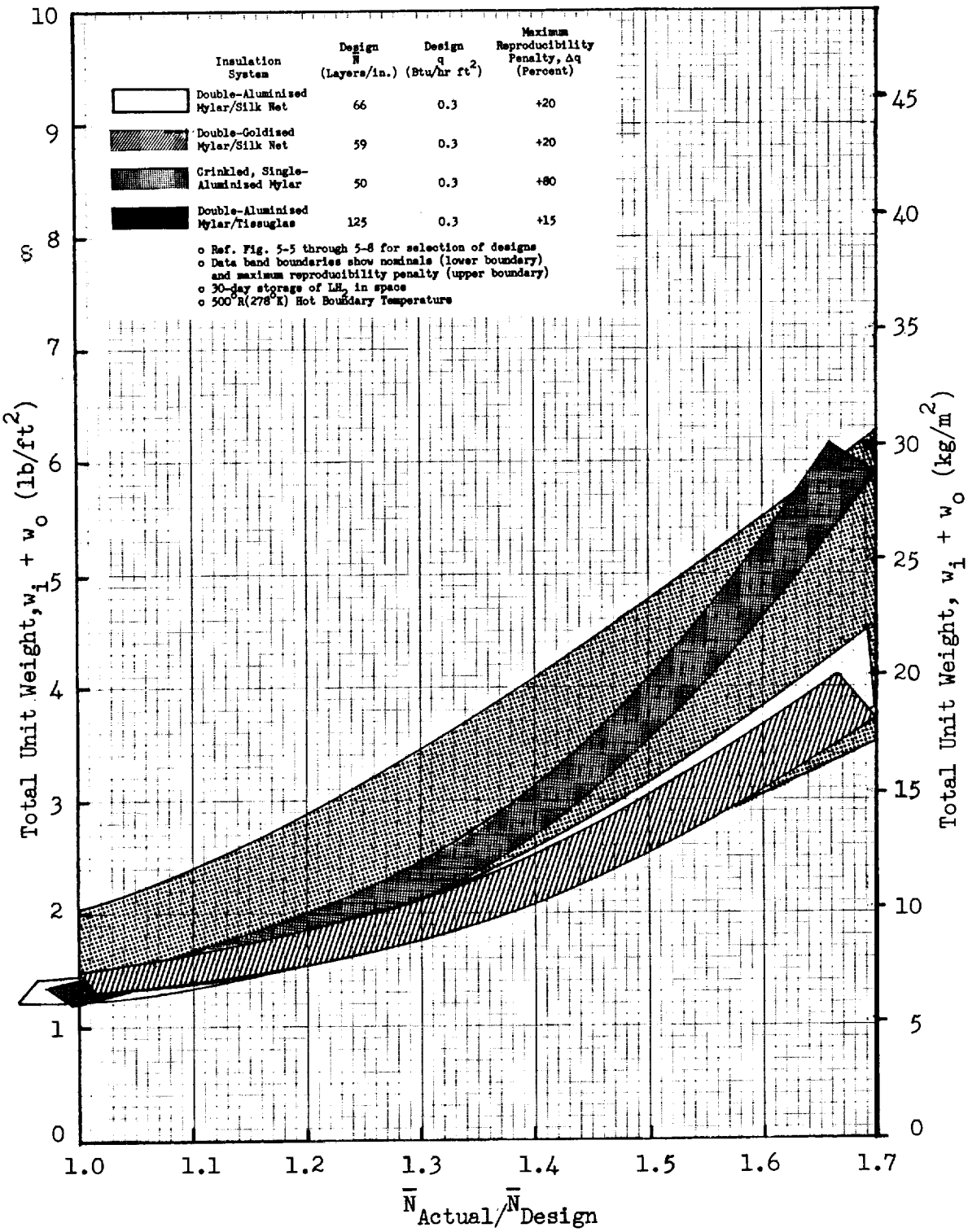

Fig. 5-9 Total Unit Weight as a Function of Actual-to-Design Layer Density Ratio for Four Multilayer Insulations

highest of those investigated. For actual-to-design layer density ratios above approximately 1.3, the double-goldized Mylar/silk net system exhibits the minimum total unit weight, considering the maximum heat flux values. For very high values of actual-to-design layer density ratio, the double-aluminized Mylar/silk net and the double-goldized Mylar/silk net systems show significantly lower total unit weights than either of the other systems. For example, total unit weights at a layer density ratio of 1.6, considering the maximum heat flux values, are 3.60 lb/ft^2 (17.6 kg/m^2), 3.80 lb/ft^2 (18.6 kg/m^2), 5.24 lb/ft^2 (25.6 kg/m^2), and 5.45 lb/ft^2 (26.6 kg/m^2), respectively, for the double-goldized Mylar/silk net, double-aluminized Mylar/silk net, double-aluminized Mylar/Tissuglas, and crinkled, single-aluminized Mylar systems.

Section 6
CONCLUSIONS

Results of analytical and experimental studies conducted under Task I, Insulation Repeatability and Calorimeter Checkout, and of Task II, Multilayer Insulation Performance, are presented and discussed in this Interim Report. Results of Task III, Insulation Installation Verification, are presented in the Final Report.

Based on the results of Tasks I and II, each of the four insulations investigated exhibited heat flux reproducibility as a function of applied compressive pressure within ± 20 percent. The silk net and Tissuglas spacer composites also exhibited heat flux reproducibility as a function of layer density within ± 30 percent. The crinkled single-aluminized Mylar insulation, however, showed generally poor reproducibility with heat flux scatter of up to ± 80 percent as a function of layer density. As expected, the total hemispherical emittance of the double-goldized Mylar reflective shields was significantly lower than that of any of the aluminized shields. This characteristic resulted in lower measured heat flux values at low values of compressive pressure and at a $610^{\circ}R$ ($339^{\circ}K$) hot boundary temperature for the double-goldized Mylar/silk net system when compared with the others investigated.

A comparative study of insulation and cryogen boiloff weight increments per unit of insulation surface area was performed to illustrate the relative performance of the four insulations for a typical mission. In the study, a design heat flux value of 0.300 Btu/hr ft^2 (0.946 w/m^2) was used. Storage of liquid hydroden for 30 days in a space environment was assumed. It was found that the double-aluminized Mylar/Tissuglas composite was optimum with a unit system weight of approximately 1.34 lb/ft^2 (6.54 kg/m^2) if the design layer density values were achieved, and if the maximum heat flux penalties due to insulation performance reproducibility were included. Unit system weights were not significantly higher for the silk net spacer systems under these conditions, but were significantly higher for the crinkled, single-aluminized Mylar system. The investigation also showed that the double-goldized Mylar/silk net system was optimum for the typical design case if the actual layer density values achieved in practice were higher than the design goals by 30 percent or more.

The conclusions which evolved from the Task I and Task II work are:

1. Thermal performance of the silk net and Tissuglas spacer composite systems investigated in this program can be predicted within approximately ± 30 percent using the analytical expressions and the data obtained from laboratory tests. The performance of the crinkled, single-aluminized Mylar system, however, can be predicted only within approximately ±80 percent. These predictibility limitations are characteristic of the variation of the solid conduction heat transfer component due to the non-reproducible behavior of multiple contact resistances between the multilayer shields and spacers.

2. Of the four insulations investigated, the double-aluminized Mylar/Tissuglas and the double-goldized Mylar/silk net composites are optimum for use on a liquid hydrogen tank exposed to a space environment for 30 days assuming a typical design heat flux of 0.300 Btu/hr ft^2 (0.946 w/m^2).

3. The characterization study of thermal performance for the double-goldized Mylar/silk net and the double-aluminized Mylar/Tissuglas composite systems should be extended to provide design data for systems composed of up to 100 layers which could be applied to the long-term storage of cryogens in space. The additional work should include FPC tests on specimens of 40 layers or less at other hot boundary temperatures, flat laboratory specimen tests of up to 100 layers to assess thermal performance and gas evacuation characteristics, and additional tank calorimeter tests of up to 100 layers to assess overall performance.

Appendix A

PURCHASE SPECIFICATIONS FOR METALLIZED MYLAR*

1.0 SCOPE

This specification establishes the requirements to be met by suppliers of vacuum-deposited aluminum and gold on 2.5 x 10^{-4}-in.- (6.4 x 10^{-4}-cm-) thick Mylar (Polyethylene terephthalate) film for use in studies of cryogenic multilayer insulations. The coated material is designated as follows:

Type A: Vacuum-deposited aluminum on one side only, film crinkled
Type B: Vacuum-deposited aluminum on both sides, film smooth
Type C: Vacuum-deposited gold on both sides, film smooth

2.0 REQUIREMENTS

2.1 Materials

The film material shall be "as supplied" by the film substrate supplier. The metal and deposition conditions shall be such as to achieve the emittance values specified in Section 2.2.1.

2.2 Properties

2.2.1 Radiative Properties - Emittance of the metallized surfaces at room temperature, 530 to 550°R (294 to 306°K), shall be as given in Table A-1. Near-normal spectral reflectance measurements may be performed in lieu of emittance determination (Table A-1).

2.2.2 Adhesion - The metallized surface shall not be removed by normal handling during shipping or fabrication of the insulation assemblies.

---

*Tradename, E. I. DuPont

Table A-1

METALLIZED SURFACE RADIATIVE PROPERTIES

Material Type	Emittance	Reflectance
A and B	≤0.030 average with no single measurement >0.035	5.0 to 25.0 μm, 0.975
C	≤0.020 average with no single measurement >0.025	5.0 to 25.0 μm, 0.985

3.0 TEST METHODS

3.1 Radiative Properties

Room temperature, 530 to 550°R (294 to 306°K), emittance measurements will be made with a Lion Research Corporation Model 25 Emissometer using standards supplied to the vendor by LMSC. These are a low range (ϵ = 0.030) and a mid-range (ϵ = 0.59) standard. The total hemispherical emittance of these standards has been measured by LMSC to provide correlation with the emittance as measured by the Lion Emissometer.

In order to assure that the specimen and standard are at the same temperatures and that the temperature remains constant during the measurements, both the standards and the metallized film shall be placed upon a suitable plate of high thermal mass; i.e., a ½-in.- (1.27-cm-) thick by 4-in.- (10.2-cm-) square aluminum plate. Measurements of standard and specimen shall be made with the emissometer head in the same position (horizontal, inverted).

In lieu of emissometer measurements, near-normal spectral reflectance may be measured from 5.0 to 25.0 μm (Gier-Dunkle Model HC-300 heated cavity reflectometer or equivalent). Apparatus and procedures for this method shall be reviewed by LMSC before approval is granted for this method.

3.2 Adhesion

No evidence of metal surface removal shall be evident during re-rolling for packaging.

4.0 SAMPLING

All specimens taken for the optical properties measurements shall be supplied to LMSC at the time of shipment of the finished material.

4.1 Aluminized Material

Three test specimens shall be cut across the web from each end of the lot (a total of six). The specimens shall be taken 6 in. (15.2 cm) from each end of the web and at the center.

4.2 Gold-Coated Material

Specimens shall be taken across the web as per 4.1. These shall be cut at the start of the roll and at 100-ft (30.5-m) intervals along the roll to the end.

APPENDIX B

DERIVATION OF HEAT TRANSFER EQUATIONS FOR MULTILAYER INSULATIONS

For multilayer insulations such as those investigated in this program, the heat flux between adjacent shields can be expressed in a general form as

$$q = \frac{\bar{k}_s(T_1-T_2)}{\ell} + \frac{\bar{k}_g(T_1-T_2)}{\ell} + \frac{(e_{b1}-e_{b2})}{\frac{3}{4}\tau_o}\left[\frac{\frac{3}{4}\tau_o\left(\frac{\bar{\epsilon}}{2-\bar{\epsilon}}\right)+\frac{1}{2}\frac{\sqrt{3\lambda'}\tau_o}{\tanh\sqrt{3\lambda'}\tau_o}+\frac{1}{2}\frac{\sqrt{3\lambda'}\tau_o}{\sinh\sqrt{3\lambda'}\tau_o}-1}{\frac{3}{4}\tau_o\left(\frac{\bar{\epsilon}}{2-\bar{\epsilon}}\right)+\frac{1}{2}\frac{\sqrt{3\lambda'}\tau_o}{\tanh\sqrt{3\lambda'}\tau_o}+\frac{1}{2}\frac{\sqrt{3\lambda'}\tau_o}{\sinh\sqrt{3\lambda'}\tau_o}}\right] \quad \text{(B.1)}$$

where $\bar{k}_s$ and $\bar{k}_g$ are equivalent thermal conductivities for the solid and gas phases of the spacer layer, respectively, $\bar{\epsilon}$ is the total hemispherical emittance of the boundary surfaces, and e_b is the blackbody radiant flux of the surface. As the parameter $\sqrt{3\lambda'}\,\tau_o$ is less than 0.2 for these insulation systems, the third term on the right side of Eq. (B.1) becomes

$$\left(e_{b1}-e_{b2}\right)\left[\frac{1+\left(\frac{\lambda'\tau_o}{3}\right)\left(\frac{2-\bar{\epsilon}}{\bar{\epsilon}}\right)}{\frac{3}{4}\tau_o+\left(\frac{2-\bar{\epsilon}}{\bar{\epsilon}}\right)}\right]$$

For boundaries of emittance $\bar{\epsilon}_1$ and $\bar{\epsilon}_2$ and $\tau_o \ll \frac{1}{\bar{\epsilon}}$ Eq. (B.1) reduces to

$$q = \frac{\bar{k}_s(T_1-T_2)}{\ell} + \frac{\bar{k}_g(T_1-T_2)}{\ell} + \left(e_{b1}-e_{b2}\right)\left(\frac{1}{\frac{1}{\bar{\epsilon}_1}+\frac{1}{\bar{\epsilon}_2}-1}\right) \quad \text{(B.2)}$$

In Eq. (B.2), the surface radiation contribution is obtained under the assumption of diffuse and gray surfaces; i.e., $\bar{\epsilon}$ is the total hemispherical emittance. In general, the directional and the polarization effects are negligible (Ref. B-1). For relatively small temperature differences between the shields, such as occur in the warmer regions of a multilayer insulation, the non-gray surface effect is small and may be neglected (Ref. B-2). Although large temperature differences may be present in several layers adjacent to the cold boundary and the non-gray

effect becomes significant, the radiation component in this region is much less than the conduction term and its effect on total heat transfer is small. For insulation systems using spacers of refractive index $n > 1$, the blackbody radiant flux of the surface becomes

$$e_b = n^2 \sigma T^4$$

and $\bar{\epsilon} = n\epsilon$ where ϵ is the total hemispherical emittance of the surface to vacuum (Ref. B-2). For the case of a shield having a single metallized surface, the emittance of the unmetallized surface is evaluated as that of an absorbing dielectric film over a metal substrate. Thus,

$$q = \frac{\bar{k}_s(T_1-T_2)}{\ell} + \frac{\bar{k}_g(T_1-T_2)}{\ell} + n^3\sigma(T_1^4 - T_2^4)\left[\frac{\epsilon_{1(T)}\epsilon_{2(T)}}{\epsilon_{1(T)}+\epsilon_{2(T)}}\right] \qquad (B.3)$$

In the first term on the right side of Eqs. (B.1), (B.2), and (B.3), the solid conductivity coefficient, $\bar{k}_s$, is dependent upon the interfact contact conductance and is not the thermal conductivity of the spacer layer itself. Thus $\bar{k}_s \equiv \frac{H\ell}{N_c}$ where H is a contact conductance, and N_c is the number of interfaces, i.e., two for a separate spacer and one for an integral spacer system. In general, the interface contact conductance follows a dimensionless relation (Ref. B-3) such that

$$H \propto k_s c(P/E)^m$$

where c is a constant depending upon surface conditions, k_s is the thermal conductivity of the spacer material, P is pressure applied to the macroscopic area, E is a deformation parameter, and m is a correlation constant. In the general case, the deformation and thermal parameters are temperature dependent.

As these properties are not easily obtainable for multilayer insulation systems, they are lumped into a correlation coefficient $c_{(T)}$. The solid conduction conductivity coefficient can now be defined as

$$\bar{k}_s = \frac{c_{(T)} P^m \ell}{N_c}$$

The second term on the right side of Eqs. (B.1), (B.2), and (B.3) contains a different conductivity coefficient for the gas phase, $\bar{k}_g$. This coefficient applies to an effective conductivity for the reduced pressure in the void spaces, and it is a function of the true conductivity of the gas and the relationship between the gas mean free path and a characteristic dimension of the void space. From probability considerations, Verschour (Ref. B-4) developed an expression for the mean free path of a contained gas in terms of the gas mean free path, L_g, and a characteristic dimension of the void space, L_s. The thermal conductivity of the contained gas phase is

$$\bar{k}_g = k_g\left(\frac{L_s}{L_s + L_g}\right)$$

where k_g is the conductivity of the unrestricted gas at temperature T. At pressures less than 10^{-3} torr, $L_g \gg L_s$ and

$$\bar{k}_g \cong k_g\left(\frac{L_s}{L_g}\right)$$

Substituting these expressions for the conductivities into Eq. (B.3) yields

$$q = \frac{c_{(T)} P^m \ell}{N_c}\left(\frac{T_1 - T_2}{\ell}\right) + k_g\left(\frac{L_s}{L_g}\right)\left(\frac{T_1 - T_2}{\ell}\right) + n^3\sigma\left(T_1^4 - T_2^4\right)\left[\frac{\epsilon_{1(T)}\ \epsilon_{2(T)}}{\epsilon_{1(T)} + \epsilon_{2(T)}}\right] \qquad \text{(B.4)}$$

When a system is composed of many shields and the temperature difference between two adjacent shields is small compared to the total temperature difference, the heat transfer across each segment composed of two neighboring shields

may be expressed by differentials rather than by differences. This implies a contininum approximation to a discrete system such as the multilayer (Ref. B-5). The approximation approaches the exact case when the number of layers is large and the temperature drop between two adjacent layers is very small.

For x = Nh, where N is the number of segments and h is the segment thickness,

$$q = \frac{c_{(T)} P^m \ell}{N_c}\left(\frac{\Delta T}{\ell}\right) + k_g \frac{L_s}{L_g}\left(\frac{\Delta T}{\ell}\right) + \frac{\epsilon_{1(T)}\ \epsilon_{2(T)}}{\epsilon_{1(T)}+\epsilon_{2(T)}}\left[\frac{n^3 \ell \sigma\ \Delta(T)^4}{\ell}\right]$$

and

$$q_x \cong \frac{c_{(T)} P^m \ell}{N_c}\left(\frac{dT}{dx}\right) + k_g \frac{L_s}{L_g}\left(\frac{dT}{dx}\right) + \frac{\epsilon_{1(T)}\ \epsilon_{2(T)}}{\epsilon_{1(T)}+\epsilon_{2(T)}}\left(n^3 \ell \sigma\right)\frac{d(T^4)}{dx}$$

or

$$q_x \cong \left[\frac{c_{(T)} P^m \ell}{N_c} + k_g \frac{L_s}{L_g} + 4\,\frac{\epsilon_{1(T)}\ \epsilon_{2(T)}}{\epsilon_{1(T)}+\epsilon_{2(T)}}\, n^3 \sigma \ell T^3\right]\frac{dT}{dx} \qquad \text{(B.5)}$$

With the heat flux described at any location, x, in the insulation, the governing one dimensional heat transfer equation, without internal heat generation is

$$\rho C_P \frac{\partial T}{\partial \Theta} = \frac{\partial}{\partial x}\, q_x$$

and for steady state conditions, $\frac{\partial T}{\partial \Theta} = 0$ so that

$$0 = \frac{d}{dx}\left[\frac{c_{(T)} P^m \ell}{N_c} + k_g \frac{L_s}{L_g} + 4\,\frac{\epsilon_{1(T)}\ \epsilon_{2(T)}}{\epsilon_{1(T)}+\epsilon_{2(T)}}\ n^3 \sigma \ell T^3\right]\frac{dT}{dx} \qquad \text{(B.6)}$$

When the parameters of Eq. (B.6) are known, the insulation heat transfer problem can be solved for the appropriate boundary conditions. First consider the case of reflective shields metallized on both surfaces with emittance $\epsilon_1 \approx \epsilon_2$

Let the temperature-dependent properties be approximated by simple power functions as

$$c_{(T)} = b_1 T^{a_1}, \quad k_g = b_2 T^{a_2}, \quad L_g = b_3 T^{(+)}, \text{ and } \epsilon = b_4 T^{a_4}$$

Then

$$\left(\frac{P^m \ell b_1 T^{a_1}}{N_c} + \frac{b_2 T^{a_2} L_s}{b_3 T} + 2n^3 \sigma \ell b_4 T^{3+a_4} \right) \frac{dT}{dx} = A = q_x \qquad (B.7)$$

and

$$\frac{P^m \ell b_1}{N_c(1+a_1)} T^{1+a_1} + \frac{b_2 L_s}{b_3 a_2} T^{a_2} + \frac{2n^3 \sigma \ell b_4}{(4+a_4)} T^{4+a_4} = A_x + B \qquad (B.8)$$

For the boundary conditions $x = 0$, $T = T_2$ and $x = N_o h$, $T = T_1$, where N_o represents the total number of layers and subscripts 1 and 2 denote the hot and cold temperatures of the exterior surfaces, respectively, it follows that

$$B = \frac{P^m \ell b_1}{N_c(1+a_1)} T_2^{1+a_1} + \frac{b_2 L_s}{b_3 a_2} T_2^{a_2} + \frac{2n^3 \sigma \ell b_4}{(4+a_4)} T_2^{4+a_4}$$

and

$$AN_o h = \frac{P^m \ell b_1}{N_c(1+a_1)} \left(T_1^{1+a_1} - T_2^{1+a_1} \right) + \frac{b_2 L_s}{b_3 a_2} \left(T_1^{a_2} - T_2^{a_2} \right) + \frac{2n^3 \sigma \ell b_4}{(4+a_4)} \left(T_1^{4+a_4} - T_2^{4+a_4} \right)$$

† Mean free path is directly proportional to the absolute temperature of the gas.

Since $A = q_x$, the equation which finally describes the temperature dependent heat flux is

$$q = \frac{P^m \ell b_1}{(1+a_1)hN_c}\left(\frac{T_1^{1+a_1}-T_2^{1+a_1}}{N_o}\right) + \frac{b_2 L_s}{b_3 h a_2}\left(\frac{T_1^{a_2}-T_2^{a_2}}{N_o}\right) + \frac{2n^3\sigma\ell b_4}{(4+a_4)h}\left(\frac{T_1^{4+a_4}-T_2^{4+a_4}}{N_o}\right) \qquad \text{(B.9)}$$

If the insulation reflective shields have widely differing emittances on the two surfaces, a numerical method can be applied for the solution of Eq. (B.4). However, for the case of the single aluminized Mylar, the temperature dependence of both aluminum and Mylar surfaces is nearly equal as shown in Section 4.2 of this report. The temperature dependent emittance properties of the two surfaces are

$$\epsilon_1 = b_4 T^{a_4} \quad \text{and} \quad \epsilon_2 = b_5 T^{a_4}$$

and Eq. (B.4) becomes

$$q = \frac{P^m \ell b_1}{(1+a_1)hN_c}\left(\frac{T_1^{1+a_1}-T_2^{1+a_1}}{N_o}\right) + \frac{b_2 L_s}{b_3 h a_2}\left(\frac{T_1^{a_2}-T_2^{a_2}}{N_o}\right) + 4\left(\frac{b_4 b_5}{b_4+b_5}\right)\frac{n^3\sigma\ell}{(4+a_4)h}\left(\frac{T_1^{4+a_4}-T_2^{4+a_4}}{N_o}\right) \qquad \text{(B.10)}$$

Application of Eq. (B.4) to multilayer insulations requires certain assumptions to define the coefficient and exponent of the solid conduction terms. Multilayer insulations present a complex structure in regard to contact geometries of spacers and shields, and no method is available for computation of the values for this undefined set of conditions. As a first approximation, a linear temperature dependence can be assumed, i.e., $a_1 = 1$, because for the materials used in multilayer constructions, the thermal and deformation prop-

erties are reasonably fit by this linear form over a large portion of the temperature range of interest. The coefficient b_1 must be derived from experimental data of heat flux versus compressive pressure for constant temperature conditions. The remaining coefficient and exponents are taken from experimental or theoretical data on the behavior of gas conductivity, mean free path, refractive index, and emittances as a function of temperature (and pressure in the case of the gas phase).

NOMENCLATURE

A = a parameter, proportional to $T^{2/3}$, used to describe total normal emittance of a metallic surface, dimensionless

A_b = blackbody surface area for calorimetric emittance measurements, ft^2 (m^2)

A_c = insulation specimen surface area for FPC heat transfer measurements, ft^2 (m^2)

A_s = insulation specimen total surface area, ft^2 (m^2)

B = an integration constant

C_1 = a constant correlation coefficient that relates electrical conductivity of a metallic film to its total normal emittance

C_2 = a constant correlation coefficient that relates electrical conductivity of a bulk metal to that of a metallic film

C_3 = a constant correlation coefficient that relates absolute temperature to the parameter A

C_4 = A constant correlation coefficient that relates absolute temperature to electrical conductivity of a bulk metal

C_p = specific heat of a substance, Btu/lbm$^{\circ}$R (joules/gm$^{\circ}$K)

E = insulation surface interface deformation parameter, psi (N/m^2)

F = compressive force, lbf (N)

F = geometric view factor for radiation heat transfer, dimensionless

H = contact conductance of an insulation surface interface, Btu/hr $ft^{2o}R$ ($w/m^{2o}K$)

ΔH_v = latent heat of vaporization of a calorimetric fluid, Btu/lbm (joules/gm)

L_g = mean free path of an interstitial gas, ft (m)

L_s = characteristic dimension of the void space between insulation radiation shields, ft (m)

N = number of elements in a system, dimensionless

$\bar{N}$ = layer density of an insulation system, No./in. (No./cm)

N_c = number of contact interfaces in an insulation system, dimensionless

N_o = number of spacer layers in an insulation system, dimensionless

N_s = number of radiation shields in an insulation system, dimensionless

P = total compressive pressure acting on an insulation specimen per unit area, psi (N/m^2)

P_a = compressive pressure acting on an insulation specimen per unit area due to an applied external force, psi (N/m^2)

P_o = compressive pressure acting on an insulation specimen per unit area due to its own weight, psi (N/m^2)

Q_c = total heat rate into the FPC, Btu/hr (w)

Q_c = power input into the calorimetric emittance apparatus during calibration, Btu/hr (w)

$\overline{Q}_c$ = extraneous heat leak into the FPC, Btu/hr (w)

Q_l = heat rate into the calorimetric emittance apparatus blackbody thermal link, Btu/hr (w)

Q_r = difference in radiated sample energy absorbed by the calorimetric emittance apparatus blackbody and that radiated by the blackbody during calibration, Btu/hr (w)

T = absolute temperature of a surface on an element, ^{o}R (^{o}K)

T_1 = absolute temperature of an insulation specimen hot boundary surface, ^{o}R (^{o}K)

T_2 = absolute temperature of an insulation specimen cold boundary surface, ^{o}R (^{o}K)

T_b = absolute temperature of the blackbody surface for calorimetric emittance measurements, ^{o}R (^{o}K)

T_c = absolute temperature of the insulation specimen during calibration of the calorimetric emittance apparatus, ^{o}R (^{o}K)

T_C = absolute temperature of the FPC cold boundary plate, ^{o}R (^{o}K)

T_H = absolute temperature of the FPC hot boundary plate, ^{o}R (^{o}K)

T_m = absolute mean temperature of an insulation specimen (i.e., average of the hot and cold surface temperatures), ^{o}R (^{o}K)

T_s = absolute temperature of an insulation specimen for calormetric emittance measurements, ^{o}R (^{o}K)

W = weight of an insulation specimen, lbm (kg)

Y_c = heat transfer loss in the calorimetric emittance apparatus due to radiation exchange between the blackbody and the chamber walls during calibration, Btu/hr (w)

Y_s = heat transfer loss in the calorimetric emittance apparatus due to radiation exchange between the blackbody and the chamber walls during a sample run, Btu/hr (w)

a = blackbody absorptance of an insulation spacer material, ft^{-1} (m^{-1})

= a constant coefficient, dimensionless

a_b = blackbody absorptance of the calorimetric emittance apparatus during a sample run, ft^{-1} (m^{-1})

a'_b = blackbody absorptance of the calorimetric emittance apparatus during calibration, ft^{-1} (m^{-1})

a_s = absorptance of a calorimetric emittance specimen during a sample run, ft^{-1} (m^{-1})

a'_s = absorptance of a calorimetric emittance specimen during calibration, ft^{-1} (m^{-1})

b_1 = a constant correlation coefficient that relates absolute temperature to the correlation constant for solid conduction heat transfer

b_2 = a constant correlation coefficient that relates absolute temperature to the thermal conductivity of an interstitial gas

b_3 = a constant correlation coefficient that relates absolute temperature to the mean free path of an interstitial gas

b_4 = a constant correlation coefficient that relates absolute temperature to the total hemispherical emittance of one particular surface of a radiation shield

b_5 = a constant correlation coefficient that relates absolute temperature to the total hemispherical emittance of the opposite surface of a radiation shield

c = a constant coefficient, dimensionless

= a correlation constant

$c_{(T)}$ = a constant correlation coefficient that relates compressive pressure to solid conduction heat flux

d = thickness of a metallic film, in. (cm)

e_{b1} = blackbody radiant flux of the hot boundary surface of an insulation specimen, Btu/hr ft^2 (w/m^2)

e_{b2} = blackbody radiant flux of the cold boundary surface of an insulation specimen, Btu/hr ft^2 (w/m^2)

h = spacing of radiation shields in an insulation system, ft (m)

k = thermal conductivity of an insulation, Btu/hr ft^oR (w/cm^oK)

k_g = thermal conductivity of an unrestricted interstitial gas, Btu/hr ft^oR (w/cm^oK)

$\bar{k}_g$ = equivalent thermal conductivity of an insulation spacer dependent on conduction through interstitial gas molecules, Btu/hr ft^oR (w/cm^oK)

k_s = thermal conductivity of an insulation spacer material, Btu/hr ft$^{\circ}$R (w/cm$^{\circ}$K)

$\bar{k}_s$ = equivalent thermal conductivity of an insulation spacer material dependent on interface contact conductance, Btu/hr ft$^{\circ}$R (w/cm$^{\circ}$K)

ℓ = clear distance between reflective shield surfaces in an insulation system, ft (m)

m = a constant exponent, dimensionless

= a correlation constant

n = index of refraction for an insulation spacer material, dimensionless

= a constant exponent, dimensionless

q = total heat flux through an insulation specimen, Btu/hr ft^2 (w/m^2)

q_r = heat flux component through an insulation specimen due to radiation, Btu/hr ft^2(w/m^2)

q_s = heat flux component through an insulation specimen due to solid conduction, Btu/hr ft^2 (w/m^2)

$\dot{v}$ = volumetric boiloff flowrate from the FPC, ft^3/hr (m^3/hr)

w = unit weight, lbm/ft^2 (kg/m^2)

x = location of an isothermal plane within an insulation system with respect to a reference boundary, ft (m)

α = a constant correlation exponent that relates absolute temperature of a metallic film to its total normal emittance, and is dependent on film thickness

a_1 = a constant correlation exponent that relates absolute temperature to the correlation constant for solid conduction heat transfer

a_2 = a constant correlation exponent that relates absolute temperature to the thermal conductivity of an interstitial gas

a_4 = a constant correlation exponent that relates absolute temperature to the total hemispherical emittance of a radiation shield surface

β = a constant correction exponent that relates absolute temperature of a metallic film to its total normal emittance, and is independent of film thickness

= extinction coefficient of an insulation spacer material, ft^{-1} (m^{-1})

Δ = increment of uncertainty of a physical parameter, dimensionless

δ = insulation thickness, in. (cm)

= percentage uncertainty of a physical parameter, dimensionless

= parameter used to describe the interaction of radiation and conduction heat transfer processes, dimensionless

ϵ = total hemispherical emittance of a surface radiating to a medium with a refractive index, n, approximately equal to unity, dimensionless

$\bar{\epsilon}$ = total hemispherical emittance of a surface radiating to a medium with a refractive index, n, other than unity, dimensionless

$\epsilon_{1(T)}$ = total hemispherical emittance of one particular surface of a radiation shield at a given temperature, dimensionless

$\epsilon_{2(T)}$ = total hemispherical emittance of the opposite surface of a radiation shield at a given temperature, dimensionless

ϵ_b = total hemispherical emittance of the calorimetric emittance apparatus blackbody surface, dimensionless

= total hemispherical emittance of a FPC boundary surface, dimensionless

ϵ_s = total hemispherical emittance of an insulation radiation shield surface, dimensionless

ϵ_{TH} = same as ϵ_s

ϵ_{TN} = total normal emittance of an insulation radiation shield surface, dimensionless

ϵ_{TR} = total hemispherical emittance of an insulation radiation shield surface at room temperature, dimensionless

ϵ_{TR4} = total hemispherical emittance of one particular surface of an insulation radiation shield at room temperature, dimensionless

ϵ_{TR5} = total hemispherical emittance of the opposite surface of an insulation radiation shield at room temperature, dimensionless

η = parameter used to describe the ratio of heat increments transferred by the conduction and radiation processes, dimensionless

θ = increment of time, hr

λ' = parameter used to describe the ratio of the radiation energy absorbed to that scattered by an insulation spacer material, dimensionless

ρ = density of the boiloff gas from the calorimetric fluid used in the FPC, lbm/ft^3 (kg/m^3)

= bulk density of a material, lbm/ft^3 (kg/m^3)

ρ_N = near-normal reflectance of an insulation radiation shield surface, dimensionless

σ = Stefan-Boltzmann constant = 1.713×10^{-9} Btu/hr $ft^{2o}R^4$ (5.669×10^{-8} $w/m^{2o}K^4$)

$\bar{\sigma}$ = electrical conductivity of a metallic film

σ_b = electrical conductivity of a bulk metal

τ_o = parameter used to describe the optical thickness of an insulation spacer material, dimensionless

Φ = increment of solid conduction heat transfer normalized for the number of layers and the boundary temperatures, Btu/hr $ft^{2o}R^2$ ($w/m^{2o}K^2$)

REFERENCES

1. Black, I. A. and Glaser, P. E., "The Performance of a Double-Guarded Cold Plate Thermal Conductivity Apparatus," Advances in Cryogenic Engineering (Plenum Press, N.Y., 1964), Vol. 9, p 52

2. Coston, R. M. and Zierman, C. A., "Crygenic Thermal Conductivity Measurements of Insulating Materials," Special Technical Publication No. 411, ASTM, 1967

3. Caren, R. P. and Cunnington, G. R., "Heat Transfer in Multilayer Insulation Systems," Chemical Engineering Progress Symposium Series, Vol. 64, No. 87, 1968, p 67

4. Caren, R. P., "Low-Temperature Emittance Determinations," Progress in Astronautics and Aeronautics, Edited by G. B. Heller (Academic Press, New York, 1966), Vol. 18, p 61

5. Jakob, M., Heat Transfer, (John Wiley & Sons, Inc., New York, 1949), Vol. I, p 52

6. Coston, R. M. and Vliet, G. C., "Thermal Energy Transport Characteristics along the Laminations of Multilayer Insulations," Progress in Astronautics and Aeronautics, Edited by G. B. Heller (Academic Press, New York, 1967), Vol. 20, p 909

7. Viskanta, R., "Heat Transfer by Conduction and Radiation in Absorbing and Scattering Materials," J. Heat Transfer (ASME, 1965) Vol. 87C, p 143

8. Wang, L. S. and Tien, C. L., "Study of the Interactions between Radiation and Conduction by a Differential Method," Proceedings of the Third International Heat Transfer Conference, (ASME, 1966), Vol. 5, p 190

9. Wang, L. S. and Tien, C. L., "A Study of Various Limits in Radiation Heat Transfer Problems," Int. J. Heat Mass Transfer (Pergamon Press, Ltd., London, 1967) Vol. 10, p 1327

10. Cunnington, G. R., et al, "Performance of Multilayer Insulation Systems for Temperatures to 700°K," NASA CR-907, Oct. 1967, p 59

11. Boehm, R. F. and Tien, C. L., "Radiative Transfer between Metallic Surfaces at Cryogenic Temperature, Part III, Small Spacing Analysis," J. Heat Transfer, to be published

12. Caren, R. P. "Radiation Transfer from a Metal to a Finely Divided Particulate Medium," J. Heat Transfer, to be published

13. Barnes, R. B. and Czerny, M., "Concerning the Reflection Power of Metals in Thin Layers for the Infrared," Physical Review, Vol. 38, 1931, p 338

14. Reuter, G. E. H. and Sandheimen, E. H., "The Theory of the Anomalous Skin Effects in Metals," Proc. Roy Soc., London, Ser. A, Vol. 195, 1948, p 336

15. Domoto, G. A., Boehms, R. F. and Tien, C. L., "Predictions of the Total Emissivity of Metals at Cryogenic Temperatures," Advances in Cryogenic Engineering, (Plenum Press, New York, 1968) Vol. 14, p 230

16. Fuchs, K., "The Conductivity of Thin Metallic Films According to Electron Theory of Metals," Camb Phil Soc, Vol. 34, 1938, p 100

17. Tien, C. L., Armaly, F. G., and Jagannathon, P. S., "Thermal Conductivity of Thin Metallic Films and Wires at Cryogenic Temperatures," Proceedings of the Eighth Thermal Conductivity Conference (Plenum Press, New York, 1969), p 13

18. Armaly, F. G. and Tien, C. L., "Emissivities of Metals at Cryogenic Temperatures," to be presented at the International Heat Transfer Conf., Paris, 1970

19. Cunnington, G. R., Bell, G. A., Armaly, B. F. and Tien, C. L., "Total Emittance Measurements of Thin Metallic Films at Cryogenic Temperatures," presented at the 8th AIAA Aerospace Sciencies Meeting, New York, Jan. 1970

REFERENCES FOR APPENDIX B

B-1 Dunkle, R. V.,"Emissivity and Inter-Reflection Relationships for Infinite Parallel Specular Surfaces," NASA SP-55, 1964, p 39

B-2 Domoto, G. A. and Tien, C. L., "Radiative Transfer Between Metallic Surfaces at Cryogenic Temperatures, Part I, Thick Film Analysis," J. Heat Transfer, to be published

B-3 Tien, C. L., "A Correlation for Thermal Contact Conductance of Nominally Flat Sufaces in Vacuum," Proceedings of the Seventh Thermal Conductivity Conference, NBS SP-302, 1968, p 755

B-4 Verschour, J. P. and Greebler, P., "Heat Transfer by Gas Conduction and Radiation in Fibrous Insulations," Trans. Am. Soc. Mech. Eng., Vol. 74, 1952

B-5 Folkman, N. R. and Lee, T. G., "Thermodynamic Design Fundamentals of High-Performance Insulation," J. Spacecraft and Rockets, Vol. 5, No. 8, Aug. 1968, p 954

DISTRIBUTION LIST FOR INTERIM REPORT, NASA CR-72605,
THERMAL PERFORMANCE OF MULTILAYER INSULATIONS

		COPIES
National Aeronautics and Space Administration Lewis Research Center 21000 Brookpark Road Cleveland, Ohio 44135		
Attention:	Contracting Officer, MS 500-313	1
	Liquid Rocket Technology Branch, MS 500-209	8
	Technical Report Control Office, MS 5-5	1
	Technology Utilization Office, MS 3-16	1
	AFSC Liaison Office, MS 4-1	2
	Library	2
	D. L. Nored, MS 500-209	1
	Office of Reliability & Quality Assurance, MS 500-111	1
	E. W. Conrad, MS 100-1	1
	W. E. Roberts, MS 3-17	1
	R. Knoll, MS 501-2	1
	J. Kennard, MS 3-14	1
National Aeronautics and Space Administration Washington, D. C. 20546		
Attention:	Code MT	1
	RPX	2
	RPL	2
	SV	1
	RV-2	1
Scientific and Technical Information Facility P. O. Box 33 College Park, Maryland 20740		
Attention:	NASA Representative Code CRT	6
Office of the Director of Defense Research & Engineering Washington, D. C. 20301		
Attention:	Dr. H. W. Schulz, Office of Asst. Dir. (Chem Technology)	1

	COPIES
Defense Documentation Center Cameron Station Alexandria, Virginia 22314	1
RTD (RTNP) Bolling Air Force Base Washington, D. C. 20332	1
Arnold Engineering Development Center Air Force Systems Command Tullahoma, Tennessee 37389 Attention: AEOIM	1
Advanced Research Projects Agency Washington, D. C. 20525 Attention: D. E. Mock	1
Aeronautical Systems Division Air Force Systems Command Wright-Patterson Air Force Base, Dayton, Ohio Attention: D. L. Schmidt, Code, ASRCNC-2	1
Air Force Missile Test Center Patrick Air Force Base, Florida Attention: L. J. Ullian	1
Air Force FTC (FTAT-2) Edwards Air Force Base, California 93523 Attention: Col. J. M. Silk	1
Air Force Officer of Scientific Research Washington, D. C. 20333 Attention: SREP, Dr. J. F. Masi	1
National Aeronautics and Space Administration Ames Research Center Moffett Field, California 94035 Attention: Library	1
National Aeronautics and Space Administration Goddard Space Flight Center Greenbelt, Maryland 20771 Attention: Library W. C. Lund, Code 623	1 1

	COPIES
National Aeronautics and Space Administration John F. Kennedy Space Center Cocoa Beach, Florida 32931	
Attention: Library	1
National Aeronautics and Space Administration Langley Research Center Langley Station Hampton, Virginia 23365	
Attention: Library	1
R. R. Heldenfels	1
National Aeronautics and Space Administration Manned Spacecraft Center Houston, Texas 77001	
Attention: Library	1
Merlyn Lausten (EP-2)	1
National Aeronautics and Space Administration George C. Marshall Space Flight Center Huntsville, Alabama 35812	
Attention: Library	1
Keith Chandler, S &E -ASTN	1
Clyde Nevins	1
E. H. Hyde	1
I. G. Yates	1
J. M. Stuckey	1
Jet Propulsion Laboratory 4800 Oak Grove Drive Pasadena, California 91103	
Attention: Library	1
Lou Toth	1
U. S. Air Force Washington 25, D. C.	
Attention: Col. C. K. Stambaugh, Code AFRST	1
Bureau of Naval Weapons Department of the Navy Washington, D. C.	
Attention: J. Kay, Code RTMS-41	1
Commanding Officer Office of Naval Research 1030 E. Green Street Pasadena, California 91101	1

	COPIES
Director (Code 6180) U. S. Naval Research Laboratory Washington, D. C. 20390 Attention: H. W. Carhart	1
Picatinny Arsenal Dover, New Jersey Attention: I. Forsten, Chief Liquid Propulsion Laboratory	1
Aerojet-General Corporation P. O. Box 296 Azusa, California 91703 Attention: Librarian	1
Aerojet-General Corporation P. O. Box 1947 Sacramento, California 95809 Attention: Technical Library 2484-2015A	1
Aeronutronic Division Philco Corporation Ford Road Newport Beach, California 92600 Attention: Library	1
Aeroprojects, Incorporated 310 East Rosedale Avenue West Chester, Pennsylvania 19380 Attention: C. D. McKinney	1
Aerospace Corporation P. O. Box 95085 Los Angeles, California 90045 Attention: J. C. Wilder, MS-2293 Library-Documents	1 1
Air Products and Chemicals, Inc. Allentown, Pennsylvania Attention: A. Lapin	1
Arthur D. Little, Inc. 20 Acorn Park Cambridge, Mass. 02140 Attention: R. B. Hinckley F. Gabron	1 1

	COPIES
Atlantic Research Corporation Shirley Highway & Edsall Road Alexandria, Virginia 22314 Attention: Security Office for Library	1
Battelle Memorial Institute 505 King Avenue Columbus, Ohio 43201 Attention: Report Library, Room 6A	1
Beech Aircraft Corporation Boulder Facility Box 631 Boulder Colorado 80302 Attention: J. H Rodgers R. L. Reed	1 1
Bell Aerosystems, Inc. Box 1 Buffalo, New York 14205 Attention: T. Reinhardt W. M. Smith	1 1
Autonetics 3370 Miraloma Avenue Anaheim, California 92803 Attention: Dr. Edward Lax Dept. 447, Bldg. 202	1
The Boeing Company Space Division P. O. Box 3868 Seattle, Washington 98124 Attention: Library C. F. Tiffany	1 1
The Bendix Corporation Instruments and Life Support Division P. O. Box 4508 Davenport, Iowa 52808 Attention: Wm. Carlson	1
Chemical Propulsion Information Agency Applied Physics Laboratory 8621 Georgia Avenue Silver Spring, Maryland 20910	1

	COPIES
Curtiss-Wright Corporation Wright Aeronautical Division Woodridge, New Jersey Attention: G. Kelley	1
University of Denver Denver Research Institute P. O. Box 10127 Denver, Colorado 80210 Attention: Security Office	1
McDonnell Douglas Corporation Santa Monica Division 3000 Ocean Park Blvd. Santa Monica, California 94005 Attention: J. W. Price	1
General Dynamics/Astronautics P. O. Box 1128 San Diego, California 92112 Attention: Library & Information Services (128-00)	1
Convair Division General Dynamics Corporation P. O. Box 1128 San Diego, California 92112 Attention: R. Tatro Paul Stevens	1 1
General Electric Company Flight Propulsion Lab. Department Cincinnati 15, Ohio Attention: D. Suichu	1
Grumman Aircraft Engineering Corporation Bethpage, Long Island, New York Attention: Joseph Gavin	1
The Garrett Corporation 1625 Eye Street, N. W. Washington, D. C. Attention: G. R. Shepard	1
IIT Research Institute Technology Center Chicago, Illinois 60616 Attention: Technical Library	1

	COPIES
Goodyear Aerospace Corporation 1210 Massillon Road Akron, Ohio Attention: Clem Shriver, Dept. 481	1
Marquardt Corporation 16555 Saticoy Street Box 2013 - South Annex Van Nuys, California 91404 Attention: Librarian W. D. Boardman, Jr.	 1 1
Martin-Marietta Corporation Martin Division Baltimore 3, Maryland Attention: Science-Technology Library	 1
McDonnell Douglas Corporation P. O. Box 6101 Lambert Field, Missouri Attention: R. A. Herzmark	 1
North American Aviation, Inc. Space & Information Systems Division 12214 Lakewood Boulevard Downey, California 90242 Attention: Technical Information Center, D/096-722 (AJ01) H. Storms	 1 1
Northrop Space Laboratories 1001 East Broadway Hawthorne, California Attention: Dr. William Howard	 1
Purdue University Lafayette, Indiana 47907 Attention: Technical Librarian	 1
Republic Aviation Corporation Farmingdale, Long Island New York Attention: Dr. William O'Donnell	 1
Rocketdyne Division of North American Rockwell, Inc. 6633 Canoga Avenue Canoga Park, California 91304 Attention: Library, Department 596-306	 1

	COPIES
Stanford Research Institute 333 Ravenswood Avenue Menlo Park, California 94025	
Attention: P. R. Gillette	1
TRW Systems, Incorporated 1 Space Park Redondo Beach, California 90200	
Attention: G. W. Elverum	1
STL Tech. Lib. Doc. Acquisitions	1
Union Carbide Corporation Linde Division P. O. Box 44 Tonawanda, New York 14152	
Attention: G. Nies	1
United Aircraft Corporation Corporation Library 400 Main Street East Hartford, Connecticut 06118	
Attention: Dr. David Rix	1
Erle Martin	1
United Aircraft Corporation United Technology Center P. O. Box 358 Sunnyvale, California 94088	
Attention: Librarian	1
Cryonetics Corporation Northwest Industrial Park Burlington, Massachusetts	
Attention: James F. Howlett	1
Martin-Marietta Corporation Denver Division Denver, Colorado	
Attention: Library	1
D. W. Murphy	1
National Research Corporation 70 Memorial Drive Cambridge, Mass.	1

	COPIES
New York University University Heights New York, New York Attention: P. F. Winternitz	1
National Aeronautics and Space Administration Flight Research Center P. O. Box 273 Edwards, California 93523 Attention: Library	1
Commander U. S. Naval Missile Center Point Mugu, California 93041 Attention: Technical Library	1